APPLIED COMPUTATIONAL ELECTROMAGNETICS SOCIETY JOURNAL

Advances in Next-Generation Antenna Systems and Their Testing Methodologies

Guest Editors:

Xiaoming Chen, Xi'an Jiaotong University, China
Zhengbo Jiang, Southeast University, China
Yingsong Li, Anhui University, China

February 2026
Vol. 41 No. 02
ISSN 1054-4887

The ACES Journal is abstracted in INSPEC, in Engineering Index, DTIC, Science Citation Index Expanded, the Research Alert, and to Current Contents/Engineering, Computing & Technology.

The illustrations on the front cover have been obtained from the ARC research group at the Department of Electrical Engineering, Colorado School of Mines

Published, sold and distributed by: River Publishers, Broagervej 10, 9260 Gistrup, Denmark

FEBRUARY 2026 REVIEWERS

Xiaoming Chen
Atef Elsherbeni
Zhengbo Jiang
Yingsong Li
Jian Liu
Nelson Santos

THE APPLIED COMPUTATIONAL ELECTROMAGNETICS SOCIETY JOURNAL

Vol. 41 No. 02 February 2026

TABLE OF CONTENTS

Introduction to the Special Issue

Advances in Next-Generation Antenna Systems and Their Testing Methodologies

Guest Editors:

Xiaoming Chen, Xi'an Jiaotong University, China

Zhengbo Jiang, Southeast University, China

Yingsong Li, Anhui University, China

Welcome to the special issue of the *Applied Computational Electromagnetics Society (ACES) Journal*. This special issue brings together a collection of state-of-the-art research findings aimed at advances in next-generation antenna systems and their testing methods.

The special issue covers the following topics

- Microwave and millimeter-wave antenna arrays
- Reconfigurable intelligent surfaces
- Reflectarray and transmitarray
- Mutual coupling role in antenna arrays
- Antenna diagnosis and measurements methodologies
- Over-the-air tests

We'd like to also thank the Editors in Chief of ACES Journal, Professor Sami Barmadi and Professor Atef Elsherbeni for their support. And we'd like to express our thanks to the editorial and publication team at ACES Journal for their assistance.

Low-Loss 16-Way Ultra-Wideband Wilkinson Power Divider

Jorge A. Caripidis Troccola[1], Satheesh Bojja Venkatakrishnan[1], Cedric W. L. Lee[2], Theng Huat Gan[2], and John L. Volakis[1]

[1]Department of Electrical Engineering
Florida International University, Miami, FL, 33174, USA
jcari006@fiu.edu, sbojjave@fiu.edu, jvolakis@fiu.edu

[2]National University of Singapore, Singapore 117411
c.lee@nus.edu.sg, thenghuat@nus.edu.sg

Abstract – Several power divider designs exist in the literature and are also commercially available. However, these dividers are not wideband. In this paper, a low-loss, ultra-wideband (UWB) 16-way power divider for UWB applications is presented. Notably, the design employs 15 cascaded multi-stage Wilkinson power dividers with a total of 90, 0402 package surface mounted chip resistors to enable operation from 0.2 to 3.6 GHz. Remarkably, the fabricated prototype achieves an 18:1 input and output impedance bandwidth with VSWR < 1.2 thanks to an optimization approach that eliminates any additive reflection from each of the power division stages. In addition, the maximum insertion loss is 3 dB at the highest frequency of operation, while the maximum phase imbalance between output ports is 4 degrees. The measurements show excellent agreement with the simulations.

Index Terms – Feed network, power divider, ultra-wideband, Wilkinson.

I. INTRODUCTION

Power dividers are essential components in RF and microwave systems, enabling signal splitting for various applications, including telecommunications, radar, and wireless communication systems [1]. Their role is to distribute signals equally or with specified ratios across multiple pathways. Power dividers are generally classified into a few types: resistive, T-Junction, Wilkinson, and hybrid. A typical limitation among these dividers is their narrow bandwidth, which makes them unsuitable for bandwidth demanding applications [2]. In modern ultra-wideband (UWB) systems, it is crucial to have a power divider that can operate over a broad range of frequencies (>2:1) while maintaining low insertion loss [3], good port isolation, and minimal phase imbalance. For instance, in the phase-array designs presented in [4–8], a power divider with the specified characteristics could serve as an effective feeding network. Other practical scenarios where UWB power dividers can be beneficial include high precision imaging and positioning systems [9, 10].

Different designs to extend the bandwidth of power dividers have been explored. For example, in [11], a two-way, multilayer slotline power divider was shown to operate from 3.1 to 10 GHz. Additionally, in [12], a microstrip power divider using a pair of stepped-impedance open-circuited stubs and parallel coupled lines achieved a bandwidth ratio of 3.4:1. Moreover, a feed network design consisting of cascaded three-stage Wilkinson power dividers was used to feed a 16-element phased antenna array across 5 to 30 GHz [13]. Also, in [14], an 8-way power divider with printed carbon ink resistors and tapered microstrip lines operated from 0.5 to 25 GHz. While these designs increased the operational bandwidth as compared to traditional power dividers, there are still some shortcomings. For instance, the designs from [11] and [12] achieved a bandwidth ratio of only 3.4:1 and for only two output ports. The design presented in [13] increased the number of output ports to 16 with a bandwidth ratio of 6:1. However, 6:1 is still not large enough for some demanding UWB applications. Lastly, the 8-way resistive power divider from [14] achieved a bandwidth ratio of 50:1, but suffered from an insertion loss of up to 7 dB at the high band. With respect to [13] and [14], our proposed design provides 3× improvement in bandwidth and a 4 dB improvement in insertion loss at higher bands, respectively.

To concurrently achieve large bandwidth, low loss, and high number of output ports, this paper introduces a 16-way power divider that exhibits 18:1 bandwidth and very low insertion loss across the frequency band. Notably, the proposed design is structured using a series of 15 cascaded multi-stage Wilkinson power

Submitted On: June 17, 2025
Accepted On: November 24, 2025

https://doi.org/10.13052/2026.ACES.J.410201

dividers, each optimized for low insertion loss and high impedance bandwidth. By incorporating a total of 90, 0402 chip resistors, the design is able to operate from 0.2 GHz to 3.6 GHz. The power divider's input and output impedance port matching are further optimized to mitigate reflective losses that could otherwise accumulate across the cascading stages.

The optimized architecture yields significant performance benefits, achieving a maximum insertion loss of only 3 dB at the highest operational frequency while maintaining the phase imbalance between output ports below 4 degrees. These characteristics make the proposed power divider highly attractive for UWB array feeding. A prototype was fabricated and measured to verify the performance. The following sections present the design methodology, implementation details, prototype fabrication, and performance analysis. A 16-port power divider achieving a bandwidth ratio greater than 15 : 1, while maintaining low insertion loss and minimal phase imbalance, is not commonly found in the literature. This work contributes a novel solution addressing these challenges within a compact and optimized architecture.

II. POWER DIVIDER DESIGN AND SIMULATION

A. Design considerations

In a traditional Wilkinson divider, the circuit splits the input power into two equal outputs through quarter-wave transmission line sections that transform the output impedance back to the input impedance. For a simple two-way divider, the impedance of each quarter wave transformer/leg is chosen as [15]:

$$Z_0' = \sqrt{2}Z_0, \tag{1}$$

where Z_0 is the characteristic impedance of the overall system (typically 50 Ω). This impedance transformation ensures that each output port maintains a matched condition with respect to the input, minimizing reflections. Furthermore, a resistor connecting the two output ports (of value $2Z_0$) absorbs any potential imbalances in power or phase between the outputs, providing isolation and preventing undesired coupling [15, 16]. Notably, a single-stage Wilkinson power divider, while effective for narrowband applications, cannot maintain low VSWR and consistent performance across ultra-wideband frequencies. This limitation arises due to the quarter-wave impedance transformation only working optimally at a specific frequency, leading to increased mismatches and higher losses outside a narrow range.

The design of each 1-to-2 Wilkinson cell division followed a systematic procedure to balance bandwidth and complexity. First, the target operating band $[f_1, f_2]$ was defined, and the center frequency was set as $f_0 = \sqrt{(f_1 f_2)}$, with all quarter-wave lines designed to be $\lambda_g/4$ at f_0. To determine the minimum number of sections, m, we began with a single quarter-wave section and evaluated the simulated return loss across the band. If the response did not meet the expected return-loss target ($\geq$ 10–15 dB), more $\lambda_g/4$ sections were added. The smallest m value that satisfied the set specification was selected to minimize both insertion loss and layout complexity.

For a single-section divider, the quarter-wave impedance per branch was set to $Z' = \sqrt{2}Z_0$ with a single isolation resistor of $R = 2Z_0$ placed between the output ports. For the multi-section designs, a progression of impedances $(Z_1, Z_2, \ldots, Z_m)$ were employed to realize the gradual transformation from Z_0 to $2Z_0$. Correspondingly, multiple resistors were distributed along the arms such that their combined effect maintained approximately $2Z_0$ isolation at the design frequency. This distribution provided a flatter isolation response across the wideband range as compared to using a single lumped resistor.

Each impedance value was then translated into physical microstrip dimensions using standard microstrip equations. To further suppress parasitic reflections, adjacent sections were connected using short linear tapers rather than abrupt width steps. The final optimization values were performed through circuit simulations to ensure that the bandwidth, insertion loss, return loss, and isolation targets were simultaneously achieved.

To overcome bandwidth limitations, a multi-stage Wilkinson power divider design is adopted. The proposed design uses a six-stage (meaning each cell includes six resistors) Wilkinson divider structure within each of the 15 cascaded cells. This approach divides the power sequentially in steps, achieving incremental impedance transformations that enable the divider to achieve large bandwidths. The layout of the proposed divider is shown in Fig. 1.

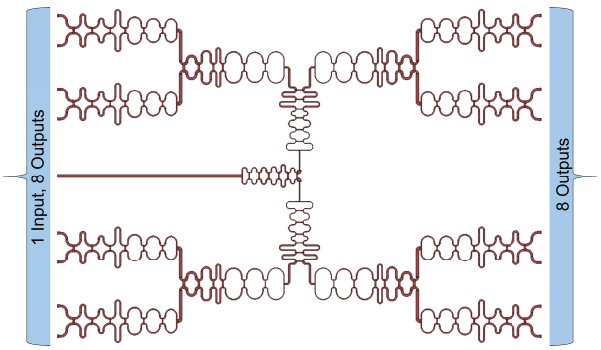

Fig. 1. Layout of the proposed 16-way power divider.

B. Geometry optimization for UWB performance

In the initial design phase of the 16-way power divider, we followed a modular approach that consisted in creating a single six-stage, two-way Wilkinson power divider unit cell able to operate from 0.2 to 3.6 GHz. These identical unit cells were then cascaded in a sequential manner, ultimately obtaining 16 outputs, by continuously splitting the signal in stages, as shown in Fig. 2.

However, this approach encountered significant challenges in a practical implementation, as evidenced by the input VSWR shown in Fig. 2. Specifically, the input VSWR plot reveals a resonance at 0.6 GHz and many more higher frequency resonances, which degraded the input matching significantly across the band. These resonances were caused by cumulative reflections that emerged due to the repeated cascading of identical unit cells. These mismatches added to one another at certain frequencies where the phase alignment of reflected signals reinforced each other. As these reflections compounded, they introduced strong resonances within the VSWR, ultimately compromising the bandwidth and performance of the divider.

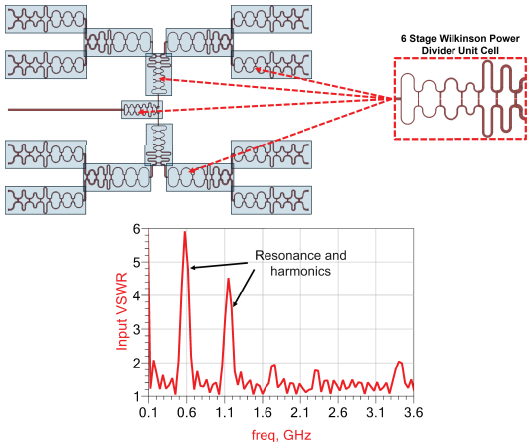

Fig. 2. Details of modular design with identical unit cells and VSWR performance. Cumulative reflection creates resonance at 0.6 GHz and its corresponding harmonics.

To address the resonances, we implemented a geometry optimization process for each stage of the divider. Rather than using identical unit cells, we optimized several design parameters for each individual power splitting section within the division stages, creating four unique modules represented by colors in Fig. 3. This careful adjustment provided a unique impedance transformation for each stage, breaking the repetitive pattern that had previously led to resonances. The schematic of the design's modules is shown in Fig. 4, with the component values and dimensions detailed in Tables 1 through 5.

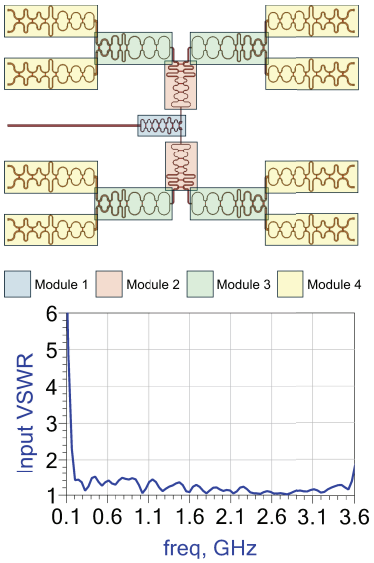

Fig. 3. Optimized design layout and VSWR performance of 16-way power divider operating from 0.2 to 3.6 GHz. Each stage of the power division, represented by different colored modules, is composed of a series of unique, optimized, two-way, six-stage Wilkinson power dividers. Any cumulative reflection is eliminated.

In the optimization process, multiple design parameters were strategically selected. The width and length of each line segment were calculated to maintain impedance matching across the operating band. In addition, gradual tapering in certain transmission line sections was introduced to facilitate smooth impedance transitions. This technique minimized abrupt impedance changes between sections, reducing reflection and enhancing bandwidth. Furthermore, the values of the 0402 chip resistors were optimized at each stage to absorb any imbalances and provide effective isolation between adjacent outputs. The resistors prevent interport coupling by dissipating unwanted signals, ensuring isolation as well as phase stability across the wide bandwidth. Moreover, the distance between consecutive sections was also adjusted to reduce coupling and minimize reflections. Importantly, each section of the power divider was meandered in order to reduce the size of the structure, as depicted in Fig. 4. Overall, the meticulous optimization created a distinct impedance transformation at each stage, effectively disrupting the repetitive structural pattern and eliminating cumulative reflections that had previously led to resonances.

C. Simulations

Simulations of the optimized design from Fig. 3 are shown in Fig. 5. A two-step optimization process was applied to refine the divider design. The first,

Table 1: Two step optimization process

Parameter Category	Initial Values (Through Derivation)	Constraints in Optimization
Transmission line widths	Calculated from closed-form microstrip equations for each impedance Z_K	Limited by available substrates and manufacturing pitch (min trace width $\geq$ 5 mil)
Transmission line lengths	Set to $\lambda_g/4$ at center frequency f_0	Tuned within $\pm$15% during circuit optimization
Isolation resistors	Set to $R = 2Z_o$ (single-section), and distributed for multi-section arms	Adjusted within $\pm$15% during circuit optimization
Number of sections per arm	Determined by return-loss target ($\geq$ 10–15 dB)	Limited to ≤ 8 to minimize complexity
Cascading strategy	Initially, identical 1-to-2 cells. Further optimized based on their dependence to previous stages	Fixed 16-way network topology

Table 2: Microstrip transmission lines dimensions

Components	Module 1		Module 2		Module 3		Module 4	
	W (mm)	L (mm)	W (mm)	L (mm)	W (mm)	L (mm)	W (mm)	L (mm)
MTL1	1.69	117.22	0.87	1.80	1.13	0.78	2.05	0.76
MTL2	0.54	2.94	0.28	5.80	0.36	4.26	0.65	2.25
MTL3	0.54	0.31	0.28	2.58	0.36	1.10	0.65	0.31
MTL4	0.54	1.69	0.28	1.97	0.33	1.86	0.65	1.01
MTL5	0.48	0.30	0.30	1.80	0.53	0.67	0.31	0.67
MTL6	0.48	0.30	0.30	0.32	0.53	0.67	0.31	0.67
MTL7	0.48	1.58	0.46	1.89	0.53	1.74	0.31	0.95
MTL8	0.75	0.31	0.47	0.58	0.71	1.04	0.78	1.33
MTL9	0.75	0.31	0.47	0.90	0.71	1.66	0.78	0.92
MTL10	0.75	1.58	0.47	1.90	0.87	7.33	0.85	1.14
MTL11	0.59	1.58	0.47	1.90	0.87	7.27	0.85	0.95
MTL12	0.59	0.73	0.46	1.77	0.87	1.56	0.85	0.87
MTL13	0.59	1.54	0.46	1.77	0.87	1.56	0.85	0.87
MTL14	0.82	2.30	0.71	7.46	1.12	3.82	1.00	1.04
MTL15	0.82	1.58	0.71	1.68	1.12	3.92	1.00	2.20
MTL16	0.82	1.58	0.71	1.68	1.12	3.92	1.00	2.20
MTL17	0.55	0.73	0.53	1.58	0.71	0.66	1.19	3.20
MTL18	0.55	0.73	0.53	0.63	0.71	0.66	1.19	3.20
MTL19	0.55	0.83	0.53	1.58	0.71	0.66	1.19	3.20
MTL20	0.87	0.38	1.13	2.05	0.30	1.43	0.30	1.43

Table 3: Microstrip T-Junction dimensions

Components	Module 1 (mm)			Module 2 (mm)			Module 3 (mm)			Module 4 (mm)		
	W1	W2	W3	W1	W2	W3	W1	W2	W3	W1	W2	W3
MTJ1	0.54	0.54	1.69	0.28	0.28	0.87	0.36	1.13	0.65	0.65	2.05	0.85
MTJ2	0.54	0.48	0.54	0.28	0.30	0.28	0.53	0.41	0.65	0.67	0.65	0.65
MTJ3	0.48	0.75	0.48	0.30	0.47	0.48	0.71	0.53	0.67	0.78	0.67	0.67
MTJ4	0.75	0.59	0.75	0.47	0.46	0.47	0.87	0.71	0.85	0.85	0.78	0.85
MTJ5	0.59	0.82	0.59	0.46	0.71	0.46	1.12	0.87	1.00	1.00	0.85	1.00
MTJ6	0.82	0.55	0.82	0.71	0.89	0.71	1.12	1.12	1.00	1.19	1.00	1.19
MTJ7	0.55	1.24	0.55	0.89	1.24	0.89	1.53	1.24	1.19	1.43	1.19	1.19

Table 4: Curved microstrip transmission lines dimensions

Components	Module 1 (mm)			Module 2 (mm)			Module 3 (mm)			Module 4 (mm)		
	W	∠ (°)	R	W	∠ (°)	R	W	∠ (°)	R	W	∠ (°)	R
MC1	0.54	180	1.51	0.28	180	2.16	0.36	180	5.08	25.56	180	4.17
MC2	0.54	90	1.27	0.28	90	1.27	0.36	90	1.36	25.56	90	1.37
MC3	0.48	90	1.27	0.30	90	1.27	0.53	90	1.36	26.40	90	1.37
MC4	0.48	180	1.51	0.30	180	2.16	0.53	180	5.08	26.40	180	4.17
MC5	0.48	90	1.27	0.30	90	1.27	0.53	90	1.36	30.58	90	1.37
MC6	0.75	90	1.27	0.47	90	1.27	0.71	90	1.36	30.58	90	1.37
MC7	0.75	180	1.51	0.47	180	2.16	0.71	180	5.08	30.58	180	4.17
MC8	0.75	90	1.27	0.47	90	1.27	0.71	90	1.36	33.51	90	2.71
MC9	0.59	90	1.35	0.46	90	1.28	0.87	90	1.27	33.51	90	2.71
MC10	0.59	180	1.51	0.46	180	1.27	0.87	180	2.84	39.53	180	3.77
MC11	0.59	90	1.27	0.46	90	1.28	0.87	90	1.27	39.53	90	3.77
MC12	0.59	90	1.27	0.71	90	1.28	1.12	90	1.27	39.53	90	3.77
MC13	0.82	180	1.27	0.71	180	1.43	1.12	180	2.84	46.77	180	3.77
MC14	0.82	90	1.27	0.71	90	1.27	1.12	90	1.27	46.77	90	3.77
MC15	0.55	90	1.27	0.89	90	1.28	1.53	90	1.27	46.77	90	3.77
MC16	0.55	180	1.27	0.89	180	1.43	1.53	180	2.84	56.14	180	3.77
MC17	0.55	90	1.27	0.89	90	1.28	1.53	90	1.27	56.14	90	3.77
MC18	2.33	90	1.27	1.24	90	1.28	1.24	90	1.27	56.14	90	3.77

Table 5: Tapered microstrip transmission lines dimensions

Components	Module 1 (mm)			Module 2 (mm)			Module 3 (mm)			Module 4 (mm)		
	W1	W2	L	W1	W2	L	W1	W2	L	W1	W2	L
MTP1	0.55	0.87	0.32	1.24	1.13	0.31	0.54	2.05	0.31	1.43	1.69	1.57

Table 6: 0402 resistor values

Components	Module 1	Module 2	Module 3	Module 4
	Resistance (Ω)	Resistance (Ω)	Resistance (Ω)	Resistance (Ω)
R1	150.00	150.00	150.00	261.00
R2	261.00	154.00	180.00	300.00
R3	300.00	267.00	242.00	300.00
R4	348.00	294.00	348.00	348.00
R5	300.00	300.00	300.00	300.00
R6	300.00	300.00	100.00	300.00

circuit-level simulations were performed in Keysight's ADS, where the cascaded 1-to-2 Wilkinson cells were optimized based on the starting values described in section II, part B. The optimization was carried out in a sequential manner, with each subsequent cell tuned while accounting for the response of the preceding stage. In this manner, no two cells remained identical in the final implementation. The latter was key to suppressing cumulative impedance mismatches and potential resonances.

Once the complete 16-way structure was finalized at the circuit level, the layout was transferred into Ansys HFSS for full-wave electromagnetic simulation. This final validation ensured that electromagnetic coupling, discontinuities, and higher-order effects were properly captured. The initial design parameters used in the optimization process were not arbitrarily selected but were derived from the synthesis procedure outlined in section II, part B (resistor selection, microstrip line width/length calculation, taper calculation, etc.). Table 1 summarizes the key parameter categories and the constraints applied during optimization.

As shown in Fig. 5, the design operates from 0.20 to 3.6 GHz and demonstrates an impressive 18:1 bandwidth with an input VSWR < 1.5 and an output VSWR < 1.8. Furthermore, the design achieves an insertion loss of only 2 dB higher than that of an ideal 16-way power divider. Additionally, the port isolation is excellent, except for neighboring ports, where the isolation is ≈ 10 dB.

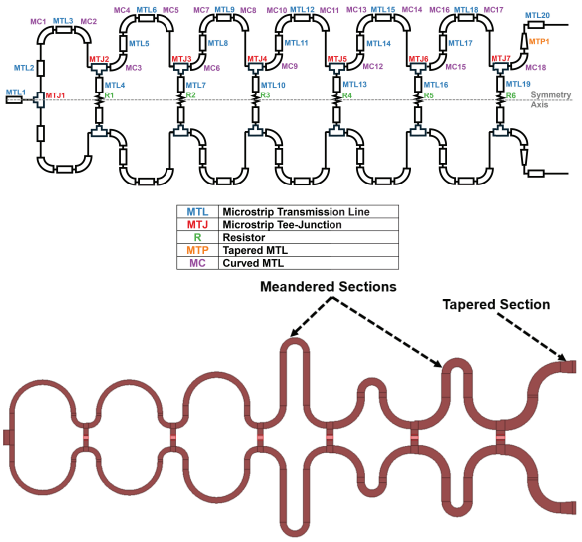

Fig. 4. Top to bottom: Power divider module schematic and Module 4 sample layout (notice meandering and tapering).

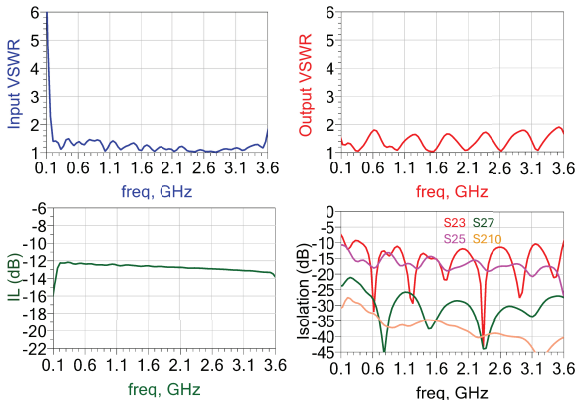

Fig. 5. Simulated input VSWR, output VSWR, insertion loss, and port isolation of the optimized, modular design from Fig. 3.

III. PROTOTYPE FABRICATION AND MEASUREMENTS

A. Fabricated prototype

A prototype of the optimized, 16-way Wilkinson power divider from Fig. 3 was fabricated on a Rogers 4350B substrate [17]. The substrate was selected for its suitable dielectric properties in high-frequency applications, featuring a relative permittivity of $\varepsilon_r = 3.66$, a loss tangent $\tan\delta = 0.0037$, and a total thickness of 0.76 mm.

The fabrication process involved the precise placement of 90 surface-mounted resistors in 0402 packages. Specifically, the 0402 resistor package size was chosen to be in compliance with the microstrip trace size. An automated pick-and-place machine was employed

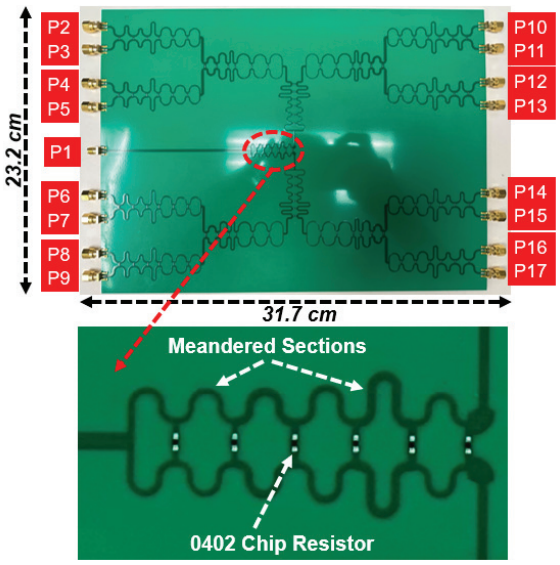

Fig. 6. Details of the fabricated 16-way power divider prototype.

to position the resistors, ensuring consistent alignment and reliable electrical contact. Notably, these resistors played a critical role in isolating output ports to maintain uniform performance across the broad bandwidth. For measurements, 17 SMA connectors were hand-soldered to the prototype. One connector was placed at the input port and 16 at the output ports. The fabricated prototype is shown in Fig. 6.

Notably, resistor tolerances and placement errors can introduce measurable amplitude and phase imbalances in power dividers, particularly in Wilkinson configurations. These variations were modeled and considered in our circuit-level and full wave electromagnetic simulation. Specifically, the deviations in values were imported from the datasheets of commercially available 0402 resistors. For example, a ±5% tolerance in the isolation resistor can lead to amplitude imbalances of up to ±0.4 dB and phase errors approaching ±5°[18], especially near the upper end of the operating frequency range. Placement inaccuracies, such as a 0.2 mm shift in resistor location or misalignment in microstrip geometry, can further increase mismatch, leading to degraded return loss and isolation performance. Simulations show that a shift of 0.2 mm in resistor placement within the transmission line can result in an increase of the insertion loss by 0.85 dB across the design frequency range.

Further, dielectric substrates used in microstrip circuits, such as FR4, Rogers 4350, and alumina (Al_2O_3), also impose power limitations governed by their thermal conductivity and dielectric breakdown thresholds. Standard substrates like FR4 and Ro4350 can only handle a few watts due to poor thermal dissipation,

while advanced ceramics such as alumina and aluminum nitride (AlN) can support power levels approaching 1–2 kW when paired with wide transmission lines and effective heat sinking. Nevertheless, MW-level power handling remains beyond the scope of microstrip technology and instead requires waveguide-based architectures, vacuum electron devices, and metal-ceramic structures.

B. Measurements

The performance of the fabricated 16-way Wilkinson power divider was measured using an E5071C ENA Vector Network Analyzer (VNA). The VNA measurements focused on evaluating several critical performance metrics, including port VSWR, insertion loss, isolation between output ports, and phase imbalance across the output ports. These measurements are plotted vs simulations in Fig. 7.

For the VSWR measurements, both input and output ports were evaluated to ensure impedance matching across the intended frequency range. As seen in Fig. 7, the measured input VSWR matches simulations, whereas the measured output VSWR is better than expected, verifying UWB operation from 0.2 to 3.6 GHz. In addition, the insertion loss was measured at every output port to assess the divider's efficiency in power distribution. Measurements of the insertion loss show good agreement with simulations. However, a slight drop in performance is seen as the frequency increases, where measurements exhibit an extra 1–2 dB of loss on average as compared to the simulations. This could be due to ohmic losses being more prevalent at high frequencies.

At upper bands, insertion loss in power dividers and similar RF structures often exceeds expected values based on ohmic losses alone. While conductor (ohmic) loss due to skin effect increases with frequency, its contribution is usually limited to ≈ 0.2–0.5 dB/inch on standard copper microstrip lines [19]. However, conductor surface roughness becomes a major contributor at these frequencies. For example, rough copper with RMS height $\approx 2\mu$m can increase effective resistance by 10-20 %, leading to additional losses of 0.5–1 dB/inch. Similarly, dielectric losses contribute meaningfully; for instance, Rogers RO4350B ($\tan\delta = 0.0037$ at 10 GHz) can cause 0.1–0.3 dB/inch loss [17], and material variability or temperature-induced dielectric drift can introduce further imbalance and phase error. Moreover, connector transitions and launch structures (e.g., SMA to microstrip) can add another 0.3—0.7 dB per interface due to imperfect impedance matching and ground continuity [20].

Still, the overall worst-case measured insertion loss is only 3 dB higher than the expected ideal 16-way

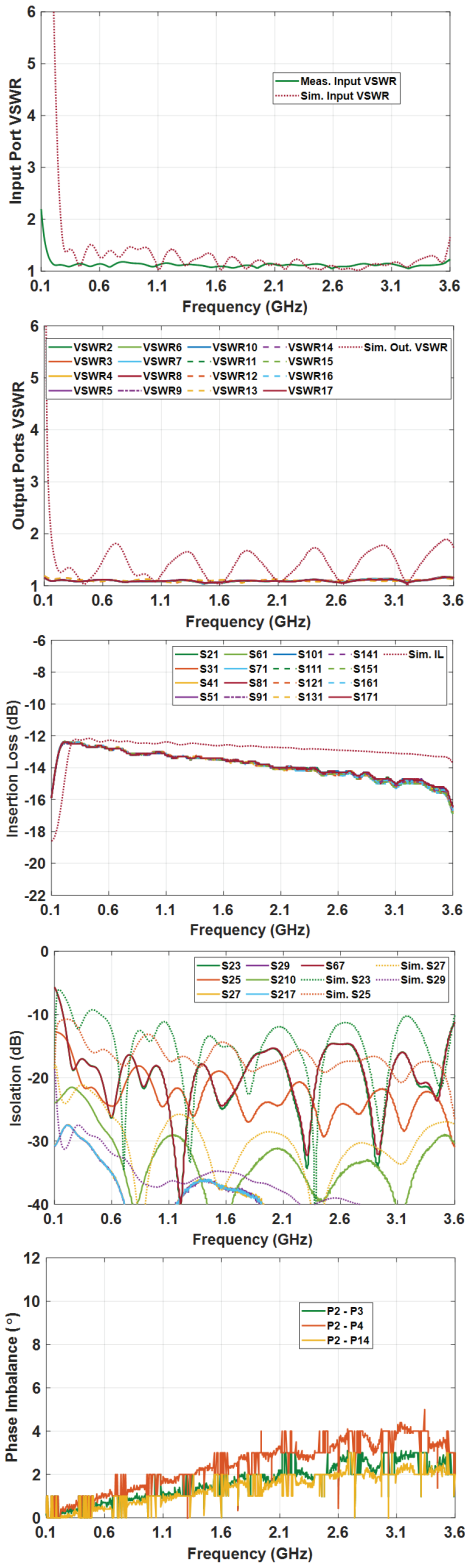

Fig. 7. Measured input VSWR, output VSWR, insertion loss, port isolation, and phase imbalance of the fabricated prototype from Fig. 6. Measured results are depicted in solid lines, while dotted lines present the simulation data.

power divider. To examine isolation between ports, measurements were taken across various port combinations. These included both neighboring ports and those spaced farther apart. As displayed in the isolation plots, measured curves show a slightly better performance across the whole band of operation, with the lowest isolation between neighboring ports being ≈15 dB. Finally, phase imbalances across the output ports were measured by assessing multiple port combinations. Both adjacent and distant port pairs were analyzed to determine the uniformity of the phase distribution. As seen from the plot, a maximum phase imbalance of 4 degrees was measured. We observed similar phase imbalance in all ports. This imbalance is well within acceptable limits, validating the divider's effectiveness in achieving stable phase performance across all output ports.

IV. CONCLUSION AND REMARKS

This work demonstrated the design, fabrication, and validation of a 16-way ultra-wideband Wilkinson power divider. The paper addressed the challenges of achieving a large number of ports for antenna array feeding across a wideband performance. Its wide bandwidth offers a clear potential for next-generation phased arrays and broadband RF systems, where uniform power distribution is essential. While the cascaded multi-stage approach was effective, some practical issues were observed, including sensitivity to resistor tolerances, complexity of the layout, and unoptimized power handling capability. These issues may restrict scalability and high-power operation. Future efforts could explore architecture simplification to enhance power handling as well as extend the concept to millimeter-wave frequencies and reconfigurable environments. Overall, the results establish a strong foundation for compact, wideband power division networks that can support the evolving demands of modern communication and sensing technologies.

REFERENCES

[1] D. M. Pozar, *Microwave Engineering*, 3rd ed. Hoboken, NJ, USA: Wiley, 2005, ch. 7, pp. 317–380.

[2] Microstrip and CPW Power Divider Design PathWave Advanced Design System (ADS). Available: https://www.keysight.com/us/en/assets/7018-05297/technical-overviews/5992-1632.pdf

[3] Microstrip Loss Calculations, https://www.microwaves101.com/encyclopedias/microstrip-loss-calculations

[4] M. Carvalho, A. D. Johnson, E. A. Alwan, and J. L. Volakis, "Semi-Resistive Approach for Tightly Coupled Dipole Array Bandwidth Enhancement," *IEEE Open Journal of Antennas and Propagation,* vol. 2, pp. 110–117, 2021.

[5] A. D. Johnson, J. Zhong, S. B. Venkatakrishnan, E. A. Alwan, and J. L. Volakis, "Phased Array With Low-Angle Scanning and 46:1 Bandwidth," *IEEE Transactions on Antennas and Propagation,* vol. 68, no. 12, pp. 7833–7841, Dec. 2020.

[6] J. Zhong, A. Johnson, E. A. Alwan, and J. L. Volakis, "Dual-Linear Polarized Phased Array With 9:1 Bandwidth and 60° Scanning Off Broadside," *IEEE Transactions on Antennas and Propagation,* vol. 67, no. 3, pp. 1996–2001, Mar. 2019.

[7] M. H. Novak, F. A. Miranda, and J. L. Volakis, "Ultra-wideband phased array for millimeter-wave ISM and 5G bands, realized in PCB," *IEEE Transactions on Antennas and Propagation,* vol. 66, no. 12, pp. 6930–6938, Dec. 2018.

[8] J. P. Doane, K. Sertel, and J. L. Volakis, "A wideband, wide scanning tightly coupled dipole array with integrated balun (TCDA-IB)," *IEEE Transactions on Antennas and Propagation,* vol. 61, no. 9, pp. 4538–4548, Sep. 2013.

[9] F. A. Shaikh and S. Khan, "Design and optimization of ultra-wideband antipodal vivaldi antenna for radar and microwave imaging application," *Sindh University Research Journal (Science Series)*, vol. 50, no. 3D, pp. 06–09, 2018.

[10] "Why Ultra-Wideband Matters | FiRa Consortium," *FiRa Consortium,* Sep. 11, 2023. https://www.firaconsortium.org/resource-hub/blog/why-ultrawideband-matters (accessed Oct. 24, 2024).

[11] K. Song and Q. Xue, "Novel ultra-wideband (UWB) multilayer slotline power divider with bandpass response," *IEEE Microwave and Wireless Components Letters,* vol. 20, no. 1, pp. 13–15, Jan. 2010.

[12] S. W. Wong and L. Zhu, "Ultra-wideband power divider with good in-band splitting and isolation performances," *IEEE Microwave and Wireless Components Letters,* vol. 18, no. 8, pp. 518–520, Aug. 2008.

[13] D. A. Ramirez, W. J. D. Johnson, and G. Mumcu, "Ultra-wideband phased antenna array time delay unit architecture optimization in presence of component non-idealities," *IEEE Open Journal of Antennas and Propagation,* vol. 5, no. 4, pp. 994–1003, Aug. 2024.

[14] R. Solanki, P. K. Tan, and T. H. Gan, "Compact ultra-wideband 8-way power divider with printed resistors," in *2023 Asia-Pacific Microwave Conference (APMC),* Taipei, Taiwan, pp. 629–631, 2023.

[15] E. J. Wilkinson, "An N-way hybrid power divider," *IRE Transactions on Microwave Theory and Techniques,* vol. 8, no. 8, pp. 116–118, Aug. 1960.

[16] E. J. Wilkinson, "Power divider," US Patent, No. 3 091 743, Cl. 333-9, 1963.

[17] "RO4350B™ Laminates," Rogerscorp.com, 2024. https://rogerscorp.com/advanced-electronics-solutions/ro4000-series-laminates/ro4350b-laminates

[18] S. B. Venkatakrishnan, A. Hovsepian, A. D. Johnson, T. Nakatani, E. A. Alwan, and J. L. Volakis, "Techniques for achieving high isolation in RF domain for simultaneous transmit and receive," *IEEE Open Journal of Antennas and Propagation*, vol. 1, pp. 358–367, 2020.

[19] https://docs.amd.com/r/en-US/ug583-ultrascale-pcb-design/Dielectric-Losses

[20] Y. G. Kim and K. W. Kim, "A new design method for ultrawideband microstrip-to-suspended stripline transitions," *International Journal of Antennas and Propagation*, vol. 1, p. 801950, 2013.

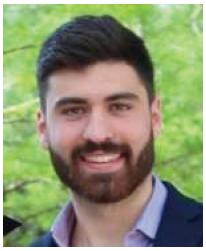

Jorge A. Caripidis Troccola (Member, IEEE) was born in Caracas, Venezuela, in 1997. He received the bachelor's degree (summa cum laude) in electrical engineering and the M.Sc. degree from Florida International University, Miami, FL, USA, in 2020 and 2024, respectively, where he is currently pursuing the Ph.D. degree in electrical and computer engineering with RFCOM Lab. His current research interests include ultrawideband arrays, deployable antennas for space applications, millimeter-wave antennas, and reconfigurable antennas.

Satheesh Bojja Venkatakrishnan (S'13 – M'18) was born in Tiruchirappalli, India, in 1987. He received his bachelor's degree in electronics and communication engineering from the National Institute of Technology, Tiruchirappalli, India, in 2009, and graduated with his M.S. and Ph.D. degrees in electrical engineering from Ohio State University (OSU), Columbus, OH, USA, in 2017. He was a Scientist for DRDO, India, from 2009 to 2013, working on the development and implementation of active electronic steerable antennas. He is currently an Assistant Professor in Electrical and Computer Engineering at Florida International University. His current research includes RF system design for secure wideband communications, data sensing and imaging, interference mitigation techniques, and RFSoC based Simultaneous Transmit and Receive System (STAR) to improve the spectral efficiency. In parallel, Bojja Venkatakrishnan has been working on developing RF sensors and circuits including fully passive neural implants and multi-modal patch sensors for bio-medical applications. Bojja Venkatakrishnan has won numerous awards and recognitions including the IEEE Electromagnetic Theory Symposium (EMTS-2019) Young Scientist Award, and the best paper award in the International Union of Radio Science General Assembly and Scientific Symposium (URSI-GASS) held at Montreal, Canada in August 2017. He is a member of Phi Kappa Phi, and also an Associate member of USNC-URSI.

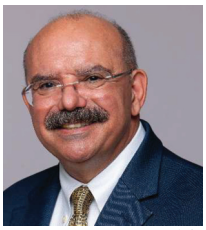

John L. Volakis (S'77-M'82-SM'89-F96) was born on 13 May 1956 in Chios, Greece, and immigrated to the USA in 1973. He obtained his B.E. degree, summa cum laude, in 1978 from Youngstown State University, Youngstown, Ohio, USA, M.Sc. in 1979 from Ohio State University, Columbus, Ohio, and Ph.D. degree in 1982, also from the Ohio State University.

Volakis started his career at Rockwell International (1982–1984), now Boeing. In 1984, he was appointed Assistant Professor at University of Michigan, Ann Arbor, MI, becoming a full Professor in 1994. He also served as the Director of the Radiation Laboratory from 1998 to 2000. From January 2003 to August 2017, he was the Roy and Lois Chope Chair Professor of Engineering at the Ohio State University, Columbus, Ohio, and served as Director of the ElectroScience Laboratory from 2003 to 2016. Effective August 2017, he is Dean of the College of Engineering and Computing and a Professor in the Electrical and Computer Engineering at Florida International University (FIU).

Over the years, he carried out research in antennas, wireless communications and propagation, computational methods, electromagnetic compatibility and interference, design optimization, RF materials, multiphysics engineering, millimeter waves, terahertz and medical sensing. His publications include eight books, 430 journal papers, nearly 900 conference papers, 29 book chapters and 25 patents/disclosures. Among his coauthored books are: Approximate Boundary Conditions in Electromagnetics, 1995; Finite Element Methods for Electromagnetics, 1998; 4th edition Antenna Engineering Handbook, 2007; Small Antennas, 2010; and Integral Equation Methods for Electromagnetics, 2011. He has graduated/mentored 95 doctoral students/postdocs with 43 of them receiving best paper awards at conferences. His service to Professional Societies include: 2004 President of the IEEE Antennas and Propagation Society (2004), Chair of USNC/URSI Commission B (2015–2017), twice the general Chair of the IEEE Antennas and Propagation Symposium, IEEE APS Distinguished Lecturer, IEEE APS Fellows Committee Chair, IEEE-wide Fellows committee member & Associate Editor of several journals. He was listed by ISI among the top 250 most referenced authors (2004), and is a Fellow of IEEE, ACES, and URSI. Among his

awards are: University of Michigan College of Engineering Research Excellence award (1993), Scott award from Ohio State University College of Engineering for Outstanding Academic Achievement (2011), IEEE AP Society C.-T. Tai Teaching Excellence award (2011), IEEE Henning Mentoring award (2013), IEEE Antennas & Propagation Distinguished Achievement award (2014), Ohio State University Distinguished Scholar Award (2016), Ohio State University ElectroScience George Sinclair Award (2017), and URSI Booker Gold Medal (2020).

Cedric W. L. Lee (Senior Member, IEEE) received B.Eng. and M.Sc. degrees in electrical engineering from the National University of Singapore, Singapore, in 2010 and 2013, respectively, and the Ph.D. degree in electrical engineering from Ohio State University, USA, in 2016, under the mentorship of John L. Volakis. He joined the Temasek Laboratories, National University of Singapore, as a Senior Research Scientist, in January 2024. He is currently Deputy Head of the Antenna Group. Previously, he was with DSO National Laboratories as a Senior Member of Technical Staff, where he was involved in the development and testing of space-borne antennas and radar systems.

Theng Huat Gan (Senior Member IEEE) received his B.Eng. degree (Hons) in electrical and Ph.D. degree from Nanyang Technological University, Singapore, in 2007 and 2015, respectively. From 2007 to 2020, he was with DSO National Laboratories, Singapore. Since 2020, he has been a Senior Research Scientist with the Temasek Laboratories, National University of Singapore, where he concurrently serves as the Head of the Antenna and the Head of Computational Electromagnetics Group. His research interests focus on antenna design and computational electromagnetics. Gan has received several awards, including the First Prize in the IEEE AP-S Student Design Competition, in 2013, and the Best Student Paper Award from the IEEE Singapore MTT/AP Chapter, in 2014. He has held several leadership roles within the IEEE Singapore MTT/AP Joint Chapter, where he was Chair, in 2025, Vice-Chair, in 2024, Secretary, in 2023, and a Treasurer, from 2021 to 2022. Additionally, he was the Founding Chair of the IEEE AP-S Student Branch Singapore Chapter.

A Phase Center Estimation Method for Automotive Antenna Measurements

Junhao Zheng[1,3], Xiaoming Chen[2], Chunxu Mao[1], Guan-Long Huang[3], Wanji Hou[4], Yuchen Ma[5], Yuxin Ren[5], and Yi Huang[6]

[1]School of Electronic and Information Engineering
South China University of Technology, Guangzhou 510641, China
1071218679@stu.xjtu.edu.cn, cxmao@scut.edu.cn

[2]School of Information and Communication Engineering
Xi'an Jiaotong University, Xi'an 710049, China
xiaoming.chen@mail.xjtu.edu.cn

[3]School of Electronic and Information Engineering
Foshan University, Foshan 528225, China
hgl@fosu.edu.cn

[4]Electromagnetic Compatibility Test Department of Changchun Automobile Test Center
Changchun, 130103 China
houwanji@catc.com.cn

[5]China Academy of Information and Communications Technology
Beijing 100191, China
mayuchen@caict.ac.cn, renyuxin@caict.ac.cn

[6]Department of Electrical Engineering and Electronics
University of Liverpool, Liverpool L69 3GJ, UK
yi.huang@liverpool.ac.uk

Abstract – This paper presents a blind phase center estimation method for hemispherical near-field automotive antenna tests. The previous method only satisfies the less edge-scattering affected conditions, whose phase center estimation stability and accuracy are not satisfactory. While, the newly proposed method utilizes image theory as filtering process to characterize the electric fields with reduced edge-scattering effects, and the phase center is more accurately derived by the local searching strategy combined with a fast least-squares-based method along the x-, y- and z-axis. Correspondingly, the improvement of the calibrated pattern is significant. The simulation and measurement results both demonstrate the superiority of the proposed method with less time cost and better accuracy for different types of automotive antennas than the previous method. More importantly, the proposed method does not need to distinguish the edge-scattering-affected condition and non-edge-scatteringaffected condition, which will lead to an easy work for estimating the phase center and ensure the accuracy of the pattern offset calibration.

Index Terms – Blind phase center estimation, calibration for displaced antenna, edge-scattering reduction, field projection, spatial convolution-deconvolution.

I. INTRODUCTION

The spherical near-field measurement is widely used in characterizing the far-field pattern and relevant radiation parameters [1–3]. However, the issue of the measurement misalignment of the antenna under test (AUT) usually causes significant deviations for the derived far-field pattern [4–10]. This is especially true for automotive antenna tests [11], where the actual position of the AUT may not be known. Besides, accurate pattern measurements are critical to engineering applications of automotive wireless communications [12],

Submitted On: October 20, 2025
Accepted On: March 04, 2026

https://doi.org/10.13052/2026.ACES.J.410202

electromagnetic compatibility tests, and the multiplexing performance based on the electronic control unit level [13]. What is more, the edge-scattering interference of, e.g., the automotive roof and lifting platform, can also lead to the inaccuracy of the near-field test [14–16]. Consequently, it is necessary to find an effective method to estimate the phase center with less edge-scattering to enable accurate pattern calibration.

Regarding the edge-scattering effect, the authors in [15] used virtual vertices and image theory to eliminate the numerical errors caused by the boundary edges. The research in [16] pointed out the feasibility of using the mode expansion theory to reduce the edge-scattering effect to improve the accuracy of the near-to-far-field transformation (NFT) pattern. As for the phase center study, the conventional method in [17] used the minimum phase variation and the far-field analysis based on known antenna structures to determine the phase center, which can now be realized by full-wave simulation when the AUT is constructed in the software. Reference [18] discussed feasible phase center calculation methods for the planar near-field measurement, which provide some useful explorations for spherical phase center estimation. Reference [19] used the path length and probe-pattern-based method to calibrate the far-field displacement.

In this work, an improved antenna calibration method with fewer truncation errors and less time cost is proposed. Specifically, the method uses spherical mode characteristics to reduce the edge-scattering effect for the near-field automotive antenna test [20], and a fast least-squares-based method is combined with a local searching strategy to swiftly obtain the phase center estimation, leading to an accurate far-field result.

II. THEORY

A. Image-theory-based mode expansion analysis

The automotive antenna is mounted on the automotive roof, which is a finite plane with finite thickness. Thus, the current on the automotive roof edge will experience a scattering effect, making it difficult to accurately estimate the phase center. To solve this problem, the image theory and edge filtering are given as follows: The hemispherical wave expansion of the near-field can be expressed as [1]

$$\boldsymbol{E}(r,\theta,\varphi)=\sum_{n=1}^{N}\sum_{m=-n}^{n}\{a_{mn}\boldsymbol{M}_{mn}(r,\theta,\varphi) + b_{mn}\boldsymbol{N}_{mn}(r,\theta,\varphi)\}, \quad (1)$$

where a_{mn} and b_{mn} are the spherical wave expansion coefficients, $\boldsymbol{M}_{mn}$ and $\boldsymbol{N}_{mn}$ are the spherical wave generating functions. According to the image theory, the hemispherical near-field can be calculated by the superimposition of the direct and the image field as

$$\begin{cases} E_{r,2}(r,\theta,\varphi)=E_r(r,\theta,\varphi)-E_{r,1}(r,\pi-\theta,\varphi) \\ E_{\theta,2}(r,\theta,\varphi)=E_\theta(r,\theta,\varphi)+E_{\theta,1}(r,\pi-\theta,\varphi) \\ E_{\varphi,2}(r,\theta,\varphi)=E_\varphi(r,\theta,\varphi)-E_{\varphi,1}(r,\pi-\theta,\varphi) \end{cases}, \quad (2)$$

where $E_{r,\theta,\varphi}$ is the component of $\boldsymbol{E}$ in equation (1), $E_{r,\theta,\varphi,1}$ is the image component, and $E_{r,\theta,\varphi,2}$ is the image-processed near-field. Besides, the generating function $P_n^{|m|}(\cos\theta)$ of $\boldsymbol{M}_{mn}$ and $\boldsymbol{N}_{mn}$ is odd when the sum of n order and $|m|$ degree is odd, and becomes even when $n+|m|$ is even. Correspondingly, the derivative $dP_n^{|m|}(\cos\theta)/d\theta$ of $\boldsymbol{M}_{mn}$ and $\boldsymbol{N}_{mn}$ is even (or odd) when $n+|m|$ is odd (or even). Based on these characteristics, the spherical wave coefficients a_{mn} and b_{mn} of equation (2) can be represented as [16]

$$a'_{mn}=\begin{cases} 2a_{mn} & |m|+n \text{ is even} \\ 0 & |m|+n \text{ is odd} \end{cases}, \quad b'_{mn}=\begin{cases} 0 & |m|+n \text{ is even} \\ 2b_{mn} & |m|+n \text{ is odd} \end{cases}. \quad (3)$$

The boundary condition for $\theta=\pi/2$ in this situation will satisfy $P_n^{|m|}(\cos\theta)=0$ when $n+|m|$ is odd and $dP_n^{|m|}(\cos\theta)/d\theta=0$ when $n+|m|$ is even, which will effectively reduce the edge-scattering effect for the hemispherical near-field test [16]. By substituting the new coefficients a'_{mn} and b'_{mn} into equation (1) and using the boundary condition for $\theta=\pi/2$, the reprocessed automotive near-field $E_{r,\theta,\varphi,2}$ will be more accurate for the phase center estimation and subsequent NFT pattern calibration.

B. Improved phase center estimation

A least-squares-based fast phase center estimation method [21] is used to approximately estimate the initial phase center O_i. Then, a local searching strategy is chosen to find the phase center along the positive and negative axes in x,y and z directions starting from O_i. The searching range is set as $\pm\Delta H$, and the phase center O_p corresponding to the minimum phase difference can be found within $\pm\Delta H$, that is: if O_p lies in the endpoint of $\pm\Delta H$, $\pm\Delta H$ will be expanded as $\pm t\Delta H, t=2,3\ldots$ until O_p is not at the endpoint of the searching range, and the local minimum point within $\pm t\Delta H$ will correspond to the O_p. The specific method of searching O_p follows.

As shown in Fig. 1, the hemispherical near-field data is sampled on S_r, where the measurement center is O_0 and the radius is r_0. The phase center of the automotive antenna is O_p, which is usually different from O_0 due in practical automotive measurement setup.

The deviation projection of O_p onto the coordinate system of the aperture plane S_0, whose plane center is O_0 (the same as S_r), is (d_x, d_y, d_z) or $d_{x,y,z}$ for short. Thus, the displacement of $d_{x,y,z}$ can be compensated when the phase center O_p is determined.

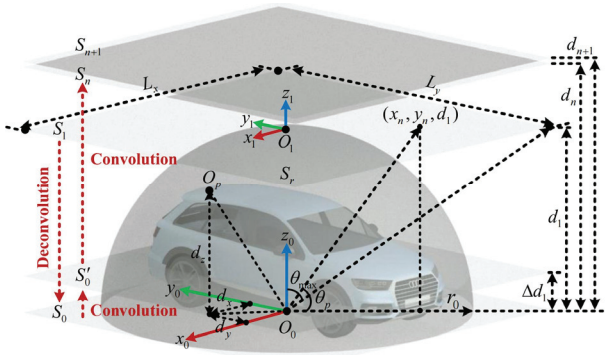

Fig. 1. Parameters of the hemispherical automotive antenna test.

Since the data on S_r can be projected onto the three planes along the x, y and z axes, the z-axis projection is selected as an example to illustrate the estimation of O_p. A plane S_1, which is tangent to S_r, is chosen with lengths of L_x and L_y to project near-field data, and the maximum projection angle $\theta_{\max} = \arctan(\sqrt{(L_x^2+L_y^2)/2}/d_1)$ is determined, where $d_1 = r_0$. The projection from S_r to S_1 includes the electric field transformation and coordinate transformation, which can be expressed as

$$\begin{cases} E_x = I(E_{r,2}\sin\theta\cos\varphi + E_{\theta,2}\cos\theta\cos\varphi - E_{\varphi,2}\sin\varphi) \\ \qquad \times e^{-jk_0\Delta d} \\ E_y = I(E_{r,2}\sin\theta\sin\varphi + E_{\theta,2}\cos\theta\sin\varphi + E_{\varphi,2}\cos\varphi) \\ \qquad \times e^{-jk_0\Delta d} \\ E_z = I\left(E_{r,2}\cos\theta - E_{\theta,2}\sin\theta\right)e^{-jk_0\Delta d} \end{cases}, \quad (4)$$

$$\begin{cases} x_n = d_1\tan(\theta_n)\cos\varphi_n \\ y_n = d_1\tan(\theta_n)\sin\varphi_n \\ \Delta d = \sqrt{x_n^2+y_n^2+d_1^2} - r_0 \end{cases}, \quad (5)$$

where $E_{r,\theta,\varphi,2}$ is the reprocessed image near-fields on S_r in equation (2), $E_{x,y,z}$ is the projected fields on S_1, k_0 is the wavelength of frequency $f_0, \Delta d$ is the propagating distance, x_n and y_n are the nth sampling position on S_1, θ_n and φ_n are the nth sampling position on S_r. $I = \sin\theta_p = d_1/\sqrt{x_n^2+y_n^2+d_1^2}$ transfers the oblique incident wave from S_r into the vertical wave on S_1, as shown in Fig. 1.

The spatial convolution-deconvolution method, as described in [22], is used to backwardly and forwardly derive the near-field and far field, respectively

$$\boldsymbol{E}_1(x_1,y_1) = \mathscr{F}^{-1}[\mathscr{F}[\boldsymbol{E}_0(x_0,y_0)] \odot \mathscr{F}[g(x_1,y_1)]], \quad (6)$$

$$\boldsymbol{E}_0(x_0,y_0) = \mathscr{F}^{-1}[\mathscr{F}[\boldsymbol{E}_1(x_1,y_1)] \oslash \mathscr{F}[g(x_1,y_1)]], \quad (7)$$

where g is the Green function, $\odot$ and $\oslash$ are the entry-wise multiplication and division between the pattern matrices, $\mathscr{F}$ and $\mathscr{F}^{-1}$ are the Fourier and inverse Fourier transformations, $\boldsymbol{E}_0$ and $\boldsymbol{E}_1$ are the electric fields on planes S_0 and $S_1, (x_0,y_0)$ and (x_1,y_1) are the coordinates on S_0 and S_1.

By combining equations (1)–(7), the phase center estimation processes of O_p can be summarized as follows:

1. The image-processed near-fields $E_{r,\theta,\varphi,2}$ on S_r are obtained by equations (1)–(3), and the least-squaresbased method is used to estimate the initial phase center O_i, based on which the desired O_p will be found within $\pm t\Delta H, t = 1,2,3\ldots$. Then $E_{r,\theta,\varphi,2}$ are projected onto S_1 as $\boldsymbol{E}_1$ using equations (4)–(5). The aperture near-field $\boldsymbol{E}_0$ on S_0 is obtained by equation (7) from $\boldsymbol{E}_1$ on S_1, and an extrapolation distance Δd_1 is selected away from S_1 (as shown in Fig. 1), where Δd_1 lies in the range of $\pm t\Delta H$, $t = 1,2,3\ldots$.
2. Equation (6) is used to convolute $\boldsymbol{E}_0$ with distance Δd_1 to derive $\boldsymbol{E}_0'$ on S_0'. Meanwhile, two close far-field planes S_n and S_{n+1} corresponding to distances d_n and d_{n+1} are chosen and fixed.
3. $\boldsymbol{E}_0'$ is convoluted by equation (6) to obtain the two far fields $\boldsymbol{E}_n$ and $\boldsymbol{E}_{n+1}$ on the two planes S_n and S_{n+1}, and the sum of the planar phase differences between $\boldsymbol{E}_n$ and $\boldsymbol{E}_{n+1}$ are calculated as $D_{n,n+1} = \sum|P_n - P_{n+1}|$, where P_n and P_{n+1} are the phases of $\boldsymbol{E}_n$ and $\boldsymbol{E}_{n+1}$.
4. Changing the value of Δd_1 and reperforming steps two and three, different phase differences $D'_{n,n+1}$ between different P_n and P_{n+1} (notably, d_n and d_{n+1} keep unchanged) are obtained. After multiple groups of iterations, the minimum value of $D'_{n,n+1}$ is found. Notably, the minimum value of $D'_{n,n+1}$ is derived from the sum of the two spherical phase differences, and the phase center corresponds to the radiating center with minimum phase difference. Therefore, the minimum $D'_{n,n+1}$ corresponds to the minimum phase center, i.e., the phase center. Then the corresponding Δd_1 is the optimal phase center along the z axis, which is noted as $d_z = \Delta d_1$.
5. Subsequently, the x-axis and y-axis phase center estimations can be realized by projecting the near-field data of S_r onto the planes along the x and y axes, and the phase centers $O_p = (d_x, d_y, d_z)$ can be finally determined.

C. Pattern offset calibration

Once the phase center is determined following the above procedures, pattern offset calibration can be readily conducted as follows. Since the samples on S_r have two coordinates of $(r_1, \theta_1, \varphi_1)$ and $(r_2, \theta_2, \varphi_2)$ corresponding to O_0 and O_p, the compensated NFT pattern can be expressed as $\boldsymbol{E}_{NFT}\Delta C_1 \Delta C_2$, where $\Delta C_1 = r_2/r_1, \Delta C_2 = e^{-jk_0\Delta p}, \Delta p = r_1 - r_2$ [19]. The compensated pattern is in the coordinates of $(r_2, \theta_2, \varphi_2)$, and should be projected into the coordinates of $(r_1, \theta_1, \varphi_1)$ to match the measurement origin O_0.

III. SIMULATION AND MEASUREMENT RESULTS

A. Simulation

The automotive model with a monopole antenna is simulated by FEKO software and the geometrical center of the monopole antenna is fixed at $(0\text{ m}, 1.5\text{ m}, 1.5\text{ m})$ to simulate the near-field phase center deviation, as shown in Fig. 2, where the frequency f_0 is 3 GHz, the measured near-field radius r_0 is $60\lambda_0$, the sampling ranges are $\theta = (0^\circ \sim 120^\circ)$ and $\varphi = (0^\circ \sim 360^\circ)$, and the sampling intervals are $\Delta\theta = \Delta\varphi = 1^\circ$. Besides, the projection angle $\theta_{\max}$ is 80°, and the projection interval on S_1 is $\Delta L = 0.4\lambda_0$. The maximum searching range along the x, y and z axes is limited within 2 m (i.e., less than r_0).

The previous global phase center searching method without edge-scattering reduction in [23] is firstly used to obtain the estimated phase center result to make comparisons with the newly proposed method, as shown in Fig. 3 (a), where the red, green and blue curves are the phase centers varied in different plane positions with a searching step of 0.1 m along the x, y and z axes, and the estimated phase center is denoted as $O_p'' = (0\text{ m}, 1.1\text{ m}, 1.6\text{ m})$. Next, the initial phase center is first determined as $O_i = (0.2\text{ m}, 2.4\text{ m}, 1.2\text{ m})$. The range $\pm\Delta H$ is set as ± 0.5 m. Notably, the simulated edge-scattering effect is mainly contributed by the automotive roof and bottom enclosed within the range of $\theta = (0^\circ \sim 120^\circ)$. The variations of the phase differences $D_{n,n+1}$ calculated by the proposed method under the local searching strategy are shown in Figs. 3 (b)–(d), where the red, green and blue curves are the phase centers varied along the x, y and z axes, respectively. Therefore, the phase center is determined as $O_p = (0.1\text{ m}, 1.3\text{ m}, 1.6\text{ m})$ (marked as asterisks in Fig. 3). Besides, the theoretical phase center calculated by the classical method in [17] is presented as $O_p' = (0\text{ m}, 1.4\text{ m}, 1.2\text{ m})$. Then, the estimated phase centers O_p and O_p'' are compared with O_p' and summarized in Table 1.

After the phase centers are acquired, the next step is to calibrate the displacement between the real center O_0 and the virtual center O_p (and O_p''). Therefore, by using the proposed calibration method and the method in [23], the theoretical and compensated NFT patterns in $\varphi = 0^\circ$ and $\varphi = 90^\circ$ are shown in Fig. 4, where the red, yellow, black and blue curves are the theoretical pattern derived from FEKO, uncalibrated NFT pattern, calibrated NFT pattern by [23], calibrated NFT pattern by the proposed method, respectively. Besides, the purple, grey and green curves are the errors between red and yellow curves, errors between red and black curves, errors between red and blue curves.

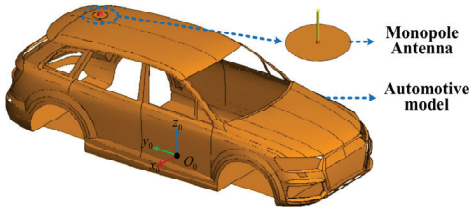

Fig. 2. Automotive model mounted with a monopole antenna.

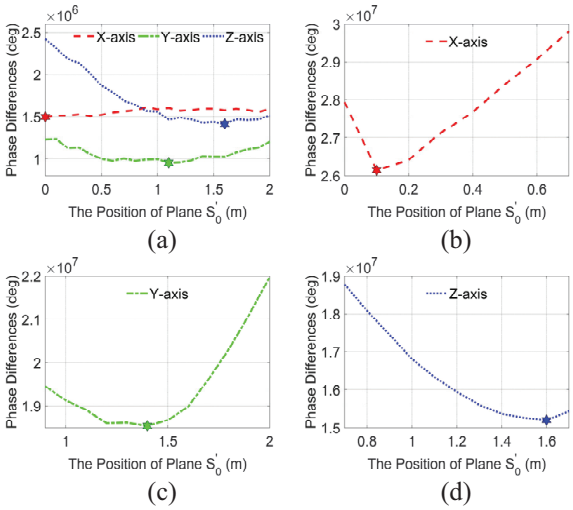

Fig. 3. Variations of $D_{n,n+1}$ for (a) global searching strategy in [23], and local searching strategy along the (b) x-, (c) y - and (d) z-axis.

Table 1: Simulated phase centers and error comparisons (unit: meter)

Axis	O_p	O_p'	O_p''	$\lvert O_p - O_p' \rvert$	$\lvert O_p' - O_p'' \rvert$
x	0.1	0.0	0.0	$1\lambda_0$	$0\lambda_0$
y	1.4	1.4	1.1	$0\lambda_0$	$3\lambda_0$
Z	1.6	1.2	1.6	$4\lambda_0$	$4\lambda_0$

B. Measurement

A monopole antenna working at $f_0 = 3$ GHz with the main lobe lying in the $x_0O_0y_0$ plane is chosen to

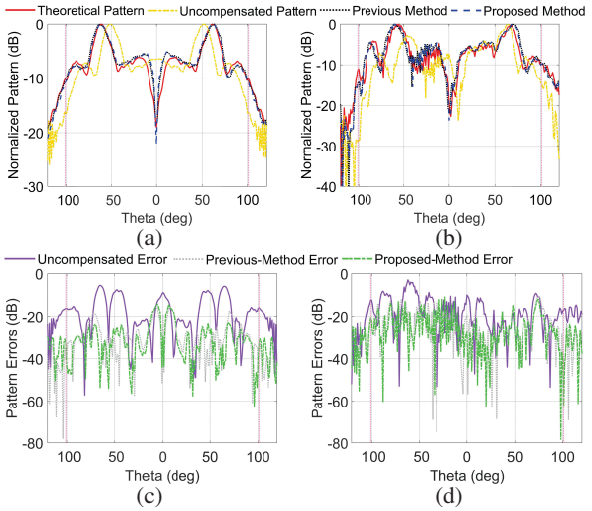

Fig. 4. Comparisons of the simulated patterns in (a) $\varphi = 0^\circ$ and (b) $\varphi = 90^\circ$, and pattern errors in (c) $\varphi = 0^\circ$ and (d) $\varphi = 90^\circ$.

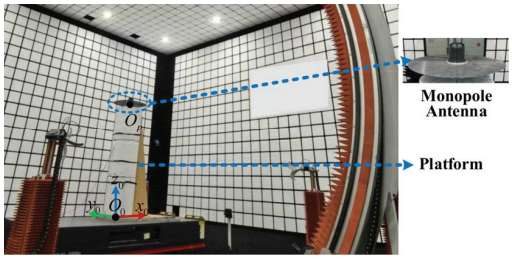

Fig. 5. Near-field measurement setup of a monopole antenna.

imitate the radiation of the automotive antenna, whose geometrical center is fixed at $(3\text{ m}, 0\text{ m}, 0\text{ m})$ to represent the near-field phase center deviation, and the measurement setups are shown in Fig. 5. The spherical near-field radius r_0 is 6.8 m, the sampling ranges are $\theta = (0^\circ \sim 120^\circ)$ and $\varphi = (0^\circ \sim 360^\circ)$, and the sampling intervals are $\Delta\theta = \Delta\varphi = 1^\circ$. The projection angle and interval on S_1 are $\theta_{\max} = 80^\circ$ and $\Delta L = 0.4\lambda_0$. The maximum searching ranges along the x, y and z axes is limited within 5 m (i.e., less than r_0). The results of the previous global phase center searching method in [23] are shown in Fig. 6 (a), where the step is 0.1 m and $O_p'' = (3.5\text{ m}, 0.4\text{ m}, 0.4\text{ m})$. Then the initial phase center is determined as $O_i = (3.7\text{ m}, 1.3\text{ m}, 0.6\text{ m})$. The range of $\pm\Delta H$ is set as ± 0.5 m. The phase difference $D_{n,n+1}$ is shown in Figs. 6 (b)–(d), where the interval of the abscissa is 0.1 m, the maximum searching range is limited within 5 m, and the phase center is determined as $O_p = (3.7\text{ m}, 0.1\text{ m}, 0\text{ m})$. While the actual phase center is $O_p' = (3\text{ m}, 0\text{ m}, 0\text{ m})$, and the corresponding estimated errors are summarized in Table 2. Then, the calibrated NFT patterns after the probe compensation [18] and their pattern errors are given in Fig. 7.

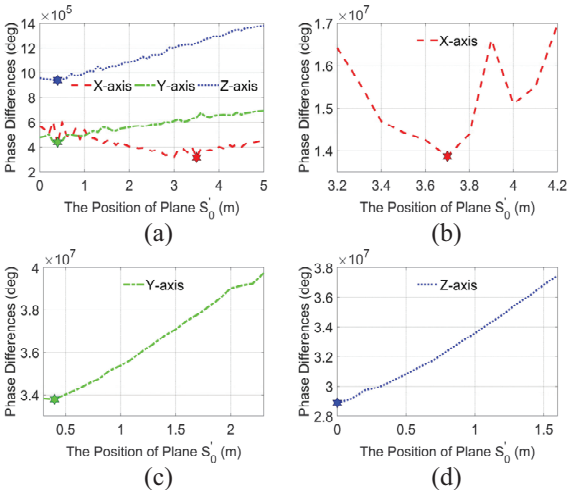

Fig. 6. Variations of $D_{n,n+1}$ for (a) global searching strategy in [23], and the local searching strategy along (b) x-, (c) y- and (d) z-axis.

Table 2: Measured phase centers and error comparisons (unit: meters)

Axis	O_p	O_p'	O_p''	$\lvert O_p - O_p'\rvert$	$\lvert O_p' - O_p''\rvert$
x	3.7	3.0	3.5	$7\lambda_0$	$5\lambda_0$
y	0.1	0.0	0.4	$1\lambda_0$	$4\lambda_0$
z	0.0	0.0	0.4	$0\lambda_0$	$4\lambda_0$

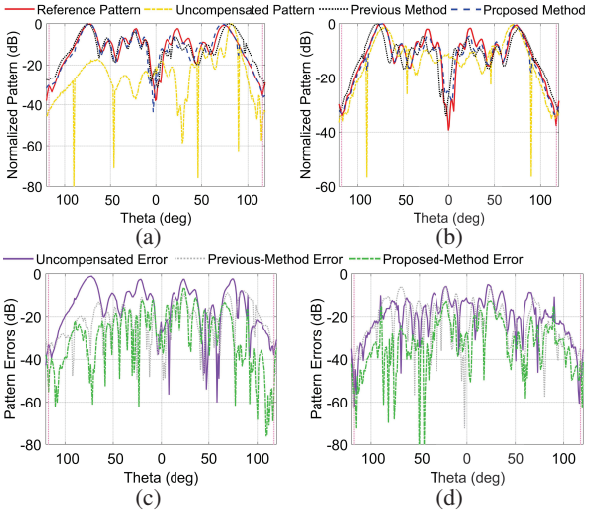

Fig. 7. Comparisons of the measured patterns in (a) $\varphi = 0^\circ$ and (b) $\varphi = 90^\circ$, and pattern errors in (c) $\varphi = 0^\circ$ and (d) $\varphi = 90^\circ$.

C. Discussions

C.1. Relative errors

In order to more accurately analyze the superiority of the proposed method, the calculation of the relative errors in Figs. 4 (a)–(d) and Figs. 7 (a)–(d) is given

below

$$Q = \frac{\sum_{-\theta_r}^{\theta_r} |E_{er}(\theta,\varphi)|^2}{\sum_{-\theta_r}^{\theta_r} |E_c(\theta,\varphi)|^2}, \tag{8}$$

where E_c is the red curve without displacement in Figs. 4 (a), (b) or Figs. 7 (a), (b), E_{er} is the error curve (purple, grey or green curves) in Figs. 4 (c), (d) or Figs. 7 (c), (d). θ_r is the reliable region of the spherical near-field test in elevation range, which is calculated by [24] as 101° and 117° for Fig. 4 and Fig. 7 (pink curve), respectively. Therefore, the calculated relative errors are given in Table 3. Notably, since the method in [23] is only available for the model with a small phase center offset and a small automotive roof, which leads to less edge-scattering effect, the performance of the method in [23] deteriorates under the current monopole testing case in Table 3. While this does not influence the usefulness of [23] for the normal phase center estimation cases where the edge-scattering and the phase center deviation is small.

Table 3: Relative errors

Fig. 4	**Uncompensated**	**Previous Method**	**Proposed Method**
$\varphi = 0°$	35.32%	9.05%	7.78%
$\varphi = 90°$	35.67%	17.57%	14.18%
Fig. 7	**Uncompensated**	**Previous Method**	**Proposed Method**
$\varphi = 0°$	76.79%	32.19%	21.22%
$\varphi = 90°$	42.06%	33.68%	12.66%

C.2. Additional edge-scattering-affected simulation results

An additional automotive model mounted with a 2 GHz right-handed circular-polarized (RHCP) antenna (i.e., helical antenna), whose geometrical center is fixed at $(0\,\text{m}, 0\,\text{m}, 1.5\,\text{m})$, is simulated to verify the wide applicability and significance of the proposed method for the circular-polarized antenna. The basic simulation setups are the same as the model in Fig. 2. The theoretical phase center is $O'_p = (0\,\text{m}, 0\,\text{m}, 1.2\,\text{m})$, and the estimated phase centers O_p and O''_p are obtained in Table 4. Correspondingly, the pattern errors for the left-handed circular-polarized (LHCP) component, RHCP component and the entire far-field component of the calibrated NFT patterns are summarized in Table 5.

C.3. Additional non-edge-scattering-affected simulation results

The following will give additional results for the non-edge-scattering-affected cases to further verify the effectiveness of the proposed method under normal condition. A single monopole antenna and a single helical antenna are chosen as the representative linearand circular-polarized antennas, respectively, working at 3 GHz. The basic sampling setups are the same as the model in Fig. 2, and the two antennas are placed at $(1.0\,\text{m}, 1.0\,\text{m}, 1.0\,\text{m})$. The estimated phase canters of the two antennas are summarized in Table 6. The corresponding pattern calibration results are listed in Table 7, where the LHCP and RHCP components of the helical antenna are omitted and only shows the overall polarization components of the farfield results.

Table 4: Edge-scattering-affected simulated phase centers and error comparisons (unit: meters)

Axis	O_p	O'_p	O''_p	$\lvert O_p - O'_p \rvert$	$\lvert O'_p - O''_p \rvert$
x	0.1	0.0	0.0	$0.6\lambda_0$	$0\lambda_0$
y	0.1	0.0	0.1	$0.6\lambda_0$	$0.6\lambda_0$
z	1.5	1.2	1.7	$2\lambda_0$	$3.3\lambda_0$

Table 5: Edge-scattering-affected relative errors

Left-Polarized	**Uncompensated**	**Previous Method**	**Proposed Method**
$\varphi = 0°$	33.57%	19.43%	16.06%
$\varphi = 90°$	26.92%	17.31%	16.54%
Right-Polarized	**Uncompensated**	**Previous Method**	**Proposed Method**
$\varphi = 0°$	14.26%	7.79%	6.18%
$\varphi = 90°$	16.78%	8.50%	7.31%
Total Component	**Uncompensated**	**Previous Method**	**Proposed Method**
$\varphi = 0°$	12.71%	5.35%	4.29%
$\varphi = 90°$	15.26%	7.40%	6.31%

Table 6: Non-edge-scattering-affected simulated phase centers and error comparisons (unit: meters)

Mono pole	O_p	O'_p	O''_p	$\lvert O_p - O'_p \rvert$	$\lvert O'_p - O''_p \rvert$
x	0.9	1.0	1.0	$1\lambda_0$	$0\lambda_0$
y	0.9	1.0	1.0	$1\lambda_0$	$0\lambda_0$
z	0.8	1.0	1.4	$2\lambda_0$	$4\lambda_0$
Helix	O_p	O'_p	O''_p	$\lvert O_p - O'_p \rvert$	$\lvert O'_p - O''_p \rvert$
x	0.8	1.0	0.9	$2\lambda_0$	$1\lambda_0$
y	0.8	1.0	1.1	$2\lambda_0$	$1\lambda_0$
z	0.9	1.0	1.4	$1\lambda_0$	$4\lambda_0$

C.4. Advantages

Based on all the results shown above, the proposed method has two significant advantages:

1. Reduction of time cost: The local searching numbers of the proposed method for the simulation and

Table 7: Non-edge-scattering-affected relative errors

Monopole	**Uncompensated**	**Previous Method**	**Proposed Method**
$\varphi = 0^\circ$	14.97%	8.14%	4.05%
$\varphi = 90^\circ$	15.03%	7.94%	4.00%
Helix	**Uncompensated**	**Previous Method**	**Proposed Method**
$\varphi = 0^\circ$	17.12%	8.83%	8.12%
$\varphi = 90^\circ$	16.58%	8.67%	8.48%

measurement results in Fig. 2 and Fig. 5 are 41 and 62. While the method in [23] for the results in Fig. 2 and Fig. 5 are 63 and 153. Thus, the proposed method leads to about 100 minutes and 450 minutes time reduction (in a personal computer with 2.6 GHz CPU of Core i9-13900H and RAM of 32 GB).

2. The wide applicability with better performance: The proposed method is a unified phase center estimation and pattern calibration method suitable for different polarized antennas, frequencies, offset positions and conditions (edge-scattering-affected and non-edge-scattering-affected conditions).

IV. CONCLUSION

This work presented an improved phase center estimation method. Specifically, it used image theory with edge-scattering reduction and a fast local searching strategy to achieve better phase center estimation of the automotive antenna. Notably, the proposed method unified the edge-scattering-affected and non-edge-scattering-affected conditions, and the time cost had been significantly reduced, which leads to an easy task for the general spherical near-field test.

ACKNOWLEDGMENT

This work was supported in part by the Key Research and Development Program of Shaanxi under Grant 2024GX-ZDCYL-01-26, and Shaanxi Province Innovation Capability Support Plan under No.2024RS-CXTD-07.

REFERENCES

[1] J. E. Hansen. *Spherical Near-Field Antenna Measurements*. London: IET, 1988.

[2] T. K. Sarkar, M. S. Palma, M. D. Zhu, and H. Chen. *Modern Characterization of Electromagnetic Systems and its Associated Metrology*. New Jersey: Wiley, pp. 453–489, 2021.

[3] F. Peng, Q. Zhang, X. Liu, Z. Wang, and X. Chen, "An efficient antenna measurements method in spherical near-field based on sparse sampling," *IEEE Antennas Wirel. Propag. Lett.*, vol. 23, no. 11, pp. 3942-3946, Nov. 2024.

[4] *Standard definition of terms for antennas*, IEEE standard 145-1993, 1993.

[5] C. Ehrenborg, "Investigation and comparison between radiation and phase center for canonical antennas," M.S. thesis, Dept. Elect. Inf. Tech., Lund Univ., GÃ¶teborg, Sweden, 2014.

[6] M. Henley and M. Pour, "Reconfigurable displaced phase center reflector antennas with focal plane arrays," *IEEE Antennas Wirel. Propag. Lett.*, vol. 18, no. 6, pp. 1298–1302, June 2019.

[7] G. B. Arfken, *Mathematical Methods for Physicists*, 4th ed. Orlando: Academic Press, pp. 1–222, 1995.

[8] C. A. Balanis. *Modern Antenna Handbook*. New Jersey: Wiley, pp. 977–1033, 2008.

[9] J. Fridén and G. Kristensson, "Calculation of antenna radiation center using angular momentum," in *Proc. Eur. Conf. Antennas Propag.* (EuCAP), Gothenburg, Sweden, pp. 1531–1535, 2013.

[10] J. Fridén and G. Kristensson, "Calculation of antenna radiation center using angular momentum," *IEEE Trans. Antennas Propag.*, vol. 61, no. 12, pp. 5923–5930, Dec. 2013.

[11] J. Zheng, F. Peng, Z. Wang, G. Huang, and X. Chen, "Far-field similarity-based pattern reconstruction method for hemi-spherical vehicular antenna tests," *IEEE Antennas Wirel. Propag. Lett.*, vol. 24, no. 5, pp. 1124–1128, May 2025.

[12] M. Emmelmann, B. Bochow, and C. Kellum, "Commercial and public use applications," in *Vehicular Networking: Automotive Applications and Beyond*. New Jersey: Wiley, pp. 1–28, 2010.

[13] C. Lupini, *Vehicle Multiplex Communication: Serial Data Net-working Applied to Vehicular Engineering*. New York: SAE, 2004.

[14] J. C. West, "On the control of edge diffraction in numerical rough surface scattering using resistive tapering," *IEEE Trans. Antennas Propag.*, vol. 51, no. 11, pp. 3180–3183, Nov. 2003.

[15] J. H. Hwang and Y. Oh, "Investigation of the effect of boundary edges placed on an infinite conducting surface and effective treatment using virtual vertices," *IEEE Antennas Wirel. Propag. Lett.*, vol. 11, pp. 913–916, 2012.

[16] E. D. Giampaolo, "A numerical filter to remove the field scattered by the edges of a finite ground plane from measured data," *Prog. Electromagn. Res. B*, vol. 9, pp. 165–178, 2008.

[17] Y. Y. Hu. "A method of determining phase centers and its application to electromagnetic horns," *J. Frankl. Inst.*, vol. 271, no. 1, pp. 31–39, Jan. 1961.

[18] P. Padilla, J. M. Fernández, J. L. Padilla, G. Expósito, M. S. Castaner, and B. Galocha, "Comparison of different methods for the experimental antenna phase center determination using a planar acquisition system," *Prog. Electromagn. Res.*, vol. 135, pp. 331–346, 2013.

[19] G. F. Hamberger, J.-A. Antón, S. J. Lachner, and B. Derat, "Correction of over-the-air transmit and receive wireless device performance errors due to displaced antenna positions in the measurement coordinate system," *IEEE Trans. Antennas Propag.*, vol. 68, no. 11, pp. 7549–7554, Nov. 2020.

[20] Automotive Association Technical Report, "Vehicular antenna test methodology," 5GAA, Munich, Germany, 2024.

[21] N. Anyutin, I. Malay, and A. Malyshev, "Reconstruction of algorithm of electromagnetic field in case of elliptic polarization of near-field probe," in *Proc. East-West Design & Test Symposium* (EWDTS), Kazan, Russia, pp. 1–4, 2018.

[22] J. Zheng, C. Pan, Z. Wang, L. Zhang, and X. Chen, "An efficient data reconstruction method for broadband planar near-field measurements based on the field distribution similarity," *IEEE Trans. Instrum. Meas.*, vol. 72, no. 1008514, 2023.

[23] J. Zheng, Y. Ren, G. L. Huang, Y. Ma, and C. Mao, "A calibration method for displaced hemispherical vehicular antenna based on blind phase center estimation," *IEEE Antennas Wirel. Propag. Lett.*, vol. 24, no. 11, pp. 3885–3889, Nov. 2025.

[24] F. J. Cano-Fácila, S. Pivnenko, and M. Sierra-Castañer, "Reduction of truncation errors in planar, cylindrical, and partial spherical near-field antenna measurements," *Int. J. Antennas Propag.*, vol. 2012, no. 1, pp. 1–19, Feb. 2012.

Junhao Zheng received the B.Sc. degree in electronic information science and technology from Shandong University, Weihai, China, in 2017, the M.Sc. degree in signal and information processing from Northwestern Polytechnical University, Xi'an, in 2020, and the Ph.D. degree in electronic science and technology from Xi'an Jiaotong University, Xi'an, in 2024. His current research interests include antenna measurement in an anechoic chamber and reverberation chamber and over-the-air (OTA) testing.

Xiaoming Chen (Senior Member, IEEE) received the B.Sc. degree in electrical engineering from Northwestern Polytechnical University, Xi'an, China, in 2006, and the M.Sc. and Ph.D. degrees in electrical engineering from the Chalmers University of Technology, Gothenburg, Sweden, in 2007 and 2012, respectively. From 2013 to 2014, he was a Post-Doctoral Researcher with the Chalmers University of Technology. From 2014 to 2017, he was with Qamcom Research and Technology AB, Gothenburg. Since 2017, he has been a Professor with Xi'an Jiaotong University, Xi'an. His research interests include MIMO antennas, over-the-air testing, reverberation chambers, and antenna measurements. He has published more than 200 journal articles on these topics. Chen received the IEEE Outstanding Associate Editor Awards six times from 2018 to 2023, and the International Union of Radio Science (URSI) Young Scientist Award 2017 and 2018. He was the General Chair of the IEEE International Conference on Electronic Information and Communication Technology (ICEICT) 2021. He currently serves as a Track Editor for IEEE Antennas and Wireless Propagation Letters and Associate Editor for IEEE Transactions on Antennas and Propagation.

Chunxu Mao (Member, IEEE) received the B.S. degree in communication engineering from the Guilin University of Electronic and Technology, Guilin, China, in 2010, the M.E. degree in RF and microwave engineering from the South China University of Technology, Guangzhou, in 2013, and the Ph.D. degree in electronic engineering from the University of Kent, Canterbury, UK, in 2018. From January 2018 to August 2019, he was a Post-Doctoral Research Fellow with the Computational Electromagnetics and Antennas Research Laboratory (CEARL), The Pennsylvania State University, University Park, PA, USA. In October 2019, he joined the Institute for Communication Systems (ICS), 5G/6G Innovation Center (5G/6GIC), University of Surrey, as a Senior Research Fellow. His research interests include multifunctional filtering antennas, circularly polarized antenna/array, 5G millimeter-wave antennas, wearable antennas, and metamaterial antennas. Mao serves as a Peer Reviewer of several journals, including IEEE Transactions on Antennas and Propagation, IEEE Transactions on Microwave Theory and Techniques, and IEEE Antennas and Wireless Propagation Letters.

Guan-Long Huang (Senior Member, IEEE) received the B.E. degree in electronic information engineering from the Harbin Institute of Technology, Harbin, China and the Ph.D. degree in electrical and computer engineering from the National University of Singapore,

Singapore. From 2011 to 2020, he was with Shenzhen University as an Associate Professor, Peng Cheng Laboratory as a Joint-Researcher, Southern University of Science and Technology as an Adjunct Lecturer, Nokia Solutions and Networks System Technology as a Senior Antenna Specialist, and Temasek Laboratories with National University of Singapore as a Research Scientist. He is currently a Distinguished Professor with Foshan University, Foshan, Guangdong, China, and the Director of Smart Antenna and Microwave & Millimeter-Wave Engineering Technology Research Centre of Foshan City. He has authored and co-authored two books and more than 200 papers in peer-reviewed journals and international conferences. He was the TPC member and special session organizer of several international conferences including APCAP-2018, ISAP-2019, ICMMT-2019/2020/2021/2022, IEEE MTT-S IMWS-AMP-2020/2021/2022, ACES-China-2021/2022. He also was the Publicity Co-Chair of ICMMT-2022. He was the recipient of the Raj Mittra Travel Grant (2021), Best Reviewer Award of IEEE AWPL (2019) and IEEE TAP (2020, 2021), all from IEEE Antenna and Propagation Society, and the recipient of the Young Scientist Award in 2021 from the Applied Computational Electromagnetics Society, Fok Ying-Tong Education Foundation Award in 2020 from the Ministry of Education of the People's Republic of China, and the Foundation for Distinguished Young Talents in Higher Education of Guangdong Province, China in 2017. His research interests include design and implementation of high-performance antenna arrays, base-station and mobile RF front-end devices/antennas, millimeter-wave antenna, antenna measurement technique and 3-D printing technology in microwave applications.

Wanji Hou was born in Changchun, China, in 1989. He received the bachelor's degree and graduated from the School of Electrical Engineering at Beijing Jiaotong University in 2013. He is currently with in Changchun Automotive Test Center Co. Ltd. His current research interests are in the field of automotive antenna testing, and electromagnetic compatibility testing.

Yuchen Ma was born in Beijing, China, in 1993. He received the B.E. and Ph.D. degrees from the School of Electronic and Information Engineering, Beijing Jiaotong University, Beijing, in 2015 and 2021, respectively. He is currently with China Academy of Information and Communications Technology, Beijing. His current research interests include the fields of antenna design and antenna measurement.

Yuxin Ren received the M.Sc. degree in electronic science and technology from the Beijing University of Posts and Telecommunications, Beijing, China, in 2014. Since 2018, he has been an Engineer with the China Academy of Information and Communications and Technology, Beijing. His current research interests include the theory of reverberation chamber and plane wave synthesizers and other OTA test systems.

Yi Huang (Fellow, IEEE) received B.Sc. in Physics (Wuhan, China) in 1984, M.Sc. (Eng) in Microwave Engineering (Nanjing) in 1987, and D.Phil. in Communications from the University of Oxford, UK, in 1994. He has been conducting research in the areas of antennas, wireless communications, applied electromagnetics, radar, and EMC since 1987. More recently, he is focused on mobile antennas, wireless energy harvesting, and power transfer. His experience includes three years spent with NRIET (China) as a Radar Engineer and various periods with the Universities of Birmingham, Oxford, and Essex in the UK as a member of research staff. He worked as a Research Fellow at British Telecom Labs in 1994 and then joined the Department of Electrical Engineering & Electronics, the University of Liverpool, UK, as a Faculty in 1995, where he is now a full Professor in Wireless Engineering, the Head of High-Frequency Engineering Group and Deputy Head of Department. Huang has published over

500 refereed papers in leading international journals and conference proceedings and authored four books, including Antennas: from Theory to Practice (John Wiley, 2008, 2021). He has received many patents, research grants from research councils, government agencies, charities, EU, and industry, and is a recipient of over 10 awards (e.g. BAE Systems Chairman's Award 2017, IET, and Best Paper Awards). He has served on a number of national and international technical committees and been an Editor, Associate Editor, or Guest Editor of five international journals. In addition, he has been a keynote/invited speaker and organizer of many conferences and workshops (e.g. IEEE iWAT2010, LAPC2012, and EuCAP2018). He is at present the Editor-in-Chief of Wireless Engineering and Technology, Associate Editor of IEEE Antennas and Wireless Propagation Letters, UK and Ireland Rep to European Association of Antenna and Propagation (EurAAP, 2016-2020), a Fellow of IET, and a Fellow of IEEE.

Experimental Assessment of a Non-Redundant Approach to Minimize Data in a Spherical NF-FF Transformation for Offset Mounted Elongated AUTs

Francesco D'Agostino, Flaminio Ferrara, Claudio Gennarelli, Rocco Guerriero, Massimo Migliozzi, and Luigi Pascarella

Department of Industrial Engineering
University of Salerno, via Giovanni Paolo II, I-84084 Fisciano (Salerno), Italy
fdagostino@unisa.it, flferrara@unisa.it, cgennarelli@unisa.it, rguerriero@unisa.it,
mmigliozzi@unisa.it, lpascarella@unisa.it

Abstract – This work concerns the experimental validation of a near-field (NF) spherical scanning for an offset mounted long antenna under test (AUT), that requires a non-redundant (NR), namely minimum, amount of NF data. We address the issue of decreasing the number of voltage samples required to execute the traditional NF-far-field transformation (NF-FFT) technique in a non-centered case scenario, which would generally need a considerably higher amount of input data as compared to the onset case. In particular, by exploiting the theory of the NR sampling representations of electromagnetic field and adopting a rounded cylinder model of the antenna, the number of required samples is exactly the same as the minimum one involved in the onset scenario. Experimental results, which prove the goodness and efficacy of the approach, are presented.

Index Terms – Antenna measurements, NF-FF transformations, non-redundant sampling representations of the electromagnetic field, offset mounting, spherical scan.

I. INTRODUCTION

Antenna characterization plays a key role in validating the performances of the antenna under test (AUT) in its realistic working conditions, since it ensures compliance with the design specifications and operational standards relevant to the intended application. The main objective of the measurement process is to determine the AUT far-field (FF) radiation pattern, which can be achieved using different methods, which exhibit distinct advantages and drawbacks in terms of accuracy, measurement setup complexity, and spatial constraints.

Conventional FF measurement techniques allow us to directly acquire the AUT FF parameters of interest but come with notable limits. Chief among these is the FF distance condition, which imposes a minimum separation between the measurement probe and the AUT, potentially leading to impractically large indoor measurement setups. These limitations have driven the spread of near-field (NF) measurement techniques over the past decades [1–11]. NF methods offer, among many others, a significant advantage by removing the need to satisfy the FF distance condition, enabling measurements to be performed at much shorter ranges than the FF ones in an anechoic chamber, a climate and electromagnetic controlled location [6]. NF techniques are classified into spherical, cylindrical, and planar NF measurements. In particular, spherical NF (SNF) methods [12–26] allow us to obtain the AUT complete FF pattern without introducing the errors resulting from the scanning area truncation but can lead to long measurement times with high related costs, due to the great number of necessary NF samples, particularly when electrically large AUTs are considered. This led to the development of innovative NF techniques aimed at reducing the massive amount of needed samples, such as non-redundant (NR) sampling representations of the electromagnetic (EM) field [27, 28], adaptive sampling [23], or compressed sensing [25, 26]. In particular, NR representations have emerged as exceedingly powerful tools, owing to their distinctive advantages. Indeed, they allow us to exploit all and only the available independent information of the problem, leading to a considerable reduction of required NF data. By properly exploiting the spatial bandlimitation of EM fields [29, 30], NR NF far-field transformation (NF-FFT) techniques with spherical scan have been developed [16, 20–22]. They necessitate the measurement of a minimum amount of samples, practically equal to the number of degrees of freedom (NDFs) of the field [30, 31], to accurately recover the voltage revealed by a non-directive probe [20–22], which exhibits a spatial bandwidth almost equal to the antenna field. Then, the NR samples, which are non-uniformly spaced, are efficiently interpolated to recover the massive NF data at the points, uniformly spaced, imposed by the traditional SNF sampling theory,

Submitted On: May 28, 2025
Accepted On: September 02, 2025

https://doi.org/10.13052/2026.ACES.J.410203

by employing a 2-D optimal sampling interpolation (OSI) expansion. Finally, the AUT far-field is obtained by executing the standard spherical NF-FFT technique. These NR NF-FFT techniques outperform the standard spherical one, not only by requiring drastically less samples, thus entailing shorter acquisition times, but also enabling to exactly determine the highest-order spherical harmonic involved in the spherical wave expansion (SWE) of the field [16].

Unluckily, mechanical constraints or specific antenna mounting configurations often inevitably prevent the alignment of the antenna center with that of the measurement sphere (offset mounting). In such offset setups, the classical spherical NF-FFT technique requires collecting a drastically higher number of samples, due to the minimum sphere rule [15], thus increasing the acquisition time and related costs. To address this issue, Foged et al. [32, 33] proposed a modified formulation based on the computation of the SWE of the field with respect to the (offset) antenna center rather than to the one of measurement sphere. A similar approach was developed in [34]. While these techniques help in reducing the number of expansion coefficients and sampling points, they entail a huge computational effort, since they require us to perform a full matrix inversion. This problem was later mitigated by the iterative method proposed in [35]. In any case, these techniques require a number of samples slightly greater than in the onset mounting.

The goal of this paper is to give an experimental assessment of NR spherical scanning developed in [36] for an elongated AUT, mounted in offset and modeled by a rounded cylinder (see Fig. 1). This approach enables us to accurately recover the antenna far-field by using a minimum number of samples, equal to that required for the NR onset case, as previously demonstrated in [37] for an offset mounted long AUT modeled by a prolate spheroid, and in [38, 39] for quasi planar antennas offset mounted and modeled by an oblate spheroid and a double bowl. The experimental proofs have been performed via the roll-over-azimuth spherical NF measurement facility present in the Antenna Characterization Laboratory of the UNIversity of SAlerno (UNISA). The showcased results have demonstrated the efficacy of the technique from a practical viewpoint.

II. NR REPRESENTATION ON THE SCANNING SPHERE

In this section, the development of an NR representation of the voltage acquired by a non-directive probe on a scan sphere M having radius d in the NF region of a non-centered elongated AUT is presented. The problem geometry is displayed in Fig. 1. Firstly, let us consider two different spherical coordinate systems:

- the onset coordinate system $S(r, \vartheta, \varphi)$ having the origin O at the center of the scanning spherical surface M;
- the offset coordinate system $S'(r', \vartheta', \varphi')$ obtained by translating the onset one S by a distance d_s along the z-axis, so that its origin O' coincides with the center of the offset mounted antenna.

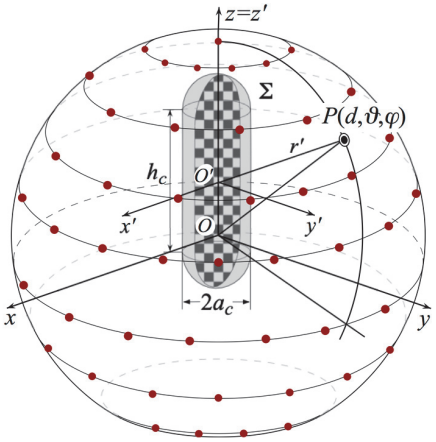

Fig. 1. Problem geometry.

While the onset coordinate system $S(r, \vartheta, \varphi)$ identifies the generic observation point $P(d, \vartheta, \varphi)$, the introduction of the offset one S' allows us to develop an appropriate NR representation of the voltage on the sphere. Therefore, the NR sampling points are computed in the offset coordinate system S' and subsequently mapped into the onset one S through the following coordinate transformation relations linking the two reference systems:

$$\varphi = \varphi'; \vartheta = \tan^{-1}[r' \sin \vartheta' / (r' \cos \vartheta' + d_s)], \quad (1)$$

$$r' = \sqrt{d^2 - (d_s \sin \vartheta')^2} - d_s \cos \vartheta', \quad (2)$$

$$\vartheta' = \tan^{-1}[d \sin(\vartheta) / (d \cos(\vartheta) - d_s)]. \quad (3)$$

In accordance with the theory developed in [27], it is possible to define an NR sampling representation of the voltage V (i.e. a representation requiring a minimum amount of samples) by adopting a suitable parameterization $\underline{r} = \underline{r}(\xi)$ to describe the observation curve and extracting an optimal phase factor $e^{j\psi(\xi)}$ from the expression of V, thus getting the so called "reduced voltage":

$$\tilde{V}(\xi) = e^{j\psi(\xi)} V(\xi), \quad (4)$$

which is a spatially quasi-bandlimited function. It is important to highlight that $V(\xi)$ is the voltage V_p revealed by the probe or V_r by the rotated probe. It

follows that, when approximating $\tilde{V}(\xi)$ by a bandlimited function, a band-limitation error arises. However, this error has step-like behavior, being very small when the bandwidth is greater than a critical value W_ξ. In particular, it is possible to ensure the validity of this condition by considering an enlargement bandwidth factor χ', so that the bandwidth of the chosen bandlimited function is $\chi' W_\xi$. It is noteworthy that χ' values slightly greater than one can be adopted when AUT sizes are large in terms of wavelengths.

As shown in [27], the number of NR samples, at Nyquist rate, necessary to accurately represent $V(\xi)$ on a closed surface (even unbounded) encircling the surface Σ modeling the antenna is proportional to the area of Σ. Therefore, to minimize the number of required samples, an appropriate choice of the most suitable rotational surface Σ is in order. In particular, Σ must be selected in such a way as to minimize any volumetric redundancy by best fitting the shape of the AUT. Since we are dealing with an elongated AUT, a suitable choice is represented by a rounded cylinder centered in O' (see Figs. 1 and 2), namely a cylinder, of radius a_c and height h_c, terminated with two hemispheres. As previously stated, the NR representation of the voltage V on the scan sphere M, that is conveniently described by parallels and meridians, must be determined in S'. The spatial bandwidth relevant to a meridian, that is still a meridian curve in S', i.e. a curve got as the intersection between M and the meridian plane through the observation point P, is [27]:

$$W_\xi = \ell(C')/\lambda, \tag{5}$$

where $\ell(C')$ is the length of the curve C', intersection between Σ and the meridian plane, and λ is the wavelength. Moreover, the optimal parameter and phase function are [27]:

$$\xi = (\pi/\ell(C'))[R_1 + s'(P_1) - R_2 + s'(P_2)], \tag{6}$$

$$\psi = (\pi/\lambda)[R_1 + s'(P_1) + R_2 - s'(P_2)], \tag{7}$$

where R_1 and R_2 are the distances from the point P to the tangency points P_1 and P_2 on C' and $s'(P_1)$ and $s'(P_2)$ are the related arclength abscissas (see Fig. 2). These parameters depend, of course, on the specific choice of the surface Σ. Having selected a rounded cylinder as a suitable surface modeling the AUT, we know that $\ell(C') = 2(h_c + \pi a_c)$ and hence:

$$W_\xi = 2(h_c + \pi a_c)/\lambda. \tag{8}$$

The related expressions for ξ and ψ are got by substituting in (6) and (7) the distances $R_{1,2}$ and the curvilinear abscissas $s'(P_{1,2})$, whose expressions depend on the positions of the points P_1 and P_2, which in turn change as the angle ϑ' varies. As shown in [34], three cases occur.

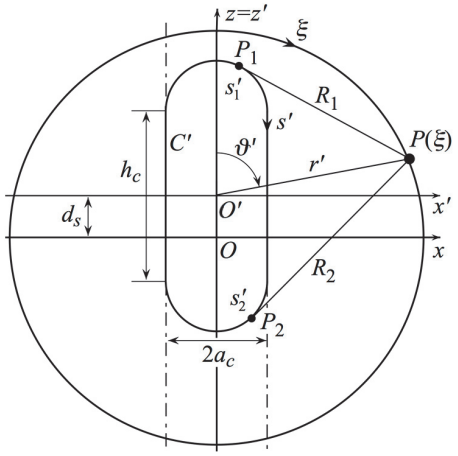

Fig. 2. Relevant to a meridian.

For $0 \le \vartheta' \le \sin^{-1}(a_c/r')$:

$$R_1 = \sqrt{(r'\sin\vartheta')^2 + (r'\cos\vartheta' - h_c/2)^2 - a_c^2}, \tag{9}$$

$$s'(P_1) = a_c \sin^{-1}\left(\frac{a_c r'\sin\vartheta' + R_1((h_c/2) - r'\cos\vartheta')}{R_1^2 + a_c^2}\right), \tag{10}$$

$$R_2 = R_1, \tag{11}$$

$$s'(P_2) = a_c \sin^{-1}\left(\frac{a_c r'\sin\vartheta' - R_2((h_c/2) - r'\cos\vartheta')}{R_2^2 + a_c^2}\right), \tag{12}$$

for $\sin^{-1}(a_c/r') \le \vartheta' \le \pi - \sin^{-1}(a_c/r')$, R_1 and $s'(P_1)$ are given by (9) and (10), while:

$$R_2 = \sqrt{(r'\sin\vartheta')^2 + (r'\cos\vartheta' + h_c/2)^2 - a_c^2}, \tag{13}$$

$$s'(P_2) = h_c + \\ + a_c\left[\pi - \sin^{-1}\left(\frac{a_c r'\sin\vartheta' + R_2((h_c/2) + r'\cos\vartheta')}{R_2^2 + a_c^2}\right)\right], \tag{14}$$

finally, for $\pi - \sin^{-1}(a_c/r') \le \vartheta' \le \pi$, R_2 and $s'(P_2)$ are given by (13) and (14), and:

$$R_1 = \sqrt{(r'\sin\vartheta')^2 + (r'\cos\vartheta' + h_c/2)^2 - a_c^2}, \tag{15}$$

$$s'(P_1) = h_c + \\ + a_c\left[\frac{\pi}{2} - \sin^{-1}\left(\frac{R_1 r'\sin\vartheta' + a_c((h_c/2) + r'\cos\vartheta')}{R_1^2 + a_c^2}\right)\right]. \tag{16}$$

For a parallel, the phase function is constant and φ' can be effectively employed as an optimal parameter. The corresponding bandwidth is:

$$W_{\varphi'} = \frac{\pi}{\lambda}\max_{\bar{z}'}\left(\sqrt{(\rho+\rho'(\bar{z}'))^2+(z'-\bar{z}')^2} - \sqrt{(\rho-\rho'(\bar{z}'))^2+(z'-\bar{z}')^2}\right), \quad (17)$$

where $\rho = r'\sin\vartheta'$ and $\rho'(\bar{z}')$ defines the rounded cylinder equation.

The maximum is achieved at:

$$\bar{z}' = \begin{cases} z' & |z'| \le \dfrac{h_c}{2} \\ \left[\dfrac{h_c}{2} + \dfrac{(|z'|-h_c/2)a_c^2}{(r'\sin\vartheta')^2+ \\ \qquad +(|z'|-h_c/2)^2}\right]\mathrm{sgn}(z') & |z'| > \dfrac{h_c}{2} \end{cases}, \quad (18)$$

where $\mathrm{sgn}(\cdot)$ is the sign function.

The obtained NR samples are uniformly spaced with respect to the optimal parameter ξ but not with respect to ϑ'. This is why a suitable interpolation of the samples must be introduced to carry out the standard NF-FFT, which requires a set of uniformly distributed input data. It must be emphasized that interpolation of the NR voltage samples in the prescribed (uniformly spaced) positions on the sphere using the classical cardinal series would entail a massive computational effort. Indeed, this well-known technique is suboptimal when dealing with a great number of data, due to the use of the Dirichlet sampling functions, that, to prevent the truncation error, implicates the involvement of all input samples to determine any output one. Furthermore, this would also cause propagation of errors, which affect the samples, from high to low voltage values. Hence, a custom-made optimal interpolation algorithm, the 2-D OSI expansion [40], is used. Such an interpolation scheme allows us to reconstruct the voltage values at any point on the scan sphere by using a traveling sampling and adopting optimal self-truncating functions, which require us to retain only a small number of samples in the proximity of the considered output one to minimize truncation error. It is thus possible to lessen the computational load and to prevent error propagation from high to low voltage levels. Hence, probe voltage at the point $P(\vartheta',\varphi')$ can be reconstructed [36]:

$$V(\xi(\vartheta'),\varphi') = \mathrm{e}^{-\mathrm{j}\psi(\xi)}\sum_{n=n_0-q+1}^{n_0+q}\left\{K(\xi,\xi_n,\bar{\xi},N,N'')\cdot\sum_{m=m_0-p+1}^{m_0+p}\tilde{V}(\xi_n,\varphi'_{m,n})K(\varphi',\varphi'_{m,n},\bar{\varphi}',M_n,M''_n)\right\}, \quad (19)$$

where $n_0 = \mathrm{Int}(\xi/\Delta\xi)$, $m_0 = \mathrm{Int}(\varphi'/\Delta\varphi'_n)$, $2q\times 2p$ is the retained samples number, and:

$$\xi_n = n\Delta\xi = 2\pi n/(2N''+1); N'' = \mathrm{Int}(\chi N')+1, \quad (20)$$

$$N = N''-N'; \quad N' = \mathrm{Int}(\chi' W_\xi)+1; \quad \bar{\xi} = q\Delta\xi, \quad (21)$$

$$\varphi'_{m,n} = m\Delta\varphi'_n = 2\pi m/(2M''_n+1); \quad M''_n = \mathrm{Int}(\chi M'_n)+1, \quad (22)$$

$$M_n = M''_n - M'_n; \quad M'_n = \mathrm{Int}[\chi^* W_{\varphi'}(\xi_n)]+1, \quad (23)$$

$$\chi^* = 1+(\chi'-1)[\sin\vartheta'(\xi_n)]^{-2/3}; \quad \bar{\varphi}' = p\Delta\varphi'_n. \quad (24)$$

In particular, Int(x) stays for the integer part function, while $\chi > 1$ is the oversampling factor, introduced to control the truncation error. Furthermore:

$$K(\alpha,\alpha_t,\bar{\alpha},H,H'') = D_{H''}(\alpha-\alpha_t)\Omega_H[(\alpha-\alpha_t),\bar{\alpha}], \quad (25)$$

where

$$\Omega_H(\alpha,\bar{\alpha}) = \frac{T_H[2\cos^2(\alpha/2)/\cos^2(\bar{\alpha}/2)-1]}{T_H[2/\cos^2(\bar{\alpha}/2)-1]}, \quad (26)$$

$$D_{H''}(\alpha) = \frac{\sin[(2H''+1)\alpha/2]}{(2H''+1)\sin(\alpha/2)}, \quad (27)$$

are, respectively, the Tschebyscheff and the Dirichlet sampling functions [27, 36].

The interested reader can find, in [40], a detailed study on the error introduced by the OSI (plots of the normalized maximum and normalized mean-square reconstruction errors for various values of the oversampling factor and versus the retained samples number). Such an expansion is computationally simple and very fast. Its validity is widely demonstrated in many papers by the authors.

III. EXPERIMENTAL VALIDATION

The showcased NR NF-FFT has been validated through laboratory proofs at the UNISA Antenna Characterization Laboratory. This facility has an anechoic chamber ($8\times 5\times 4$ m) sized for both NF and FF measurements, depending on the FF distance requirements. The chamber is paneled by pyramidal absorbers, guaranteeing a background noise level lower than -40 dB in the X band. Three rotary tables and a vertical linear scanner equip a versatile system (see Fig. 6 in [39]), allowing us to perform NF measurements not only using classical scans, like cylindrical, spherical, and plane-polar, but also the innovative helicoidal, spherical-spiral, and

planar-spiral scans. A vector network analyzer (VNA) is utilized to perform accurate amplitude and phase measurements. Such a measurement facility provides an additional rotary table too, allowing us to execute direct FF or radar cross section measurements of electrically small AUTs/targets. A photo of the NF facility of the UNISA Antenna Characterization Laboratory is shown in Fig. 3. The interested reader can find a more detailed description of this NF facility and additional photos in Chapter 1 of [11].

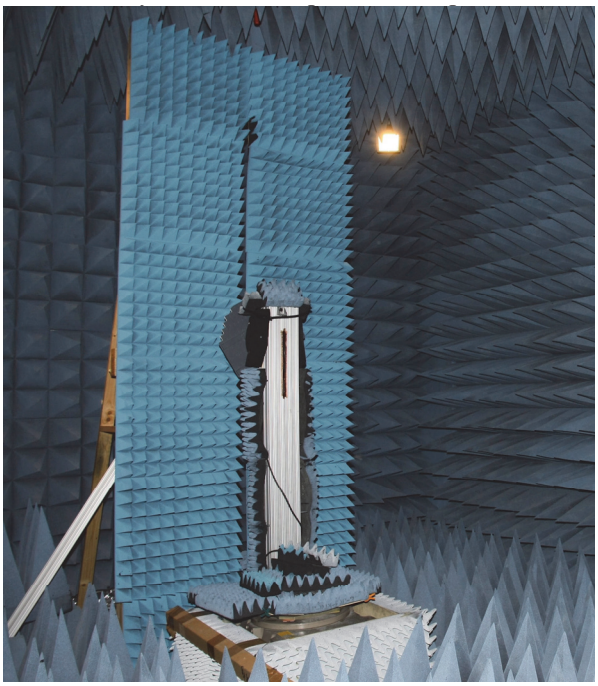

Fig. 3. Photo of the NF measurement system available at the UNISA Antenna Characterization Laboratory.

In the reported experimental results, the employed antenna is a slotted waveguide array operating at 10 GHz. It was obtained by realizing eight rounded-ended slots in the large walls of a tapered rectangular waveguide and feeding it by means of a coaxial to rectangular wave-guide transition. It has been mounted with its broad walls parallel to the $x = 0$ plane and its axis coinciding with the z one. An open-ended WR90 rectangular waveguide is utilized as the scanning probe. The standard spherical NF-FFT [15] is carried out by the MI-3000 package and is employed to compute both the reference FF patterns, directly got by processing the considerably great amount of (offset) NF data collected at the classical lattice [15], and those attained from the NF data recovered by interpolating the drastically lower amount of gathered NR NF samples. In the considered experimental tests, the AUT has been shifted along the z-axis by a distance $d_s = 5.37\ \lambda$.

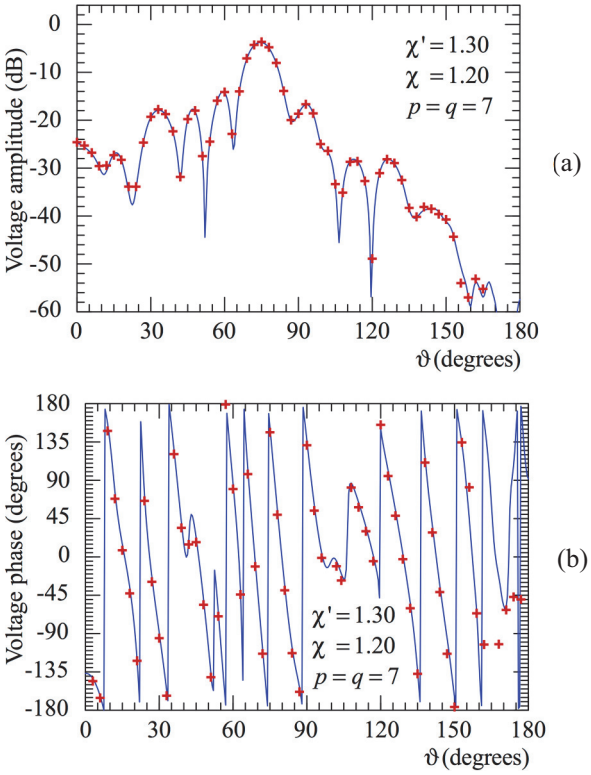

Fig. 4. Voltage amplitude (a) and phase (b) on the meridian at $\varphi = 0°$ — measured. + + + NR data.

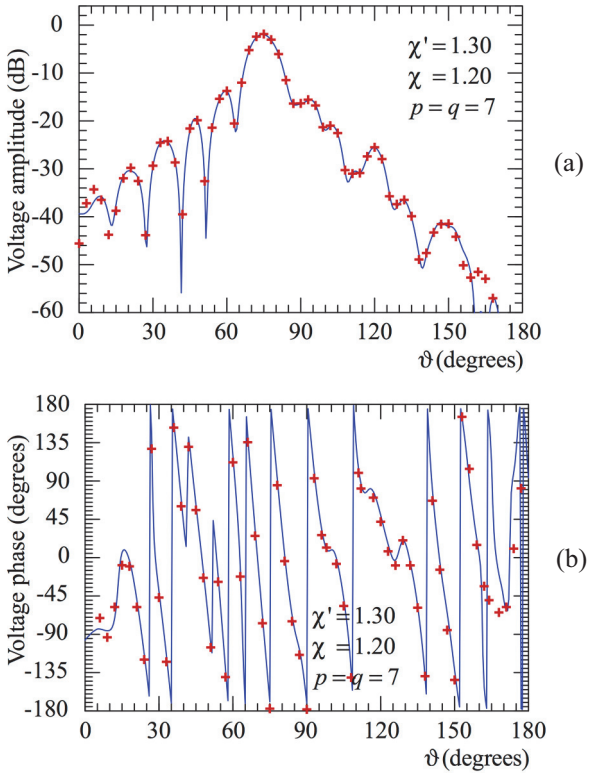

Fig. 5. Voltage amplitude (a) and phase (b) on the meridian at $\varphi = 90°$. — measured. + + + NR data.

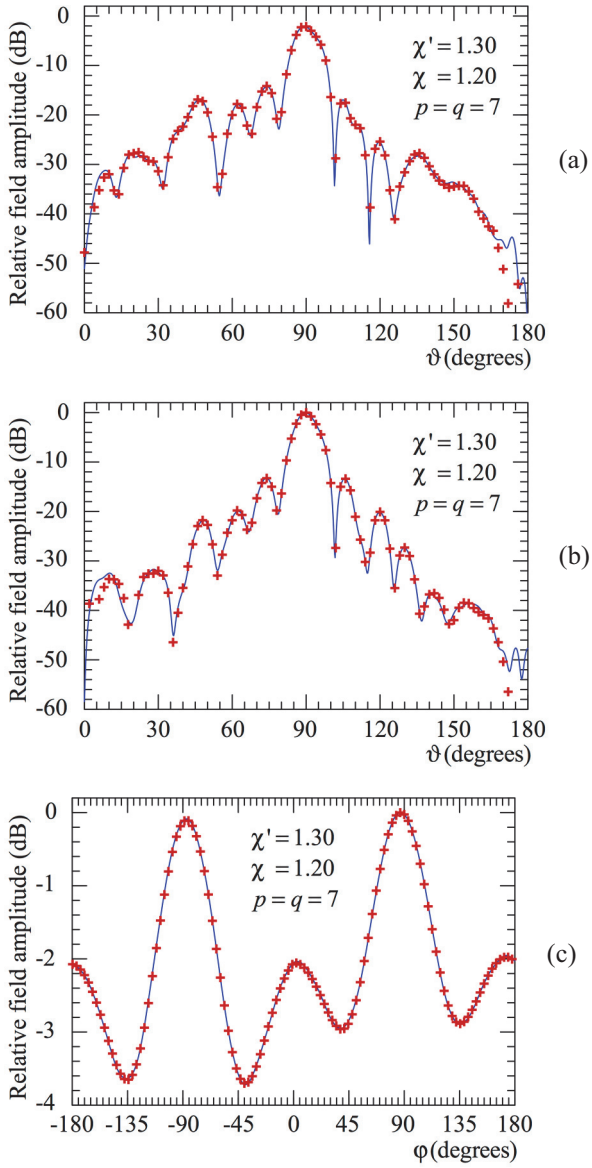

Fig. 6. FF patterns at $\varphi = 0^\circ$ (a), $\varphi = 90^\circ$ (b), and $\vartheta = 90^\circ$ (c). — reference. + + + NR data.

The parameters of the rounded cylinder employed for modeling the AUT are $h_c = 10\ \lambda$ and $a_c = 0.85\ \lambda$. The voltages have been measured on a sphere with radius $d = 20\ \lambda$ and the shown recoveries have been got by adopting $p = q = 7$, $\chi' = 1.30$, and $\chi = 1.20$. In Figs. 4 and 5, the amplitudes and phases of the recovered voltage V_r on the meridians at $\varphi = 0^\circ$ and $\varphi = 90^\circ$ are compared with the directly acquired ones on the same meridians. The FF patterns at $\varphi = 0^\circ$, $\varphi = 90^\circ$, and $\vartheta = 90^\circ$, obtained from the NR NF samples, are compared in Figs. 6 (a–c) with those (references) taken from the massive number of offset data directly acquired on the NF grid for the standard NF-FFT. As can be clearly observed, both the NF and the FF recoveries results are very accurate, save for the regions where the voltage/field is very low, thus fully demonstrating the practical effectiveness of the approach.

It must be highlighted that the proposed technique allows a drastic decrease of the number of samples to be acquired and, consequently, a huge saving of acquisition time. Indeed, the AUT testing required only 705 NR NF samples, a remarkably lower amount of data than the 7320 required by the traditional spherical NF-FFT. It is interesting to compare the corresponding times employed to acquire the needed NF samples, namely 4.65 and 24.38 hours, respectively.

Further experimental results, which validate the effectiveness of the developed NR NF-FFT with spherical scanning for offset mounted elongated antennas and relevant to a different AUT and working frequency, are reported in [41].

IV. CONCLUSION

In this paper, experimental validation of an NR NF-FFT technique with spherical scan for offset mounted long antennas is presented. The proposed approach, with respect to other existing techniques, requires the gathering of the same minimum number of NF samples fixed by the NR sampling for the onset mounting scenario, entailing not only a massive reduction in terms of needed NF data, but also of acquisition time. The experimental results are relevant to a rounded cylinder modeling of an elongated AUT, which represents the optimal choice since it suitably fits its shape without introducing any volumetric redundancy. Then, a custom-made 2-D OSI expansion allows us to accurately and efficiently reconstruct the NF data necessary to execute the standard spherical NF-FFT from the gathered NR ones. The accuracy and effectiveness of this innovative approach are experimentally confirmed by the very satisfactory agreement obtained in both the NF and FF reconstructions.

REFERENCES

[1] A. D. Yaghjian, "An overview of near-field antenna measurements," *IEEE Trans. Antennas Propag.*, vol. AP-34, pp. 30–45, Jan. 1986.

[2] J. Appel-Hansen, J. D. Dyson, E. S. Gillespie, and T.G. Hickman, "Antenna Measurements," in *The Handbook of Antenna Design*, A. W. Rudge, K. Milne, A. D. Olver, and P. Knight, Eds. London, UK: Peter Peregrinus, pp. 584–694, 1986.

[3] E. S. Gillespie, "Special Issue on near-field scanning techniques," *IEEE Trans. Antennas Propag.*, vol. 36, pp. 727–901, June 1988.

[4] S. Gregson, J. McCormick, and C. Parini, *Principles of Planar Near-Field Antenna Measurements*. London, UK: IET, 2007.

[5] M. H. Francis and R. C. Wittmann, *Near-Field Scanning Measurements: Theory and Practice*, in *Modern Antenna Handbook*. Hoboken, NJ, USA: John Wiley & Sons, pp. 929–976, 2008.

[6] *IEEE Recommended Practice for Near-Field Antenna Measurements*, IEEE Standard 1720-2012, 2012.

[7] C. Gennarelli, A. Capozzoli, L. Foged, J. Fordham, and D. J. van Rensburg, "Special issue on recent advances in near-field to far-field transformation techniques," *Int. Jour. Antennas Propag*., vol. 2012, ID 243203, 2012.

[8] F. Ferrara, C. Gennarelli, and R. Guerriero, "Near-Field Antenna Measurement Techniques," in *Handbook of Antenna Technologies*, Z. N. Chen, D. Liu, H. Nakano, X. Qing, and T. Zwick, Eds. Singapore: Springer, pp. 2107–2163, 2016.

[9] M. Sierra Castañer and L. J. Foged, *Post-Processing Techniques in Antenna Measurement*. London, UK: SciTech Publishing IET, 2019.

[10] C. Parini, S. Gregson, J. McCormick, D. J. Van Resburg, and T. Eibert, *Theory and Practice of Modern Antenna Range Measurements*. London, UK: SciTech Publishing IET, 2020.

[11] C. Gennarelli, F. Ferrara, R. Guerriero, and F. D'Agostino, *Non-Redundant Near-Field to Far-Field Transformation Techniques*. London, UK: SciTech Publishing IET, 2022.

[12] F. Jensen, "On the probe compensation for near-field measurements on a sphere," *Archiv Elektr. Übertr*., vol. 29, pp. 306–308, Aug. 1975.

[13] F. H. Larsen, "Probe correction of spherical near-field measurements," *Electr. Lett.*, vol. 13, pp. 393–395, 1977.

[14] A. D. Yaghjian and R. C. Wittmann, "The receiving antenna as a linear differential operator: Application to spherical near-field measurement," *IEEE Trans. Antennas Propag*., vol. AP-33, pp. 1175–1185, Nov. 1985.

[15] J. Hald, J. E. Hansen, F. Jensen, and F. H. Larsen, *Spherical Near-Field Antenna Measurements*. London, UK: Peregrinus, 1998.

[16] O. M. Bucci, C. Gennarelli, G. Riccio, and C. Savarese, "Data reduction in the NF-FF transformation technique with spherical scanning," *Jour. Electromagn. Waves Appl.*, vol. 15, pp. 755–775, 2001.

[17] T. Laitinen and S. Pivnenko, "Probe correction technique for symmetric odd-order probes for spherical near-field antenna measurements," *IEEE Antennas Wirel. Propag. Lett.*, vol. 6, pp. 635–638, 2007.

[18] T. Laitinen, S. Pivnenko, J. M. Nielsen, and O. Breinbjerg, "Theory and practice of the FFT/ matrix inversion technique for probe-corrected spherical near-field antenna measurements with high-order probes," *IEEE Trans. Antennas Propag.*, vol. 58, pp. 2623–2631, Aug. 2010.

[19] T. B. Hansen, "Numerical investigation of the system-matrix method for higher-order probe correction in spherical near-field antenna measurements," *Int. Jour. Antennas Propag*., vol. 2012, ID 493705, 2012.

[20] F. D'Agostino, F. Ferrara, C. Gennarelli, R. Guerriero, and M. Migliozzi, "Effective antenna modellings for NF-FF transformations with spherical scanning using the minimum number of data," *Int. Jour. Antennas Propag*., vol. 2011, ID 936781, 2011.

[21] F. D'Agostino, F. Ferrara, C. Gennarelli, R. Guerriero, and M. Migliozzi, "Non-redundant spherical NF - FF transformations using ellipsoidal antenna modeling: Experimental assessments," *IEEE Antennas Propag. Magaz.*, vol. 55, pp. 166–175, Aug. 2013.

[22] F. D'Agostino, F. Ferrara, C. Gennarelli, R. Guerriero, and M. Migliozzi, "Experimental testing of nonredundant near-field to far-field transformations with spherical scanning using flexible modellings for nonvolumetric antennas," *Int. Jour. Antennas Propag*., vol. 2013, ID 517934, 2013.

[23] M. A. Qureshi, C. H. Schmidt, and T. F. Eibert, "Adaptive sampling in spherical and cylindrical near-field antenna measurements," *IEEE Antennas Propag. Magaz.*, vol. 55, pp. 243–249, 2013.

[24] F. R. Varela, B. G. Iragüen, and M. Sierra Castañer, "Under-sampled spherical near-field antenna measurements with error estimation," *IEEE Trans. Antennas Propag*., vol. 68, pp. 6364–6371, Aug. 2020.

[25] A. Bangun and C. Culotta-Loìpez, "Optimizing sensing matrices for spherical near-field antenna measurements," *IEEE Trans. Antennas Propag.*, vol. 71, pp. 1716–1724, Feb. 2023.

[26] F. Peng, Q. Zhang, X. Liu, Z. Wang, and X. Chen, "An efficient antenna measurements method in spherical near field based on sparse sampling," *IEEE Antennas Wirel. Propag. Lett.*, vol. 23, pp. 3492–3496, 2024.

[27] O. M. Bucci, C. Gennarelli, and C. Savarese, "Representation of electromagnetic fields over arbitrary surfaces by a finite and nonredundant number of samples," *IEEE Trans. Antennas Propag*., vol. 46, pp. 351–359, Mar. 1998.

[28] O. M. Bucci and C. Gennarelli, "Application of nonredundant sampling representations of electromagnetic fields to NF-FF transformation techniques," *Int. Jour. Antennas Propag*., vol. 2012, ID 319856, 2012.

[29] O. M. Bucci and G. Franceschetti, "On the spatial bandwidth of scattered fields," *IEEE Trans. Antennas Propag*., vol. AP-35, pp. 1445–1455, Dec. 1987.

[30] O. M. Bucci and G. Franceschetti, "On the degrees of freedom of scattered fields," *IEEE Trans. Antennas Propag*., vol. 37, pp. 918–926, July 1989.

[31] O. M. Bucci and M. D. Migliore, "Degrees of freedom and sampling representation of electromagnetic fields: Concepts and applications," *IEEE Antennas Propag. Magaz.*, vol. 67, pp. 10–22, June 2025.

[32] L. J. Foged, F. Saccardi, F. Mioc, and P. O. Iversen, "Spherical near field offset measurements using downsampled acquisition and advanced NF/FF transformation algorithm," in *Proc. of EUCAP 2016*, Davos, Switzerland, pp. 1–3, 10–15 Apr. 2016.

[33] F. Saccardi, F. Rossi, F. Mioc, L. J. Foged, and P. O. Iversen, "Application of the translated-SWE algorithm for the characterization of antennas installed on cars using a minimum number of samples," in *Proc. of AMTA 2017*, Atlanta, GA, USA, pp. 1-6, 15-20 Oct. 2017.

[34] R. Cornelius and D. Heberling, "Spherical wave expansion with arbitrary origin for near-field antenna measurements," *IEEE Trans. Antennas Propag*., vol. 65, pp. 4385–4388, Aug. 2017.

[35] F. R. Varela, B. G. Iragüen, and M. Sierra Castañer, "Fast spherical near-field to far-field transformation for offset-mounted antenna measurements," *IEEE Antennas Wirel. Propag. Lett.*, vol. 19, pp. 2255–2259, Dec. 2020.

[36] F. D'Agostino, F. Ferrara, C. Gennarelli, R. Guerriero, and M. Migliozzi, "Nonredundant NF-FF transformation with spherical scan accounting for an offset mounting of a long AUT," in *Proc. of AMTA 2016*, Austin, TX, USA, pp. 167–172, 30 Oct. 4 Nov. 2016.

[37] F. D'Agostino, F. Ferrara, C. Gennarelli, R. Guerriero, and M. Migliozzi, "A nonredundant sampling representation managing an offset mounting of an elongated antenna in a spherical near-field facility," *IEEE Antennas Wirel. Propag. Lett.*, vol. 18, pp. 2671–2675, Dec. 2019.

[38] F. D'Agostino, F. Ferrara, C. Gennarelli, R. Guerriero, and M. Migliozzi, "A non-redundant sampling representation requiring the same number of spherical near-field measurements for both onset and offset mountings of a quasi-planar antenna," *Int. Jour. Commun. Antenna Propag.*, vol. 9, pp. 311–319, Oct. 2019.

[39] F. D'Agostino, F. Ferrara, C. Gennarelli, R. Guerriero, and M. Migliozzi, "A spherical near-to-far-field transformation using a non-redundant voltage representation optimized for non-centered mounted quasi-planar antennas," *Electronics*, vol. 9, ID 944, pp. 1–13, June 2020.

[40] O. M. Bucci, C. Gennarelli, and C. Savarese, "Optimal interpolation of radiated fields over a sphere," *IEEE Trans. Antennas Propag*., vol. 39, pp. 1633–1642, Nov. 1991.

[41] F. D'Agostino, F. Ferrara, C. Gennarelli, R. Guerriero, and M. Migliozzi, "Experimental validation of a non-redundant NF-FF transformation for long AUTs mounted in offset configuration in a spherical NF facility," in *Proc. of AMTA 2019*, San Diego, CA, USA, pp. 115–120, 6–11 Oct. 2019.

Francesco D'Agostino received his Laurea degree in electronic engineering from the University of Salerno, Italy. At the same university he also received the Ph.D. degree in information engineering and then was appointed Associate Professor of electromagnetics. His research activity includes application of sampling techniques to electromagnetics and to innovative NF-FF transformations, diffraction problems, radar cross section evaluations, and electromagnetic compatibility. In this area, D'Agostino has coauthored five books and over 300 scientific papers, published in peer-reviewed international journals and conference proceedings. He serves as a regular Reviewer for several journals and conferences and has been invited speaker and chair for international events and conferences. D'Agostino is a senior member and fellow of Antenna Measurement Techniques Association (AMTA), senior member of the Institute of Electrical and Electronics Engineers (IEEE), member of the Editorial Board of *MDPI Electronics* and of the *Journal of Electronics and Electrical Engineering*, member of the European Association on Antennas and Propagation (EurAAP) and of the Italian Electromagnetic Society (SIEM).

Flaminio Ferrara (Member, IEEE) was born in Salerno, Italy, in 1972. He received the Laurea degree in electronic engineering and the Ph.D. degree in information engineering from the University of Salerno, Fisciano, Salerno, Italy, in 1999 and 2003, respectively. Since 1999, he has been with the Research Group in Applied Electromagnetics, University of Salerno, where he is currently an Associate Professor of electromagnetic fields. He is the co-author of about 300 scientific articles, mainly in international journals and conference proceedings. In particular, he is the co-author of four books on NF-FF transformation techniques and the co-author of the chapter "Near-Field Antenna Measurement Techniques" of the *Handbook of Antenna Technologies*. His scientific interests include the application of sampling techniques to the efficient reconstruction of electromagnetic fields and to NF-FF transformation techniques, monostatic radar cross section evaluations of corner reflectors, and electromagnetic wave diffraction from canonical and complex structures. Ferrara is a reviewer for several international journals and a member

of the Editorial Board of the *International Journal of Antennas and Propagation and of Electronics*.

Claudio Gennarelli (Senior Member, IEEE) was born in Avellino, Italy, in 1953. He received the Laurea degree (*summa cum laude*) in Electronic Engineering from the University "Federico II" of Naples in 1978. From 1978 to 1983, he worked with the Research Group in Electromagnetics at the same University. In 1983, he became an Assistant Professor at the Istituto Universitario Navale of Naples. In 1987, he was appointed as Associate Professor of Antennas, formerly at the University of Ancona, Italy, and subsequently at the University of Salerno, Italy. In 1999, was appointed as Full Professor at the same University. He retired in November 2023. He has coauthored more than 480 scientific articles, mainly in international journals and conference proceedings. In particular, he has co-authored four books on near-field to far-field (NF-FF) transformation techniques, the chapter Near-field antenna measurement techniques of the *Handbook of Antenna Technologies*, and the book *Non-Redundant Near-Field To Far-Field Transformation Techniques* published by Scitech. The main topics of his scientific activity are reflector antennas analysis, antenna measurements, diffraction problems, radar cross section evaluations, application of sampling techniques to electromagnetics and to NF-FF transformations, NF-FF transformations with spiral scannings, and compensation of the probe positioning errors in the NF-FF transformations. He is a member of the Editorial board of the *International Journal of Antennas and Propagation* and was a member of the Editorial board of the *Open Electrical and Electronic Engineering Journal* from 2007 to 2019.

Rocco Guerriero (Member, IEEE) received the Laurea degree in electronic engineering and the Ph.D. degree in information engineering from the University of Salerno, Fisciano, Italy, in 2003 and 2007, respectively. Since 2003, he has been with the Research Group in Applied Electromagnetics, University of Salerno, where he is currently an Associate Professor of electromagnetic fields. He is the co-author of more than 270 scientific articles, mainly in international journals and conference proceedings. In particular, he has co-authored three books on NF-FF transformation techniques and is the co-author of the chapter "Near-Field Antenna Measurement Techniques" of the *Handbook of Antenna Technologies*. His scientific interests include the application of sampling techniques to the efficient reconstruction of electromagnetic fields and to NF-FF transformation techniques, antenna measurements, inversion of ill-posed electromagnetic problems, analysis of microstrip reflectarrays, and diffraction problems. Guerriero is a reviewer for several international journals and conferences and a member of the Editorial Board of the *International Journal of Antennas and Propagation and of Electronics*.

Massimo Migliozzi received the Laurea degree in electronic engineering and the Ph.D. degree in information engineering from the University of Salerno, Fisciano, Italy, in 1999 and 2009, respectively. He is currently a Research Fellow in electromagnetic fields. His scientific research interests include the application of sampling techniques to the efficient reconstruction of electromagnetic fields and to NF-FF transformation techniques, antenna measurements, electromagnetic compatibility, antenna design, and diffraction problems. He has coauthored about 200 scientific papers, mainly in international journals and conference proceedings and he serves as a reviewer for several international journals.

Luigi Pascarella received the Bachelor's and Master's degrees (*summa cum laude*), both in Electronic Engineering, from the University "Federico II" of Naples, in 2020 and 2022, respectively. Since November 2022, he is a Ph.D. candidate in Industrial Engineering at the University of Salerno, Fisciano, Italy, with the Research Group in Applied Electromagnetics. His research focuses on developing innovative approaches for the synthesis of antenna arrays capable of radiating complex waveforms in the near-field, the application of advanced sampling techniques to electromagnetics and also to innovative NF-FF transformation techniques. He is a member of the Italian Electromagnetic Society (SIEM).

A Hybrid Efficient Iterative ACA-PO and Chebyshev Approximation Technique for Fast Radiation Analysis Over a Broad Frequency Band

Junjun Wu

Xi'an Yuanfang Aviation Technology Development Co. Ltd.
Yanliang District, Xi'an City 710089, Shaanxi Province, China
wu18792802634@outlook.com

Abstract – In this paper, a novel approach integrated efficient iterative adaptive cross approximation-physical optics (EI-ACA-PO) and Chebyshev approximation technique (CAT) is proposed to efficiently calculate the broadband solution of antenna placed on electrically large platforms. The adaptive cross-approximation (ACA) method is employed to compress the self-impedance matrix of the Method of Moments (MoM) region, and the interaction matrices between the MoM and physical optics (PO) regions. By introducing CAT technology, the iterative hybrid method is capable of efficiently calculating the wideband results. First, the outer surface is divided into two regions. Then, the integral equation is solved by the EI-ACA-PO method to obtain the induced current at the Chebyshev nodes. Afterwards, the current in a desired frequency band is represented by the Chebyshev series. To improve accuracy, the Chebyshev series is matched with the Maehly approximation. The current at any frequency point in the bandwidth can be calculated. Finally, the broadband electromagnetic radiation characteristics can be obtained.

Index Terms – Adaptive cross-approximation (ACA), carrier antenna analysis, Chebyshev approximation technique (CAT), hybrid method, iterative technology.

I. INTRODUCTION

In recent years, broadband radiation analysis of integrated antenna-platform systems has become increasingly critical for modern wireless systems. Early radiation analysis of integrated antenna-platform systems primarily relied on full-wave numerical methods such as the Method of Moments (MoM) [1]. These methods achieve electromagnetic modeling by precisely discretizing both platform and antenna structures, but they face exponential growth in unknowns when dealing with electrically large platforms, leading to prohibitive computational costs. To address this, high-frequency approximation methods such as physical optics (PO) [2] were widely adopted. PO simplifies calculations by neglecting the coupling between field triangles, making it suitable for rapid estimation of radiation characteristics at high frequencies. However, it struggles to accurately model complex phenomena arising from antenna coupling.

The hybrid method of MoM and PO is effective for modeling the electromagnetic problems of antennas around platforms [3–9]. In hybrid analysis, the entire structure is divided into MoM-regions and PO-regions. It is assumed that the currents in the PO-region are radiated and excited by the currents in the MoM-region. Then, the PO contributions can either be coupled into the MoM impedance matrix on the left-hand side of the equation, or represented in the equation as additional excitations, with an iterative approach used to drive the system to a steady state. Meanwhile, algorithms like adaptive cross approximation (ACA) [10] and multilevel fast multipole algorithm (MLFMA) [11] emerged, significantly improving the efficiency of full-wave methods. They are also integrated into hybrid methods, such as MLFMA combined with PO (MLFMA-PO) [12], ACA combined with PO (ACA-PO) [13] and adaptive integral method (AIM) combined with PO (AIM-PO) [14].

Nevertheless, confronted with the wideband challenges, these techniques still require independent matrix factorization for each frequency point, which leads to enormous time consumption. The process of repetitive solution of the matrix equations can be bypassed when employing the Chebyshev approximation technique (CAT) [15] and asymptotic waveform evaluation (AWE) [16]. Compared with AWE, CAT is widely used due to its better convergence and easier integration with other methods without adding additional memory.

In this paper, a hybrid efficient iterative adaptive cross approximation-physical optics (EI-ACA-PO)-CAT method is presented to achieve efficient wideband radiation analysis of antenna around electrically large platforms. In the proposed method, the whole PEC system can be divided into two regions: ACA-region and PO-region. the initial current coefficients in the ACA-region at the Chebyshev nodes can be independently

Submitted On: May 19, 2025
Accepted On: July 01, 2025

https://doi.org/10.13052/2026.ACES.J.410204

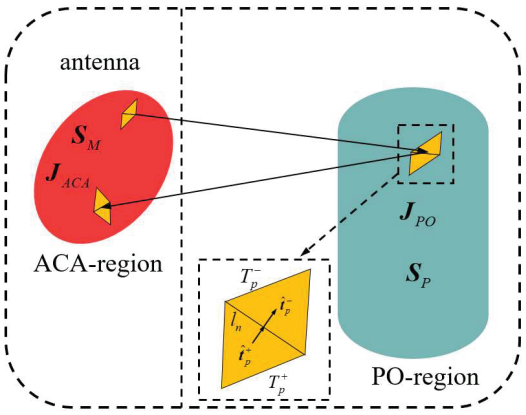

Fig. 1. EI-ACA-PO model of the perfect electric conductor (PEC) system.

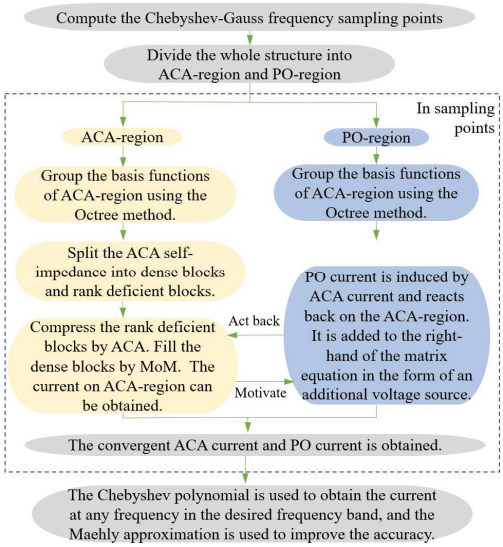

Fig. 2. Flow chart of the EI-ACA-PO-CAT method.

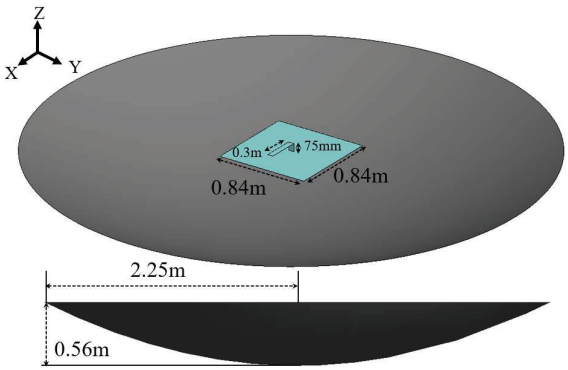

Fig. 3. Geometry of the inverted-L antenna placed above a paraboloid.

calculated by ACA. An iterative process is implemented to make the system become stable and obtain the current coefficients that have converged in two regions at Chebyshev nodes. CAT is employed to expand the current coefficients at any frequency point over the desired frequency band. Finally, to achieve a better accuracy, the Chebyshev series is transformed into a rational function by applying the Maehly approximation. Numerical examples show that the EI-ACA-PO-CAT can significantly improve calculation efficiency without loss of accuracy.

II. EI-ACA-PO-CAT FORMULATION

Consider an antenna mounted onto a perfectly conducting carrier. In the hybrid EI-ACA-PO-CAT analysis, the whole system is divided into two parts, namely the ACA-region and the PO-region. The surface currents in the ACA-region and the PO-region are denoted $\boldsymbol{J}_{ACA}$ and $\boldsymbol{J}_{PO}$, respectively, as depicted in Fig. 1. The desired frequency band and the corresponding wave number band are represented by $[f_a, f_b]$ and $[k_a, k_b]$, respectively. Generally, the scattered fields $(\boldsymbol{E}^s, \boldsymbol{H}^s)$ induced by the current $\boldsymbol{J}$ can be expressed as

$$\boldsymbol{E}^s = \boldsymbol{L}^E \boldsymbol{J}, \tag{1}$$

$$\boldsymbol{H}^s = \boldsymbol{L}^H \boldsymbol{J}, \tag{2}$$

where

$$\boldsymbol{L}^E \boldsymbol{J} = -jk\eta \int_S \left[\boldsymbol{J} G(\boldsymbol{r}, \boldsymbol{r}') + \frac{1}{k^2} \nabla \nabla' \boldsymbol{J} G(\boldsymbol{r}, \boldsymbol{r}') \right] ds', \tag{3}$$

$$\boldsymbol{L}^H \boldsymbol{J} = \nabla \times \int_S \boldsymbol{J} G(\boldsymbol{r}, \boldsymbol{r}') ds', \tag{4}$$

where $k = \omega\sqrt{\mu_0 \varepsilon_0}$ is the wavenumber, $\eta = (\varepsilon_0/\mu_0)^{1/2}$ is the wave impedance, $G(\boldsymbol{r}, \boldsymbol{r}') = e^{-jk|\boldsymbol{r}-\boldsymbol{r}'|}/(4\pi|\boldsymbol{r}-\boldsymbol{r}'|)$ denotes the Green's function of free space. $\boldsymbol{r}$ and $\boldsymbol{r}'$ are the observation and source points.

In the Chebyshev approximation approach, first, we need to compute the $Q+1$ Chebyshev-Gauss frequency sampling points $\tilde{k}_q$ that are the roots of the Chebyshev polynomial $T_{Q+1}(x)$ by

$$\tilde{k}_q = \cos\left[\frac{\pi(2q+1)}{2(n+1)}\right], \quad q = 0, 1, 2, \ldots, Q, \tag{5}$$

where Q is the truncated order of the Chebyshev series. These Chebyshev-Gauss sampling points need to be mapped from the interval $[-1, 1]$ to the desired band $[k_a, k_b]$ by

$$k_q = \frac{1}{2}[\tilde{k}_q(k_b - k_a) + (k_b + k_a)]. \tag{6}$$

After obtaining the frequency sampling points k_q, we calculate the initial current coefficients in the

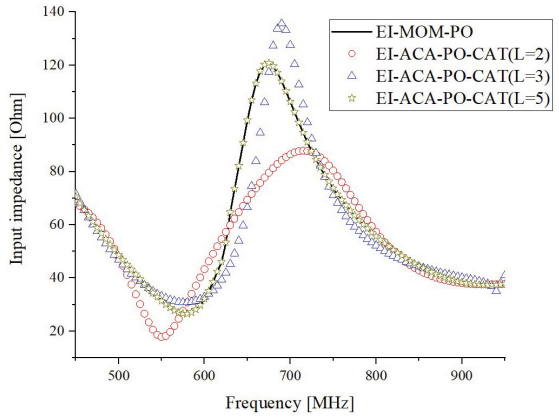

Fig. 4. Input impedance frequency response of an inverted-L antenna placed above a PEC plane by using three different orders of EI-ACA-PO-CAT.

Table 1: CPU time and memory requirement of different methods for the inverted-L antenna placed above a paraboloid

Method	Number of Unknowns		Sweep Points	Memory (MB)	Total CPU Time (s)	RMSE
	ACA	PO				
EI-MoM-PO	1512	10142	101	1396.5	45961	\
EI-ACA-PO-CAT (L=2)				1414.4	582	13.11
EI-ACA-PO-CAT (L=3)				1443.4	663	9.72
EI-ACA-PO-CAT (L=5)				1444.8	1314	0.1

ACA-region at each k_q using pure ACA method. Assume that there are M basis functions situated in the ACA-region and P basis functions existing within the PO-region. The total number of basis functions for the EM system is defined as $N = M + P$. Using the PEC boundary condition and Galerkin testing procedure, the matrix equation at the sampling points can be set up as

$$\boldsymbol{Z}^{ACA}(k_q)\boldsymbol{I}^{0,ACA}(k_q) = \boldsymbol{V}(k_q), \tag{7}$$

where the superscript 0 of $\boldsymbol{I}^{0,ACA}(k_q)$ denotes the number of iterations. The basis functions of the ACA-region are grouped by the octree method, and the self-impedance matrix $\boldsymbol{Z}^{ACA}$ is now a block structure with rank deficient off-diagonal blocks. By using the standard ACA to decompose the off-diagonal blocks, the MVM can be expressed as

$$\begin{aligned}
\boldsymbol{Z}^{ACA}\boldsymbol{I}^{0,ACA} &= (\boldsymbol{Z}^{ACA}_{dia} + \boldsymbol{Z}^{ACA}_{od})\boldsymbol{I}^{0,ACA} \\
&= \begin{pmatrix} \boldsymbol{Z}^{ACA}_{dia(1,1)} & \cdots & \boldsymbol{Z}^{ACA}_{od(1,n)} \\ \vdots & \ddots & \vdots \\ \boldsymbol{Z}^{ACA}_{od(n,1)} & \cdots & \boldsymbol{Z}^{ACA}_{dia(n,n)} \end{pmatrix} \boldsymbol{I}^{0,ACA} \\
&= \sum_{i=1}^{N_{dia}} (\boldsymbol{Z}^{ACA}_{dia(i_x,i_y)} \cdot \boldsymbol{I}^{0,ACA}_{(i_x,i_y)}) \\
&\quad + \sum_{i=1}^{N_{od}} (\boldsymbol{Z}^{ACA}_{od(i_x,i_y)} \cdot \boldsymbol{I}^{0,ACA}_{(i_x,i_y)}) \\
&= \sum_{i=1}^{N_{dia}} (\boldsymbol{Z}^{ACA}_{dia(i_x,i_y)} \cdot \boldsymbol{I}^{0,ACA}_{(i_x,i_y)}) \\
&\quad + \sum_{i=1}^{N_{od}} ((\boldsymbol{L}^{ACA}_{m_i \times r_i} \cdot \boldsymbol{R}^{ACA}_{r_i \times n_i}) \cdot \boldsymbol{I}^{0,ACA}_{(i_x,i_y)}),
\end{aligned} \tag{8}$$

where the subscripts *dia* and *od* represent the diagonal blocks and the off-diagonal blocks, respectively. N_{dia} and N_{od} are the total number of $\boldsymbol{Z}^{ACA}_{dia}$ and $\boldsymbol{Z}^{ACA}_{od}$. (i_x, i_y) is the serial number of ith block. $\boldsymbol{I}^{0,ACA}_{(i_x,i_y)}$ is the corresponding part in vector $\boldsymbol{I}^{0,ACA}$. $\boldsymbol{L}^{ACA}_{m_i \times r_i}$ and $\boldsymbol{R}^{ACA}_{r_i \times n_i}$ are dense rectangular matrices obtained by compression of $\boldsymbol{Z}^{ACA}_{dia(i_x,i_y)}$. m_i and n_i denote the dimension of $\boldsymbol{Z}^{ACA}_{dia(i_x,i_y)}$. r_i is the effective rank.

Let us now consider the effect of the PO-region. For radiation, we suppose that the impressed fields just exist at the feeding point of the antenna. Consequently, the current in the PO-region is only induced by the ACA current solved by (7). The basis functions in the PO-region are also grouped through the octree method, resulting in interaction matrices with block structures. Blocks formed by sufficiently separated basis function groups in both ACA- and PO-regions are defined as far-field matrix blocks. These blocks possess low-rank characteristics and can be accelerated via ACA:

$$\begin{aligned}
\boldsymbol{I}^{i,PO} &= \boldsymbol{\tau}^{PO\text{-}ACA}\boldsymbol{I}^{i-1,ACA} \\
&= (\boldsymbol{\tau}^{PO\text{-}ACA}_{\text{far}} + \boldsymbol{\tau}^{PO\text{-}ACA}_{\text{near}})\boldsymbol{I}^{i-1,ACA} \\
&= \left(\sum_{a=1}^{N_{\text{far}}} \boldsymbol{L}^{PO\text{-}ACA}_{N^a_{PO} \times r^a_{PO\text{-}ACA}} \boldsymbol{R}^{PO\text{-}ACA}_{rPO\text{-}ACA^a \times N^a_{ACA}} \right) \boldsymbol{I}^{i-1,ACA} \\
&\quad + \tau^{PO\text{-}ACA}_{\text{near}} \boldsymbol{I}^{i-1,ACA}, \quad i = 1, 2, \ldots, Iter,
\end{aligned} \tag{9}$$

where i stands for the ith iterative process and *Iter* is the total number of iterations. The induced current in the PO-region will inversely affect the ACA-region. It is added to the right-hand side of (7) in the form of additional exciting voltages, expressed as

$$\boldsymbol{V}^i = \boldsymbol{V} + \Delta\boldsymbol{V}^i, \tag{10}$$

$$\begin{aligned}
\Delta\boldsymbol{V}^i &= -\boldsymbol{Z}^{ACA\text{-}PO}\boldsymbol{I}^{i,PO} \\
&= (\boldsymbol{Z}^{\text{far}}_{ACA\text{-}PO} + \boldsymbol{Z}^{\text{near}}_{ACA\text{-}PO}) \cdot \boldsymbol{I}^{i,PO}
\end{aligned}$$

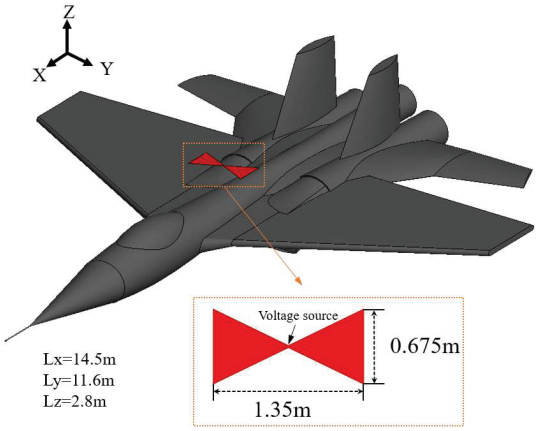

Fig. 5. Geometry of a trapezoidal dipole antenna placed above the aircraft.

$$= \left[\left(\sum_{j=1}^{N_{\text{far}}} \boldsymbol{L}^{\text{ACA-PO}}_{N^j_{ACA} \times r^j_{ACA\text{-}PO}} \boldsymbol{R}^{\text{ACA-PO}}_{r^j_{ACA\text{-}PO} \times N^j_{ACA}} \right) + \boldsymbol{Z}^{\text{near}}_{ACA\text{-}PO} \right] \cdot \boldsymbol{I}^{i,PO}, \tag{11}$$

where $r^j_{ACA\text{-}PO}$ and $r^a_{PO\text{-}ACA}$ are the effective ranks of jth matrix block of $\boldsymbol{Z}^{\text{far}}_{ACA\text{-}PO}$ and ath block of $\boldsymbol{\tau}^{\text{far}}_{PO\text{-}ACA}$. $r^j_{ACA\text{-}PO} < \min(N^j_{ACA}, N^j_{PO})$, $r^a_{PO\text{-}ACA} < \min(N^a_{ACA}, N^a_{PO})$, $\boldsymbol{L}^{PO\text{-}ACA}_{N^a_{\text{PO}} \times r^a_{PO\text{-}ACA}}$ and $\boldsymbol{R}^{PO\text{-}ACA}_{r^a_{PO\text{-}ACA} \times N^a_{ACA}}$, $\boldsymbol{L}^{ACA\text{-}PO}_{N^j_{ACA} \times r^j_{ACA\text{-}PO}}$ and $\boldsymbol{R}^{ACA\text{-}PO}_{r^j_{ACA\text{-}PO} \times N^j_{ACA}}$ represent two dense rectangular matrices obtained by compressing the far-field matrix blocks, respectively.

Then we apply the iterative process from (10) to (11) until the current in the ACA-region stabilizes. The error ε_i is used to evaluate whether the ACA current is stable, expressed as

$$\varepsilon_i = \frac{\|\boldsymbol{I}^{i,ACA} - \boldsymbol{I}^{i-1,ACA}\|}{\|\boldsymbol{I}^{i-1,ACA}\|}, \tag{12}$$

where $\|\cdot\|$ is the 2-norm.

Once the currents $\boldsymbol{I}^{ACA}(k_q)$ and $\boldsymbol{I}^{PO}(k_q)$ at the sampling frequencies are obtained, any surface current $\boldsymbol{I}^{ACA/PO}(k)$ within the desired frequency band $[k_a, k_b]$ can be given by Chebyshev series as

$$I_n(k) = \sum_{q=0}^{Q} c_{n,q} T_q(k_q) - \frac{c_{n,0}}{2}, \tag{13}$$

where the Chebyshev polynomial satisfies the recursion relation as

$$\begin{cases} T_0(x) = 1 \\ T_1(x) = x \\ T_{n+1}(x) = 2xT_n(x) - T_{n-1}(x) \end{cases}, \quad x \in [-1,1], \quad n = 1,2,\ldots,\infty, \tag{14}$$

where $\boldsymbol{m}_q$ are the expanding coefficients.

$$c_{n,q} = \frac{2}{Q} \sum_{q=1}^{Q+1} I_n(k_q) T_q(\tilde{k}_q), \quad q = 1,2,\ldots,Q. \tag{15}$$

Chebyshev series typically employ the Maehly approximation [15] for rational functions. By integrating the Maehly approximation with Equation (13), the components of $\boldsymbol{I}(k)$ are reformulated as

$$\begin{aligned} I_n(k) &\cong \sum_{q=0}^{Q} c_{n,q} T_q(k_q) - \frac{c_{n,0}}{2} \\ &= \frac{\sum_{i=0}^{L} a_{n,i} T_i(\tilde{k}_q)}{1 + \sum_{j=1}^{M} b_{n,j} T_j(\tilde{k}_q)} \\ &\Rightarrow \sum_{i=0}^{L} a_{n,i} T_i(\tilde{k}_q) \\ &= \left(\sum_{p=0}^{\infty} c_{n,p} T_p(\tilde{k}_q) - \frac{c_0}{2} \right) \\ &\quad \times \sum_{j=0}^{M} b_{n,j} b_{n,j} T_j(\tilde{k}_q) \\ &= \sum_{j=0}^{M} b_{n,j} \sum_{p=0}^{\infty} c_{n,p} T_p(\tilde{k}_q) T_j(\tilde{k}_q) \\ &\quad - \frac{1}{2} \sum_{j=0}^{M} b_{n,j} c_{n,0} T_j(\tilde{k}_q), \end{aligned} \tag{16}$$

where $Q = L + 2M$. According to the identity property $T_i(x)T_j(x) = \frac{1}{2}[T_{i+j}(x) + T_{|i-j|}(x)]$ Equation (16) can be simplified as

$$\begin{aligned} &\sum_{i=0}^{L} a_{n,i} T_i(k_q) \\ &= \left(\frac{1}{2} c_{n0} b_{n0} + \frac{1}{2} \sum_{j=1}^{M} b_{n,j} c_{n,j} \right) T_0(k_q) \\ &\quad + \sum_{l=1}^{\infty} \left[b_{n,0} c_{n,l} \right. \\ &\quad \left. + \frac{1}{2} \sum_{j=1}^{M} b_{n,j} (c_{n,j+l} + c_{n,|l-j|}) \right] T_l(k_q). \end{aligned} \tag{17}$$

By matching the two sides, the coefficients in the numerator and the denominator can be obtained by

$$\begin{cases} a_{n,0} = \frac{1}{2} \sum_{j=1}^{M} b_{n,j} c_{n,j} + \frac{1}{2} b_{n,0} c_{n,0} \\ a_{n,i} = \sum_{j=1}^{M} \frac{1}{2} b_{n,j} (c_{n,|i-j|} + c_{n,j+i}) + b_{n,0} c_{n,i} \\ \quad i = 1,2,\ldots,Q \end{cases}$$

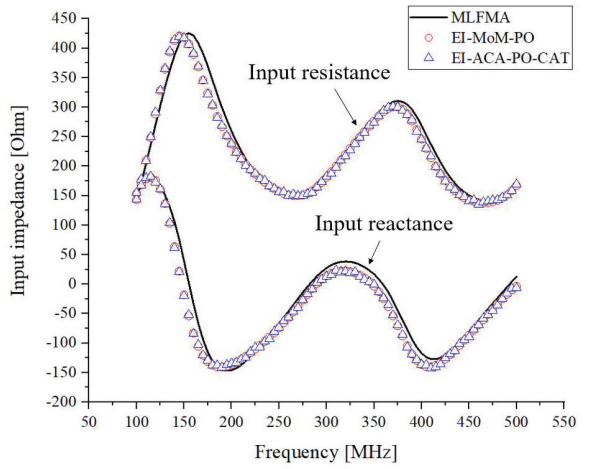

(a)

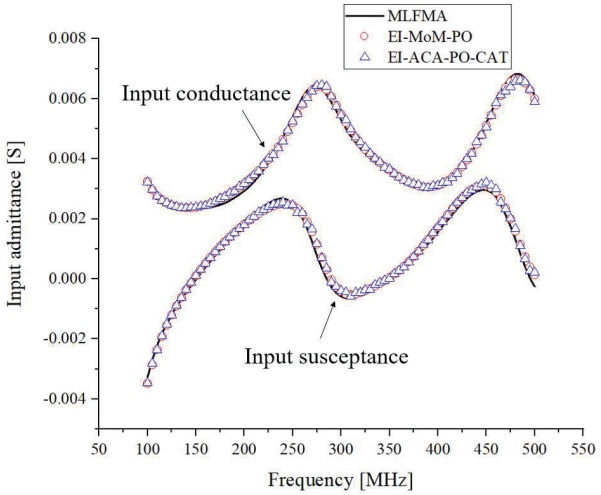

(b)

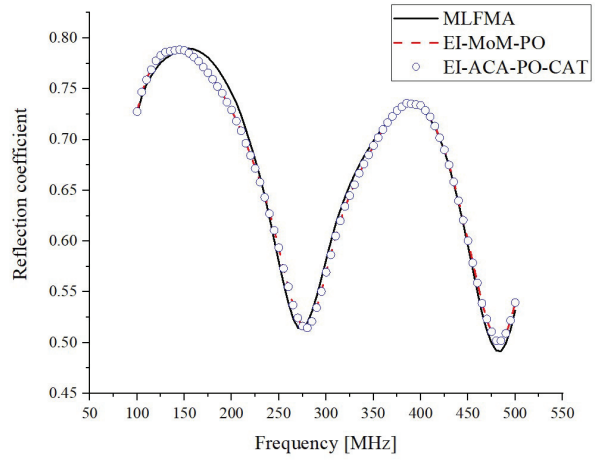

(c)

Fig. 6. Wideband results obtained from EI-ACA-PO-CAT compared with MLFMA and EI-MoM-PO methods: (a) input impedance, (b) input admittance, (c) reflection coefficient.

Table 2: CPU time and memory requirement of different methods for a trapezoidal dipole antenna placed above the aircraft

Method	Number of Unknowns		Sweep Points	Memory (MB)	Total CPU Time (s)
	ACA	PO			
MLFMA	108904	\	81	35026	43888
EI-MoM-PO	1269	25959		3106	58401
EI-ACA-PO-CAT(L=7)				3127	12256

$$\begin{bmatrix} c_{n,L}+c_{n,L+2} & \cdots & c_{n,L-M+1}+c_{n,L+M+1} \\ c_{n,L+1}+c_{n,L+3} & \cdots & c_{n,L-M+2}+c_{n,L+M+1} \\ \cdots & \cdots & \cdots \\ c_{n,L+M-1}+c_{n,L+M+1} & \cdots & c_{n,L}+c_{n,L+2M} \end{bmatrix} \times \begin{bmatrix} b_{n,1} \\ b_{n,2} \\ \cdots \\ b_{n,M} \end{bmatrix} = -2 \begin{bmatrix} c_{n,L+1} \\ c_{n,L+2} \\ \cdots \\ c_{n,L+M} \end{bmatrix}. \tag{18}$$

Finally, the current coefficients at any point within the desired frequency band can be obtained. For ease of understanding, a flowchart of the EI-ACA-PO-CAT method is shown in Fig. 2.

III. NUMERICAL RESULTS

In this section, two simple examples are demonstrated to show the accuracy and efficiency of the proposed EI-ACA-PO-CAT method for fast analysis of antennas on platforms over a broad frequency band. The error tolerance of the iteration between ACA- and PO-regions is selected as 0.003. All results are produced on a 64-bit PC with 3.67 GHz of CPU and 48 GB of RAM.

A. Inverted-L antenna placed above a paraboloid

The first example is an inverted-L antenna placed above a paraboloid. The dimensions of the structure are depicted in Fig. 3. The inverted-L antenna is mounted on the center of a PEC rectangular plane. The length and width are both 0.84 m. An ideal slot voltage source is set at the connection edge between the antenna and the plane. The paraboloid has an aperture radius of 2.25 m and a depth of 0.56 m. In hybrid analysis, the antenna and the plane are selected as the ACA-region, and the paraboloid is the PO-region. The desired frequency band ranges from 450 MHz to 950 MHz. The ACA- and PO-regions are discretized into 1042 and 6821 triangles, leading to 1512 and 10142 basis functions, respectively.

Figure 4 shows the input impedance obtained from EI-ACA-PO-CAT with three different ($L = M = 2, 3, 5$)

order results and the EI-MoM-PO method. It is observed that there are significant errors in the second and third order of EI-ACA-PO-CAT but the result of the fifth order just agrees with EI-MoM-PO solution. In order to better represent the differences, the root mean square error (RMSE) is defined as follows

$$\mathrm{RMSE} = \sqrt{\frac{1}{Num}\sum_{i=1}^{Num}(y_i - y_i^{EI\text{-}MOM\text{-}PO})^2}, \qquad (19)$$

where *Num* is total number of the results. The superscript of y means the method. Table 1 displays the memory, total CPU time and RMSE compared EI-ACA-PO-CAT method with EI-MoM-PO. Although the proposed EI-ACA-PO-CAT costs a bit more memory, it can significantly reduce the CPU time compared to direct calculation with the EI-MoM-PO.

B. Trapezoidal dipole antenna placed above the aircraft

In the second example, we consider a trapezoidal dipole antenna placed above the aircraft. The dimensions of the structure are depicted in Fig. 5. The trapezoidal dipole antenna is defined as the ACA-region, and the aircraft is defined as the PO-region. An ideal slot voltage source is set at the center of the trapezoidal dipole antenna. The desired frequency band ranges from 100 MHz to 500 MHz with 5 MHz spacing. For the full-wave method, the whole system is discretized into 72622 triangles, leading to 108904 basis functions. For the hybrid analysis, the ACA- and PO-regions are discretized into 754 and 21724 triangles, leading to 1269 and 25959 basis functions, respectively.

Figures 6 (a–c) show the input impedance, the input admittance and the reflection coefficient obtained by EI-ACA-PO-CAT ($L = M = 7$) compared with the MLFMA and the EI-MoM-PO method. It is observed that the results of the EI-ACA-PO-CAT method are in good agreement with the results of the direct sweep calculation of the other two methods. Table 2 shows the comparison of memory consumption and computing time from different methods. The EI-ACA-PO-CAT method achieves a significant reduction in computing time without taking up too much memory.

IV. CONCLUSION

This paper proposes a novel approach integrating efficient iterative adaptive cross approximation-physical optics (EI-ACA-PO) and Chebyshev approximation technique (CAT) to efficiently calculate broadband solutions for antennas mounted on electrically large platforms. The outer surface is divided into ACA- and PO-regions, where the ACA method compresses the self-impedance matrix of the ACA-region and interaction matrices between ACA- and PO-regions. The iterative technology further reduces computational complexity. CAT is introduced to solve the surface integral equation at Chebyshev nodes using EI-ACA-PO to obtain induced currents, which are used by Chebyshev series and Maehly approximation to calculate currents at any frequency point in the desired bandwidth, finally deriving the broadband electromagnetic radiation characteristics. This method effectively addresses the challenge of efficient broadband computation for antennas mounted on the electrically large platform by combining matrix compressing and frequency-interpolation approximation, ensuring both computational efficiency and accuracy.

REFERENCES

[1] S. Rao, D. Wilton, and A. Glisson, "Electromagnetic scattering by surfaces of arbitrary shape," *IEEE Trans. Antennas Propag.*, vol. 30, no. 3, pp. 409–418, May 1982.

[2] U. Jakobus and F. M. Landstorfer, "Improved PO-MM hybrid formulation for scattering from three-dimensional perfectly conducting bodies of arbitrary shape," *IEEE Trans. Antennas Propag.*, vol. 43, no. 2, pp. 162–169, Feb. 1995.

[3] U. Jakobus and F. I. C. Meyer, "A hybrid physical optics/method of moments numerical technique: Theory, investigation and application," in *Proc. IEEE AFRICON*, Stellenbosch, South Africa, vol. 1, pp. 282–287, Sep. 1996.

[4] J. Ma, S.-X. Gong, X. Wang, Y. Liu, and Y.-X. Xu, "Efficient wideband analysis of antennas around a conducting platform using MoM-PO hybrid method and asymptotic waveform evaluation technique," *IEEE Trans. Antennas Propag.*, vol. 60, no. 12, pp. 6048–6052, Dec. 2012.

[5] W.-J. Zhao, J. L.-W. Li, and L. Hu, "Efficient current-based hybrid analysis of wire antennas mounted on a large realistic aircraft," *IEEE Trans. Antennas Propag.*, vol. 58, no. 8, pp. 2666–2672, Aug. 2010.

[6] C. S. Kim and Y. Rahmat-Samii, "Low profile antenna study using the physical optics hybrid method (POHM)," in *Proc. Antennas Propag. Soc. Symp. Dig.*, London, ON, Canada, vol. 3, pp. 1350–1353, June 1991.

[7] R. E. Hodges and Y. Rahmat-Samii, "An iterative current-based hybrid method for complex structures," *IEEE Trans. Antennas Propag.*, vol. 45, no. 2, pp. 265–276, Feb. 1997.

[8] Z.-L. Liu and C.-F. Wang, "Efficient iterative method of moments: Physical optics hybrid technique for electrically large objects," *IEEE Trans. Antennas Propag.*, vol. 60, no. 7, pp. 3520–3525, July 2012.

[9] Z.-L. Liu, X. Wang, and C.-F. Wang, "Installed performance modeling of complex antenna array mounted on extremely large-scale platform using fast MoM-PO hybrid framework," *IEEE Trans. Antennas Propag.*, vol. 62, no. 7, pp. 3852–3858, July 2014.

[10] K. Zhao, M. N. Vouvakis, and J.-F. Lee, "The adaptive cross approximation algorithm for accelerated method of moments computations of EMC problems," *IEEE Trans. Electromagn. Compat.*, vol. 47, no. 4, pp. 763–773, Nov. 2005.

[11] C. B. Wu, L. Guan, P. F. Gu, and R. S. Chen, "Application of parallel CM-MLFMA method to the analysis of array structures," *IEEE Trans. Antennas Propag.*, vol. 69, no. 9, pp. 6116–6121, Sep. 2021.

[12] Y. Zhang and H. Lin, "MLFMA-PO hybrid technique for efficient analysis of electrically large structures," *IEEE Antennas Wireless Propag. Lett.*, vol. 13, pp. 1676–1679, 2014.

[13] Z. Xu, X. Wang, H. Zhang, L. Zhao, C. Liu, and Y. Liu, "A hybrid method of ACA-PO for efficient analysis of antenna array mounted on electrically large platforms," *IEEE Trans. Antennas Propag.*, vol. 72, no. 6, pp. 5426–5431, June 2024.

[14] X. Wang, S.-X. Gong, J. Ma, and C.-F. Wang, "Efficient analysis of antennas mounted on large-scale complex platforms using hybrid AIM-PO technique," *IEEE Trans. Antennas Propag.*, vol. 62, no. 3, pp. 1517–1523, Mar. 2014.

[15] X. Wang, H. X. Gong, S. Zhang, Y. Liu, R. P. Yang, and C. H. Liu, "Efficient RCS computation over a broad frequency band using subdomain MoM and Chebyshev approximation technique," *IEEE Access*, vol. 8, pp. 33522–33531, 2020.

[16] M. A. M. Hassan and A. A. Kishk, "A combined asymptotic waveform evaluation and random auxiliary sources method for wideband solutions of general-purpose EM problems," *IEEE Trans. Antennas Propag.*, vol. 67, no. 6, pp. 4010–4021, June 2019.

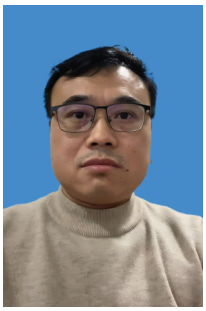

Junjun Wu was born in Shaanxi province, is a senior engineer at China Flight Test Research Institute and Xi'an Yuanfang Aviation Technology Development Co. Ltd. and is a master's candidate. His research direction is airborne antenna and their layout, including communication antenna, navigation antenna, beacon antenna as well as research on corresponding testing methods.

A Single-Layer Reflectarray Unit Cell with Enhanced Performance Using Dual Concentric Split-Circle Rings

Likaa S. Yahya[1] and Khalil H. Sayidmarie[2]

[1]Polytechnic College Mosul
Northern Technical University, Mosul, Iraq
likaasalim@ntu.edu.iq

[2]College of Electronics Engineering
Ninevah University, Mosul, Iraq
kh.sayidmarie@uoninevah.edu.iq

Abstract – This paper proposes a dual-ring unit cell design for a single-layer reflectarray antenna. The element is attained using two concentric split-ring resonators, where each ring is divided into four equal sections. By adjusting the width, scaling, and radius of the concentric split-rings, two distinct resonance frequencies are realized in each ring, attributable to the electric length inside the rings. This approach yields a wider phase range for the reflection coefficient, with a nearly linear phase response. Three different configurations are investigated to identify the best performance parameters. The electromagnetic behavior of the proposed unit element is simulated using CST Microwave Studio Suite. The reflection characteristics are analyzed using the infinite-array model with Floquet port excitation. Hexahedral meshing is employed for the antenna configuration, with the mesh density adjusted according to the wavelength to validate sufficient resolution of the structural features. The unit cell was also investigated using the HFSS frequency-domain solver based on the finite integration technique. An equivalent circuit was found using the Advanced Design System (ADS). The simulation results indicate that all three configurations offer a broad phase variation, with the minimum phase of approximately 885° at 10 GHz in case 2, and a maximum phase slope of 68°/mm at 12 GHz in case 1, over the 8–12 GHz frequency range. The configuration in case 3 achieves the widest operational bandwidth of 26.8% centered at 10 GHz.

Index Terms – Bandwidth improvement, single-layer, split-circle rings, unit cell, wideband reflectarray.

I. INTRODUCTION

Reflectarray antennas symbolize a promising class of high-gain antennas with several advantages, including lightweight construction, low profile, low cost, and reduced fabrication complexity. Furthermore, they enable higher antenna gains by developing the reflective behavior of their elements [1]. In its essential configuration, a reflectarray antenna comprises a feed element and an aperture composed of an array of microstrip patches. The primary purpose of the reflectarray is to reflect the incident waves from the feed and to shape and direct the resulting collimated beam in a specific direction. Each element in the array is designed to provide the required phase shift upon reflection, ensuring proper wave collimation and steering the beam toward the intended target direction [2, 3]. Nevertheless, the performance of reflectarrays may degrade due to improper reflection phase settings and their inherently narrow-band behavior. Numerous studies have proposed different techniques to extend the phase range of the reflection coefficient and enhance bandwidth. Some approaches involve multilayer configurations; for instance, multilayers of double concentric annular rings for X-band applications were proposed in [4]. The design described in [5] involves stacked microstrip patches and demonstrates good performance in dual-frequency operation. Additionally, a reflectarray consisting of three stacked layers with rectangular patches was presented in [6], offering dual-polarization functionality that is suitable for space applications. A 4-layer transmitarray antenna composed of double square-ring elements was discussed in [7]. Other techniques focus on element rotation; for example, adjusting the rotation angle of the elements as explored in [8–11]. A third method involves attaching phase delay lines to the radiating elements for phase compensation. By varying the lengths of arc stubs or phase delay lines, broadband performance can be attained, as demonstrated in [12–15]. The fourth technique, which is the most commonly used and the simplest to manufacture, involves

Submitted On: July 22, 2025
Accepted On: March 08, 2026

https://doi.org/10.13052/2026.ACES.J.410205

varying the size of an element within a multi-resonant geometry to produce phase variation, as detailed in [16–20].

An essential feature in the design of a reflectarray microstrip antenna is the selection of a suitable element shape, commonly referred to as the unit cell, along with its size, followed by the total number of cells, and the overall array configuration. Each element independently contributes to phase amendment, thus enabling the achievement of the desired directivity [21]. The choice of the radiating element's shape is particularly critical, as the scattering of the incident electromagnetic field is strongly influenced by its geometry. Thus, an important objective is to identify a cell category that provides a broad reflection coefficient phase range when its properties are varied [21]. It is well-established that a phase variation restricted to less than 360° can result in a reduction of the antenna's directivity [16]. Conversely, research indicates that the phase variation with respect to any geometrical parameter should be as linear as possible, confirming a smooth slope in the phase response [22]. This requires that the full 360° phase shift is attained through very gradual variations of the parameter. In practical applications, abrupt phase changes tend to lead to narrower working bandwidths and complicate the manufacturing process of the radiating elements due to tight tolerances [23]. Usually, the phase of the reflection coefficient as a function of the patch dimensions is calculated to assess whether the phase range is adequately wide and whether the curve reveals a smooth slope. Accordingly, extensive effort is often invested in identifying a unit cell capable of providing the desired phase characteristics. Commonly employed microstrip patch shapes include squares, crosses, rectangles, circles, and rings [24–29].

In this study, double split-circle rings are used to enhance both the phase range and the bandwidth of a unit cell for a reflectarray antenna. The dual split-ring resonator elements create multiple resonance frequencies. By separating each ring into four segments and systematically varying the scale, width, and size of these segments, two adjacent resonances are generated by each ring. This modification improves the phase coverage and bandwidth of the unit element reflectarray.

The paper is arranged as follows. Section II details the design methodology of the proposed dual-band unit cell. Section III presents the obtained simulation results for both the single split-circle ring and the dual split-circle ring reflectarray unit cells. Section IV describes the equivalent circuit of the proposed double split-circle rings reflectarray unit cell. A comparative investigation of the proposed unit cell with existing published work is presented in section V. Lastly, the conclusions are explained in section VI.

II. DUAL-BAND SPLIT-CIRCLE RINGS CONFIGURATION

The reflectarray antenna suggested in [30] is adopted as a baseline for the current research. In this design, the original circular shape, divided into four quadrants, is now modified into a split circular ring and then transformed into a double split circular ring. The element is designed on a 0.16 mm thick Taconic TLC-32 substrate, characterized by a relative permittivity of $\varepsilon_r = 3.2$ and a loss tangent tan $\delta = 0.003$. This substrate is supported by a 3 mm thick foam layer with $\varepsilon_r = 1.05$, backed by a conducting ground plane with a thickness of 0.035 mm. The chosen unit cell dimensions are 18×18 mm, corresponding to approximately $(0.6\times0.6)\lambda_o$, where λ_o is the free-space wavelength at the operating frequency of 10 GHz. For the design of the dual split circular ring structure, the permittivities of the two substrates are denoted as ε_{r1} and ε_{r2}, with heights H_1 and H_2, respectively. Initially, the total thickness (H_T) and the effective permittivity (ε_{eq}) can be determined using equations (1) and (2) [31]

$$H_T = H_1 + H_2. \tag{1}$$

$$\varepsilon_{eq} = \frac{\varepsilon_{r1}H_1 + \varepsilon_{r2}H_2}{H_1 + H_2}. \tag{2}$$

The unit cell dimensions in a split-circle ring reflectarray are classically governed by the resonant performance of the ring elements. A ring patch acts as a resonant loop. Common practice is to relate the ring circumference to the effective wavelength λ_e. The frequency features of the dual split-ring antenna were calculated as follows.

A ring of average radius R has a perimeter 2πR. The ring resonates when

$$2\pi R \cong m\lambda_e, \tag{3}$$

where m is the harmonic number, which is unity in this case, and λ_e is the effective wavelength that can be calculated as [2]

$$\lambda_e = C/f_0\sqrt{\varepsilon_{eff}}, \tag{4}$$

where C is the speed of light in meters/second, and f_0 is the resonant frequency of each ring [11]:

$$f_0 = \frac{C}{2\pi R\sqrt{\varepsilon_{eff}}}, \tag{5}$$

where ε_{eff} is the effective permittivity relative to the ground plane and can be calculated as [2]

$$\varepsilon_{eff} = \frac{\varepsilon_{eq}+1}{2} + \frac{\varepsilon_{eq}-1}{2}\left[1+12\frac{H_T}{W}\right]^{\frac{-1}{2}}. \tag{6}$$

Since the unit cell is designed to operate in the 8–12 GHz frequency band, the outer ring is designed to operate at 8 GHz, while the inner ring is designed to operate at 12 GHz. Substituting into equations (1–6), $\varepsilon_{-eq} = 1.1599$, $\varepsilon_{eff} = 1.124$. Thus, the mean radius of the outer ring is equal to 5.6 mm, while the mean radius of the inner ring is equal to 3.75 mm.

The design methodology for the dual-band split circular ring-based reflectarray is illustrated in Fig. 1. The configuration of the unit cell used for the proposed phase shifting element is depicted in Fig. 2. This element consists of two concentric split circular rings, with the diameters of the inner and outer rings being varied to achieve the desired phase variation over the specified operational band. The two rings are separated by a small, constant gap to facilitate the excitation of two adjacent resonant frequencies. All the designs presented in this work were analyzed using CST Studio Suite, modeling the unit cells within an infinite array structure. The excitation was modeled using Floquet port boundary conditions. This approach thoroughly accounts for the true shape of the radiating elements and the effects of the mutual coupling and is widely regarded as a sound simulation methodology for reflectarray antenna design.

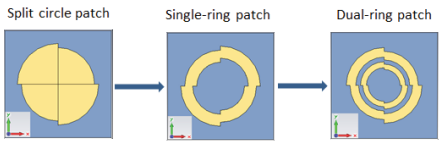

Fig. 1. Design methodology of a dual-band split-circle ring reflectarray element.

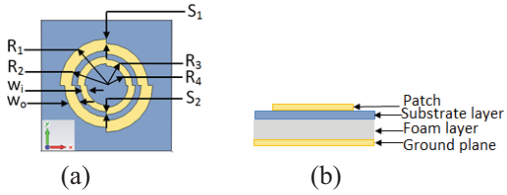

Fig. 2. Configuration of the unit cell for the proposed phasing element (a) front view and (b) side view.

III. SIMULATION RESULTS

A. Single split-circle ring reflectarray unit cell

The investigation starts with a basic unit cell comprising a single disk of a split-circle element operating at a central frequency of 10 GHz within the X-band [30]. The outer sector radius, R_1 (d/2), is set to 6.1 mm, while the inner sector radius is defined as $R_1 - 0.1R_1$, corresponding to a scale factor S = 0.9. The amplitude and phase responses as functions of frequency are presented in Fig. 3 (a). The phase of the reflected field is zero at the nominal operating frequency of 10 GHz and shows a phase variation of approximately 601° across the frequency range of 8 to 12 GHz. At the resonance point, the scattered field magnitude drops to a minimum of −0.4 dB, corresponding to very low attenuation. Figure 3 (b) explains the variation of the amplitude and phase of the reflected field at 10 GHz for different values of the outer diameter. It can be noted that the reflected phase can be effectively controlled within a range from −94.7° to −660.7°, corresponding to a phase range of 566°, by varying the outer diameter from 4 mm to 13 mm. Within this range, the amplitude variation is approximately −0.43 dB.

For enhanced phase response performance, a split-circle ring is derived from the original disk split-circle. This split-circle ring is designed specifically for X-band microstrip reflectarrays. The element introduces three degrees of freedom to tailor the phase response: the first is the overall size, the second is the width of the ring, and the third is the scaling factor for the inner ring radius, which represents the differences in the distances between adjacent sectors. These parameters are carefully considered to select the element shape that demonstrates optimal performance in terms of lower phase slope relative to size and frequency, quantified by the derivatives ($\Delta\varphi/\Delta L$), and ($\Delta\varphi/\Delta f$), respectively. Figure 4 (a) illustrates the amplitude and phase variation versus frequency for a split-circle ring with a scale factor of 0.9. The results reveal that the resonance frequency shifts toward the lower band, from 10 GHz to approximately 8.87 GHz, compared to the original disk element. Figure 4 (b) displays the amplitude and phase of the reflected field at 10 GHz for this split-circle ring. It is evident that the reflected phase can be controlled over a range from −102.3° to −729°, corresponding to a phase variation of 626.7°, when the outer diameter is varied from 4 mm to 13 mm. This represents a phase range improvement of approximately 60.7° compared to the original disk split-circle. Within this range, the amplitude variation remains minimal, about −0.04 dB.

Figure 5 (a) examines the phase and amplitude variation of the reflected field for the split-circle ring with four different scale factors (S = 1, 0.9, 0.8, 0.7). The widths of both sectors are fixed at 1.8 mm, and the ratio between the widths of consecutive sectors remains constant at 1. It is observed that when S=1, corresponding to a traditional ring, the phase range is approximately 274.3° (from −60.1° to −334.4°), which is less than the required 360° phase range for the reflectarray. Conversely, reducing the scale from 1 to 0.7 significantly increases the phase range to approximately 627° from (−102° to −729°), with a slight decrease in the phase slope as the scale is reduced. Figure 5 (b) depicts the variation of the reflected phase and amplitude

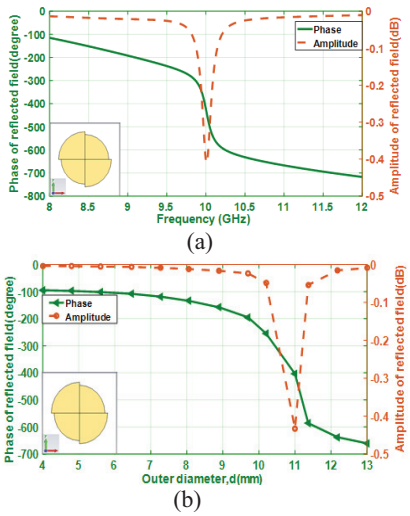

Fig. 3. Amplitude and phase characteristics of the reflected field from the split-circle reflectarray unit cell (a) variation with frequency and (b) variation with outer diameter at 10 GHz.

for split-circle rings with various sector width ratios (w1/w2 = 0.7, 0.6, 0.5, 0.4), maintaining a constant scale factor (S = 0.8). The results indicate that decreasing the width ratio slightly reduces the phase range. The maximum phase range of approximately 649° occurs at w1/w2 = 0.7, while the minimum of about 617° is observed at w1/w2 = 0.4. Additionally, the phase slope becomes more linear as the width ratio decreases.

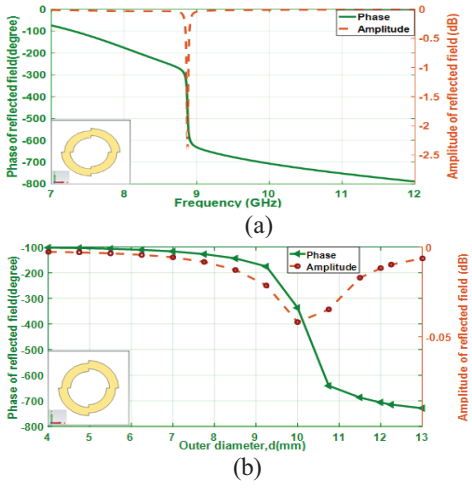

Fig. 4. Amplitude and phase of the scattered field by the split-circle ring unit cell: (a) frequency variations and (b) outer diameter variations at 10 GHz.

B. Dual split-circle rings reflected array unit cell

To enhance the phase characteristics of a unit cell, uniplanar phasing elements in the form of double

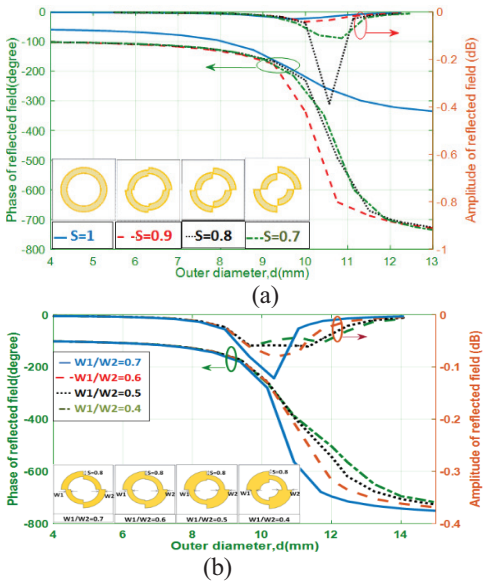

Fig. 5. Amplitude and phase of the scattered field from the split-circle ring unit cell: (a) outer diameter variations for four different scales (S = 1, 0.9, 0.8, 0.7) and (b) outer diameter variations for four different widths (w1/w2 = 0.7, 0.6, 0.5, 0.4) at 10 GHz.

split-circle rings are considered, as illustrated in Figs. 6, 7, and 8. This study investigates three distinct structures. Figure 6 presents the amplitude and phase responses of a unit cell containing two concentric split-circle rings, conforming to the first case. In this configuration, the scale factor of the outer ring (S_1) is equal to 0.92, which relates to the gap between two adjacent outer sectors, while the scale factor of the inner ring (S_2) is equal to 0.84. The ratio of the width of the inner ring (wi) to that of the outer ring (wo) is equal to 0.7 (wi/wo = 0.7). Additionally, the size ratio of the inner to outer rings is approximately 0.67. In the inner ring, each sector makes contact only with its adjacent sector. Three resonant frequencies are observed in Fig. 6 (a): the first, at 8 GHz, is primarily attributed to the outer ring, and the second and third, at 11 GHz and 12 GHz, are attributed to the inner ring. Differences in the splitting of the sectors create two distinct current paths within the inner ring, resulting in dual resonances. Figure 6 (b) illustrates the phase variation of the reflected wave from the unit cell as a function of the outer diameter (d = 2*R_1) at four frequencies (10, 11, 12, and 13 GHz), with the calculated values listed in Table 1. It is apparent that increasing the frequency from 10 GHz to 13 GHz broadens the phase range from approximately 979.5° to 1338.3°, with the phase slope increasing from 42.65°/mm at 10 GHz to 82.95°/mm at 13 GHz. The phase range enhancement of approximately 35% is significant compared to a single split-circle ring at 10 GHz.

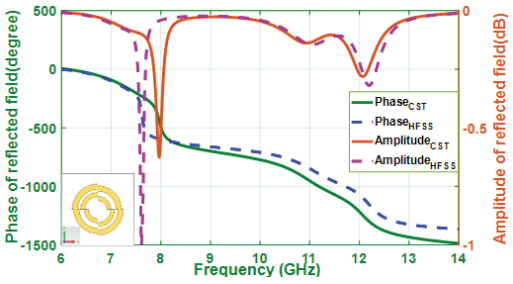

(a)

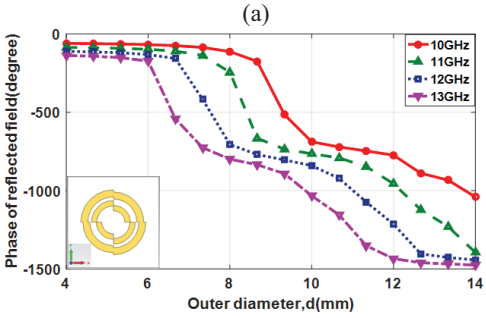

(b)

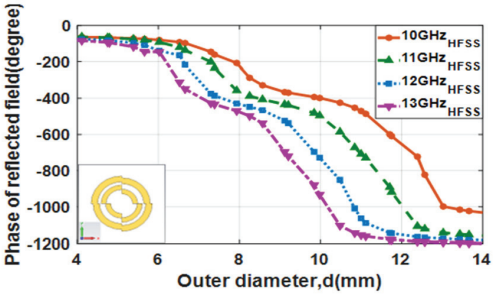

(c)

Fig. 6. Amplitude and phase of the scattered field by the double split-circle rings unit cell (case 1): (a) frequency variations in CST and HFSS; (b) variation with outer diameter at frequencies 10, 11, 12, and 13 GHz in CST; and (c) variations with outer diameter at frequencies 10, 11, 12, and 13 GHz in HFSS.

To validate the simulation results, another simulation was performed for the design shown in the first case using the HFSS software package, and the obtained results are shown in Figs. 6 (a) and (c) and Table 2. The figure shows a good match between the results of the two software packages, although the results obtained using the CST simulation seem better in terms of the frequency range being higher and the slope being lower. It is known that the HFSS package uses the finite element method, while the CST uses the finite integration technique, which means that two different approaches are used. Therefore, one approach can be considered as a confirmation of the other one. The good agreement between the results obtained from both can be considered a validation.

In the second structure, the widths of the two inner ring sectors differ, with the narrow sector's width being

Table 1: Characteristics and phase response of the double split-circle rings reflectarray unit cell in CST (case 1)

	Case 1 CST			
Parameter	**10 GHz**	**11 GHz**	**12 GHz**	**13 GHz**
Slope (°/mm)	42.65	55.73	67.5	82.95
Slope (°/GHz)	48	107	90	119
Max. phase (°)	−59.5	−84.8	−110.6	−136.7
Min. phase (°)	−1039	−1394	−1442	−1475
Phase range (°)	979.5	1309	1331.4	1338.3

Table 2: Characteristics and phase response of double split-circle rings reflectarray unit cell in HFSS (case 1)

	Case 1 HFSS			
Parameter	**10 GHz**	**11 GHz**	**12 GHz**	**13 GHz**
Slope (°/mm)	50.3	60.12	79	92.22
Slope (°/GHz)	82.33	175	207	78
Max. phase (°)	−63.4	−62	−73	−73.5
Min. phase (°)	−1031	−1158	−1183	−1202
Phase range (°)	967.6	−1096	−1110	1128.5

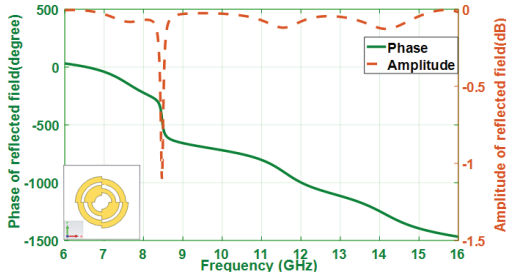

(a)

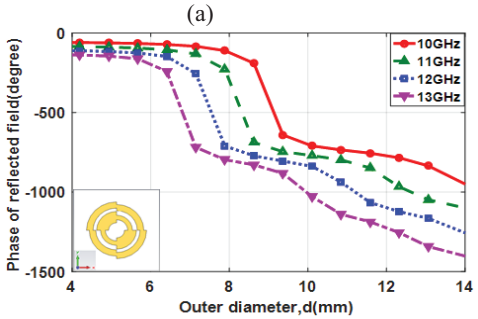

(b)

Fig. 7. Amplitude and phase of the field scattered by the double split-circle rings reflectarray unit cell (case 2): (a) frequency variations and (b) outer diameter variations at frequencies 10, 11, 12, and 13 GHz.

0.4 times that of the wider sector (w1/w2 = 0.4), and the ratios of their widths to the outer ring being w1/wo = 0.72 and w2/wo = 1.83, respectively. Figure 7 shows the amplitude and phase characteristics as a function of frequency and the outer diameter (d = 2*R_1), with the corresponding data listed in Table 3.

Figure 7 (a) demonstrates four resonance frequencies. The first resonance happens at 7.57 GHz, followed

by the next resonance at 8.47 GHz. These double frequencies are attributed to the outer ring shape. The third and fourth resonances are detected at 11.57 GHz and 14.1 GHz, respectively, and are related to the inner ring. Figure 7 (b) illustrates the variation of the outer diameter in relation to the phase of the reflected field at frequencies of 10 GHz, 11 GHz, 12 GHz, and 13 GHz. The phase slope ($\Delta\varphi/\Delta$d) values at the four frequencies decrease as compared to the first case, indicating increased linearity, and the overall phase range declines compared to the first case. In the third case, the inner ring size is set to 62.5% of the outer ring size, with the outer ring width at $0.25R_1$ and the inner ring width at $0.15R_1$. Figure 8 (a) reveals two resonance frequencies at approximately 8.15 GHz and 11.8 GHz. Figure 8 (b) presents the phase responses at four frequencies (10, 11, 12, and 13 GHz), with the corresponding values listed in Table 4. The minimum phase range is approximately 897° at 10 GHz. As the frequency increases from 10 GHz to 13 GHz, the phase range increases to a maximum of approximately 1276° at 13 GHz.

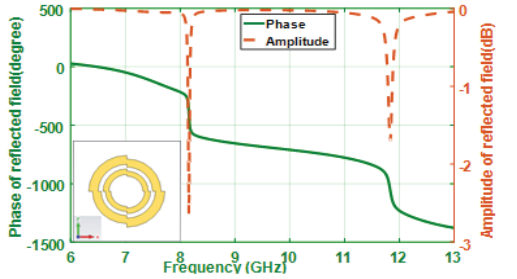

(a)

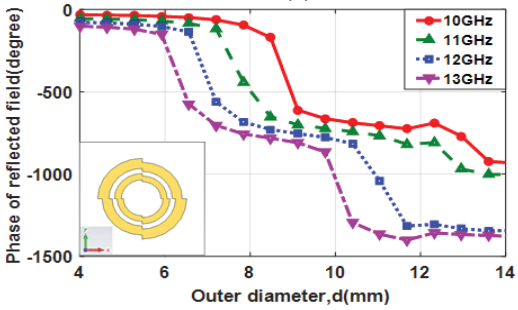

(b)

Fig. 8. Amplitude and phase of the field scattered by the double split-circle rings reflectarray unit cell (case 3): (a) frequency variations and (b) outer diameter variations at frequencies 10, 11, 12, and 13 GHz.

C. Bandwidth of dual split-circle rings reflected array unit cell

It has been demonstrated in [32] that the major factor influencing the bandwidth of a microstrip reflectarray is the bandwidth of the singular radiating elements. The bandwidth can be expressed as the frequency range over which the phase variation reaches a specified value; ϕ. ϕ was considered to be π in [32]. The bandwidth is defined as (B.W. = f2–f1), where f1 and f2 are the frequencies corresponding to phase variation of $\pm 90°$, and can be determined from the curves presented in Figs. (3 (a), 6 (a), 7 (a), and 8 (a)). Table 5 summarizes the reflection phase bandwidths of the split-circle and double split-circle ring reflectarray unit cells for the three cases discussed above. It can be seen that adding a second ring results in a wider band, and the third case achieved the highest bandwidth of 26.8%.

Table 3: Characteristics and phase response of double split-circle rings reflectarray unit cell (case 2)

	Case 2			
Parameter	**10 GHz**	**11 GHz**	**12 GHz**	**13 GHz**
Slope (o/mm)	41	52	62	72
Slope (o/GHz)	66	73	86	93.7
Max. phase (°)	−60	−85.3	−111	−137.4
Min. phase (°)	−945	−1094	−1254	−1398
Phase range (°)	885	1008.7	1143	1261

Table 4: Characteristics and phase response of double split-circle rings reflectarray unit cell (case 3)

	Case 3			
Parameter	**10 GHz**	**11 GHz**	**12 GHz**	**13 GHz**
Slope (o/mm)	44.5	52	68	78
Slope (°/GHz)	63	68.5	69.5	80.3
Max. phase (°)	−31	−54.5	−77.6	−101.8
Min. phase (°)	−928	−1004	−1345	−1378
Phase range (°)	897	949.5	1267.4	1276.2

Table 5: The achieved bandwidth for the unit cells of the three proposed designs compared to that for the split-circle at 10 GHz

	Φ at fr [°]	**f1 at $\phi+90$ GHz**	**f2 at $\phi-90$ GHz**	**B.W. = f2–f1**	**B.W %**
Split-circle element at s = 0.9	−423	9.93	10.06	0.13	1.3
Case 1	−773	8.78	10.64	1.86	18.6
Case 2	−755	8.66	10.9	2.24	22.4
Case 3	−710	8.54	11.22	2.68	26.8

IV. EQUIVALENT CIRCUIT OF THE UNIT CELL

To better understand the proposed design, the structure is represented as an equivalent circuit. The equivalent circuit diagram of the proposed double split-circle rings reflectarray unit cell (the second design) is simulated using the Advanced Design System (ADS)

software and is presented in Fig. 9. As each ring is split, the external split-ring is modeled via a pair of series RLC circuits, and the internal split-ring is similarly modeled by a pair of series RLC circuit, the two parallel branches combination are connected through capacitance C1, which characterizes the mutual coupling between the dual-rings. The resonant modes are mode-1 at fr1 = 7.62 GHz, mode-2 at fr2 = 8.2 GHz, mode-3 at fr3 = 10.9 GHz, and mode-4 at fr4 = 11.8 GHz, which are characterized by the electrical triplets parameters (R1, L1, C1), (R2, L2, C2), (R3, L3, C3), and (R4, L4, C4), respectively. The antenna transmission line is represented by inductance L1 and capacitance C2, where L1 accounts for higher-order modes, and C2 corresponds to the quasi-static input capacitance, while Term1 symbolizes the Floquet port. The electrical parameters are tuned to support the resonance frequencies of modes 1, 2, 3, and 4. Figure 10 compares S11 magnitude and phase plots between the ADS equivalent circuit and CST simulation results. The figure shows that the results from the equivalent circuit model are in good agreement with those from CST. A small discrepancy in magnitude (<0.03 dB) is seen at the second frequency band, which can be attributed to higher-order modes of the structure. It is noted that the proposed equivalent-circuit model, as defined, is an approximate representation circuit. Although it does not perfectly match the CST simulations, it remains a useful tool for explaining the structure's operating principle and confirming the results.

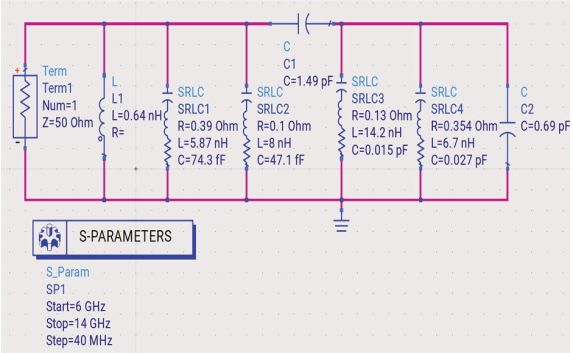

Fig. 9. Equivalent circuit model of the proposed unit cell reflectarray.

V. COMPARISON WITH OTHER PUBLISHED WORK

The performance of the proposed reflectarray antenna is compared with that of other designs reported in the literature, as summarized in Table 6. This specifies that the established design attains the broadest phase range, nearly 885°, and the lowest phase slope 41° per mm, over the X-band frequency range (8–12 GHz)

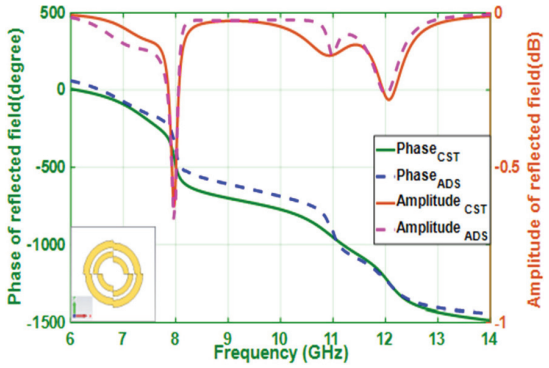

Fig. 10. Reflection coefficient values (in amplitude and phase) obtained from the equivalent circuit compared to those found from the CST simulations.

among all configurations studied. The smooth phase of the proposed unit cell results in the lowest phase sensitivity of 66° per GHz compared with the values reported in [36, 37]. It is perceived that the proposed antenna combines the improvements of both phase-range enhancement approaches and displays superior performance in terms of slope, dispersion, and design simplicity relative to most designs.

The advantages of the proposed design stem from the dual-ring feature, which inherently exhibits dual-resonance behavior. Moreover, splitting the ring further enhances multi-resonance performance. Although the dual circular ring features have been used in other designs [13, 16, 28, 37], but the split-ring has enhanced the phase response compared to other designs.

VI. CONCLUSION

The paper demonstrated a low-profile, single-layer microstrip reflectarray element incorporating dual split circular rings as the fundamental unit cell. The design aimed to enhance phase range coverage and bandwidth performance by altering the geometric parameters of the split-rings. The inclusion of dual concentric split-circle rings creates multiple resonant modes, thereby extending the bandwidth and supporting a near-linear phase response over a wide frequency range. The proposed design comprises double split-ring shapes printed onto a thin (0.16 mm) Taconic TLC-32 substrate, supported by a 3 mm thick layer of low-permittivity foam (relative permittivity of 1.05). By adjusting the geometric parameters of the rings, the phase characteristic can be approximated as a linear function of the ring dimensions. The study tests three distinct cases, which offered a minimum phase range of 885° and a phase slope of 41°/mm at 10 GHz, along with a relative bandwidth of 18.65%. The results demonstrated significant improvements in phase coverage and bandwidth performance compared to previous reflectarray designs.

Table 6: Comparing the proposed design with other published works

Ref. Year	Configuration	Unit Cell	Phase Range (°)	Center Freq. (GHz)	Area mm^2 $\lambda o * \lambda o$	Slope ○/mm	Slope ○/GHz	Unit Cell Thick-ness (mm)	ε_{r1}
[33] 2022	Clip-shaped elements		398	10	9*9 (0.3*0.3)	NA	NA	3.175	2.2
[19] 2021	Multi-resonance unit		≅ 400	9,11.5,14	15*15	NA	NA	3.5	2.2
[34] 2016	Two circular rings with a pair of gaps and two identical phase-delay lines		550	10	15*15 (0.5*0.5)	NA	44	3.5	3.48
[35] 2019	Double Minkowski rings		397	5.8	15*15 (0.29*0.29)	≅ 66	NA	5.6	4.4
[36] 2024	Bowtie double ring	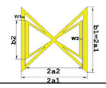	700	8	20*20 (0.5*0.5)	145	357_1st 473_2nd	3.16	2.2
[28] 2014	Multiresonance square-rings elements		500	13.5	11*11 (0.5*0.5)	≅114	NA	3.75	2.2
[16] 2008	Dual circular rings.		600	10	15*15 (0.5*0.5)	≅ 80	NA	3.16	3.4
[13] 2017	Phase-delay line attached to a circular ring loaded with a circular disc microstrip		440	11.5	15*15 (0.58*0.58)	NA	NA	3.683	2.2
[15] 2020	Slotted square patch with four delay line		650	10	9*9 (0.3*0.3)	NA	57	5.4	4.3
[37] 2011	Double rings tapered corners		421.5	10	15*15 (0.5*0.5)	52	79	4	2.2
[38] 2020	Circular ring with 4 sectors		590	28	5.25*5.25 (0.5*0.5)	120 (estimated from Fig. 6)	NA	1.6	2.55
[39] 2020	Cross + 4 squares		348.6	26.5-29.5	5.25*5.25 (0.5 * 0.5)	NA.	NA	0.127	2.2
[40] 2019	Double conformal rings		600	10	12*12 (0.59*0.59)	200 (estimated from Fig. 3)	NA	Two 3 mm thick layers sepa-rated by 3 mm	2.2
This Work (case 2)	Dual split-circle rings	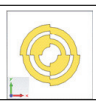	885	10	18*18 (0.6*0.6)	41	66	3.16	3.2

The equivalent circuit results showed that the dual split-ring unit cell has four resonance frequencies corresponding to the two split-rings.

The split circular ring unit cell utilizes multi-resonance configurations to avoid the complex and costly fabrication of multi-layer reflectarrays while still achieving wide bandwidth, thereby making it suitable for a range of applications, including satellite communications, radar systems, and remote sensing.

REFERENCES

[1] J. Huang and J. A. Encinar, *Reflectarray Antennas*. New Jersey: Wiley, 2007.

[2] R. D. Javor, X.-D. Wu, and K. Chang, "Design and performance of a microstrip reflectarray antenna," *IEEE Transactions on Antennas and Propagation*, vol. 43, no. 9, pp. 932–939, Sep. 1995.

[3] P. Nayeri, F. Yang, and A. Z. Elsherbeni, *Reflectarray Antennas: Theory, Designs, and Applications*. New Jersey: John Wiley & Sons Ltd, 2018.

[4] N. Misran, R. Cahill, and V. Fusco, "Design optimisation of ring elements for broadband reflectarray antenna," *IEE Proc.-Microw. Antennas Propag.*, vol. 150, no. 6, pp. 440–444, 2003.

[5] J. A. Encinar, "Design of a dual frequency reflectarray using microstrip stacked patches of variable size," *Electronics Letters*, vol. 32, no. 12, pp. 1049–1050, 1996.

[6] G. Zhao and Y.-C. Jiao, "Broadband dual-polarization dual coverage reflectarray antenna," in *Proceedings of the IEEE 4th International Symposium on Microwave, Antenna, Propagation, and EMC Technologies for Wireless Communications* (*MAPE '11*), pp. 102–105, Nov. 2011.

[7] X. Chua, T. Chia, and K. B. K. Chia, "Design of a transmitarray antenna using 4 layers of double square ring elements," *Progress in Electromagnetics Research Letters*, vol. 94, pp. 141–149, 2020.

[8] J. Huang and R. J. Pogorzelski, "A Ka-band microstrip reflectarray with elements having variable rotation angles," *IEEE Transactions on Antennas and Propagation*, vol. 46, no. 5, pp. 650–656, May 1998.

[9] R. Florencio, J. A. Encinar, R. R. Boix, G. Pérez-Palomino, and G. Toso, "Cross-polar reduction in reflectarray antennas by means of element rotation," in *IEEE 10th European Conference on Antennas and Propagation* (*EuCAP*), pp. 1–5, 2016.

[10] X. Yang, S. Xu, F. Yang, M. Li, Y. Hou, S. Jiang, and L. Liu, "A broadband high-efficiency reconfigurable reflectarray antenna using mechanically rotational elements," *IEEE Transactions on Antennas and Propagation*, vol. 65, no. 8, pp. 3959–3966, 2017.

[11] B. Strassner, C. Han, and K. Chang, "Circularly polarized reflectarray with microstrip ring elements having variable rotation angles," *IEEE Transactions on Antennas and Propagation*, vol. 52, no. 4, pp. 1122–1125, Apr. 2004.

[12] I. Derafshi, N. Komjani, E. G. Mizuji, and M. Mohammadirad, "A novel FSS backed unit cell with quasi spiral phase delay line," *Journal of Microwaves, Optoelectronics and Electromagnetic Applications*, vol. 15, no. 3, pp. 225–236, Sep. 2016.

[13] W. S. Elshennawy and A. M. Attiya, "Modified phasing element for broadband reflectarray antennas," *Progress in Electromagnetics Research C*, vol. 71, pp. 9–16, 2017.

[14] R. S. Malfajani and Z. Atlasbaf, "Design and implementation of a broadband single-layer circularly polarized reflectarray antenna," *IEEE Transactions on Antennas and Propagation*, vol. 11, pp. 973–976, 2012.

[15] T. Shabbir, M. T. Islam, N. Misran, S. S. Al-Bawri, and S. Singh, "Broadband single-layer reflectarray antenna loaded with meander-delay-lines for X-band applications," *Alexandria Engineering Journal*, vol. 60, no. 1, pp. 1105–1112, 2021.

[16] M. E. Bialkowski and K. H. Sayidmarie, "Investigations into phase characteristics of a single-layer reflectarray employing patch or ring elements of variable size," *IEEE Transactions on Antennas and Propagation*, vol. 56, no. 11, pp. 3366–3372, 2008.

[17] Y. Li, M. E. Bialkowski, K. H Sayidmarie, and N. V. Shuley, "Investigations into a circular ring with variable length arc element for phasing wideband reflectarray," in *Proceedings of Asia-Pacific Microwave Conference*, IEICE pp. 2013–2016, 2010.

[18] J. A. Encinar, "Analysis and design of dual frequency reflectarrays using microstrip stacked patches of variable size," in *Proceedings of the 26th IEEE European Microwave Conference,* vol. 1, pp. 221–224, Sep. 1996.

[19] T. Liao, Z.-Q. Zhang, Y.-C. Jiao, Y.-D. Yan, G.-T. Chen, and Z.-B. Weng, "Broadband circular polarized reflectarray based on multi-resonance unit," *International Journal of RF and Microwave Computer-Aided Engineering*, vol. 31, no. 6, pp. 1–9, 2021.

[20] M. E. Cooley, J. F. Walker, D. G. Gonzalez, and G. E. Pollon, "Novel reflectarray element with variable phase characteristics," *IEE Proceedings*, vol. 144, no. 2, pp. 149–151, 1997.

[21] R. Fathurrahman, U. Umaisaroh, and M. Alaydrus, "Design of reflectarray antenna with ring-loaded patches for 5G applications," in *IEEE International Conference on Radar, Antenna, Microwave, Electronics, and Telecommunications*, pp. 60–63, 2021.

[22] K. H. Sayidmarie and M. E. Bialkowski, "Phasing of a microstrip reflectarray using multi-dimensional scaling of its elements," *Progress in*

Electromagnetics Research B, vol. 2, pp. 125–136, 2008.

[23] K. H. Sayidmarie and M. E. Bialkowski, "Fractal unit cells of increased phasing range and low slopes for single-layer microstrip reflectarrays," *IET Microw. Antennas Propag.,* vol. 5, no. 11, pp. 1371–1379, 2011.

[24] H. D. Cuong, M.-T. Le, and N. Q. Dinh, "A reflectarray antenna using crosses and square rings for 5G millimeter-wave application," in *IEEE International Conference on Advanced Technologies for Communications* (*ATC*), pp. 126–130, 2020.

[25] K. H. Sayidmarie and M. E. Bialkowski, "Broadband microstrip reflectarray formed by double circular ring elements," in *IEEE 17th International Conference on Microwaves, Radar and Wireless Communications*, pp. 1–4, 2008.

[26] B. Mohammadi, J. Nourinia, C. Ghobadi, and I. Aryanian, "Analysis, design and fabrication of a reflectarray antenna using elements with reduced reflection phase sensitivity," in *IEEE 9th International Symposium on Telecommunications* (*IST'2018*), pp. 696–699, 2018.

[27] Y. Li, M. E. Biakowski, K. H. Sayidmarie, and N. V. Shuley, "Single-layer microstrip reflectarray with double elliptical ring elements for bandwidth enhancement," *Microwave and Optical Technology Letters*, vol. 53, no. 5, pp. 1083–1087, 2011.

[28] A. Vosoogh, K. Keyghobad, A. Khaleghi, and S. Mansouri, "A high-efficiency Ku-band reflectarray antenna using single-layer multiresonance elements," *IEEE Antenna and Wireless Propagation Letters*, vol. 13, pp. 891–894, 2014.

[29] H. Yu and L. Guo, "Broadband single-layer reflectarray antenna employing circular ring elements dented with sectorial slits," *IEEE Access*, vol. 7, pp. 165814–165819, 2019.

[30] K. H. Sayidmarie and L. S. Yahya, "Characterization of a split-circle element for microstrip reflectarrays," *Journal of Telecommunications and Information Technology*, vol. 3, no. 3, pp. 62–67, Sep. 2023.

[31] A. Murugesan, D. Natarajan, and K. T. Selvan, "Low-cost, wideband checkerboard metasurfaces for monostatic RCS reduction," *IEEE Antennas and Wireless Propagation Letters*, vol. 20, no. 4, pp. 493–497, 2021.

[32] D. M. Pozar, "Bandwidth of reflectarrays," *Electronics Letters*, vol. 39, no. 21, pp. 1490–1491, Oct. 2003.

[33] M. Guo, L. Guo, and W. Feng, "A wideband planar reflectarray antenna using clip-shaped elements for X-band applications," *International Journal of RF and Microwave Computer-Aided Engineering*, vol. 32, no. 4, pp. 1–10, 2022.

[34] C. Han, Y. Zhang, and Q. Yang, "A novel single-layer unit structure for broadband reflectarray antenna," *IEEE Antennas and Wireless Propagation Letters*, vol. 16, pp. 681–684, 2016.

[35] C. Tian, J. Zhang, and Y. Liu, "A microstrip reflectarray antenna based on double Minkowski rings," in *Cross Strait Quad-Regional Radio Science and Wireless Technology Conference* (*CSQRWC*), pp. 1–3, 18–21 July 2019.

[36] R. A. Abdul Jabbar and K. H. Sayidmarie, "A unit cell element for reflectarrays based on the bowtie shape," in *Proceedings of Ninth International Congress on Information and Communication Technology* (*ICICT 2024*), London, pp. 421–429, 19–22 Feb. 2024.

[37] K. H. Sayidmarie and A. M. Saleh, "Comparison of phase responses of proposed element shapes for reflectarray unit cells," in *2011 4th IEEE International Symposium on Microwave, Antenna, Propagation and EMC Technologies for Wireless Communications*, pp. 367–371, 2011.

[38] M. A. Qureshi, A. Aziz, A. Amin, H. F. Rasool, and F. Hayat, "Design of a new wideband single-layer reflective metasurface unit cell for 5G-communication," *Applied Computational Electromagnetics Society (ACES) Journal*, vol. 35, no. 8, pp. 975–978, Aug. 2020.

[39] T. Bashir, H. Xiong, A. Aziz, M. A. Qureshi, H. Ahmed, A. Wahab, and M. Umaid, "Design and analysis of reflectarray compound unit cell for 5G communication," *Applied Computational Electromagnetics Society (ACES) Journal*, vol. 35, no. 12, pp. 1513–1518, Dec. 2020.

[40] K. Yan, X. Lv, Z. Han, and Y. Zhang, "A transmitarray antenna with double conformal rings as the cell elements," *Applied Computational Electromagnetics Society (ACES) Journal*, vol. 34, no. 7, pp. 1032–1037, July 2019.

Likaa S. Yahya received the M.Sc. in Electrical Engineering and Ph.D. in Communication Engineering from the University of Mosul in 2002 and 2017, respectively. She is currently Assistant Professor in the Department of Electronic and Communication Engineering Techniques, Northern Technical University, Mosul, Iraq. She has published more than 10 papers in international journals and conferences. Her interests include antenna design and antenna modeling.

Khalil H. Sayidmarie received the B.Sc. degree in Electronics and Communication Engineering from Mosul University, Iraq, in 1976, and the Ph.D. Degree in Antennas and Propagation from Sheffield University, UK, in 1981. He joined the College of Engineering at Mosul University in 1983 and was promoted to full professor in 1992. He worked as head of the electrical engineering department for nine years. Sayidmarie served as Professor of Communication Engineering at the College of Engineering, University of Amman, Jordan, from October 2006 to September 2009, and as Dean of that college from September 2008 to September 2009. He has been Professor of communication engineering at the College of Electronics Engineering, Ninevah University, since July 2002. He is currently Professor Emeritus with the College of Electronics Engineering, Ninevah University. His research interests include antennas, propagation, and microwaves, and he has published more than 160 papers in international journals and conferences.

A 3 dB Coupler With Defected Ground Structure for Feeds Applied to High-Power Intelligent Metasurface

Weidong Kong[1,2], Jinyu Wang[1], Shixiong Deng[2], Qiaonan Wang[1,2], Leiqiang Ma[4], Biao Zhou[2], Xuefeng Song[2], Kuang Zhang[1], Guohui Yang[1], Yang Li[3], and Cong Wang[1]

[1]School of Electronic & Information Engineering
Harbin Institute of Technology, Harbin 150001, China
23b905073@stu.hit.edu.cn, jinyuwang@stu.hit.edu.cn,
wangqn8678@163.com, zhangkuang@hit.edu.cn,
gh.yang@hit.edu.cn, kevinwang@hit.edu.cn

[2]Hebei Semiconductor Research Institute
Shijiazhuang 050051, China
shixiode@163.com, CZ1314233@163.com, hsri_sxf@163.com

[3]School of Integrated Circuits
Shandong University, Shandong 250100, China
yang.li@sdu.edu.cn

[4]Southwest China Research Institute of Electronic Equipment
Chengdu, China
lqma_hit@126.com

***Abstract* –** This paper proposes a 3 dB coupler with high-power handling capability feeds applied to high-power intelligent metasurface, based on loosely coupled structures and defected ground structure (DGS). The proposed coupler structure consists of two tandem coupled couplers with a coupling coefficient of 8.34 dB and a DGS, a design that significantly enhances the couplers' ability to handle high power levels. The measurement results are in good agreement with the simulation results: within the 3.5 to 4.5 GHz range, the return loss exceeds 21.4 dB, the isolation is at least 20.8 dB, the insertion loss is less than 0.3 dB, and the phase difference between output ports is 93–94.5°. Furthermore, the coupler can handle high power exceeding 1.5 kW with a 10% duty cycle. The proposed 3 dB coupler features low insertion loss, high isolation, low return loss, high-power capability, and can improve the power capability of intelligent metasurface systems.

***Index Terms* –** 3 dB coupler, defected ground structure (DGS), high power, metasurface.

I. INTRODUCTION

In next-generation communication systems, the application of metasurface will attract significant attention. Compared to traditional phased array beam scanning methods, metasurface-based beam scanning systems rely on a single active amplifier for feeding, thereby imposing higher output power requirements on the amplifier than conventional active phased array beam scanning. To advance the engineering application of metasurface, high-power electromagnetic energy feeding sources will be indispensable, as show in Fig. 1. Therefore, high-power couplers play a critical role in metasurface-based communication systems for power combining [1].

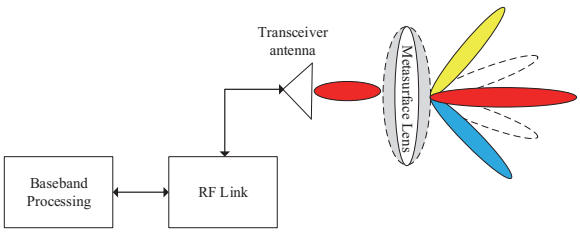

Fig. 1. Metasurface beam scanning system.

With the rapid advancement of modern communication systems, miniaturization has become an irreversible trend, driving the transition from traditional discrete

Submitted On: July 08, 2025
Accepted On: September 08, 2025

https://doi.org/10.13052/2026.ACES.J.410206

components to hybrid integrated circuits (HICs). HICs integrate multiple functional modules into a single package, significantly reducing system size while enhancing performance and reliability [2]. In the radio frequency (RF) domain, couplers are typically constructed using coaxial lines, waveguides, and microstrip lines. Coaxial lines and waveguides exhibit high-power handling capability but are bulky and unsuitable for HICs [3], whereas microstrip couplers are more suitable for HICs due to their compact structure [4]. Conventionally, couplers fabricated by printed circuit board (PCB) suffer from poor heat dissipation, are prone to overheating and line burnout at high power, and have large dimensions [5]. For heat dissipation requirements, thin-film technology on alumina ceramic substrates is an optimal choice: 99.6% pure alumina ceramics with a thermal conductivity of 37 W/(m·K) offer advantages of good heat dissipation, low loss, small size, and excellent performance in high-temperature environments [6, 7].

Traditional Lange couplers are difficult to manufacture due to the narrow spacing and width of coupling lines and are prone to arc breakdown at high power [8]. Therefore, the proposed 3 dB coupler employs two tandem connected loose couplers to solve the problem of close coupling line spacing, and a defected ground structure (DGS) is introduced to further increase the coupling line spacing and enhance power handling capability, achieving a high-power handling capability of 1.5 kW. The proposed coupler based on thin-film technology on alumina ceramic substrates features high-power handling capability, low insertion loss, and small size, with measurement results in good agreement with simulations.

II. CIRCUIT ANALYSIS AND DESIGN FOR HIGH POWER

A. Structure of the proposed 3 dB coupler

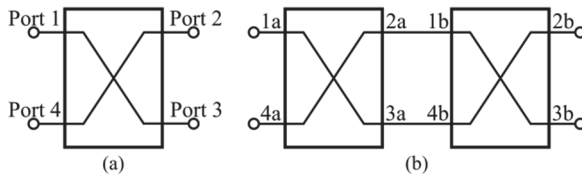

Fig. 2. Four-port network. (a) Single coupler and (b) two-stage tandem coupler.

Figure 2 (a) shows a four-port coupler structure. Assume that the signal level of Port 1 is 1, the signal level of Port 4 is 0 and the coupling coefficient is C. Therefore, the signal level of Port 2 is C, and the signal level of Port 3 is $\sqrt{1-C^2}$ [9, 10]. Then the scattering parameter matrix of this coupler can be written:

$$S = \begin{bmatrix} 0 & C & j\sqrt{1-C^2} & 0 \\ C & 0 & 0 & j\sqrt{1-C^2} \\ j\sqrt{1-C^2} & 0 & 0 & C \\ 0 & j\sqrt{1-C^2} & C & 0 \end{bmatrix}. \tag{1}$$

Two identical couplers are connected in series as shown in Fig. 2 (b), and the signal levels of its two output ports can be calculated from (1):

$$V_{2b} = V_{1b} \cdot S_{21} + V_{4b} \cdot S_{24} = 2C^2 - 1. \tag{2}$$

$$V_{3b} = V_{1b} \cdot S_{31} + V_{4b} \cdot S_{34} = j2C\sqrt{1-C^2}. \tag{3}$$

For a 3 dB coupler, both output ports are equal in level amplitude:

$$|V_{2b}| = |V_{3b}|. \tag{4}$$

The values of C are obtained from (4), $C = 0.3827$ (-8.34 dB) or 0.9239 (-0.69 dB). Therefore, a 3 dB coupler can be composed of tandem two loose couplers, thus increasing the coupling line spacing and power handling capability. A 3 dB coupler, designed by cascading two 8.34 dB couplers, demonstrates the simulated electric field (E-field) distribution shown in Fig. 3, with a 1.5 kW pulse wave at a 10% duty cycle fed into the input port.

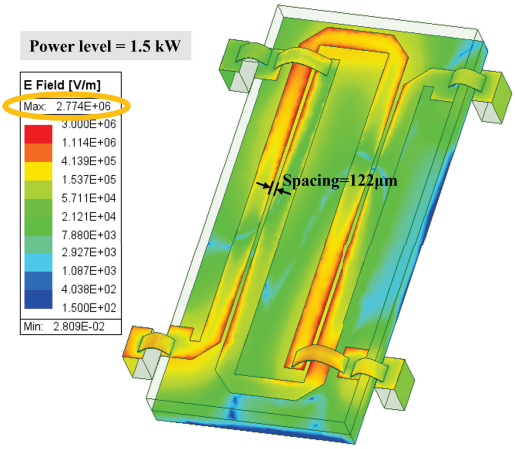

Fig. 3. E-field distribution simulation of the 3 dB coupler.

The 3 dB coupler has a coupling line spacing of 122 μm. In Fig. 3, the maximum field strength is 2.77×106 V/m, which is close to the breakdown field strength of air (3×106 V/m). In practice, the coupler must be designed with a maximum field strength of less than 70% of the ultimate breakdown field strength to ensure stable operation over long periods of time. Therefore, the coupling line spacing needs to be further increased to reduce the maximum field strength.

B. Analysis of DGS

From [11, 12], the coupling coefficients of a typical coupler can be calculated as follows:

$$|C| = \left| \frac{Z_{even} - Z_{odd}}{Z_{even} + Z_{odd}} \right|, \tag{5}$$

where Z_{even}, Z_{odd} are the even and odd mode impedances, respectively. Further transformations of (5) are given:

$$|C| = \left| \frac{k-1}{k+1} \right|, \quad k = \frac{Z_{even}}{Z_{odd}}. \tag{6}$$

Clearly, the coupling coefficient C is increasing with k. The DGS enhances the field coupling between the coupling lines as seen in [13]. The effect of DGS on coupling lines is:

$$k_2 > k_1, \tag{7}$$

where k_2 means with DGS and k_1 means without DGS. The result is obtained by substituting equation (7) into equation (6):

$$C_2 > C_1, \tag{8}$$

where C_2 means with DGS and C_1 means without DGS. The results indicate that adding DGS below the coupled microstrip lines can improve the coupling effect between them. Therefore, couplers with DGS can achieve 3 dB coupling with wider coupling line spacing to increase power tolerance.

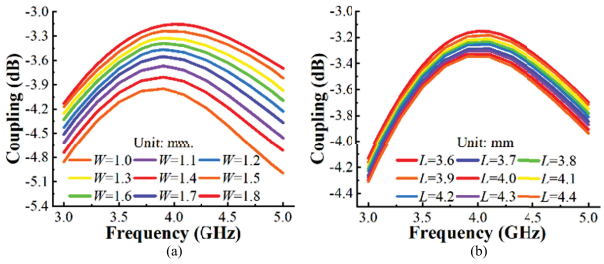

Fig. 4. The influence of DGS size on coupling coefficient: (a) when $L = 4$ mm and (b) when $W = 1.4$ mm.

To obtain the optimal DGS size, the width and length of the DGS are independently swept for simulation. The effect of DGS size on the coupling coefficient is shown in Fig. 4. The highest coupling coefficient is obtained using a DGS with $W = 1.4$ mm and $L = 4$ mm. For microstrip lines, the coupling reduces as the lines separate [14]. Therefore, using a DGS with $W = 1.4$ mm and $L = 4$ mm maximizes the coupled line spacing [8]. The proposed 3 dB tandem coupler layout is shown in Fig. 5 with three layers: top metal, alumina ceramic substrate, and bottom metal with DGS. Ultimately, the designed 3 dB coupler has a coupling line spacing of 200 μm, which is a 64% increase compared to the coupling line spacing of the coupler without DGS.

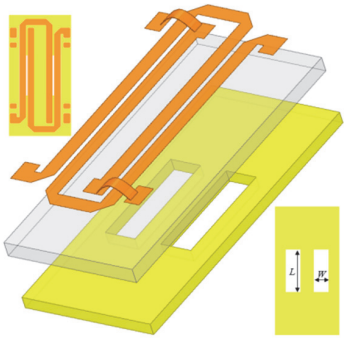

Fig. 5. Layout of the 3 dB coupler with DGS.

C. Simulation verification for high power

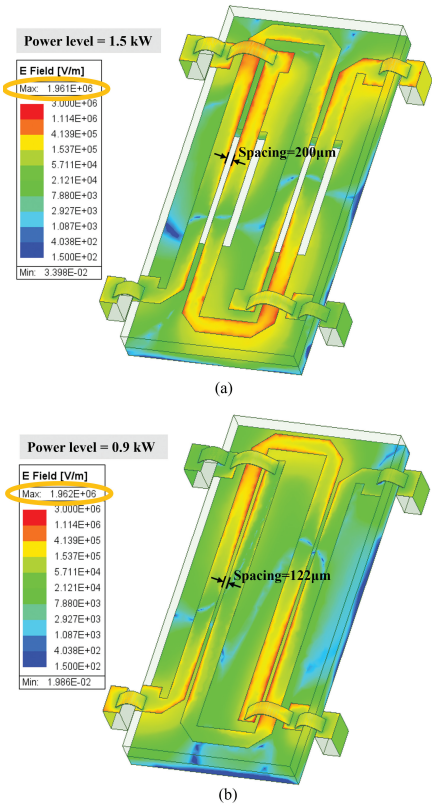

Fig. 6. E-field distribution simulation of the 3 dB coupler: (a) with DGS and (b) without DGS.

To validate the effect of DGS on enhancing the coupler's power handling capability, a 1.5 kW pulse wave with a 10% duty cycle is applied to the input port, and the simulated E-field distribution is shown in Fig. 6 (a). The highest E-field intensity is primarily

concentrated between the coupled lines, reaching a value of 1.96 × 106 V/m. For comparison, an E-field distribution simulation was performed for the 3 dB coupler without DGS, with the input power adjusted to achieve the same maximum field intensity as in Fig. 6 (a). The simulation results are shown in Fig. 6 (b). For the 3 dB coupler without DGS, the maximum field strength of 1.96×106 V/m was reached when the input power was 0.9 kW. The implementation of DGS effectively improves the power handling capability of the coupler, increasing it by 67% compared to the coupler without DGS, thus meeting the requirements for sustained high-power operation. But DGS may increase fabricating complexity due to sensitivity to dimensional tolerances (as hinted in Fig. 4) and could be less effective at frequencies outside the 3.5–4.5 GHz band due to substrate constraints. Additionally, DGS structures might not scale well to lower frequencies without larger sizes.

The results of the temperature distribution simulation of the proposed coupler are shown in Fig. 7. The ambient temperature is set to 70°C, using the same input conditions as the E-field simulation. The thermal conductivity of the alumina substrate is set at 37 W/(m·K), while that of the top and bottom metallic layers is established at 400 W/(m·K). The maximum temperature is 87.6°C at the coupling line, which is lower than the limiting temperature of the process (260°C). The above simulation results verify the high-power handling capability of the proposed coupler.

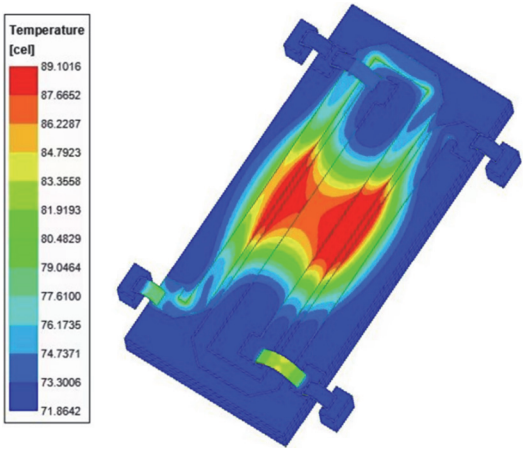

Fig. 7. Temperature distribution simulation.

III. FABRICATION AND MEASUREMENT RESULTS

The proposed 3 dB coupler is fabricated by an alumina ceramic substrate with a thickness of 635 μm, a purity of 99.6%, and relative dielectric permittivity $\varepsilon r = 9.8$. Alumina ceramic substrates (99.6% purity) offer a high thermal conductivity of 37 W/(m·K). This property is critical for high-power handling, as it efficiently dissipates heat generated during operation, preventing overheating and line burnout, a common issue in PCB-based couplers. The alumina ceramic's high thermal conductivity directly enhances power handling. This substrate allows for good heat dissipation, low loss, small size, and excellent performance in high-temperature environments. For HICs, alumina ceramics support miniaturization and reliability. Alumina substrates facilitate this through thin-film technology, allowing for compact dimensions and compatibility with high-frequency applications.

The top layer is plated with 2 μm of gold using thin-film technology and the bonding wires are 500 × 25 μm gold strips. The design process involved optimizing DGS dimensions to maximize coupling coefficients, Manufacturing tolerances, such as changes in film line width and DGS position alignment, may affect coupling efficiency and field distribution. A 10% tolerance online spacing in thin film processes can alter the maximum electric field strength. The fabricated 3 dB coupler is shown in Fig. 8, with dimensions of $w_2 \times w_1 = 6.15 \times 12.15$ mm^2, which is well suited to HIC. The detailed physical parameters are (Unit: mm): $w_3 = 0.2$, $w_4 = 0.6$, $w_5 = 10$, $w_6 = 1.2$, $w_7 = 9.4$.

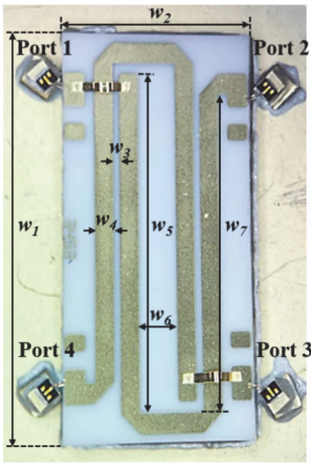

Fig. 8. Photograph of the fabricated 3 dB coupler.

Figure 9 shows the small-signal measure results of the fabricated 3 dB coupler. The measured S_{31} and S_{21} are −3.29 dB and −3.3 dB at 4 GHz, with good performance. The coupling coefficient is 3.29–3.49 dB, and the insertion loss is less than 0.3 dB, across the frequency range of 3.5 to 4.5 GHz. Return loss and isolation also perform well, greater than 21.4 dB and 20.8 dB, respectively. And $\angle S_{31} - \angle S_{21}$ (phase difference) is 93–94.5° within the operating frequency.

The fabricated coupler was tested for high-power operation and operated continuously for 120 minutes

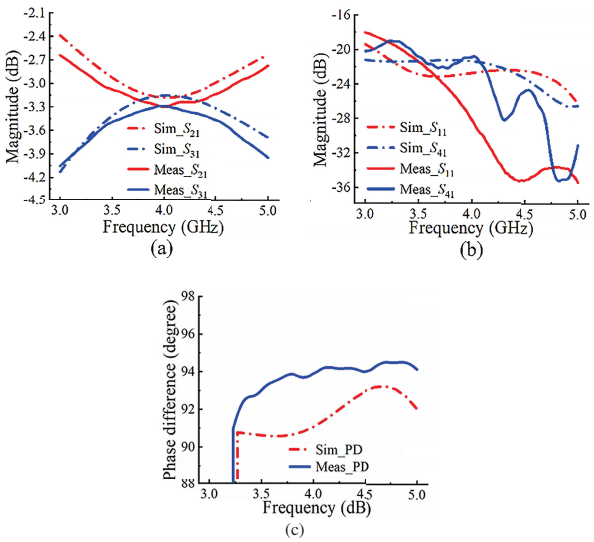

Fig. 9. Small-signal simulation and measured results: (a) $|S_{21}|$ and $|S_{31}|$, (b) $|S_{11}|$ and $|S_{41}|$, and (c) phase difference ($\angle S_{31} - \angle S_{21}$).

at an input of 1.5 kW with a 10% duty cycle without any abnormalities, with lower duty cycles reducing thermal accumulation and achieving higher peak power tolerance. The duty cycle directly affects thermal management and continuous operation. Our power endurance test ran stably at an ambient temperature of 70°C and a relative humidity of 40%. Humidity may affect dielectric performance or arc risk. High humidity may lower the air breakdown threshold (currently designed to be below 70% of 3×10^6 V/m according to section II.A), affecting long-term reliability. Therefore,

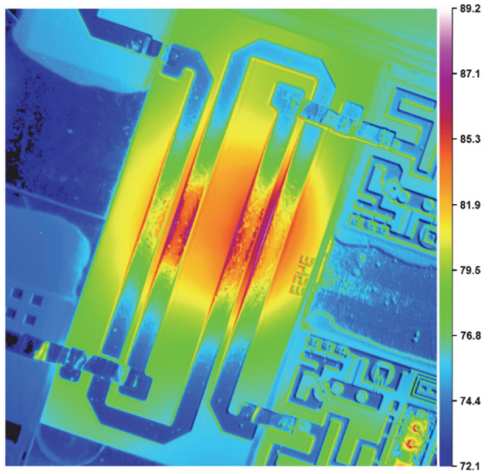

Fig. 10. Temperature distribution measured results at high power.

it is required to use airtight sealing or substrate coating to ensure low humidity levels. However, arcing occurs when the input power is increased to 2 kW. The results of the high-power temperature test, conducted with a 1.5 kW pulsed wave input and a constant temperature surface maintained at 70°C at the bottom, are presented in Fig. 10. In agreement with the simulation results, the peak temperature is 89.2°C at the position of the coupling line, which is less than the tolerable temperature of alumina ceramics. The coupler operates well without any detachment, proving that the coupler can withstand high power exceeding 1.5 kW. Compared with other work, the results are also competitive as shown in Table 1.

Table 1: Comparison with high-power and 3 dB couplers

Ref.	**Technology**	**Center Frequency (GHz)**	**Band Width (%)**	**Power Handling Capability (kW)**	**Coupling Coefficient (dB)**	**Through (dB)**	**Isolation (dB)**	**Phase Difference (°)**	**Size**
[3]	Coaxial Line	0.0775	187.1	2	45±1.3	<0.65	>80	N/A	0.04 (λ_0)
[15]	Coaxial Line	0.55	163.6	0.3	20	<0.3	40	N/A	0.14 (λ_0)
[4]	Microstrip (PCB)	0.44	7.8	1	25	0.2	66.2	N/A	0.04×0.03 (λ_0^2)
[12]	Microstrip (Al_2O_3)	2.5	48	N/A	4	2.5	21.4	89.2-89.5	0.11 (λ_0)
[16]	Cross-slot (PCB)	3.44	30	N/A	3.59	3.39	29.18	89.1	0.19×0.17 (λ_0^2)
[17]	SISPSL (PCB)	5	16.45	N/A	3.7±0.22	3.606±0.08	15-45	90±0.5	0.40×0.40 (λ_0^2)
This Work	Microstrip (Al_2O_3)	4	25	1.5	3.29-3.49	3.08-3.3	>20.8	93-94.5	0.08×0.16 (λ_0^2)

SISPSL: Substrate Integrated Suspended Parallel Strip Line. λ_0 is the wavelength in air at the center frequency.

IV. CONCLUSION

This paper presents a novel 3 dB coupler with a power handling capacity exceeding 1.5 kW. Two innovative solutions are proposed to address the challenge of excessively narrow coupling line spacing: cascading two loosely coupled coupler structures in tandem configuration and introducing a DGS to enhance the coupling coefficient of the transmission lines by 64%. Consequently, the power handling capability is improved by 67% compared to 3 dB couplers without DGS. Comprehensive electromagnetic simulations and experimental measurements validate the excellent performance in terms of S-parameters and high-temperature characteristics. This study can effectively enhance the power handling capacity of metasurface-based communication systems, thereby extending their coverage range.

ACKNOWLEDGMENT

This work was supported in part by the National Natural Science Foundation of China under Grant 62320106002 and Grant U22A2014; in part by the Key Research and Development Program of Shandong Province, China, under Grant 2024KJHZ013; in part by Shandong Provincial Natural Science Foundation of China under Grant ZR2023ZD03.

REFERENCES

[1] S. Yang, X. Wang, H. Zhu, and G. Lu, "A coupling-path reconfigurable quadrature coupler with wide range of tunable frequencies and power division ratios," *IEEE Transactions on Microwave Theory and Techniques*, vol. 72, no. 6, pp. 3530–3541, June 2024.

[2] F. Gardes, A. Shooa, G. De Paoli, I. Skandalos, S. Ilie, T. Rutirawut, W. Talataisong, J. Faneca, V. Vitali, and Y. Hou, "A review of capabilities and scope for hybrid integration offered by silicon-nitride-based photonic integrated circuits," *Sensors*, vol. 22, no. 11, p. 4227, 2022.

[3] Z.-B. Wang, X. Wei, H.-P. Fang, H.-M. Zhang, and Y.-R. Zhang, "A compact and broadband directional coupler for high-power radio frequency applications," *IEEE Microwave and Wireless Components Letters,* vol. 30, no. 2, pp. 164–166, Feb. 2020.

[4] S.-M. Sohn, A. Gopinath, and J. T. Vaughan, "A compact, high power capable, and tunable high directivity microstrip coupler," *IEEE Transactions on Microwave Theory and Techniques*, vol. 64, no. 10, pp. 3217–3223, Oct. 2016.

[5] H.-P. Fang and X. Wei, "Compact directional coupler for high-power applications," in *2018 12th International Symposium on Antennas, Propagation and EM Theory (ISAPE)*, Hangzhou, China, pp. 1–3, 2018.

[6] S. Li, L. Zhang, H. Xie, X. Yao, Z. Hao, and H. Dong, "Effect of AlN/Al_2O_3 thin-film protective layer on the high-temperature performance of ITO thin-film strain gauge," *IEEE Sensors Journal*, vol. 23, no. 11, pp. 11490–11497, June 2023.

[7] Z. Zhang, X. Yuan, and L. Xie, "A new package for SiC power modules with ceramic heatsink," in *2022 IEEE Energy Conversion Congress and Exposition (ECCE)*, Detroit, MI, USA, pp. 1–7, 2022.

[8] J. Zhang, Z. Wu, F. Xu, and D. Li, "An interdigitated coupler with defect ground structure," in *2015 IEEE MTT-S International Microwave Workshop Series on Advanced Materials and Processes for RF and THz Applications (IMWS-AMP)*, Suzhou, China, pp. 1–3, 2015.

[9] H. Hayashi, "Tandem Lange 3-dB 90° hybrid implemented on FR4 substrate," in *2014 NORCHIP,* Tampere, Finland, pp. 1–3, 2014.

[10] K. Wincza, K. Staszek, and S. Gruszczynski, "Reduced-length tandem directional couplers composed of coupled-line sections with fixed coupling coefficient," *IEEE Transactions on Microwave Theory and Techniques*, vol. 69, no. 3, pp. 1625–1634, Mar. 2021.

[11] M. Abe, Y. Tahara, and N. Yoneda, "A tandem 3-dB hybrid coupler using coupled lines with series capacitance," in *The 40th European Microwave Conference,* Paris, France, pp. 164–167, 2010.

[12] R. Behera, K. Sangam, S. S. Lonkadi, A. Andhiwal, K. Singh, and A. V. Nirmal, "Realization of Lange coupler using hybrid technology and its characterization," in *2022 Trends in Electrical, Electronics, Computer Engineering Conference (TEECCON)*, Bengaluru, India, pp. 135–141, 2022.

[13] B. Qian, X. Chen, and A. Kishk, "Decoupling of microstrip antennas with defected ground structure using the common/differential mode theory," *IEEE Antennas and Wireless Propagation Letters*, vol. 20, no. 5, pp. 828–832, May 2021.

[14] M. Steer, *Microwave and RF Design II—Transmission Lines*. Raleigh, NC, USA: NC State University, p. 203, 2019.

[15] G. Lin, X. Yin, S. Ren, Z. Wang, Y. Zhi, and T. He, "Compact and broadband directional coupler for high power applications," *Journal of Electromagnetic Waves and Applications*, vol. 35, no. 15, pp. 1980–1986, 2021.

[16] K. Abouhssous, L. Wakrim, A. Zugari, and A. Zakriti, "A compact patch coupler using cross-slots for 5G applications," in *2023 IEEE 3rd International Maghreb Meeting of the Conference on Sciences and Techniques of Automatic Control*

and Computer Engineering (MI-STA), Benghazi, Libya, pp. 590–594, 2023.

[17] J. Liu, Y. Wang, K. Ma, and W. An, "A differential SISPSL branch-line coupler with common-mode suppression using compensated stub," *IEEE Transactions on Circuits and Systems II: Express Briefs*, vol. 70, no. 2, pp. 511–515, Feb. 2023.

Weidong Kong received the B.E. and M.E. degrees in Electronics and Information Engineering from Harbin Institute of Technology University, China, in 2014 and 2016, respectively. He is currently pursuing a Doctor of Engineering degree with a specialization in Electronics and Information at Harbin Institute of Technology University.

Jinyu Wang is currently pursuing the M.E. degree at Harbin Institute of Technology, China. His research specializes in microwave power amplifiers and filter design.

Shixiong Deng received the M.E. degree from Beihang University, China, in 2014 and the Ph.D. degree from National University of Defense Technology in 2024. His research focuses on microwave limiters and electromagnetic protection.

Qiaonan Wang received the M.E. degree from the University of Electronic Science and Technology of China. His research interests include microwave voltage-controlled attenuators and microwave filter design.

Leiqiang Ma received the M.E. degree in Electronics and Information Engineering from Harbin Institute of Technology, China, in 2015. His research focuses on microwave receiver module design.

Biao Zhou received the M.E. degree from Hebei Semiconductor Research Institute, China, in 2009. His research interests include microwave active phased array systems.

Xuefeng Song received the M.E. degree from Hebei Semiconductor Research Institute, China. His research specializes in microwave semiconductor chips.

Kuang Zhang (Member, IEEE) received the B.Sc. degree in electronics and information engineering, the M.Eng. degree in electronics engineering, and the Ph.D. degree in communication and information systems from Harbin Institute of Technology (HIT), Harbin, China, in 2005, 2007, and 2011, respectively. He was a Visiting Professor with the University of Wisconsin-Madison, Madison, WI, USA, from 2015 to 2016. Since 2010, he has been with the Department of Microwave Engineering, School of Electronics and Information Engineering, HIT, where he is currently a Professor.

Guohui Yang (Member, IEEE) received the B.S. degree in telecommunication, the M.S. degree in instrument science and technology, and the Ph.D. degree in electromagnetics from the Harbin Institute of Technology, Harbin, China, in 2003, 2006, and 2009, respectively. Since 2009, he has been with the Department of Microwave Engineering, Harbin Institute of Technology, where he is currently an Associate Professor. His current research interests are radio frequency micro electromechanical system (RF MEMS) devices, tunable antennae, frequency selective surface (FSS), electromagnetic compatibility (EMC), and final difference time domain (FDTD).

Yang Li (Senior Member, IEEE) received the Ph.D. degree from the Department of Electronic, Kwangwoon University, Seoul, South Korea, in 2015. He has been a Professor at the School of Microelectronics at Shandong University, Jinan, China, since 2022. His research interests include nanostructured flexible materials, flexible electronics, gas sensors, and memristors.

Cong Wang (Senior Member, IEEE) was born in Qingdao, Shandong, China, in 1982. He received the B.S. degree in automation engineering from Qingdao Technological University, Qingdao, in 2005, and the M.S. and Ph.D. degrees in electronic engineering from Kwangwoon University, Seoul, South Korea, in 2008 and 2011, respectively. Since 2016, he has been with the Department of Microwave Engineering, Harbin Institute of Technology, Harbin, where he is currently a Professor. His major interests include passive device design and fabrication, humidity sensors, and biosensors.

Wideband Dual-Polarized Metasurface Antenna Array with High Isolation

Yue-Chen Liu[1], Xiaoyun Qu[2], Cheng Ju[1], and Wei-Hua Zong[1*]

[1]College of Electronics and Information Qingdao University
Qingdao 266000, China
liuyuechen@qdu.edu.cn, jucheng719@qdu.edu.cn, weihuazong@126.com*
*Corresponding Author

[2]Shandong Institute of Space Electronic Technology
Yantai, China
selina.qu@163.com

Abstract – This paper presents a dual-polarized 1×4 antenna array with wide bandwidth and high isolation. The antenna element consists of three metallic layers, a 4×4-unit metasurface (MTS) on the top layer, a patch fed by two ports on the middle layer, and a ground plane on the bottom layer. By exciting different feeding ports, the antenna achieves X-axis linear polarizations (X-LP) or Y-axis linear polarizations (Y-LP). Isolation slots etched on the patch, combined with a via-hole structure, effectively block the coupling between ports and improve port isolation. Experimental results demonstrate that the proposed antenna achieves an impedance bandwidth of 17.4% (4.975–5.925 GHz), with $S_{11} < -10$ dB and $S_{21} < -20$ dB. The measured peak gain attains 12.5 dBi.

Index Terms – Antenna array, dual polarization, high isolation, low profile, metasurface (MTS).

I. INTRODUCTION

Dual-polarized antennas enable Multiple-Input Multiple-Output (MIMO) polarization diversity by simultaneously transmitting and receiving two orthogonal polarizations, such as horizontal/vertical polarization and ±45° cross-polarization. This capability helps reduce co-channel interference, mitigate multipath effects, and improve communication capacity along with data transmission rates. As a result, such antennas are widely used in macro and micro base stations, access point (AP) systems, and terminal devices for applications in mobile communications, Wireless Local Area Networks (WLAN), and Internet of Things (IoT). The design of dual-polarized antennas entails addressing several challenges: minimizing port coupling, suppressing cross-polarization, and simultaneously achieving wideband impedance matching and high gain, all with the overarching goal of satisfying the stringent application demands of modern communication systems.

Extensive research has been conducted on dual-polarized antennas, which mainly fall into two categories: dipole antennas [1–7] and planar patch antennas [8–14]. For dipole antennas, two orthogonal radiators are employed to achieve dual polarization. These two radiators are isolated from each other without any metallic connection, and their respective feeding strips are arranged in a crossed pattern on different layers, resulting in high port isolation. Metallic reflectors are placed beneath the radiators, and a large air gap is maintained between the reflectors and radiators to achieve directional radiation. However, this leads to the drawback of a large antenna volume.

Planar patch antennas feature a compact size, as they utilize a single patch with two feeding ports to realize dual polarization. Since the two polarizations share the same patch, strong mutual coupling occurs. Existing decoupling techniques include metamaterial-based electromagnetic bandgap (EBG) structures between the radiation patch and ground plane [8], shorting pins loaded between the radiator and ground [9], open- and short-circuited stubs added to the feeding strips [10], the use of coupled feeding methods [11–13], and slot etching on the patch combined with shorted feeding strips [14].

Antenna arrays are designed to improve antenna gain. Coupling between antenna elements needs to be considered in array antenna design. The commonly used decoupling techniques include adopting parasitic patches [10, 15–18], defected ground structures [19, 20], adding isolating walls and metasurface (MTS) [21, 22], and reducing the radiator's size by means of bending its shape [23].

Submitted On: October 01, 2025
Accepted On: March 08, 2026

https://doi.org/10.13052/2026.ACES.J.410207

In applications involving antennas for wearable devices, unmanned aerial vehicles (UAVs), compact passenger vehicles, automobiles, and micro-satellites, miniaturization of antennas is a core requirement. Patch antennas without an air gap are more suitable for integration in these scenarios. However, they suffer from a narrow bandwidth. The antennas exhibit much narrower bandwidths: 1.4% (lower band) and 0.8% (upper band) in [8], and 2.2% in [10]. In contrast, antennas with an air gap achieve significantly wider bandwidths: 51.3% in [9], 38.7% in [11], and 21.9% in [14].

This paper aims to design a dual-polarized patch antenna with wide bandwidth and high isolation. An MTS is adopted to enhance antenna bandwidth. Meanwhile, isolation slots are etched on the radiating patch, and a via-hole structure is integrated to improve isolation. Additionally, a 1×4 antenna array is proposed to improve antenna gain.

II. ANTENNA ELEMENT DESIGN AND MEASUREMENT

A. Configuration of antenna element

The configuration of the proposed antenna is shown in Fig. 1. The antenna consists of three metal layers, a 4×4-unit MTS on the top layer, a square patch loaded with slots on the middle layer and a ground plane on the bottom layer, printed on two pieces of FR-4 ($\varepsilon r = 4.4$, $\tan\delta = 0.02$) substrate. The two substrates are tightly bonded without air gap between them. Linear polarization (LP) along x/y axial is obtained by feeding Port 1/Port 2. The patch is etched with 3×3 slots, with each slot loaded with a via hole, to enhance isolation between the two feeding ports. The antenna dimensions are $d_1 = 0.5$ mm, $d_2 = 1.7$ mm, $d_3 = 3$ mm, $g = 0.2$ mm, $h_1 = 1.5$ mm, $h_2 = 0.8$ mm, $L_1 = 2$ mm, $L_2 = 8$ mm, $L_3 = 0.2$ mm, $P = 7.6$ mm, $W = 32$ mm, $W_p = 12$ mm, $W_1 = 4$ mm, $W_2 = 1.8$ mm, $W_3 = 1.5$ mm, and $W_4 = 1$ mm.

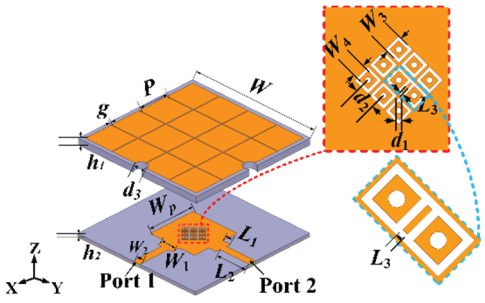

Fig. 1. Configuration of the proposed antenna.

B. Bandwidth enhancement using MTS

Two reference antennas are illustrated in Fig. 2. Ant.2 is derived from the proposed antenna by removing the slots and via-holes. Ant.1 is obtained by further removing the MTS from Ant.2. The S-parameters of these two antennas are presented in Fig. 3. For Ant.1, its resonant frequency is 5.15 GHz, and its bandwidth is 5.1–5.25 GHz (with $S_{11} < -10$ dB). For Ant.2, adding the MTS layer excites a second resonance at 5.95 GHz. Its bandwidth is improved to 4.85–6.3 GHz. However, the coupling between Port 1 and Port 2 of Ant.2 is stronger than that of Ant.1. Specifically, $S_{12} > -15$ dB in 5.2–5.35 GHz and $S_{12} > -20$ dB in 5.1–5.65 GHz.

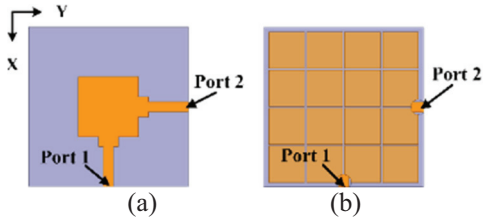

Fig. 2. Reference antennas in bandwidth enhancement design (a) Ant.1 and (b) Ant.2.

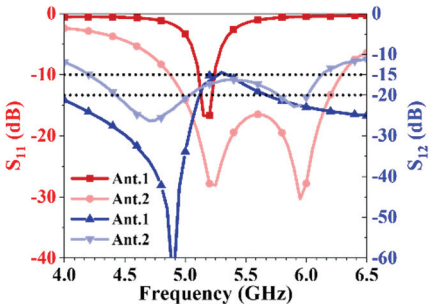

Fig. 3. Simulated S parameters of Ant.1 and Ant.2.

The size of the radiation patch can be calculated using the following formula [24]:

$$W_p = \frac{c}{2f_0}\sqrt{\frac{2}{\varepsilon_r + 1}}. \quad (1)$$

In consideration of the dual-port, dual-polarized design and required structural symmetry, the square radiation patch is dimensioned as $W_p = 16.6$ mm.

Loading MTS is an effective method to improve the antenna bandwidth. After adding the MTS structure, the antenna frequency shifts toward the low-frequency. W_p is optimized to adjust the frequency. As shown in Fig. 4, with $W_p = 12$ mm, the S_{11} is below -10 dB over 4.54–6.17 GHz. It provides the optimal bandwidth and impedance matching performance. $W_p = 12$ mm is adopted as the width of the antenna radiation patch.

As shown in Figs. 5 and 6, the dimensions of the MTS structure affect S_{11}. When $P = 7.6$ mm, S_{11} is below -10 dB in 4.54–6.17 GHz. This is the widest

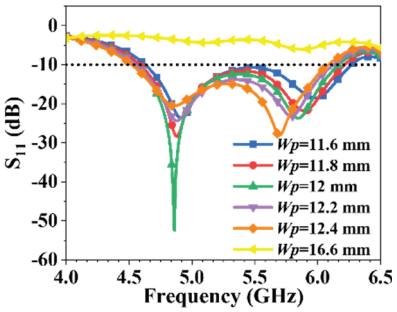

Fig. 4. The effect of W_p on S_{11}.

bandwidth among all cases. As shown in Fig. 6, the antenna exhibits the optimal impedance matching at $g =$ 0.2 mm, with S_{11} below -10 dB over 4.54–6.17 GHz. Therefore, $P = 7.6$ mm and $g = 0.2$ mm are determined.

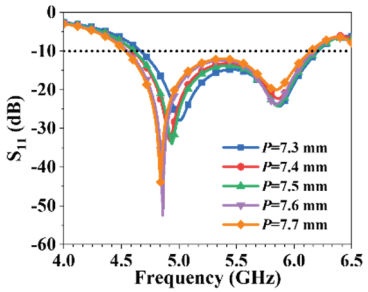

Fig. 5. Effect of P on S_{11}.

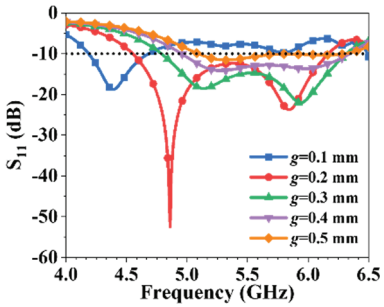

Fig. 6. Effect of g on S_{11}.

C. Decoupling enhancement adopting slots with via holes

Based on Ant.2, geometry of the radiation patch is designed for decoupling as shown in Fig. 7. For Ant.3, two independent slots lading with via holes are etched in the patch. As shown in Fig. 8, compared with Ant.2, the S_{12} of Ant.3 decreases in 5.3–5.85 GHz. However, it remains higher than -20 dB in 4.8–5.5 GHz. With the addition of shorted slots, the coupling is further reduced. Ant.4, which incorporates 3 slots, exhibits a 1.6 dB lower coupling than Ant.3 in 5.45–5.5 GHz. Nevertheless, its coupling is still above -20 dB in 4.9–5.45 GHz. Ant.5, which is configured with a 3×3 array of independent slots, exhibits further reduced coupling. However, its S_{12} remains slightly higher than -20 dB in 5–5.25 GHz.

The proposed antenna is modified from Ant.5. Metal segments 1 and 2, located below the patch's diagonal, are connected. The rectangular ring slot is extended accordingly. For this antenna, the port isolation $|S_{12}|$ is below -20 dB over 4.3–5.61 GHz.

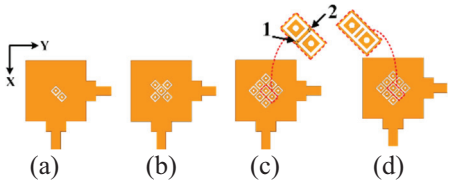

Fig. 7. Decoupling geometries of the radiation patch (a) Ant.3, (b) Ant.4, (c) Ant.5, (d) Proposed.

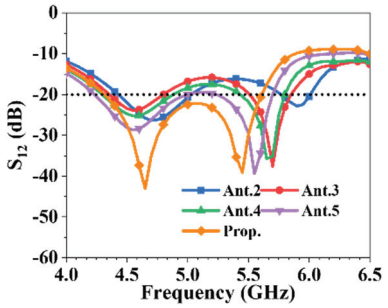

Fig. 8. Isolation of Ant.2-5 and prop. antenna.

Figure 9 illustrates the effect of the distance between vias (d_2) on S_{11}. $d_2 = 1.7$ mm provides the minimum S_{11} and optimal impedance matching and is thus adopted.

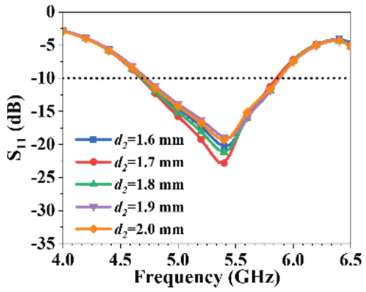

Fig. 9. The effect of d_2 on S_{11}.

Figure 10 illustrates the variation of the antenna's port isolation with the slot extension length (L_3). When $L_3 = 0$ mm, the nine square slots are in an independent state, with one via hole loaded on each slot. In this case, S_{12} is slightly higher than -20 dB over 5–5.25 GHz.

When $L_3 = 0.1$ mm, there is no significant improvement in the S_{12}, and the S_{12} is basically the same as that when $L_3 = 0$ mm. However, when $L_3 = 0.2$ mm, the S_{12} is significantly improved. S_{12} falls below -20 dB in 4.3–5.61 GHz. Nevertheless, the bandwidth of this band is slightly reduced compared with that when $L_3 = 0$ mm.

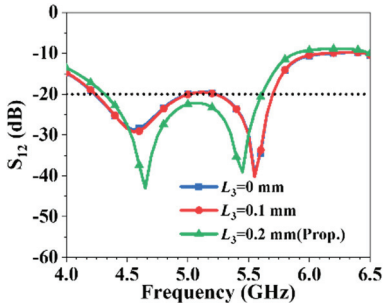

Fig. 10. The effect of L_3 on S_{12}.

D. Fabrication and measurement of the proposed antenna element

To verify its performance, the proposed antenna was fabricated and measured. Figure 11 presents a photograph of the fabricated antenna. The measured S_{11}, S_{12}, and realized gain of the antenna are shown in Fig. 12. For LP states, the overlapping impedance bandwidth of the antenna ranges 4.875–5.745 GHz, while its isolation bandwidth (with $S_{12} < -20$ dB) spans 4.4–6.1 GHz, and the realized gain of 4–6.2 dBi is achieved within this impedance bandwidth.

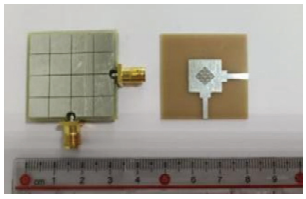

Fig. 11. Top layer and bottom layer of the fabricated antenna.

Radiation patterns in Figs. 13–14 show the measured and simulated results of the antenna under X-axis linear polarizations (X-LP) and Y-axis linear polarizations (Y-LP) at 5.1 GHz and 5.45 GHz in YOZ plane, with cross-polarization levels exceeding 15 dB in all cases.

III. ANTENNA ARRAY DESIGN AND MEASUREMENT

A. Antenna array design

A 1×4 antenna array was designed as shown in Fig. 15. The distance (dx) between two adjacent elements center is 40 mm. There is an 8 mm gap between adjacent antenna elements.

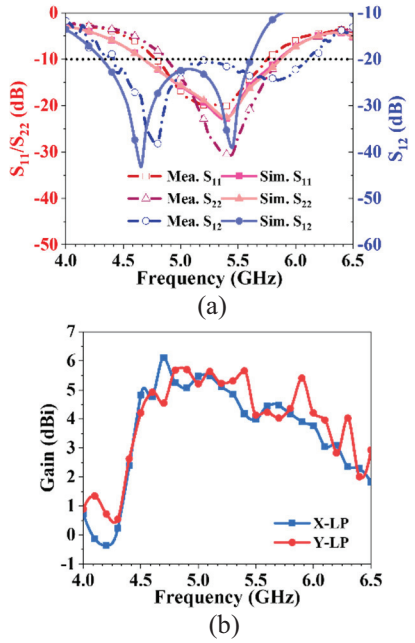

Fig. 12. Measured (a) S-parameters and (b) gain of the proposed antenna.

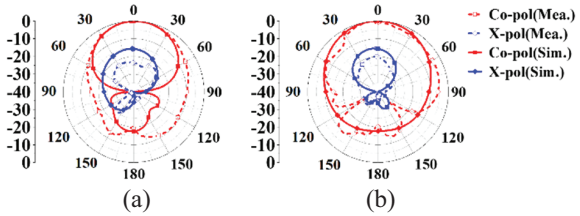

Fig. 13. Radiation pattern at 5.1 GHz in YOZ plane (a) X-LP and (b) Y-LP.

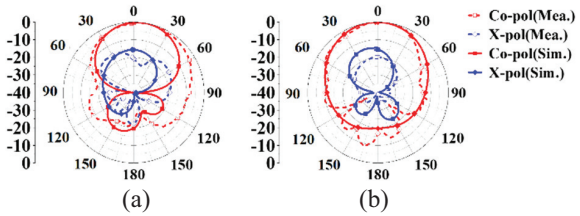

Fig. 14. Radiation pattern at 5.45 GHz in YOZ plane (a) X-LP and (b) Y-LP.

The dx affects the isolation between adjacent ports. Since the isolation between adjacent ports is highly similar, only S_{13} is presented in Fig. 16 (a). It can be observed that S_{13} improves as dx increases. At $dx =$ 40 mm, S_{13} is below -20 dB in the range of 4.65–5.64 GHz. Considering structural compactness, the dx is finally set to 40 mm. Figure 16 (b) illustrates that the isolation between two ports of one element and those of two adjacent elements is below -20 dB when $dx =$ 40 mm.

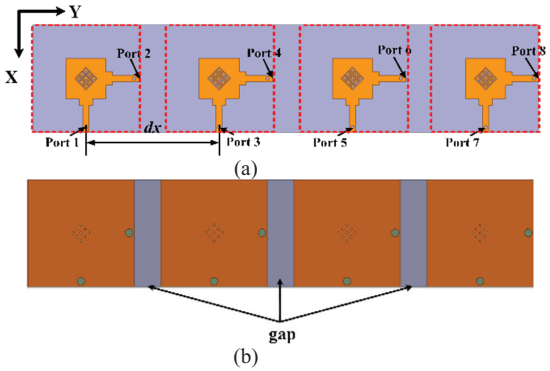

Fig. 15. Configuration of the proposed antenna array (a) top layer and (b) bottom layer.

The port reflection coefficients deteriorate when four elements form the antenna array. As illustrated in Fig. 17 (a), the reflection coefficients S_{44}, S_{55}, and S_{66} exceed -10 dB within the frequency range of 5.1–5.25 GHz. By introducing gaps into the antenna ground plane, the reflection coefficients (S_{ii}) of all ports are reduced to below -10 dB, as depicted in Fig. 17 (b).

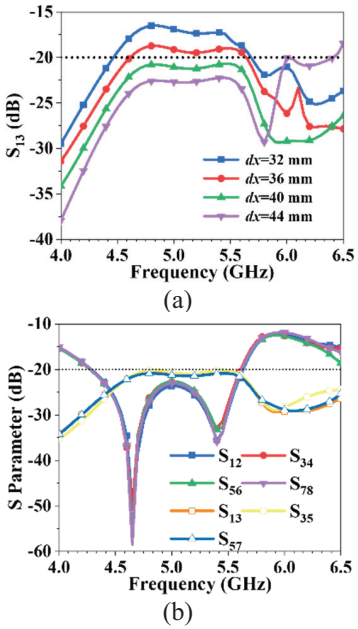

Fig. 16. Isolation between ports (a) the effect of dx and (b) $dx = 40$ mm.

B. Fabrication and measurement of the antenna array

To verify the feasibility of the proposed antenna, the antenna prototype was fabricated and measured. To enable simultaneous excitation of the array antenna's horizontal/vertical ports, the antenna ports were connected via a 1-to-4 power divider, as shown in Fig. 18.

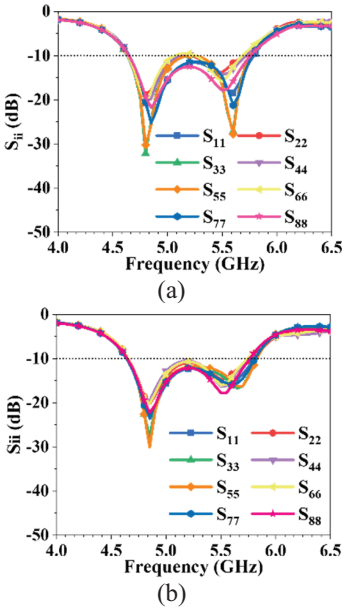

Fig. 17. The effect of antenna ground connectivity on S_{ii} (a) without gap and (b) with gap.

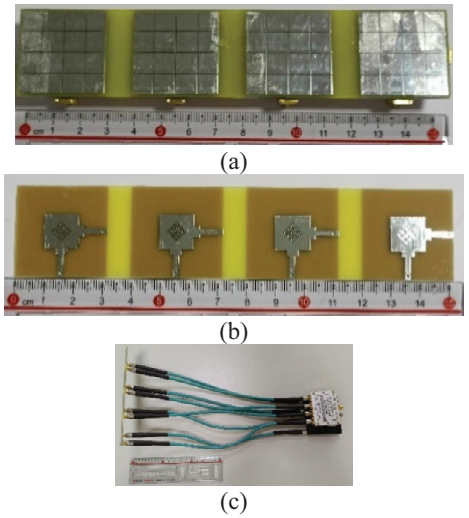

Fig. 18. Photographs of the array antenna prototype (a) top layer, (b) bottom layer, and (c) power divider.

The measured impedance bandwidth, isolation, gain, and efficiency of the antenna are shown in Fig. 19. For LP states, the overlapping impedance bandwidth ranges 4.975–5.925 GHz. The isolation bandwidth (with $S_{12} < -20$ dB) spans 4.3–6 GHz, the peak realized gain within this impedance bandwidth reaches 12.5 dBi, and the efficiency can reach 75.4%.

The radiation patterns in Figs. 20–22 show the measured and simulated results for X-LP and Y-LP at 5, 5.4, and 5.9 GHz in XOZ plane.

A comparison of the proposed antenna with existing designs is provided in Table 1. Compared with

Table 1: Comparison of the published dual-polarized antennas

Ref.	AS	Size (λ_0^3)	Air Gap	Peak Gain (dBi)	Iso (dB)	BW (%)	Efficiency
[23]	1×3	0.51×1.92×0.08	With	11.5	17	20.3	85%
[13]	Unit	1.11×1.11×0.11	With	9.0	47	32.9	NA
[12]	Unit	1.3×1.3×0.13	With	9.1	28	25.1	NA
[22]	4×6	2.46×6.77×0.26	With	19.4	20	14.1	NA
[6]	2×1×2	1.26×1.26×0.315	With	5.9	22	17.1	91.7%
[19]	1×2	0.8×0.4×0.006	WO	NA	19	0.86	NA
[18]	2×2	0.6×0.6×0.04	WO	6.2	27	5.2	80%
[4]	2×2	3.05×2.02×0.14	WO	13	14	25.2	NA
[7]	Unit	1.15×1.15×0.28	WO	9.2	25	50.4	90%
This Work	1×4	2.7×0.58×0.042	WO	12.5	20	17.4	75.4%

NA: Not applicable; WO: Without; Iso: Isolation; BW: Bandwidth; AS: Array scale.

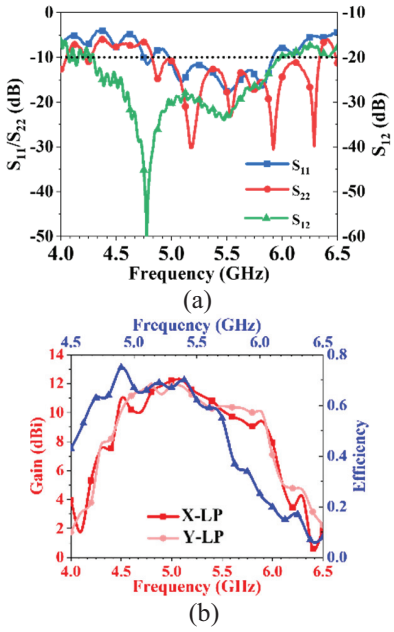

Fig. 19. Measured (a) S-parameters and (b) gain of the proposed antenna.

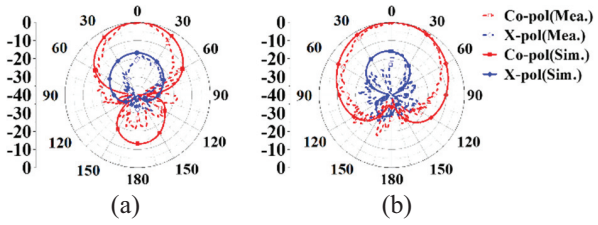

Fig. 20. Radiation pattern at 5 GHz in XOZ plane (a) X-LP and (b) Y-LP.

antennas that have an air gap in [6, 12, 13, 22, 23], the proposed antenna features a low profile, compact structure, and ease of fabrication. Compared with air-gap-free antennas in [18, 19], the proposed antenna

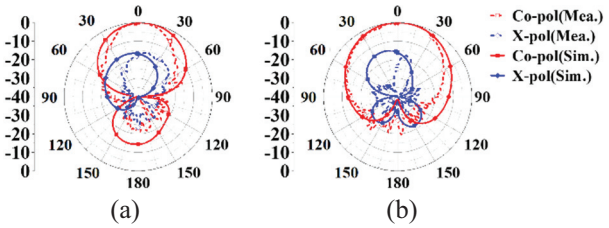

Fig. 21. Radiation pattern at 5.4 GHz in XOZ plane (a) X-LP and (b) Y-LP.

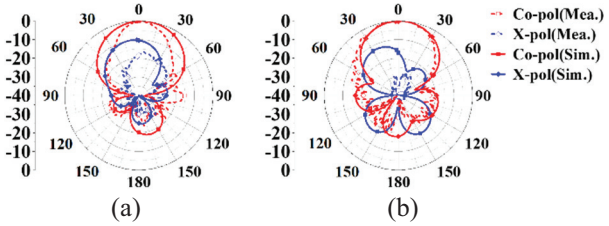

Fig. 22. Radiation pattern at 5.9 GHz in XOZ plane (a) X-LP and (b) Y-LP.

exhibits a slightly higher profile but a significantly wider bandwidth. Moreover, its profile is much lower than that in [4, 7]. Its realized gain reaches 12.5 dBi, higher than that of the antennas in [6, 7, 12, 13, 18, 19, 23]. Overall, the proposed antenna demonstrates superior performance in isolation, structural compactness, and operating bandwidth.

IV. CONCLUSION

In this paper, a dual-polarized antenna with low profile and high isolation is proposed. The polarization state of the antenna can be switched by selecting different feeding ports. The measurement results indicate that the antenna has a −10 dB impedance bandwidth of 4.975–5.925 GHz in different states, with a relative bandwidth of 17.4%. Arranging the antenna elements

into a 1×4 array effectively improves the antenna gain. The peak gain of the array antenna reaches 12.5 dBi. The simulated and measured results are in good agreement, verifying the correctness of the design. Additionally, the proposed dual-polarized antenna benefits from low profile, compact size, low cost, and high isolation. It is suitable for various communication systems with space constraints, intelligent requirements, and anti-interference needs.

REFERENCES

[1] J. Li, S.-J. Hao, Y.-G. Cui, and X. Chen, "A miniaturized wideband dual-polarized planar antenna based on multi resonance," *IEEE Antennas and Wireless Propagation Letters*, vol. 21, no. 2, pp. 242–246, Feb. 2022.

[2] J.-Y. Yang, X.-H. Ding, W.-W. Yang, and J.-X. Chen, "Compact wideband dual-polarized antenna using shared dipoles loaded with partially coupled stubs," *IEEE Antennas and Wireless Propagation Letters*, vol. 22, no. 12, pp. 2886–2890, Dec. 2023.

[3] Y. Zhang and Y. Zhang, "Dual-band dual-polarized antenna using a simple radiation restoration and decoupling structure," *IEEE Antennas and Wireless Propagation Letters*, vol. 22, no. 4, pp. 709–713, Apr. 2023.

[4] H. C. Ye, C. Mao, L. L. Dai, and X. Y. Zhang, "Dual-band dual-polarized antenna and array with enhanced bandwidth for 5G millimeter-wave applications," *IEEE Antennas and Wireless Propagation Letters*, vol. 24, no. 7, pp. 1829–1833, July 2025.

[5] R. Wu, C.-R. Li, and F.-C. Chen, "Tri-band dual-polarized shared-aperture antenna array for base station applications," *IEEE Antennas and Wireless Propagation Letters*, vol. 24, no. 9, pp. 3213–3217, Sep. 2025.

[6] H. Yuan and F.-C. Chen, "A mixed decoupling scheme based on AMC and ADS for dual-polarized antenna array," *IEEE Transactions on Antennas and Propagation*, vol. 71, no. 7, pp. 6150–6155, July 2023.

[7] J. Qi, J. Pan, Y. Li, and G.-L. Huang, "A wideband base station antenna loaded with bow-tie-like parasitic elements," *Applied Computational Electromagnetics Society (ACES) Journal*, vol. 37, no. 08, pp. 893–900, Aug. 2022.

[8] B. P. Smyth and A. K. Iyer, "Low-profile uniplanar dual-band and dual-polarized microstrip patch antenna using embedded MTM-EBGs," *IEEE Transactions on Antennas and Propagation*, vol. 69, no. 7, pp. 3645–3653, July 2021.

[9] C. Zhou, J. Sun, W.-W. Yang, M. Li, and H. Wong, "A wideband low-profile dual-polarized hybrid antenna using two different modes," *IEEE Antennas and Wireless Propagation Letters,* vol. 22, no. 1, pp. 114–118, Jan. 2023.

[10] J. Liu, H. Liu, X. Dou, Y. Tang, C. Zhang, L. Wang, R. Tang, and Y. Yin, "A low profile, dual-band, dual-polarized patch antenna with antenna-filter functions and its application in MIMO systems," *IEEE Access*, vol. 9, pp. 101164–101171, 2021.

[11] X. Zhang, D. Zhou, Y. Li, K. Wei, and Z. Zhang, "A simple dual-polarized patch antenna array for Wi-Fi 6/6E application," *IEEE Transactions on Antennas and Propagation*, vol. 70, no. 11, pp. 11143–11148, Nov. 2022.

[12] M. Ciydem, "A low-profile dual-polarized antenna with high isolation and high front-to-back ratio for 5G base stations," *Applied Computational Electromagnetics Society (ACES) Journal*, vol. 36, no. 09, pp. 1229–1236, Nov. 2021.

[13] M. Ciydem and E. A. Miran, "A low-profile hybrid-fed dual-polarized antenna with high isolation and high cross-polar discrimination," *Applied Computational Electromagnetics Society (ACES) Journal*, vol. 36, no. 09, pp. 1164–1172, Nov. 2021.

[14] S. Aminu, N. Yan, Y. Luo, K. Ma, I. Bello, and E. N. Moro, "High isolation dual-polarized SISL antenna with out-of-band rejection improvement using artificial magnetic conductor," *IEEE Antennas and Wireless Propagation Letters*, vol. 23, no. 11, pp. 3882–3886, Nov. 2024.

[15] Y. Xu, R. Li, Z.-X. Liu, Y. Hu, C. Wang, and Y. Liu, "Dual-polarized crossed-dipole base station antenna array with high-isolation and wide-angle scanning," *IEEE Transactions on Antennas and Propagation*, vol. 72, no. 11, pp. 8394–8403, Nov. 2024.

[16] B. Qian, A. Zhang, X. Chen, and A. A. Kishk, "Ultralow-profile decoupling patch structure for E-plane microstrip antenna arrays," *IEEE Antennas and Wireless Propagation Letters*, vol. 24, no. 10, pp. 3799–3803, Oct. 2025.

[17] B. Chen, A. Zhang, and X. Chen, "Decoupling of planar circularly polarized patch array by ADS and parasitic structure," *IEEE Antennas and Wireless Propagation Letters*, vol. 24, no. 9, pp. 2979–2983, Sep. 2025.

[18] C. Guo, Y. Jia, Y. Wang, and H. Zhai, "A dual-polarized antenna array with high port isolation through TM03/04 modes cancellation," *IEEE Antennas and Wireless Propagation Letters*, vol. 22, no. 8, pp. 1987–1991, Aug. 2023.

[19] M. Li, T. Yang, X.-X. Yang, D. Zeng, and Z. Yi, "A defected ground structure for TE and TM coupling reduction of dual-polarized antenna array," *IEEE Antennas and Wireless Propagation Letters*, vol. 23, no. 9, pp. 2648–2652, Sep. 2024.

[20] Y. Wang, X. Wang, J. Wang, and R. Shao, "Dual-band highly isolated eight-element MIMO antenna for 5G mobile phone," *Applied Computational Electromagnetics Society (ACES) Journal*, vol. 37, no. 05, pp. 588-596, May 2022.

[21] T. Yoon, U. Park, and J. Oh, "Band-stop behavior vertically extended ground isolator based on transmission line theory for IBFD TRx decoupling applications," *IEEE Transactions on Microwave Theory and Techniques*, vol. 72, no. 2, pp. 1405–1415, Feb. 2024.

[22] F.-F. Fan, P.-P. Ma, and Q.-L. Chen, "Wide-angle scanning and high isolation dual-polarized base station antennas for sub-6 GHz applications," *Applied Computational Electromagnetics Society (ACES) Journal*, vol. 39, no. 02, pp. 149–155, Feb. 2024.

[23] T.-Y. Yan, X.-H. Ding, J.-Y. Yang, and J.-X. Chen, "A low-cost compact dual-polarized patch antenna array for 5G massive MIMO base station," *IEEE Antennas and Wireless Propagation Letters*, vol. 23, no. 4, pp. 1381–1385, Apr. 2024.

[24] Rachmansyah, A. Irianto, and A. Mutiara, "Designing and manufacturing microstrip antenna for wireless communication at 2.4 GHz," *International Journal of Computer and Electrical Engineering*, vol. 3, no. 5, Oct. 2011.

Yue-Chen Liu was born in Handan, Hebei, China, in 2000. She received the B.E. degree in Electronic Information Engineering from Xi'an University of Posts & Telecommunications, Xi'an, Shaanxi, in 2018. She is currently pursuing the M.E. degree in electronic science and technology in Qingdao University, Qingdao, Shandong. Her research interest is antennas.

Xiaoyun Qu was born in Yantai City, Shandong Province, China, in 1974. She received the B.S. in applied mathematics from Yantai University, in 1996, M.S. degree in electromagnetic fields and microwave technology from Nanjing Electronics research Center, Nanjing, Jiangsu Province, in 1990. She is with Shandong Institute of Space Electronic Technology, Yantai, as a Senior Engineer. Her research interest is antenna design.

Cheng Ju received the Ph.D. degree from Beijing University of Posts and Telecommunications in 2015. He joined the School of Electronic Information at Qingdao University in 2017 as a lecturer. He is mainly engaged in researching DSP algorithms for space laser communication systems and FPGA implementation of DSP algorithms.

Wei-Hua Zong was born in Penglai City, Shandong Province, China, in 1975. She received the B.S. in applied mathematics from Yantai University, in 1997, M.S. degree in electromagnetic fields and microwave technology from Nanjing Electronics research Center, Nanjing, Jiangsu Province, in 2000, and the Ph.D. degree in electromagnetic fields and microwave technology from Xidian University, Xian, Shanxi Province, in 2004. In 2004, she joined Qingdao University, Qingdao, Shandong Province, as a lecturer. Since 2005, she has been an Associate Professor in Qingdao University. From February to August 2010, she was a Visiting Scholar Assistant with Electrical and Computation Engineering Department, National University of Singapore. Her research interests include antenna design and electromagnetic material measurement.

A V-Band Magnetoelectric Dipole Filtering Antenna Based on Rectangular Micro-Coaxial Lines

Nan Wang[1], Ying Zhu[2], Jing Wang[3], Xinjiang Liu[3], Chaoyu Feng[4], Xinzhan Cai[1], Xiaolan Zhang[1], Xuefeng Zhao[1], Wensen Wang[1], Guang Dai[3], and Jiawei Yang[5]

[1]Power Research Institute of State Grid Shaanxi Electric Power Corporation Limited
Xi'an 710100, China
18066661276@163.com, 969079361@qq.com, 18629051767@163.com,
78345659@qq.com, wangwensen@yeah.net

[2]School of Information and Communications Engineering
Xi'an Jiaotong University, Xi'an 710049, China
itszhuying@stu.xjtu.edu.cn

[3]State Grid Shaanxi Electric Power Corporation Limited
Xi'an 710048, China
44974545@qq.com, 670058424@qq.com, guang.gdai@gmail.com

[4]State Grid Shaanxi Electric Power Co. Ltd. Ultra High Voltage Company
Xi'an 710000, China
402266878@qq.com

[5]State Grid Shaanxi Electric Power Co. Ltd. Information and Communication Company
Xi'an 710000, China
792639824@qq.com

Abstract – A high-selectivity filtering magnetoelectric (ME) dipole antenna based on rectangular micro-coaxial lines (RMCLs) is presented, fabricated using micro-metal additive manufacturing (M-MAM) for V-band operation. The structure integrates two $\lambda/4$ resonators, one $\lambda/2$ resonator, and an ME dipole antenna, coupled through J/K-inverters realized as RMCL gaps and short-circuited stubs. Notably, while a standalone ME dipole inherently supports an impedance bandwidth over 30%, this design achieves a 5.04% operating bandwidth centered at 59.5 GHz after integrating filtering functionality. Simulations confirm a peak gain of 4.53 dBi within the passband, with cross-polarization consistently below -20 dB. A sharp gain roll-off to -10 dBi at $1.048f_0$ and 40 dB out-of-band suppression demonstrates exceptional frequency selectivity. Owing to inherent miniaturization, lightweight construction, and low-loss characteristics, the antenna exhibits significant potential for low-earth-orbit (LEO) satellite internet systems.

Index Terms – Filter antenna, low-earth-orbit (LEO) satellite, magnetoelectric (ME) dipole antenna, V-band.

I. INTRODUCTION

The Q/V frequency band (40–75 GHz) encompasses dual sub-bands, namely the Q-band (40–50 GHz) and V-band (50–75 GHz), belonging to the millimeter-wave extremely high frequency (EHF) spectrum regime. Its ultra-wide bandwidth, high directivity, and low interference characteristics render it a crucial spectral resource for high-speed satellite communications, low-earth-orbit (LEO) internet access, and scientific research missions [1–3]. Corresponding radio frequency components must satisfy stringent requirements for ultra-miniaturization, ultra-low loss, and multifunctional integration. Filtering antennas with integrated filtering-radiating capabilities have emerged as a promising approach to address these challenges [4, 5].

Conventional filtering antenna implementations typically follow three approaches: (1) cascading antennas as terminal resonators with filter structures [6–8], (2) embedding band-rejection elements within feed networks to create transmission zeros [9], or (3) loading parasitic structures to modify radiation characteristics [10]. However, fabrication constraints

Submitted On: July 06, 2025
Accepted On: September 10, 2025

https://doi.org/10.13052/2026.ACES.J.410208

at millimeter-wave frequencies often preclude direct application of these techniques. Recent studies have proposed solutions based on substrate integrated waveguide (SIW) [11], gap-waveguide (GWG) [12], frequency selective surfaces (FSS) [13, 14], and differential feeding networks [15]. Nevertheless, challenges persist, such as high integration complexity or excessive loss.

Notably, micro-metal additive manufacturing (M-MAM) technology, utilizing sequential thick-photoresist lithography and copper electroforming processes [16–18], enables the monolithic fabrication of multi-layer metallic structures without assembly. The rectangular micro-coaxial line (RMCL) structure developed based on this technology has been successfully applied in millimeter-wave antenna designs owing to its low transmission loss characteristics [19–22]. However, the integration of filtering functionality within this structure remains an unresolved challenge.

This work proposes a novel filtering magneto-electric (ME) dipole antenna implemented in RMCL technology. The design offers three key innovations: (1) a modular architecture permitting independent optimization of filtering and radiating sections before integration, (2) implementation of $\lambda/4$ resonators with short-circuited stubs connecting the feed and radiator, reducing dielectric support requirements and minimizing insertion loss, and (3) angular orientation of the dipole patches toward the ground plane to enhance front-to-back ratio (FBR) without increasing footprint. The prototype demonstrates 5.04% impedance bandwidth centered at 59.5 GHz, exceeding 40 dB out-of-band rejection, and stable cross-polarization below -20 dB.

II. FILTERING ANTENNA GEOMETRY AND ANALYSIS

A. Antenna geometry

The proposed filtering antenna is constructed using RMCLs based on M-MAM technology, with its monolithic 3D integration achieved through nine stacked copper layers. Figure 1 illustrates the RMCL fabrication schematic, wherein SU-8 support strips ($\varepsilon_r = 4.2$, $\tan\delta = 0.045$) mechanically suspend the inner conductor to prevent inter-conductor short circuits. Release holes perforating the outer conductor walls facilitate post-processing removal of residual photoresist [18]. The characteristic impedance of the RMCL structure is determined by the inner conductor width w_i and the conductor-to-outer-wall gap dimension w_g, with optimized values of $w_i = 0.32$ mm and $w_g = 0.32$ mm achieving 50 Ω impedance matching.

Figure 2 presents the three-dimensional topology of the integrated filtering antenna system, synergistically combining a hybrid resonator filter section with an ME dipole radiating element. The filtering compartment integrates two $\lambda/4$ resonators and a single $\lambda/2$ resonator interconnected through capacitive gap coupling, while employing short-circuited stubs for input/output port connections. The radiating element comprises vertical arms, a ground plane, and angularly oriented planar patches, where feeding is accomplished through a tapered trapezoidal transition structure with a probe pin directly coupled to an inclined patch to establish electric dipole excitation. Electromagnetically, co-directional surface currents on the inclined patches constitute the equivalent electric dipole, while the vertical arms in conjunction with the ground plane form $\lambda/4$ short-circuited patch structures generating complementary magnetic dipole radiation. By leveraging the modular design pattern inherent in RMCL technology and maintaining the dimensional consistency of the inner/outer conductors at the filter ports and antenna feed interfaces, independent optimization and seamless integration of the two functional modules are achieved. The optimized structural parameters are detailed in Table 1.

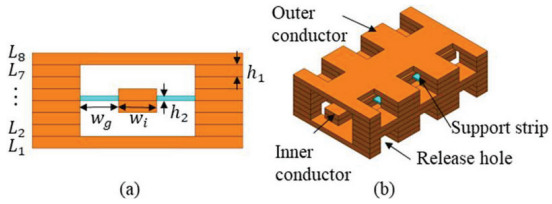

Fig. 1. RMCL based on M-MAM. (a) Main view. (b) Side view. Main critical dimensions: $h_1 = 100$ and $h_2 = 40$ (unit: μm).

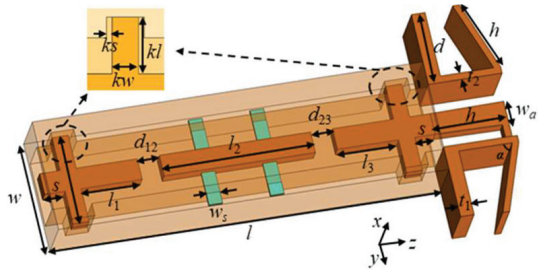

Fig. 2. Geometry of the proposed filtering antenna.

Table 1: Design parameters of the proposed filtering antenna (unit: mm)

Para.	w	w_s	w_a	ks	kw	kl
Value	1.66	0.20	0.35	0.05	0.236	0.507
Para.	l	l_1	l_2	l_3	d_{12}	d_{23}
Value	5.71	0.89	2.21	0.89	0.321	0.321
Para.	s	d	h	t_1	t_2	α
Value	0.30	1.08	1.08	0.20	0.10	70°

B. Filter design

Conventional capacitive-gap coupled filters typically require each resonator to exhibit a physical length of approximately $\lambda/2$ at the center frequency f_0, with inter-resonator coupling achieved through adjacent open-end gaps. This coupling mechanism can be equivalently modeled as a J-inverter network [23]. However, such architectures inherently suffer from excessive longitudinal dimensions and substantial dielectric support requirements, significantly degrading insertion loss performance. To mitigate these limitations, this work innovatively introduces $\lambda/4$ resonators combined with K-inverters at the input/output ports, achieving over 40% reduction in overall filter dimensions while minimizing support structures to enhance transmission efficiency. The topological configuration of the proposed hybrid resonator filter is illustrated in Fig. 3.

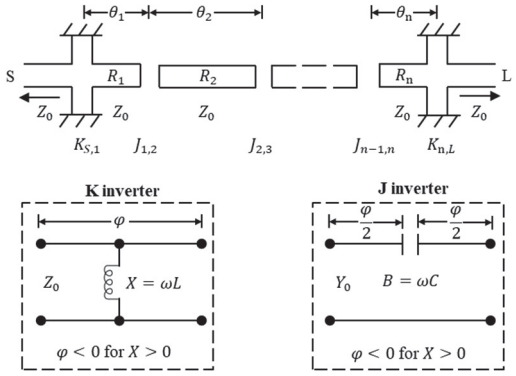

Fig. 3. Illustration of a hybrid resonator filter structure with J/K-inverters.

Within the electromagnetic model of this filter, the electrical length of each resonator is determined by the following equation:

$$\lambda/4\text{: } \theta_j = \frac{\pi}{2} + \frac{1}{2}(\varphi_{j-1,j} + \varphi_{j,j+1}), \tag{1}$$

$$\lambda/2\text{: } \theta_j = \pi + \frac{1}{2}(\varphi_{j-1,j} + \varphi_{j,j+1}), \tag{2}$$

where φ represents the phase contribution from adjacent coupling elements.

The physical length l is then derived as:

$$l_j = \frac{\theta_j \lambda_0}{2\pi}, \tag{3}$$

where λ_0 is the wavelength at f_0.

For a 3rd-order filter centered at 60 GHz with 3.33% fractional bandwidth (FBW) and 20 dB return loss (RL), the Chebyshev low-pass prototype values [23] are given as:

$$g_0 = 1.00, \quad g_1 = 1.0315, \quad g_2 = 1.1474,$$
$$g_3 = 1.0315, \quad g_4 = 1.00.$$

Theoretical calculations determine the initial resonator lengths as:

$$l_1 = 1.1051 \text{ mm}, \quad l_2 = 2.4617 \text{ mm}, \quad l_3 = 1.1051 \text{ mm}.$$

Corresponding J/K-inverter equivalent circuit parameters are:

$$L_{S,1} = L_{3,L} = 0.217 \text{ nH},$$
$$C_{1,2} = C_{2,3} = 1.2774 \times 10^{-3} \text{ pF}.$$

Leveraging the RMCL structure shown in Fig. 1, parameterized physical models of the J/K-inverters are established. Figure 4 demonstrates that the extracted J-inverter's equivalent capacitance C exhibits a monotonic decrease with increasing gap distance d. Analysis of the K-inverter model in Fig. 5 reveals that the equivalent inductance L increases with stub length kl while decreasing with width kw. These parametric relationships provide theoretical foundations for determining initial J/K-inverter dimensions.

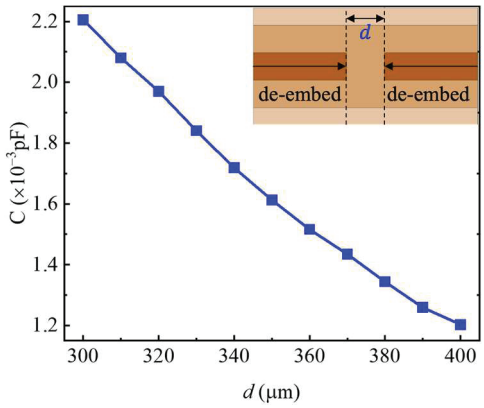

Fig. 4. The value of C with different gaps d (including J-inverter).

Using these models, a 3D electromagnetic model of the hybrid resonator filter is constructed in CST Microwave Studio. Following parametric optimization, the final design exhibits excellent agreement between full-wave simulation results (Fig. 6) and ideal Chebyshev responses, validating the theoretical approach. Key optimized dimensional parameters are comprehensively tabulated in Table 1.

C. ME dipole antenna design

The evolutionary process of the ME dipole antenna design is depicted in Fig. 7. Antenna I (Ant. I) constitutes the baseline ME dipole configuration featuring a conventional Γ-shaped feed and planar patches. Inspired by [24], structural modifications yield Antenna II (Ant. II): a bent probe pin directly coupled to the planar

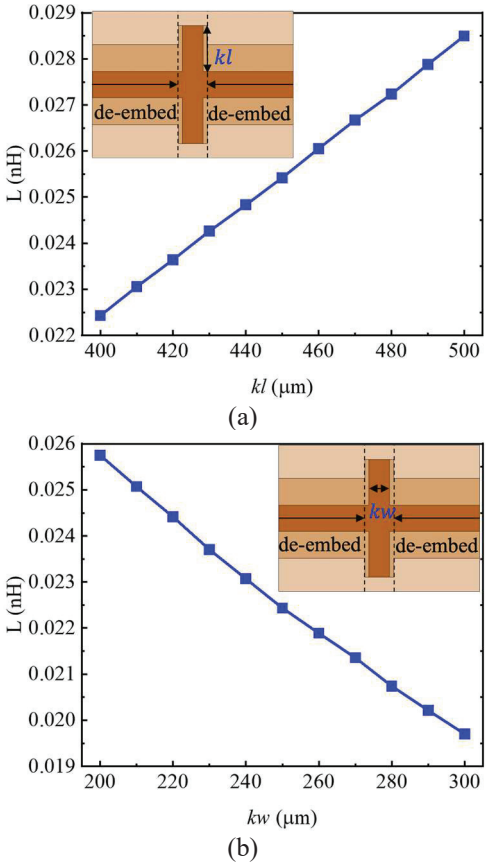

Fig. 5. The value of L with different (a) length kl and (b) width kw (including K-inverter).

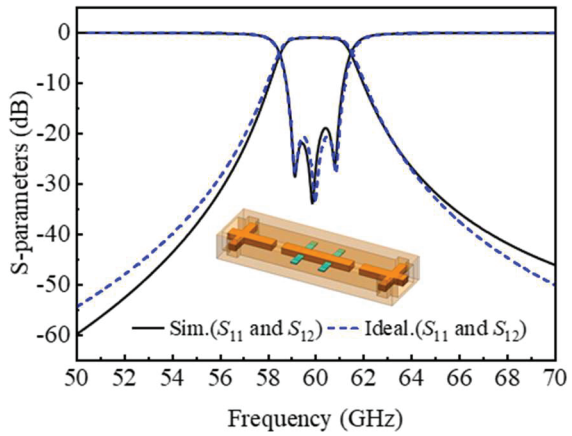

Fig. 6. Full-wave response of the designed filter (solid lines). The ideal Chebyshev characteristic (dashed lines) is reported for comparison.

patches provides integrated excitation, while the inner conductor is reconfigured into a tapered trapezoidal topology. The final proposed radiator structure is realized through the angular orientation (α) of the planar patches toward the ground plane.

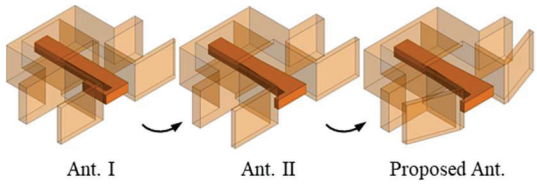

Fig. 7. Design process of the proposed ME dipole antenna.

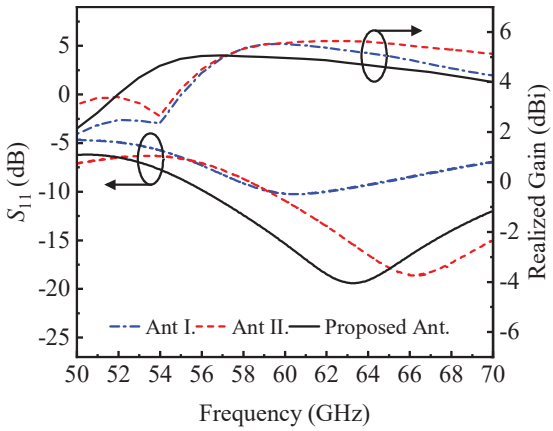

Fig. 8. Simulated S_{11} and realized gains of Ant I, Ant II, and the proposed Ant.

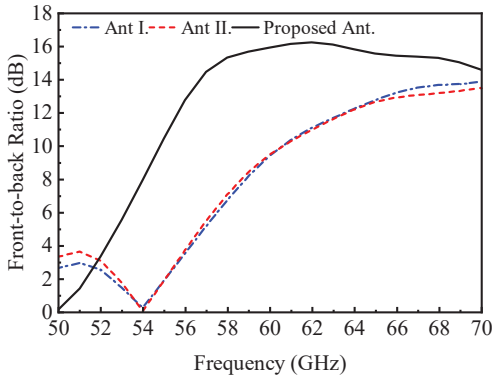

Fig. 9. Simulated front-to-back ratio of Ant I, Ant II, and the proposed Ant.

Figures 8 and 9 present the simulated S_{11} and FBR for Ant I, Ant II, and the proposed antenna. Analysis indicates that while Ant I exhibits resonance at 60 GHz, but it suffers from severe impedance mismatch. The bent probe implementation in Ant II shifts the resonant frequency upward and achieves gain enhancement relative to Ant I, with the tapered transition, simultaneously improve impedance matching. However, both configurations demonstrate unsatisfactory FBR below 15 dB. The angular orientation technique proposed herein successfully elevates FBR to 16 dB while achieving a broad impedance bandwidth spanning 55–75 GHz ($|S_{11}| < -10$ dB) under the optimized parameters in Table 1.

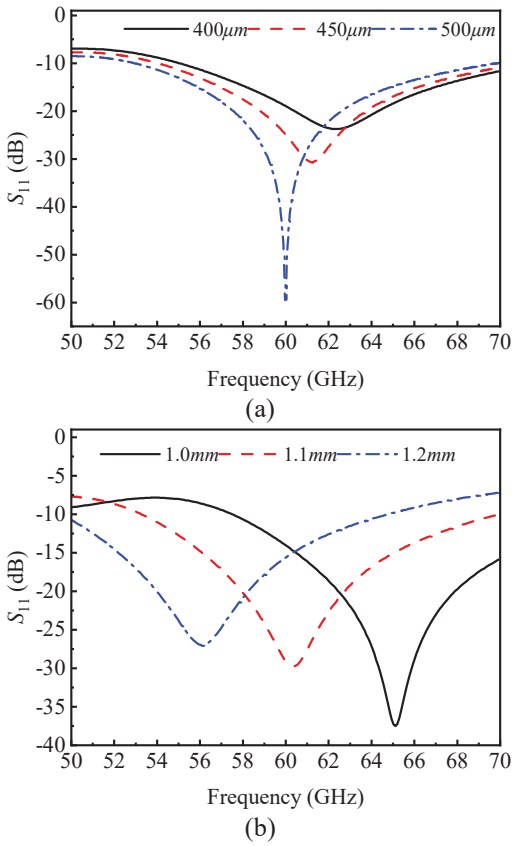

Fig. 10. Simulated S_{11} of the proposed ME dipole antenna with different values of (a) w_a and (b) h.

To elucidate the underlying electromagnetic mechanisms, Fig. 10 investigates the influence of critical parameters w_a and h on S_{11} characteristics. Increasing w_a primarily reduces resonant frequency while optimizing impedance matching, whereas parameter h predominantly modulates resonant frequency with negligible impact on matching. Current and electric field distributions in Fig. 11 reveal the physical origins: variation in h alters the resonant frequency by extending the effective current path length across the patch surface, while w_a induces frequency-shifting effects through reduced vertical arm spacing during matching optimization.

Figure 12 further quantifies the effect of the tilt angle α on the radiation characteristics. It can be observed that the greater the inclination, which means the smaller α, the FBR of the antenna increases. The backward radiation is suppressed to some extent with an unchanged ground floor, but this is accompanied by a sacrifice in gain.

D. Filtering antenna integration

Owing to dimensional consistency between inner and outer conductors in the RMCL utilized for both filter and antenna structures, direct interconnection enables system-level integration of the filtering antenna. Figure 13 presents comparative simulated S_{11} and realized gain characteristics for the ME dipole antenna configurations with and without integrated filtering functionality. The proposed filtering antenna satisfies $|S_{11}| < -10$ dB impedance matching across 58–61 GHz. Although the incorporated filter structure introduces insertion loss, it significantly enhances frequency selectivity. The realized gain peaks at 4.53 dBi, while exhibiting a sharp roll-off to -10 dBi at 62.4 GHz ($1.048f_0$), demonstrating a characteristic bandpass response.

Figure 14 quantifies radiation patterns of the proposed filtering antenna and ME antenna at operating frequencies of 59 GHz and 60 GHz. The filtering antenna exhibits little change in the H-plane

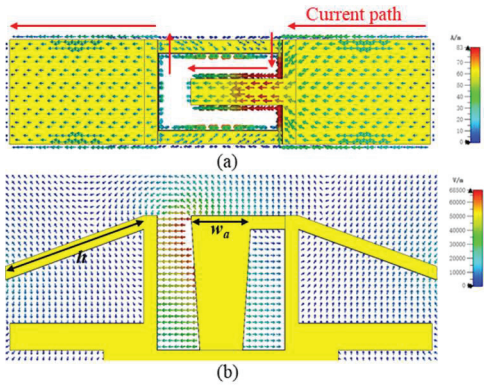

Fig. 11. (a) Simulated current distribution on planar patches. (b) Simulated electric field distribution on the xoy plane.

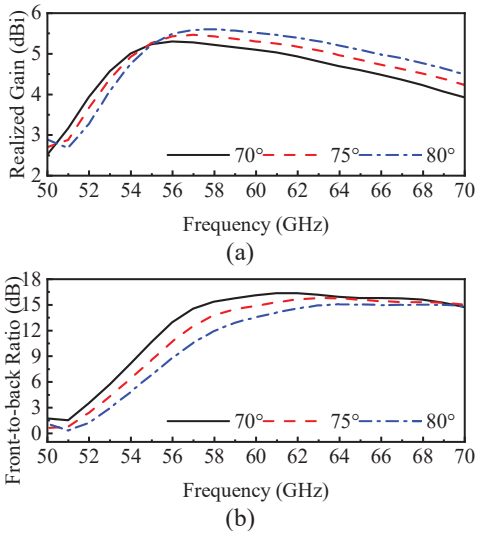

Fig. 12. Simulated realized gain and front-to-back ratio of the proposed ME dipole antenna with different values of α.

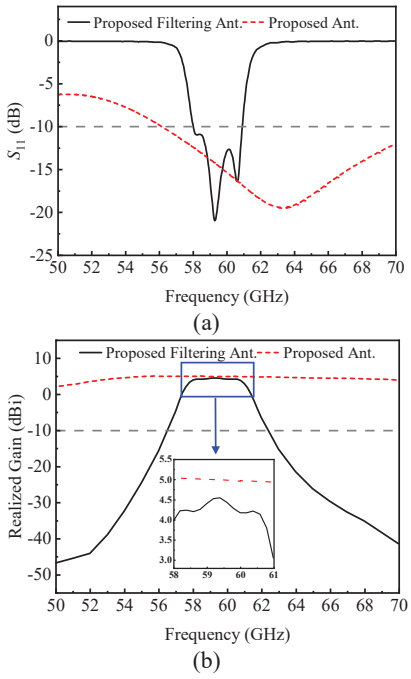

Fig. 13. (a) Simulated S_{11} and (b) realized gain of the proposed antenna and the proposed filtering antenna.

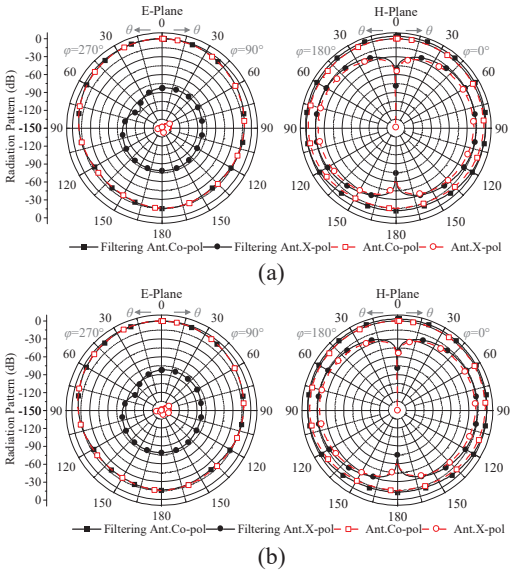

Fig. 14. Comparison of simulation radiation patterns between the proposed filter antenna and the independent ME antenna: (a) E-plane and H-plane at 59 GHz. (b) E-plane and H-plane at 60 GHz.

pattern compared to the ME antenna, but the cross-polarization in the E-plane has increased. Specifically, the proposed filtering antenna achieves cross-polarization suppression exceeding 78 dB in the E-plane, with a half-power beamwidth (HPBW) of 77°. The H-plane maintains cross-polarization levels below −20 dB with an extended HPBW of 170°, indicating quasi-omnidirectional coverage capability. Furthermore, optimized design achieves consistent FBR exceeding 15 dB, effectively suppressing back-lobe radiation.

III. MEASUREMENT AND COMPARISON

A. Measurement

Given the constraints imposed by available fabrication and testing facilities, this study focused on the physical realization and experimental validation only of the hybrid resonator filter based on the RMCL structure, as described in section IIB. Considering that mainstream millimeter-wave measurement systems rely on planar probing platforms, the fabricated filter incorporates a broadband transition structure at its ports. This structure provides an optimized connection from the RMCL to Ground-Signal-Ground (GSG) probe pads [25], specifically designed for millimeter-wave on-wafer probing. A photograph of the final packaged device is depicted in the inset of Fig. 15.

As shown in Fig. 15, the measured results exhibit a center frequency shift of 0.7% compared to simulations, with $f_0 = 60.42$ GHz (vs. simulated 60 GHz), FBW reduction to 2.5% (vs. 3.3%), IL degradation to 2.44 dB (vs. 1.05 dB), and RL >10 dB (vs. >20 dB).

A Monte Carlo sampling (MCS) sensitivity analysis was conducted on 13 primary dimensional parameters (Fig. 16) with manufacturing tolerance limits of ± 5 μm (the typical tolerance of the M-MAM technology [26]). Two hundred uniformly distributed random samples were simulated, excluding transition interfaces. The observed deviations between measured and simulated results are attributed to these factors: (1) critical dimension deviations exceeding ± 5 μm tolerance;

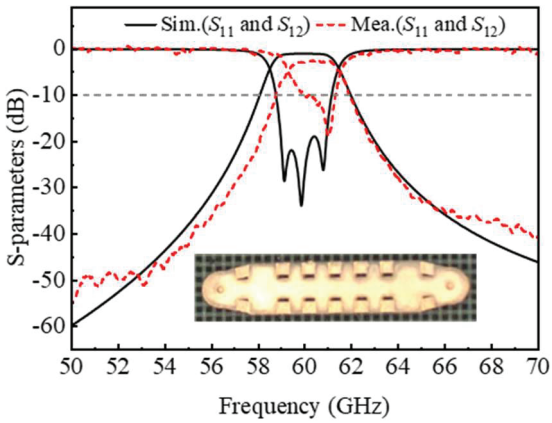

Fig. 15. The simulated and measured results of the proposed filter, accompanied by the fabricated prototype (inset).

Table 2: Comparison with the previous filtering antennas

Ref.	Impedance Bandwidth (GHz)	Peak Gain (dBi)	Stopband Suppression Level (dB)	F_L/F_U^a (%/%)	Profile (mm/λ_0)
[27][b]	5.00–5.42 (8.0%)	3.06	∼27	∼4.2 / ∼3.8	0.288 / 0.005
[28][c]	33.7–36.3 (7.40%)	7.10	∼13	∼2.3 / ∼5.4	0.962 / 0.112
[29][b]	18.9–30.3 (46.3%)	6.00	∼25	∼8.9 / ∼6.9	3.937 / 0.323
[30][b]	24.0–28.6 (17.5%)	6.20	∼20	6.1 / 10.6	2.330 / 0.204
This Work[c]	58.0–61.0 (5.04%)	4.53	40	3.2 / 3.4	0.800 / 0.158

[a]Definition of frequency selectivity: $F_L = (f_{10L} - f_{\Delta 20L})/f_0$, $F_U = (f_{\Delta 20U} - f_{10U})/f_0$. f_{10L} and f_{10U} are the frequencies at the edges of the −10 dB impedance bandwidth. $f_{\Delta 20L}$ and $f_{\Delta 20U}$ are the frequencies with suppression more than 20 dB.
[b]All dates provided by this line are measurement dates.
[c] All dates provided by this line are simulation dates.

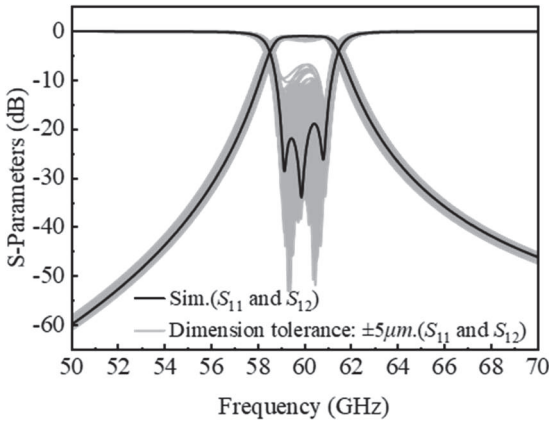

Fig. 16. Sensitivity analysis of the proposed filter.

(2) unremoved dielectric material at K-inverter corners; (3) probe contact error and system calibration drift.

B. Comparison

As shown in Table 2, the filter antenna proposed in this paper has significant performance characteristics compared to the existing typical designs. Compared with the 3.06 dBi gain level reported in [27], the present work achieves a gain enhancement of 4.53 dBi. Although the cascaded magneto-electric dipole and hybrid resonator configuration yields lower gain than the 6.0–7.1 dBi range in [28–30], our design demonstrates three significant advancements at the demanding 59.5 GHz millimeter-wave frequency: (1) an ultra-compact vertical profile of only 0.158λ0, (2) superior out-of-band suppression exceeding 40 dB, and (3) sharp frequency selectivity of 3.2/3.4%.

IV. CONCLUSION

This paper presents an innovative design of a V-band filter antenna based on RMCL, which centers on the realization of a modular split design and easy integration of a hybrid resonator filter structure and an ME dipole antenna. The antenna exhibits an impedance bandwidth of 5.04% at the center frequency of 59.5 GHz and maintains a cross-polarization level below −20 dB. The overall size of the antenna structure is optimized to $6.79 \times 3.19 \times 0.8$ mm (including the ground plane), corresponding to a profile height of only 0.158λ0. In particular, the design exhibits excellent out-of-band suppression characteristics. Outside the frequency band of ±4.8% from the center frequency, rapid gain attenuation below −10 dBi is achieved. This feature significantly reduces the risk of adjacent channel interference in V-band antenna systems, providing an effective solution for high-density integrated RF front ends.

ACKNOWLEDGMENT

This work was supported by the project of State Grid Shaanxi Electric Power Corporation Limited (5226KY250015).

REFERENCES

[1] P. Smulders, “Exploiting the 60 GHz band for local wireless multimedia access: Prospects and future directions,” *IEEE Commun. Mag*., vol. 40, no. 1, pp. 140–147, Jan. 2002.

[2] T. S. Rappaport, S. Sun, R. Mayzus, H. Zhao, Y. Azar, K. Wang, G. N. Wong, J. K. Schulz, M. Samimi, and F. Gutierrez, “Millimeter wave mobile communications for 5G cellular: It will work!,” *IEEE Access*, vol. 1, pp. 335–349, 2013.

[3] D. Liu, B. Gaucher, U. Pfeiffer, and J. Grzyb, *Advanced Millimeterwave Technologies: Antennas, Packaging and Circuits*. Hoboken, NJ, USA: Wiley, 2009.

[4] F. Queudet, I. Pele, B. Froppier, Y. Mahe, and S. Toutain, “Integration of pass-band filters in patch antennas,” in *The 32nd European Microwave Conference*, pp. 685–688, 2002.

[5] Y.-F. Cao, Y. Zhang, and X.-Y. Zhang, "Filtering antennas: From innovative concepts to industrial applications," *Frontiers Inf. Technol. Electron. Eng.*, vol. 21, no. 1, pp. 116–127, Jan. 2020.

[6] Z. H. Jiang and D. H. Werner, "A compact, wideband circularly polarized co-designed filtering antenna and its application for wearable devices with low SAR," *IEEE Trans. Antennas Propag.*, vol. 63, no. 9, pp. 3808–3818, Sep. 2015.

[7] C.-X. Mao, S. Gao, Y. Wang, Q. Luo, and Q.-X. Chu, "A shared-aperture dual-band dual-polarized filtering-antenna-array with improved frequency response," *IEEE Trans. Antennas Propag.*, vol. 65, no. 4, pp. 1836–1844, Apr. 2017.

[8] M.-C. Tang, Y. Chen, and R. W. Ziolkowski, "Experimentally validated, planar, wideband, electrically small, monopole filtennas based on capacitively loaded loop resonators," *IEEE Trans. Antennas Propag.*, vol. 64, no. 8, pp. 3353–3360, Aug. 2016.

[9] C.-T. Chuang and S.-J. Chung, "New printed filtering antenna with selectivity enhancement," in *2009 European Microwave Conference (EuMC)*, pp. 747–750, 2009.

[10] X. Y. Zhang, W. Duan, and Y.-M. Pan, "High-gain filtering patch antenna without extra circuit," *IEEE Trans. Antennas Propag.*, vol. 63, no. 12, pp. 5883–5888, Dec. 2015.

[11] H.-T. Hu and C. H. Chan, "Substrate-integrated-waveguide-fed wideband filtering antenna for millimeter-wave applications," *IEEE Trans. Antennas Propag.*, vol. 69, no. 12, pp. 8125–8135, Dec. 2021.

[12] X. Cheng, X. Chen, J. Liu, X. Liu, J. Li, S. Gao, and A. A. Kishk, "Compact dual-polarized low sidelobe monopulse slot antenna array based on gap waveguide technology," *IEEE Trans. Antennas Propag.*, vol. 73, no. 2, pp. 1215–1220, Feb. 2025.

[13] G. Q. Luo, W. Hong, H. J. Tang, J. X. Chen, X. X. Yin, and Z. Q. Kuai, "Filtenna consisting of horn antenna and substrate integrated waveguide cavity FSS," *IEEE Trans. Antennas Propag*., vol. 55, no. 1, pp. 92–98, Jan. 2007.

[14] Z. Wang, S. Lin, Y. Ge, Z. Chen, J. Zhao, and J. H. Chen, "Unlock the potential of large-element-spacing arrays: A meta-lens solution for grating-lobe suppression and gain enhancement," *Electromagn. Sci.*, vol. 2, no. 4, 2024.

[15] S. J. Yang, Y. M. Pan, L.-Y. Shi, and X. Y. Zhang, "Millimeter-wave dual-polarized filtering antenna for 5G application," *IEEE Trans. Antennas Propag.*, vol. 68, no. 7, pp. 5114–5121, July 2020.

[16] X. Wen, Y. Yu, G. Shi, Z. Wang, Q. Cheng, and Y. Li, "WR-3.4 band waveguide and bandpass filters using copper additive manufacturing," *IEEE Trans. Microw. Theory Techn.*, vol. 71, no. 3, pp. 1190–1200, Mar. 2023.

[17] Z. Wu, G. Shi, X. Lu, R. Liang, X. Wen, J. Wang, B. Zhou, Z. Wang, C. Guo, and A. Zhang, "A W-band air-filled coaxial bandpass filter employing micro metal additive manufacturing technology," *Int. J. RF Microw. Comput.-Aided Eng.*, vol. 31, no. 9, pp. 1–10, Sep. 2021.

[18] R. Liang, C. Guo, Q. Yang, G. Shi, Z. Wang, and A. Zhang, "A micromachined ultra-wide stop-band lowpass filter based on stepped impedance resonator loaded T-shaped structure," *Int. J. RF Microw. Comput.-Aided Eng.*, vol. 32, no. 12, pp. 1–7, Dec. 2022.

[19] X. Wen, H. Yang, Z. Wu, Y. Yu, G. Shi, and Z. Wang, "A 100-180-GHz coaxial frequency tripler based on copper additive manufacturing," *IEEE Trans. Microw. Theory Techn.*, vol. 71, no. 10, pp. 4337–4345, Oct. 2023.

[20] H. Zhou, N. A. Sutton, and D. S. Filipovic, "Surface micromachined millimeter-wave log-periodic dipole array antennas," *IEEE Trans. Antennas Propag.*, vol. 60, no. 10, pp. 4573–4581, Oct. 2012.

[21] Y. Saito, M. V. Lukic, D. Fontaine, J.-M. Rollin, and D. S. Filipovic, "Monolithically integrated corporate-fed cavity-backed antennas," *IEEE Trans. Antennas Propag.*, vol. 57, no. 9, pp. 2583–2590, Sep. 2009.

[22] J. M. Oliver, J.-M. Rollin, K. Vanhille, and S. Raman, "A W-band micromachined 3-D cavity-backed patch antenna array with integrated diode detector," *IEEE Trans. Microw. Theory Techn.*, vol. 60, no. 2, pp. 284–292, Feb. 2012.

[23] J. S. Hong and M.J. Lancaster, "Microstrip filters for RF/microwave applications," *IEEE Microw. Mag.*, vol. 3, no. 3, pp. 62–65, Nov. 2002.

[24] X. Zhong, Q. Li, C. Guo, J. Li, Z. Wang, J. Shi, X. Chen, and A. Zhang, "A D-band wideband magnetoelectric dipole antenna array based on micro-metal additive manufacturing," *IEEE Trans. Antennas Propag.*, vol. 72, no. 8, pp. 6500–6509, Aug. 2024.

[25] Q. Yuan, T. Sun, B. Tang, Z. Wang, G. Shi, C. Guo, and A. Zhang, "A non-50Ω-RMCL transition designed for on-chip measurement in the 0-170 GHz frequency range," *IET Microwaves, Antennas & Propagation*, vol. 17, no. 11, pp. 857–862, Aug. 2023.

[26] Q. Yang, H. Yi, J. Sheng, J. Xu, Q. Zhang, and Z. Cao, "An H-plane high-flatness ridge waveguide dual-directional coupler based on copper additive manufacturing," *IEEE Microw. Wireless Technol. Lett.*, vol. 34, no. 7, pp. 879–882, July 2024.

[27] S. Yan, C. Zhang, Q. Chen, and M. Tong, "A novel compact filtering antenna for 5.0-GHz WLAN communication system," *Applied Computational Electromagnetics Society (ACES) Journal*, vol. 37, no. 09, pp. 996–1004, Sep. 2022.

[28] P. Jia, C. Xing, X. Jiang, and Y. Shi, "A Ka-band microstrip millimeter-wave filter antenna fed by ridge gap waveguide," in *Proc. Int. Conf. Microw. Millim. Wave Technol. (ICMMT)*, pp. 1–3, May 2024.

[29] Y. Z. Tian, Y. M. Pan, X. Y. Liu, and K. W. Leung, "An SIW-based wideband endfire filtering magneto-electric dipole antenna for millimeter-wave applications," *IEEE Trans. Antennas Propag.*, vol. 71, no. 12, pp. 9986–9991, Dec. 2023.

[30] Y. Gong, X.-L. Yang, and X.-W. Zhu, "Millimeter-wave filtering antenna and array with multiple flexible radiation nulls based on hybrid coupling of SIW cavities and split-ring slots," *IEEE Antennas Wireless Propag. Lett.*, vol. 24, no. 4, pp. 823–827, Apr. 2025.

Nan Wang received his M.Sc. degree in electromagnetic and microwave technology from Xidian University, Xi'an, China, in 2010. His current research interests include the research of operation and maintenance technology of power transmission and transformation equipment.

Ying Zhu was born in Xi'an, China, in 1999. She received the B.Eng. degree in information engineering from Xi'an Jiaotong University, Xi'an, in 2021, where she is currently pursuing the master's degree in electromagnetic field and microwave technology. Her research interests include the design of microwave passive components.

Jing Wang received her master's degree in software engineering from Xi'an Jiaotong University, Xi'an, China, in 2012. Her research interests include digital technology management and application.

Xinjiang Liu obtained a master's degree in electronic and communication engineering from the University of Chinese Academy of Sciences, China, in 2020. His current research interests include trustworthy artificial intelligence and advanced communication technologies.

Chaoyu Feng graduated with a bachelor's degree from Huazhong University of Science and Technology, China, in 2014, majoring in electrical engineering and its automation. He obtained his master's degree from North China Electric Power University in 2020,majoring in control engineering. His current research interests include the maintenance and overhaul of transmission lines.

Xinzhan Cai obtained a master's degree in Electronic Science and Technology Engineering from Nankai University, China, in 2022. His current research interests include the application technology of power communication and artificial intelligence in the power grid field.

Xiaolan Zhang received her M.Eng. degree in electrical machines and apparatuses from Xi'an Jiaotong University, Xi'an, China, in 2014. Her main research directions include the detection and analysis of switchgear equipment, and the research on auxiliary monitoring systems for smart substations.

Xuefeng Zhao received her Ph.D. degree in electrical engineering from Xi'an Jiaotong University, Xi'an, China, in 2011. Her current research interests include the research of power cable test technology and fault diagnosis.

Wensen Wang received his MSc degree in electrical engineering from Xi'an Jiaotong University, Xi'an, China, in 2016. His current research interests include the research of intelligent operation inspection of power equipment and high voltage engineering.

Guang Dai received his B.Eng. degree in mechanical engineering from Dalian University of Technology, China, and M.Phil. degree in computer science from the Zhejiang University and the Hong Kong University of Science and Technology. He is currently a senior research scientist at State Grid Corporation of China, and also the founder of SGIT AI Lab, State Grid Corporation of China. His main research interests include Bayesian statistics, deep learning, reinforcement learning, optimization computation, and related applications.

Jiawei Yang graduated from the department of electronics and communications engineering of North China Electric Power University, BaoDing, China, in 2023. He is currently involved in the research of new communication technology applications and Beidou communications.

An S-Band Low-Probability Intercept Radar Antenna With Low Sidelobe Level

Zhengliang Lv[1], Shuai Yan[1], Zizhen Zheng[1], Yi Zeng[2], and Xing Wang[2]

[1]China Academic Electronic and Information Technology
Beijing 100041, China
lvzhengliang@cetc.com.cn, Yangshuai6@cetc.com.cn,
bitzhengzizhen@163.com

[2]National Key Laboratory of Radar Detection and Sensing
Xi'an, Shaanxi 710071, China
yizeng@stu.xidian.edu.cn, wangxing@mail.xidian.edu.cn

Abstract – A half-wave dipole array antenna design for S-band low probability of intercept (LPI) radar is presented. The antenna structure comprises 24×2 linearly polarized dipole elements. A 24-column Taylor distribution weighted feed in the azimuth plane realizes low sidelobe level (SLL) of -26.0 dB. The antenna achieves an operational bandwidth of 100 MHz with a voltage standing wave ratio (VSWR) below 1.4. A prototype was fabricated and measured for verification. The measured gain is 22.3 dBi, with half-power beamwidth (HPBW) of 6.5° and 24.5° in azimuth and elevation, respectively. Results show that the array scans from -45° to $+45^\circ$ with a gain loss below 2.1 dB, while maintaining an SLL under -20.2 dB across this wide scanning range.

Index Terms – Array antenna, high-gain, low probability of interception (LPI) radar, low sidelobe level (SLL).

I. INTRODUCTION

Low probability of intercept (LPI) radar is a new radar system which uses a variety of technologies to prevent radar signals from being intercepted by the enemy intercept receiver. Hence, much research and design are carried out focused on LPI radar [1–3]. It is generally believed that the time taken by the enemy to intercept the radar depends on the main lobe gain, sidelobe level (SLL) and beam width of the radar antenna. Low probability of interception radar should be equipped with a planar antenna array, which has high gain and low SLL performances.

Sidelobe manipulation techniques for antenna array have been developed by many researchers. The common approach of reducing SLLs in array antennas is amplitude control and phase correction by the feeding network. Waveguide slot array antennas with Taylor's distribution have been proposed for radar systems [4–6]. In [6], array antennas combined with Schelkunoff's unit circle technique have achieved less than -28.5 dB SLL by utilizing Taylor synthesis. Taylor's distribution can also be used in slots array antenna with T-junction power divider [7], slots array antenna with inverted microstrip gap waveguide [8], slotted ridge waveguide antenna array [9] and monopulse slotted antenna with gap waveguides [10]. Besides Taylor's distribution, the Chebyshev amplitude distribution can be used in a series-fed linear dielectric resonator antenna array to get a low SLL [10]. In [11], Dolph-Chebyshev distributions are utilized by periodic stub-loaded slow wave transmission line feed networks to reach low SLL performances in compact series-fed microstrip patch arrays.

Another method for sidelobe manipulation is modifying the structure or position of feeding line in microstrip antenna arrays. The U-shaped series-feed network and corner series-feed network are used in linear microstrip antenna arrays to provide low SLL and low cross polar level in [12]. In addition, the feeding line in a microstrip patch array antenna was modified as the step-impedance microstrip line to decrease the SLL in [13]. In [14], the two halves of the structure were fed in parallel and each arm was fed in a series-series feed network to achieve the low SLL of -26.5 dB. However, the impedance bandwidth in the X-band was only 5.3% (VSWR < 1.92).

This paper is organized as follows. Section II presents the required technical specifications for the antenna. Section III details the theory of LPI radar and the antenna design process. Section IV covers antenna fabrication and measurement. Conclusions are provided in section V.

Submitted On: July 03, 2025
Accepted On: September 10, 2025

https://doi.org/10.13052/2026.ACES.J.410209

II. TARGET SPECIFICATIONS AND CONFIGURATIONS OF ANTENNA

Table 1 defines target specifications for the scaled model sample of LPI radar antenna. The proposed antenna should have linear-horizontal polarization and achieve wide-scanning performance with $\pm 45^\circ$ in the azimuth plane.

Table 1: Target specifications of the antenna

Specification	Value
Frequency	2.25 GHz
Array Form	2×24 elements
Size	2000×270 mm
VSWR	$<$1.6 (per element) $<$1.4 (average)
Polarization	Linear-Horizontal
SLL (Azimuth)	-26 dB max
HPBW (Azimuth/Elevation)	6.8°/26° max
Scanning Angle (Azimuth)	45° min
Gain (0°/30°/45° in azimuth)	21.7 dBi/20.7 dBi/18.8 dBi min
Weight	$<$ 43000 g

III. DESIGN AND SIMULATION

LPI radar is designed to minimize the probability of its signals being intercepted by an enemy receiver. This probability is quantified by the intercept probability factor α. Based on the LPI radar theory in [15], the intercept probability factor is defined as:

$$\alpha = \frac{R_i}{R_r}, \tag{1}$$

where R_i represents the interception range of intercept receiver and R_r represents the detection range of radar. They can be expressed as:

$$R_i^2 = \frac{P_{rL} G_{rI} G_I \lambda^2}{(4\pi)^2 S_I L_I}, \tag{2}$$

$$R_r^4 = \frac{P_t G_t G_r \lambda^2 \sigma}{(4\pi)^3 S_r L_r}, \tag{3}$$

where P_t is the radar transmitter power, P_{rL} is the radar transmitter power with loss of L_{rt}, which can be taken as $P_{rL} = P_t / L_{rt}$, G_t is the gain of radar's transmit antenna, G_r is the gain of radar's receive antenna, G_I is the gain of the intercept receiver antenna in the direction of radar, G_{rI} is the gain of the radar's transmit antenna in the direction of the intercept receiver, S_I and S_r are the sensitivity of intercept receiver and radar receiver, L_I and L_r are the system loss factor of intercept receiver and radar receiver, λ is the wavelength of transmitted signal, and σ is radar cross-section of target.

When the maximum operating range of the radar $R_{r\max}$ is determined, the intercept probability factor of radar system with common antenna can be written as:

$$\alpha = R_{r\max} \left[\frac{4\pi S_r L_r G_{rI} G_I}{\sigma S_I L_I G_t^2 L_{rt}} \right]^{1/2}. \tag{4}$$

Without considering sensitivity and system loss factors, the intercept probability factor has the following relationship with the radar's transmit antenna and intercept receiver antenna:

$$\alpha \propto \left[\frac{G_{rI} G_I}{G_t^2} \right]^{1/2}. \tag{5}$$

According to Equation (5), besides the influence of intercept receiver antenna, the intercept probability factor can be reduced by increasing the gain of the radar's transmit antenna. Meanwhile, the intercept probability factor is proportional to the square root of the radar's transmit antenna SLL when the intercept receiver intercepts the radar in the sidelobe direction. Thus, low SLL antenna is also an important LPI characteristic.

Hence, we tend to design an antenna with high gain of main lobe and low level of sidelobe. Initially, the half-wave dipole antenna is chosen as a fundamental form for high gain characteristic. Then, the SLL is reduced effectively by Taylor distribution in the feeding design. During the process, all the simulated data are provided by the commercial electromagnetic simulation tool HFSS.

A. Antenna element design

A half-wave dipole antenna is one of the most widely used antenna types in antenna engineering, including communication, radio, television, navigation and other engineering systems. When the half-wave dipole antenna is directly placed, the radiation performance is omnidirectional radiation. Therefore, a reflecting plate is loaded to give the antenna directional radiation. At the same time, referring to the radiation principle of Yagi-Uda antenna, the directional structure is added to improve the directional radiation performance of the antenna element. Figure 1 shows the final structure of the antenna element (purple) and epoxy glass fibrous cloth used as the radome (green).

Figure 2 shows the measured 3-D radiation pattern of the proposed antenna element where the peak gain reaches 7.6 dBi. The simulated bandwidths for VSWR$<$1.4 are 145 MHz (6.4%). The antenna array element has good directional radiation characteristics, simple installation process and is easy to use.

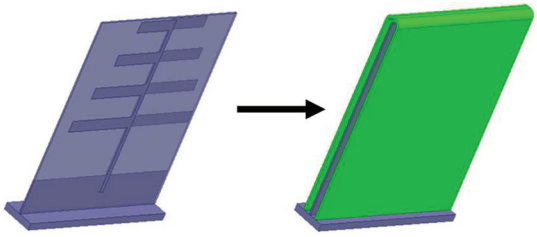

Fig. 1. Structure of the proposed antenna element with radome.

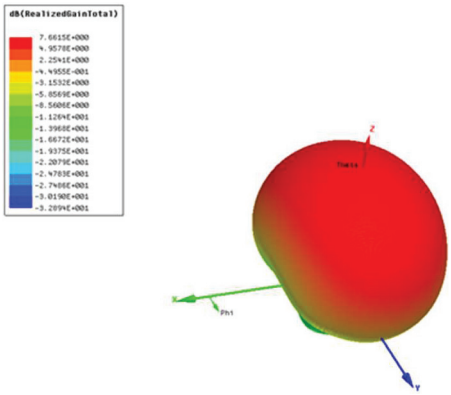

Fig. 2. Simulated 3-D radiation pattern of the antenna element.

B. Array synthesis

The antenna array consists of 48 units, with two rows of elevation plane and 24 columns of azimuth plane, as shown in Fig. 3 ($N = 48$). The A_N and B_N represent the N-th element of two rows, respectively.

Element spacing in the elevation plane is set as 150 mm ($Y = 150$ mm) and each two array elements in the same elevation plane are designed with equal amplitude and phase feeding by power division units, which can narrow the beam width in the elevation plane to improve gain. The 24 column Taylor distribution weighted feed in the azimuth plane reduces the pattern sidelobe. After sidelobe reduction technique employment, the SLL of the array pattern is reduced while the main lobe width becomes wider. Relatively, the lower the SLL, the wider the main lobe width. In order to fulfill the requirements of beam width, the element spacing is increased to and finally selected at 76.5 mm ($X = 76.5$ mm), which can improve the gain and effectively control the beam width. It's worth noting that the element spacing shall not be so large as to cause grating lobes during scanning.

The antenna array elements are fed by the phase-shifting attenuation module to realize antenna azimuth scanning. The phase-shift attenuation module is mainly used to test whether the technical parameters of

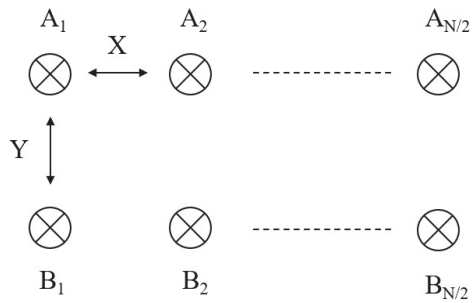

Fig. 3. Schematic diagram of array layout.

the phase scanning antenna array fulfills the design indicators under different frequencies, different wave positions, different amplitude weighted values and other conditions.

C. Array configuration and simulation

The 3-D view and front view diagrams of the proposed antenna are shown in Fig. 4. The antenna is mainly composed of antenna element, power divider, auxiliary unit, reflecting plate, phase shift attenuation module, installation framework and RF front-end.

As shown in Fig. 4 (a), the radiating antenna consists of four groups of antenna cell with a total of 48 antenna elements. Four auxiliary units are located at both ends of the radiating antenna, with a pitch spacing of 76.5 mm. A total of 26 power dividers are located behind the antenna element, connected to the antenna element and auxiliary unit by blind plugs of Blind-mate

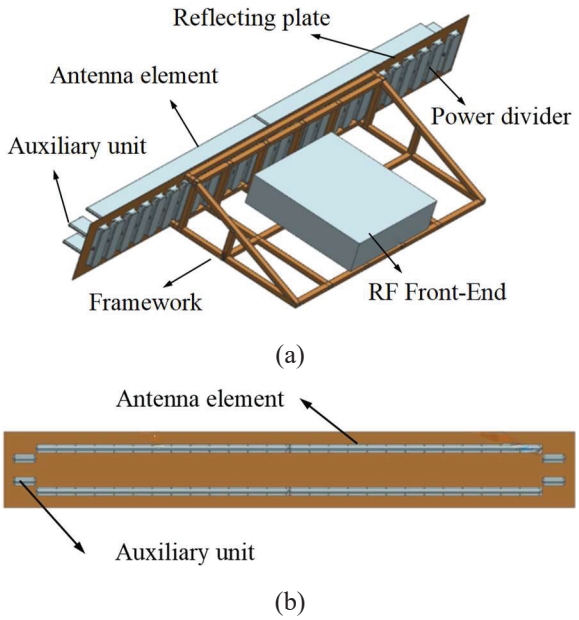

Fig. 4. (a) 3-D view and (b) front view of the proposed antenna.

A (BMA) connectors, and fixed with the reflecting plate through screws. Figure 4 (b) shows the front view of the antenna array. The radiating antenna array is composed of 48 elements with two rows of elevation plane and 24 columns of azimuth plane.

Figure 5 shows the E-plane simulated array scanning patterns at 2.25 GHz. When the phase scan of the radar antenna is 0°, the maximum gain of simulation results is 22.72 dBi with the first SLL of −29.6 dB. Also, high beam gains of 21.8 and 19.9 dBi are obtained in the scan angle of 30° and 45°, respectively.

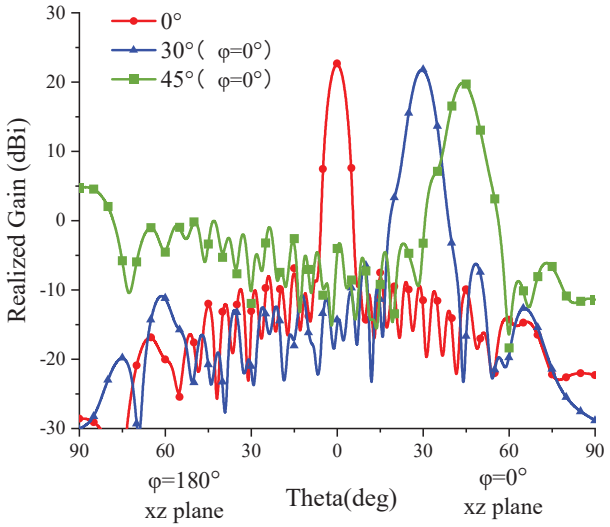

Fig. 5. Simulated scanning performance of the proposed antenna array at 2.25 GHz.

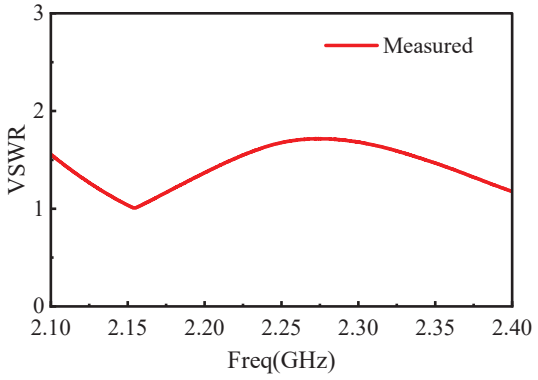

Fig. 6. Measured VSWR of antenna array.

IV. EXPERIMENTAL VERIFICATION AND RESULTS

In this section, a prototype of the proposed antenna array is fabricated and measured to verify its feasibility. The total dimension of antenna is 2000 × 270 mm with a weight of 42.8 kg, while the radiating aperture is 1900 × 270 mm.

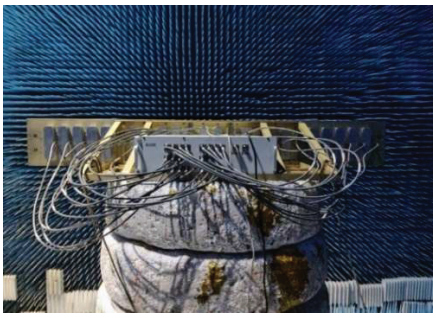

Fig. 7. Antenna fabricated model in measurement environment.

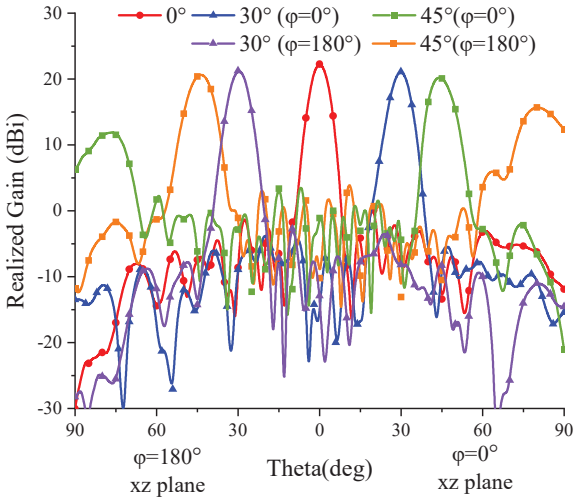

Fig. 8. Measured scanning performance of the proposed antenna array at 2.25 GHz.

Table 2: Realized gain in different scan angles

Scan angle in xz plane (deg)	Realized gain at 2.25 GHz (dBi)	SLL at 2.25 GHz (dB)
0	22.3	−26.0
30 ($\varphi = 0°$)	21.1	−26.4
45 ($\varphi = 0°$)	20.2	−20.2
30 ($\varphi = 180°$)	21.2	−28.4
45° ($\varphi = 180°$)	20.7	−20.4

The voltage standing wave ratio (VSWR) of the antenna is measured by a network analyzer, as shown in Fig. 6. The VSWR of each array element is less than 1.8. The antenna electrical performance test is validated in a microwave anechoic chamber as shown in Fig. 7.

The scanning performance of the fabricated antenna array is measured and shown in Fig. 8. A maximum realized gain of 22.3 dBi can be obtained at 2.25 GHz with the low SLL of −26.0 dB. Table 2 shows the

Table 3: Performance comparison of the array antennas

Ref.	Size ($\lambda \times \lambda$)	Freq. (GHz)	BW	VSWR	Gain (dBi)	HPBW (deg)		SLL (dB)	
						E-plane	H-plane	E-plane	H-plane
[4]	55.8×17	9.3	4.3%	<1.37	37.7	3.8	1.3	-17	-22.5
[6]	7.3×7.3	8.9	2.8%	<1.43	23.2	8.9	9	-28.5	-29.6
[9]	26.5×5.3	24.1	1.03%	<1.92	22.3	54.4	3.2	-19.6	-29.8
[13]	9.1×1.25	9.41	1.9%	<1.92	21.3	8.1	41.8	-27.8	-21.4
[14]	16.8×3.5	9.35	5.3%	<1.92	24.0	4.5	21.5	-26.2	-19.7
This Work	15×2	2.25	4.4%	<1.4	22.3	6.5	24.5	-26.0	N/A

realized gain and SLL of proposed antenna at different scan angles.

The performance of the proposed antenna is benchmarked against existing antennas in the literature in Table 3. The proposed design exhibits several advantageous features, including a realized gain of 22.3 dBi, a SLL of -26.0 dB, a compact size of $15 \times 2\lambda$ mm^2, and a scanning capability of up to 45° with only a 2.1 dB gain loss.

V. CONCLUSION

This paper proposes an S-band half-wave dipole antenna with low SLL. The feed network employs a 24-column Taylor distribution weighting to reduce the pattern sidelobes. Results demonstrate an operational bandwidth of 4.4% (2.2–2.3 GHz) with an active voltage standing wave ratio <1.4. A 2×24 prototype array was fabricated for the experimental validation. The antenna achieves a peak gain of 22.3 dBi, scanning over $\pm 45°$ with only 2.1 dB gain loss and SLL below -20.2 dB. Thus, the proposed antenna design serves as a suitable candidate for LPI radar applications.

REFERENCES

[1] K. Chen, C. Xie, F. Yang, M. Huang, Y. Chen, and S.-W. Qu, "Integrated radar and communication design with low probability of intercept based on 4-D antenna arrays," *IEEE Trans. Antennas Propag.*, vol. 70, no. 9, pp. 8496–8506, Sep. 2022.

[2] K. Chen, S. Yang, Y. Chen, D. Yang, M. Huang, and S.-W. Qu, "LPI beamforming based on 4-D antenna arrays with pseudorandom time modulation," *IEEE Trans. Antennas Propag.*, vol. 68, no. 3, pp. 2068–2077, Mar. 2020.

[3] K. Chen, S. Yang, Y. Chen, S.-W. Qu, and J. Hu, "Transmit beamforming based on 4-D antenna arrays for low probability of intercept systems," *IEEE Trans. Antennas Propag.*, vol. 68, no. 5, pp. 3625–3634, May 2020.

[4] M. Atamanesh, A. Zahedi, and B. Abbasi-Arand, "Design, simulation, and fabrication of a high-gain low-sidelobe-level waveguide slot array antenna at X-band with zero beam tilts in both azimuth and elevation directions," *IEEE Antennas Wireless Propag. Lett.*, vol. 19, no. 5, pp. 811–815, May 2020.

[5] R. A. Bhatti, B.-Y. Park, Y.-T. Im, and S.-O. Park, "Design of a planar slotted waveguide array antenna for X-band radar applications," *J. Korean Inst. Electromagn. Eng. Sci.*, vol. 11, no. 2, pp. 97–103, June 2011.

[6] P. Kumar, A. Kedar, and A. K. Singh, "Design and development of lowcost low sidelobe level slotted waveguide antenna array in X-band," *IEEE Trans. Antennas Propag.*, vol. 63, no. 11, pp. 4723–4731, Nov. 2015.

[7] P. Liu, G. F. Pedersen, and S. Zhang, "Wideband low-sidelobe slot array antenna with compact tapering feeding network for E-band wireless communications," *IEEE Trans. Antennas Propag.*, vol. 70, no. 4, pp. 2676–2685, Apr. 2022.

[8] J. Liu, F. Yang, K. Fan, and C. Jin, "Unequal power divider based on inverted microstrip gap waveguide and its application for low sidelobe slot array antenna at 39 GHz," *IEEE Trans. Antennas Propag.*, vol. 69, no. 12, pp. 8415–8425, Dec. 2021.

[9] J. Chen, T. Hu, Y.-T. Zhao, L. Li, M. Bao, T. Su, and J. Ding, "Realization of high-gain low-sidelobe wide-sector beam using inductive diaphragms loaded slotted ridge waveguide antenna array for air detection applications," *IEEE Trans. Antennas Propag.*, vol. 70, no. 4, pp. 2698–2707, Apr. 2022.

[10] X. Cheng, X. Ming, J. Liu, X. Liu, J. Li, S. Gao, and A. A. Kishk, "Compact dual-polarized low sidelobe monopulse slot antenna array based on gap waveguide technology," *IEEE Trans. Antennas Propag.*, vol. 73, no. 2, pp. 1215–1220, Feb. 2025.

[11] J. Lin, W. Shen, and K. Yang, "A low-sidelobe and wideband series-fed linear dielectric resonator antenna array," *IEEE Antennas Wireless Propag. Lett.*, vol. 16, pp. 513–516, 2017.

[12] M. Li, Z. Zhang, M.-C. Tang, D. Yi, and R. W. Ziolkowski, "Compact series-fed microstrip patch arrays excited with Dolph-Chebyshev distributions realized with slow wave transmission line feed networks," *IEEE Trans. Antennas Propag.*, vol. 68, no. 12, pp. 7905–7915, Dec. 2020.

[13] R. Chopra and G. Kumar, "Series- and corner-fed planar microstrip antenna arrays," *IEEE Trans. Antennas Propag.*, vol. 67, no. 9, pp. 5982–5990, Sep. 2019.

[14] Z. Wang, J. Zhou, Y. Wang, Z. Zhu, S. Fang, and H. Liu, "A compact feeding network with radiation contribution for X-band marine radar antenna array applications," *Microw. Opt. Technol. Lett.*, vol. 61, no. 12, pp. 2819–2825, Aug. 2019.

[15] M. Pehlivan and K. Yegin, "X-band low-probability intercept marine radar antenna design with improved bandwidth and high isolation," *IEEE Trans. Antennas Propag.*, vol. 69, no. 12, pp. 8949–8954, Dec. 2021.

[16] P. Pace, *Detecting and Classifying Low Probability of Intercept Radar*, 2nd ed. Norwood, MA: Artech, 2008.

Zhengliang Lv obtained his doctoral degree from Xidian University in 2014. He is currently a senior engineer at the China Academic Electronic and Information Technology. He has long been engaged in system integration, electromagnetic simulation, electromagnetic compatibility design, and other work related to major integrated electronic information systems. He has published over ten papers in core domestic and international journals such as the *Chinese Journal of Electronics*, *Journal of Electromagnetic Waves and Applications*, and *Microwave Journal*.

Shuai Yang received the B.Sc. degree in electronics and information engineering, and the Ph.D. degree in communication and information systems from the Harbin Institute of Technology (HIT), Harbin, China. His current research interests include electromagnetic metasurfaces, computational electromagnetics (CEM), and engineering electromagnetic compatibility (EMC).

Zizhen Zheng obtained her master's degree from Beijing Institute of Technology, China, in 2024 and is currently an engineer at the China Academic Electronic and Information Technology. She is engaged in array antenna design, electromagnetic compatibility design, and has published multiple papers in journals such as *Electronics* and *International Conference on Microwave and Millimeter Wave Technology*.

Yi Zeng was born in Zhejiang, China, in 2000. He received the B.Eng. degree in electronic engineering from Xidian University, Xi'an, China, in 2022, where he is currently pursuing the Ph.D. degree in electronic science and technology. His focus is antenna analysis and design.

Xing Wang received the Ph.D. degree from Xidian University, Xi'an, China, in 2011. He is currently a Full Professor with the National Key Laboratory of Radar Detection and Sensing, Xidian University. His research interests include computational electromagnetic, fast algorithms for electromagnetic scattering and radiation, hybrid methods, and EMC analysis.

Figures of Merit Analysis for Over-the-Air Testing of the Non-Terrestrial Network Direct-to-Smartphone Handsets

Siyang Sun[1], Meijun Qu[2], and Zheng Liu[1*]

[1]China Telecommunication Technology Labs
China Academy of Information and Communications Technology, Beijing 100191, China
sunsiyang@caict.ac.cn
*Corresponding: liuzheng@caict.ac.cn

[2]National Key Laboratory of Scattering and Radiation
Beijing 100854, China
qumeijun@126.com

Abstract – The Non-Terrestrial Network (NTN) is a critical component of the 6G integrated space-air-ground-sea network. The comprehensive Over-the-Air (OTA) performance evaluation of NTN terminals is essential for ensuring wireless connection reliability and quality of experience. However, major international standards bodies including 3rd Generation Partnership Project (3GPP) and Cellular Telecommunications and Internet Association (CTIA) remain in the preliminary stages of developing their OTA specifications for mobile terminals supporting NTN communications. Accordingly, the objective of this paper is to investigate key Figures of Merit (FoMs) for OTA testing of NTN handsets from the perspective of satellite coverage multiplicity, to better characterize, distinguish, and rank OTA performance of different NTN handsets for future testing methodology development. During the analysis, coverage models are created for Low Earth Orbit (LEO) and Geosynchronous Orbit (GEO) constellations separately, based on which the coverage multiplicity for Starlink Direct-to-Cell (DTC) and TianTong-1 constellations is evaluated and determined for different target regions quantitatively. By comparing the coverage multiplicity and usage scenarios with those of the Global Positioning System (GPS), whose OTA FoMs and testing methods have been clearly defined in specifications, the FoMs for OTA testing of NTN handsets are recommended, including integrated FoMs for LEO (e.g., Total Isotropic Sensitivity [TIS] and Upper Hemisphere Isotropic Sensitivity [UHIS] metrics for receiver performance, and Total Radiated Power [TRP] and new Upper Hemisphere Radiated Power [UHRP] metric [corresponding to the UHIS] for radiation performance evaluation) as well as directional FoMs (e.g., requiring the average or minimum of Effective Isotropic Radiated Power [EIRP] and Effective Isotropic Sensitivity [EIS] values within a specific zenith angular range to exceed the limit) for GEO constellations, respectively.

Index Terms – Direct-to-Smartphone (DTS), Figures of Merit (FoMs), Non-Terrestrial Network (NTN), Over-the-Air (OTA) testing.

I. INTRODUCTION

Driven by the advancement of telecommunications, the exponential growth of smart devices, and the rising demand for ubiquitous connectivity, satellite-enabled Non-Terrestrial Networks (NTNs) are globally expected to be integrated into terrestrial network infrastructures as an indispensable complement, playing important roles in 5G and beyond by providing seamless space-air-ground-sea coverage that eliminates service deserts and fulfills the goal of truly global connectivity [1–7]. As defined by the 3rd Generation Partnership Project (3GPP) [8], an NTN refers to a network where spaceborne or airborne vehicles act either as a relay node or as a base station, thereby distinguishing transparent and regenerative satellite architectures. Since the 3GPP Rel-17 standard integrates NTN as part of 5G Advanced (5G-A) and enables Internet of Things NTN (IoT-NTN) and New Radio NTN (NR-NTN) features for handheld devices connected with Low Earth Orbit (LEO) and Geosynchronous Orbit (GEO) satellites [9, 10], satellite-enabled NTN has been playing an increasingly critical role in 5G-A and future 6G networks.

As a key enabler for 5G-A and 6G IoT-NTN and NR-NTN, Direct-to-Smartphone (DTS) technology has been a global research focus. The DTS technology allows commercial mobile terminals to establish direct wireless connections with satellites for data transmission and communication without relying on relay nodes

Submitted On: September 30, 2025
Accepted On: December 16, 2025

https://doi.org/10.13052/2026.ACES.J.410210

or dedicated satellite equipment. It thereby supports a wide range of applications, including satellite IoT and Mobile Satellite Services (MSS). In DTS communication scenarios, the reliability, coverage, responsiveness, and security of wireless links are critical factors affecting both user experience and system quality of service, which are heavily dependent on agile and high-performance antennas [11–13]. Consequently, Over-the-Air (OTA) testing, which can accurately characterize the wireless performance of devices under test (DUTs) under realistic operating conditions, is essential for optimizing antenna and wireless performance of DTS smartphones and enhancing their quality of user experience [14–18]. OTA testing has been established as the standard methodology for wireless performance evaluation of DUTs by major standards bodies such as 3GPP and the Cellular Telecommunications and Internet Association (CTIA), as well as by leading network operators [19–24].

For DTS handheld devices, the OTA testing methodology is under discussion in both CTIA and 3GPP while relevant testing specifications have not been determined and officially released yet. Currently, the consensus is to maintain and re-use the methodology for cellular smartphones temporarily as a starting point to meet the urgent testing requests from the industry, i.e., the device manufacturers and network operators, while proceeding with the methodology development in parallel. Accordingly, current Figures of Merit (FoMs) for OTA testing of DTS DUTs are Total Radiated Power (TRP) and Total Isotropic Sensitivity (TIS) for both radiated power and receiver performance, respectively. Considering the differences between cellular and satellite communication scenarios, including the following aspects:

(1) Different signal angles of arrival (AoAs): for cellular, the signal mainly comes from the angular region within $\pm 45^{\circ}$ of the horizon, while for NTN DTS, it comes from a certain angular range of the zenith;
(2) Different testing or holding positions: in cellular scenarios, smartphones can be held in both portrait and landscape positions; in contrast, in NTN scenarios, DTS DUTs can only be held in portrait mode with the top side pointing to the sky, even though the internal antenna design in current commercial DTS terminals has been significantly enhanced compared to the original external antenna design.

Therefore, the current temporary FoMs for OTA testing of NTN DTS terminals are deemed incapable of comprehensively characterizing and distinguishing the OTA performance of different NTN DTS DUTs.

The primary objective of this work is to investigate key FoMs for OTA testing of NTN DTS handsets, with a specific focus on satellite coverage multiplicity. To this end, coverage models are first established for both LEO and GEO constellations. Using the latest publicly available Two-Line Element (TLE) ephemeris data, the coverage capacity of both the Starlink Direct-to-Cell (DTC) and China Telecom TianTong-1 constellations, serving as representative cases, is then quantitatively evaluated across different target regions. Subsequently, the recommended OTA testing FoMs for LEO and GEO constellations are derived through a comparative analysis of their calculated coverage multiplicity and usage scenarios against those of the Global Positioning System (GPS) constellation, whose OTA testing methodologies and associated OTA FoMs have been rigorously defined in standard specifications.

II. COVERAGE MULTIPLICITY ANALYSIS

The 3GPP Rel-17 standard enables IoT-NTN and NR-NTN features for handheld devices connected to GEO and LEO satellites. Correspondingly, coverage multiplicity analysis and related coverage models are established for both LEO and GEO constellations, respectively. In this analysis, coverage multiplicity is reflected in N Asset Coverage, which represents the number of satellites visible simultaneously from an observation point.

A. LEO mode

The direct connection to LEO satellites has become the dominant DTS technical mode due to its significant advantages, including relatively low latency, high data rates, and better link budget. In this mode, traditional terrestrial base stations are replaced by LEO satellite payloads. Challenges including latency issues and substantial Doppler frequency shift are mitigated by either the satellite payloads or the ground systems. This architecture enables existing commercial handsets to access the NTN without requiring dedicated modules or applications. Given the vast number of existing mobile terminals, this DTS mode is highly appealing. Representatives include the Starlink DTC constellation and the AST Space-Mobile (ASTS) BlueBird Block-1 constellation. Among them, the Starlink DTC constellation takes a leading position due to its larger constellation scale and higher commercial maturity. In February 2025, Starlink and T-Mobile jointly announced the official launch of the Starlink DTC satellite service. Starlink plans to further expand its service scope in 2026, gradually enabling data, IoT, and voice services. Therefore, the Starlink DTC constellation is chosen as the representative for the analysis. As of 1 September 2025, there are a total of 605 Starlink DTC satellites in orbit.

For the LEO mode, coverage multiplicity is one of the most important performance indicators and is

thus analyzed here. The simulation period is set to 24 hours, from 04:00:00.000 UTCG on 31 August 2025 to 04:00:00.000 UTCG on 1 September 2025, to ensure that each satellite achieves orbital recurrence. Publicly available TLE data for the Starlink DTC and GPS constellations are used in the Satellite Tool Kit (STK) to create coverage models for the analysis, respectively. The analysis grid granularity for the target regions is set to 1° in both latitude and longitude. The calculated coverage multiplicity over time for US, California, and Washington, D.C. regions is illustrated in Fig. 1. For each curve, every data point represents the calculated maximum, minimum, and average count of simultaneously visible satellites across all grid points in the target region at that given time instance.

In this work, the GPS constellation is analyzed as a reference, and its coverage multiplicity over time for the same target regions is calculated and depicted in Fig. 2 for comparison. During the analysis, GPS Block IIF, IIR, IIR-M, and III satellites are considered, for a total of 31 satellites.

The following observations could be obtained from the comparison:

(1) For a LEO satellite at an altitude of 500 km, the visibility duration to a ground user spans a mere 442.64 seconds. This fundamental constraint necessitates frequent inter-satellite handovers to maintain continuous service, which in turn requires dozens of satellites to be visible to a user simultaneously over the upper hemisphere and as evenly distributed as possible to ensure completely seamless handovers. The current Starlink DTC constellation is designed to meet this requirement and can provide 24-hour continuous coverage over the entire US mainland, as shown in Fig. 1. Consequently, the coverage multiplicity is high: for most of the day, the maximum and minimum values exceed 30 and 20, respectively. The average multiplicity fluctuates around 25, maintaining a relatively constant margin of approximately 5 from both extremes. This high-density coverage remains robust at the regional level: for the California region, the satellite distribution becomes more uniform. The maximum and minimum values converge toward the average, which remains nearly identical to that of the entire US mainland, hovering around 25. This increased uniformity is due to the significantly smaller size of the analyzed region. For the DC region, the coverage multiplicity curve follows a trend very similar to the averages of the US and California but exhibits more pronounced fluctuations.

(2) In contrast, the GPS constellation, residing in Medium Earth Orbit (MEO), operates with a distinct coverage profile. Across the entire US mainland, the maximum and minimum coverage multiplicities are approximately 13 and 9, respectively, with the average value fluctuating around 11. Despite this lower density, it demonstrates a similar scaling effect at the regional level: the California region again shows a more uniform satellite distribution, where the maximum and minimum curves converge toward the average, similar to what is observed in the LEO scenario. Similarly, the DC region's coverage multiplicity closely follows the averages of the US and California while exhibiting its own characteristic fluctuations.

(3) Notably, despite the differences in orbital altitude and the resulting coverage multiplicity between the LEO (DTC) and MEO (GPS) constellations, they share essential system characteristics. Both systems,

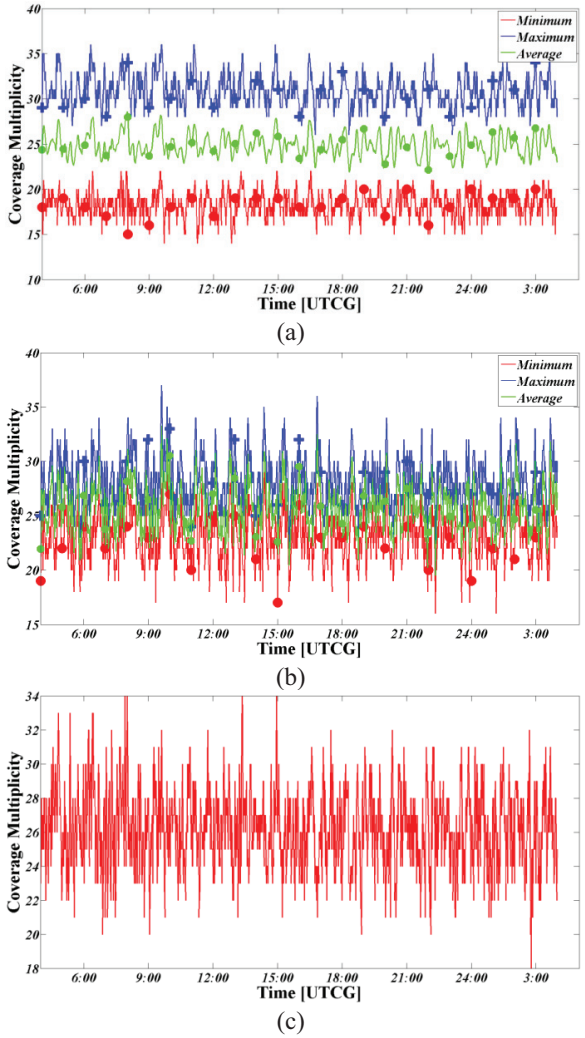

Fig. 1. Calculated coverage multiplicity over time of the Starlink DTC constellation for US, California, and Washington, D.C. regions: (a) US mainland, (b) California region, (c) Washington, D.C. region.

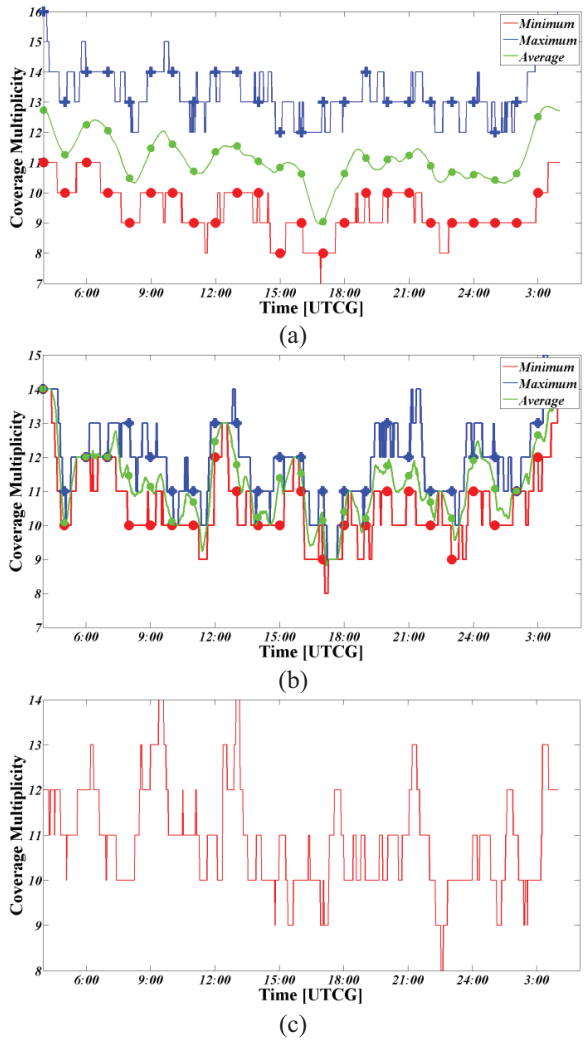

Fig. 2. Calculated coverage multiplicity over time of the GPS constellation for US, California, and Washington, D.C. regions: (a) US mainland, (b) California region, (c) Washington, D.C. region.

as satellite-dependent applications, require more than 10 concurrently visible satellites distributed as uniformly as possible across the upper hemisphere to ensure service stability and reliability. Furthermore, both operate in highly similar usage scenarios (e.g., handheld operation in portrait mode). The common characteristics and usage scenarios lead to closely aligned antenna performance requirements for both DTS and GPS handsets, specifically, a consistent and well-distributed upper-hemisphere radiation pattern to maximize the capture of visible satellites. Accordingly, the proposed OTA FoMs should reflect and distinguish the differences in the capability of different DUTs in terms of upper-hemisphere radiation pattern uniformity and further satellite capture capability, i.e., measured coverage multiplicity.

Therefore, the OTA testing methodologies and associated FoMs for GPS terminals can serve as a reference, while the FoMs for OTA testing of LEO handsets can be derived from those of GPS by comparing their coverage multiplicity. Since GPS terminals do not involve transmission, the currently required OTA FoMs are limited to receiver performance metrics, namely TIS and Upper Hemisphere Isotropic Sensitivity (UHIS). For a complete sphere measured with N theta intervals and M phi intervals, both with even angular spacing, they can be calculated [24]:

$$TIS \cong \left[\frac{1}{2}\sum_{i=0}^{N}\omega_i cut_i\right]^{-1}, \tag{1}$$

$$UHIS \cong \left[\frac{1}{2}\left(\sum_{i=0}^{\frac{N}{2}-1}\omega(\theta_i)cut_i + \frac{\omega(\theta_{\frac{N}{2}})cut_{\frac{N}{2}}}{2}\right)\right]^{-1}, \tag{2}$$

where

$$cut_i = \frac{1}{M}\sum_{j=0}^{M-1}\left[\frac{1}{EIS_\theta(\theta_i,\varphi_j)} + \frac{1}{EIS_\varphi(\theta_i,\varphi_j)}\right], \tag{3}$$

is the average for the conical phi cut at each theta angle, and

$$\theta_i = i\Delta\theta \quad \text{where } \Delta\theta = \frac{\pi}{\mathrm{N}}, \tag{4}$$

$$\varphi_j = j\Delta\varphi \quad \text{where } \Delta\varphi = \frac{2\pi}{\mathrm{M}}, \tag{5}$$

$$\omega(\theta_i) = \frac{c_i}{N}\left[1 - \sum_{j=1}^{int\left(\frac{N}{2}\right)}\frac{b_j}{4j^2-1}\cos(2j\theta_i)\right], \tag{6}$$

with

$$b_j = \begin{Bmatrix}1, & j = N/2\\ 2, & j < N/2\end{Bmatrix}, \quad c_j = \begin{Bmatrix}1, & i = 0 \text{ or } N\\ 2, & otherwise\end{Bmatrix}. \tag{7}$$

Here $\omega(\theta_i)$ is the theta-dependent weighting function. In this work, the Clenshaw-Curtis quadrature in equation (6) is utilized for TIS/UHIS calculations. The standard TRP measurement grid with 15-degree intervals in both theta and phi is illustrated in Fig. 3. The samples and weights for the Clenshaw-Curtis quadrature with the reference grid configuration ($\Delta\theta = 15^\circ$) are illustrated in Table 1.

Therefore, the TIS and UHIS can be reused for receiver performance evaluation of LEO DTS handsets, while the TRP metric can be reused for radiation performance evaluation. Furthermore, a new FoM corresponding to the UHIS, namely Upper Hemisphere Radiated

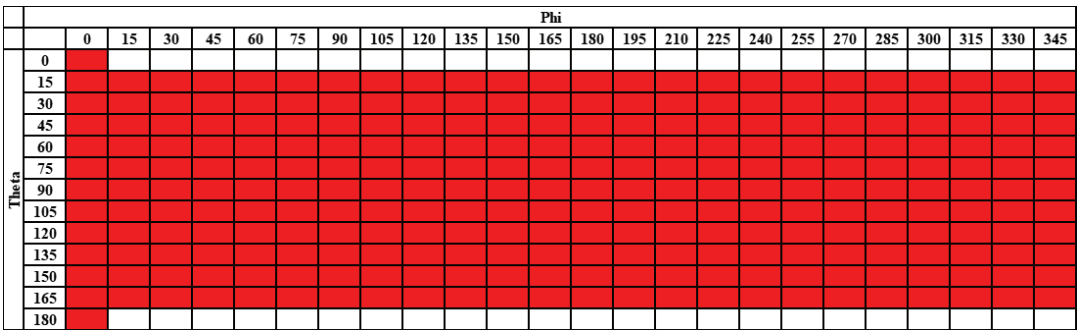

Fig. 3. Illustration of the standard 15-degree TRP grid as reference.

Table 1: Samples and weights for the Clenshaw-Curtis quadrature with $\Delta\theta = 15^\circ$

Clenshaw-Curtis quadrature		
i	**θ [deg]**	**Weights**
0	0	0.007
1	15	0.0661
2	30	0.1315
3	45	0.1848
4	60	0.227
5	75	0.2527
6	90	0.262
7	105	0.2527
8	120	0.227
9	135	0.1848
10	150	0.1315
11	165	0.0661
12	180	0.007

Power (UHRP), is introduced to characterize the uniformity of the upper-hemisphere radiation pattern. The UHRP metric can be calculated correspondingly as:

$$UHRP \cong \left[\frac{1}{2} \left(\sum_{i=0}^{\frac{N}{2}-1} \omega(\theta_i) cut_i + \frac{\omega(\theta_{\frac{N}{2}}) cut_{\frac{N}{2}}}{2} \right) \right], \quad (8)$$

where

$$cut_i = \frac{1}{M} \sum_{j=0}^{M-1} [EIRP_\theta(\theta_i, \varphi_j) + EIRP_\varphi(\theta_i, \varphi_j)], \quad (9)$$

is the average power for the phi cut at each theta angle.

B. GEO mode

Most early NTN deployments focus on using GEO satellites for fixed broadband and IoT applications, particularly those that are not delay-sensitive. Operating in a circular equatorial orbit at an altitude of 35,786 km, GEO satellites appear stationary to ground observers. This allows them to provide long-term, stable, and continuous coverage with a much larger single-satellite footprint than LEO satellites, making them especially suitable for scenarios that demand high communication continuity (e.g., emergency communications in remote areas). Moreover, establishing an NTN system with equivalent coverage requires far fewer GEO satellites than LEO satellites, significantly reducing both deployment and operational costs. Representative examples include the Huawei Mate60 Pro and China Telecom Tianyi Platinum smartphones (using the TianTong-1 satellite), as well as the IsatPhone Pro handset and Skylo-certified devices (utilizing Inmarsat satellites). Since the TLE ephemeris data of the TianTong-1 constellation is the only one available to us, it is analyzed as the representative; however, the proposed analysis and related conclusions also apply to other GEO constellations. As of 1 September 2025, there are a total of three TianTong-1 satellites in orbit.

The elevation analysis of the TianTong-1 constellation relative to ground users is performed with the same simulation period as that of the Starlink DTC. Publicly available TLE data is used to develop a coverage model in the STK. The calculated elevation angles over time for the Beijing and Shenzhen regions are summarized in Table 2.

It can be seen that the calculated elevation angles cover the wobble effect, even for GEO satellites that are supposed to stay stationary. Accordingly, for such GEO satellites (e.g., the TianTong-1 satellites used as the representative in this research), the elevation angle from the observation point varies within a very limited angular range over a 24-hour period (e.g., with a maximum variation of less than 6°).

Given that only three satellites are visible simultaneously and a handset can maintain a signaling connection with only one satellite concurrently, users can easily adjust their device posture to align the DUT or its antenna toward the serving satellite as much as possible for better communication performance. Consequently,

Table 2: Calculated elevation angles over time for the Beijing and Shenzhen regions

	Elevation (deg)	TianTong-1_1_41725	TianTong-1_2_46916	TianTong-1_3_47321
Shenzhen	Min	58.63	57.86	45.96
	Max	64.94	61.48	49.63
	Mean	61.78	59.68	47.81
Beijing	Min	38.16	40.96	29.35
	Max	44.45	45.02	33.89
	Mean	41.30	42.99	31.62

the key performance metric for GEO handset antennas should emphasize their EIRP or gain within a specific angular range of the zenith. This differs from GPS terminals, which are designed with a uniform upper-hemisphere pattern to capture as many visible satellites as possible for better Position Velocity Time (PVT) precision. Accordingly, it is recommended to adopt some directional FoMs, such as requiring the Cumulative Distribution Function (CDF) curves, the average, or the minimum of EIRP or EIS values within a specific angular range of the zenith to be larger than the limit, to comprehensively characterize the OTA performance of GEO terminals.

To sum up, the recommended OTA testing FoMs are derived through a comparative analysis of their calculated coverage multiplicity and usage scenarios with those of GPS, and further separated for LEO and GEO constellations, respectively. For LEO mode, such as Starlink DTC in this case, it is reasonable to reuse TIS and UHIS metrics for receiver performance evaluation, while reusing the TRP metric and introducing a new FoM named UHRP (corresponding to UHIS) for radiation performance evaluation. For GEO mode, such as TianTong-1 in this case, it is suggested to define some directional FoMs (e.g., requiring the CDF curves, the average, or the minimum of EIRP and EIS values within a specific angular range of the zenith to be larger than the limit) to characterize radiated power and receiver performance, respectively.

III. CONCLUSION

The objective of this work is to determine key FoMs for OTA testing of NTN handsets, aiming to better characterize, distinguish, and rank the OTA performance of different NTN handsets. During the analysis, coverage models are first established in the STK, and the related quantitative coverage multiplicity analyses are then conducted for GEO and LEO constellations separately. The recommended OTA testing FoMs are then derived through a comparative analysis of their usage scenarios and calculated coverage multiplicity with those of GPS. Based on the calculated coverage multiplicity as well as the usage scenarios comparison, it is recommended to reuse the TIS and UHIS metrics for receiver performance evaluation of LEO DTS terminals, while reusing the TRP metric and introducing a new FoM named UHRP (corresponding to the UHIS) for their radiation performance evaluation. Meanwhile, some directional FoMs (e.g., requiring the CDF curves, the average, or the minimum of EIRP and EIS values within a specific angular range of the zenith to be larger than the limit) are proposed for GEO handsets' OTA performance evaluation. The recommended FoMs for OTA testing of NTN DTS handsets are considered to be a good starting point for related OTA methodology development.

ACKNOWLEDGMENT

This work was supported by Beijing Natural Science Foundation under Grant L253002.

REFERENCES

[1] X. You, C.-X. Wang, J. Huang, X. Gao, Z. Zhang, M. Wang, Y. Huang, C. Zhang, Y. Jiang, J. Wang, M. Zhu, B. Sheng, D. Wang, Z. Pan, P. Zhu, Y. Yang, Z. Liu, P. Zhang, X. Tao, S. Li, Z. Chen, X. Ma, C.-L. I, S. Han, K. Li, C. Pan, Z. Zheng, L. Hanzo, X. S. Shen, Y. J. Guo, Z. Ding, H. Haas, W. Tong, P. Zhu, G. Yang, J. Wang, E. G. Larsson, H. Q. Ngo, W. Hong, H. Wang, D. Hou, J. Chen, Z. Chen, Z. Hao, G. Y. Li, R. Tafazolli, Y. Gao, H. V. Poor, G. P. Fettweis, and Y.-C. Liang, "Towards 6G wireless communication networks: Vision, enabling technologies, and new paradigm shifts," *Sci. China Inf. Sci.*, vol. 64, pp. 1–74, 2021.

[2] M. M. Azari, S. Solanki, S. Chatzinotas, O. Kodheli, H. Sallouha, A. Colpaert, J. F. M. Montoya, S. Pollin, A. Haqiqatnejad, A. Mostaani, E. Lagunas, and B. Ottersten, "Evolution of non-terrestrial networks from 5G to 6G: A survey," *IEEE Comm. Surveys & Tutorials*, vol. 24, no. 4, pp. 2633–2672, 2022.

[3] M. Vaezi, A. Azari, S. R. Khosravirad, M. Shirvanimoghaddam, M. M. Azari, D. Chasaki, and P. Popovski, "Cellular, wide-area, and non-terrestrial IoT: A survey on 5G advances and the road toward 6G," *IEEE Comm. Surveys & Tutorials*, vol. 24, no. 2, pp. 1117–1174, 2022.

[4] I.-K. Fu, O. Liberg, S. Chatzinotas, T. Q. S. Quek, and P. Xiao, "Guest Editorial: 6G

non-terrestrial networks," *IEEE Wireless Communications*, vol. 30, no. 6, pp. 10–11, Dec. 2023.

[5] F. Rinaldi, H.-L. Mättänen, J. Torsner, S. Pizzi, S. Andreev, A. Iera, Y. Koucheryavy, and G. Araniti, "Non-terrestrial networks in 5G & beyond: A survey," *IEEE Access*, vol. 8, pp. 165178–165200, 2020.

[6] H. Al-Hraishawi, H. Chougrani, S. Kisseleff, E. Lagunas, and S. Chatzinotas, "A survey on nongeostationary satellite systems: The communication perspective," *IEEE Comm. Surveys & Tutorials*, vol. 25, no. 1, pp. 101–132, 2023.

[7] Q. T. Ngo, Z. Tang, B. Jayawickrama, Y. He, E. Dutkiewicz, and B. Senanayake, "Timeliness of information in 5G non-terrestrial networks: A survey," *IEEE Internet Things J.*, vol. 11, no. 21, pp. 34652–34675, Nov. 2024.

[8] 3GPP, TR 38.811: "Study on New Radio (NR) to support non-terrestrial networks," V1.0.0, 2018.

[9] 3GPP, TR 38.821: "Solutions for NR to support Non-Terrestrial Networks (NTN)," V16.2.0, 2023.

[10] G. Araniti, A. Iera, S. Pizzi, and F. Rinaldi, "Toward 6G non-terrestrial networks," *IEEE Network*, vol. 36, no. 1, pp. 113–120, Jan. 2022.

[11] A. Sattarzadeh, Y. Liu, A. Mohamed, R. Song, P. Xiao, Z. Song, H. Zhang, R. Tafazolli, and C. Niu, "Satellite-based non-terrestrial networks in 5G: Insights and challenges," *IEEE Access*, vol. 10, pp. 11274–11283, 2022.

[12] Y. He, Y. Xiao, S. Zhang, M. Jia, and Z. Li, "Direct-to-smartphone for 6G NTN: Technical routes, challenges, and key technologies," *IEEE Network*, vol. 38, no. 4, pp. 128–135, July 2024.

[13] S. Saleh, P. Zheng, X. Liu, H. Chen, M. F. Keskin, B. Priyanto, M. Beale, Y. Ettefagh, G. Seco-Granados, T. Y. Al-Naffouri, and H. Wymeersch, "Integrated 6G TN and NTN localization: Challenges, opportunities, and advancements," *IEEE Commun. Stand. Mag.*, vol. 9, no. 2, pp. 63–71, 2025.

[14] S. Huang, X. Chen, S. Yan, Y. Ren, J. Yi, and Y. Huang, "An effective method for episphere total radiated power tests of millimeter-wave antenna arrays," *IEEE Trans. Instrum. Meas.*, vol. 72, pp. 1–3, 2023.

[15] X. An, F. Liu, M. Qu, and S. Sun, "Measurement grid optimization for OTA testing of 5G smart watches," *Sensors*, vol. 25, p. 3185, 2025.

[16] M. Qu, G. Liu, P. Wang, and S. Sun, "Removing phase misalignment in the validation of a compact antenna test range for 5G mm-Wave UE OTA testing," *IEEE Trans. Electromagn. Compat.*, vol. 63, no. 4, pp. 1295–1299, Aug. 2021.

[17] X. Chen, X. Liu, and S. Sun, "Research on OTA testing optimization of 5G IoT devices," *Applied Computational Electromagnetics Society (ACES) Journal*, vol. 38, no. 01, pp. 1–6, Jan. 2023.

[18] S. Huang, F. Li, and X. Chen, "An improved method for total radiated power tests in anechoic chambers," *IEEE Trans. Instrum. Meas.*, vol. 71, pp. 1–9, 2022.

[19] CTIA Certification Program: "Test Plan for Wireless Device Over-the-Air Performance," V3.9.3, Sep. 2021.

[20] CTIA Certification Program: "Test Plan for 2x2 Downlink MIMO and Transmit Diversity Over-the-Air Performance," V1.2.2, Dec. 2021.

[21] CTIA Certification Program: "Test Plan for Millimeter-Wave Wireless Device Over-the-Air Performance," V1.0.2, Dec. 2020.

[22] 3GPP, TR 37.977: "Universal Terrestrial Radio Access (UTRA) and Evolved Universal Terrestrial Radio Access (E-UTRA); Verification of radiated multi-antenna reception performance of User Equipment (UE)," V16.0.0, June 2020.

[23] 3GPP, TR 38.810: "NR; Study on test methods," V16.6.0, Sep. 2019.

[24] CTIA Certification Program. CTIA 01.20: "Test Methodology, SISO, Anechoic Chamber," V4.0.0; Feb. 2022.

Siyang Sun received the Ph.D. degree from the School of Electronic Engineering, Beijing University of Posts and Telecommunications (BUPT), Beijing, China, in 2011. He is currently an Associate Professor with China Telecommunication Technology Labs (CTTL), China Academy of Information and Communications Technology (CAICT). Since 2018, he has been a senior algorithm researcher at CTTL, CAICT and has been deeply involved in the research, standardization, and globalization of 5G/5G-Advanced MIMO OTA. He currently serves as the Co-Chair of the CTIA MIMO OTA Working Group. His research interests include MIMO antennas, metamaterials, and OTA testing for 5G, 5G-Advanced, and 6G communications.

Meijun Qu received the Ph.D. degree from the School of Information and Communication Engineering, Beijing University of Posts and Telecommunications (BUPT), Beijing, China, in 2020. From 2020 to 2025, she was with the School of Information and Communication Engineering, Communication University of China. Since 2025, she has been with the National Key Laboratory of Scattering and Radiation, Beijing, as an Associate Professor. Her research interests include antenna, metamaterial, and electromagnetic compatibility.

Zheng Liu received the B.S. degree from the Communication University of China in 2006 and the M.S. degree from the School of Information and Communication Engineering, Beijing University of Posts and Telecommunications (BUPT) in 2010. He is currently a senior engineer with China Telecommunication Technology Labs (CTTL), China Academy of Information and Communications Technology (CAICT). From 2010 to 2015, he led the TDD LTE/LTE-Advanced MIMO OTA research, standardization, and globalization at CAICT. Since 2015, he has been leading the R&D of 5G and 6G MIMO OTA at CAICT. He currently serves as the Chair of the CCSA TC9 WG5. His research interests include 5G-A and 6G channel models and transmission new techniques, AI enabled channel prediction and digital twin, and measurement and testing.

Design of Wideband High Out-of-Band Suppression Filtering Antenna Based on Multi-Lobe Dipole Structure

Jiangling Dou[1,2], Yinsu Yuan[2], Tao Shen[3], and Jian Song[2]

[1]Yunnan Key Laboratory of Computer Technologies Application
Kunming University of Science and Technology
Kunming, 650500, Yunnan, China
jianglingdou@kust.edu.cn

[2]School of Information Engineering and Automation
Kunming University of Science and Technology
Kunming, 650500, Yunnan, China
20232204060@stu.kust.edu.cn, songjian@kust.edu.cn

[3]Yunnan Vocational College of Mechanical and Electrical Technology
Kunming, 650500, Yunnan, China
shentao@kust.edu.cn

Abstract – A two-layer filtering antenna based on a multi-lobe dipole structure is presented in this paper. Parasitic substrates and vertical copper elements are incorporated between the upper and lower substrates, with impedance matching improved by overcoming the closed magnetic flux limitation. Filtering performance is achieved through interaction with semi-circular-rectangular dual-mode matching structures and vertical metal, the composite structure can generate reverse current distribution. As a result, high-roll-off radiation nulls are formed and frequency selectivity is enhanced. In order to simultaneously enhance out-of-band suppression, high-current etching technology is employed to reconstruct the current path, etching semi-circular-rectangular dual-shape composite matching structures on the radiation patch, thus a significant improvement in gain stability is achieved. Distributed current control technology is utilized to decompose the dipole into multiple lobes, ensuring uniform current distribution and reducing concentration effects. Etched rectangular holes in the surrounding electromagnetic shielding isolation walls help reduce cross-polarization by suppressing surface waves and edge diffraction. The design achieves an impedance bandwidth exceeding 36%, out-of-band suppression exceeding 32 dB, a peak gain of 8.9 dBi, with cross-polarization levels below -30dB and -26dB in the E- and H-planes, respectively.

Index Terms – Dual-mode impedance matching structures, electromagnetic shielding isolation wall, filtering antenna, multi-lobe dipole

I. INTRODUCTION

In recent years, filtering antennas have played a significant role in wireless communication systems. Filtering characteristic are achieved in traditional filtering antennas by integrating filters. For instance, Yagi-Uda antennas incorporate absorbing branches [1] or combine band-stop filters with grounded resistors [2] to realize filtering functionality. Moreover, bandpass filters can be integrated with antennas, such as monopoles coupled with bandpass filters [3], or antenna systems incorporating power amplifiers and RF bandpass filters [4]. However, these designs typically increase the overall dimensions and profile of the antenna. Reference [5] proposed a compact, low-profile broadband filtering antenna without additional filtering structures. The design uses inverted Y-shaped branches and quarter-wavelength impedance matching, achieving over 33.2% impedance bandwidth and out-of-band suppression of more than 17 dB at low frequencies and 10 dB at high frequencies. In [6], the antenna consisted of two folded arms and an extended arm printed on a single-layer substrate. Two tunable radiation nulls are generated at the edges of the passband without requiring filtering circuits. Ultimately, a 15.5% impedance bandwidth and an average gain of 2 dBi are achieved. Nevertheless, the bandwidth and out-of-band suppression levels of the filtering antennas in [5] and [6] still require further improvement.

Reference [7] proposed a dual-band filtering antenna. By incorporating two and four metal–insulator–metal (MIM) capacitors, the design significantly enhanced high-frequency out-of-band suppression while

Submitted On: July 26, 2025
Accepted On: September 08, 2025

https://doi.org/10.13052/2026.ACES.J.410211

achieving a 2.3% bandwidth, over 20dB upper stopband suppression, and cross-polarization levels below −15 dB. In [8], a single-layer filtering patch antenna was introduced, featuring a rectangular patch embedded in a ring patch, operating in the higher-order TM_{12} mode. It achieved a 6.9% impedance bandwidth, 9.0 dBi peak gain, over 16 dB out-of-band suppression, and cross-polarization below −20 dB. Reference [9] introduced a broadband filtering antenna using substrate integrated suspended line (SISL) technology with a double-headed structure and open-stub design. It achieved a 32.9% impedance bandwidth, over 15.5 dB out-of-band suppression, and cross-polarization below −20 dB. Reference [10] presents an improved defected ground slot antenna with a 114% ultra-wideband impedance bandwidth, but the passband stability is weak, and the out-of-band suppression is inadequate. Reference [11] introduces a 5G filtering antenna combining U-shaped resonators and a Γ-shaped antenna. It achieves less than −24 dBi out-of-band gain and good suppression, but the peak gain is 3.056 dBi with an 8% impedance bandwidth, indicating that improvements are still necessary. In [12], a magnetoelectric dipole filtering antenna is proposed. By utilizing the magnetoelectric (ME) dipole antenna's radiation null characteristics, traditional methods are enhanced, with the integration of vertical parasitic metal planes and T-shaped shorted lines, a 49.4% impedance bandwidth is achieved, along with over 16.6 dB of low-frequency out-of-band suppression and more than 26 dB of high-frequency stopband suppression. However, despite these significant breakthroughs, existing designs still face some challenges, such as antenna size and complex manufacturing processes. The issue of simultaneously achieving high radiation performance and wide-frequency high gain remains unresolved, so further research and improvements are needed in filtering antenna.

In order to achieve high radiation performance while improving out-of-band suppression levels, strong current coupling control technology is applied in this study. The radiation dipoles are decomposed into multiple sub-lobes. This decomposition establishes a strong current distribution pattern and significantly improves out-of-band suppression. The isolation wall reduces the cross-polarization level, optimizing the radiation performance. Furthermore, isolation walls improve the out-of-band suppression level of the filtering antenna while maintaining good radiation performance. The filtering antenna achieves over 36% impedance bandwidth, 8.9 dBi peak gain, with cross-polarization levels below −30 dB and −26 dB in the E- and H-planes, respectively. In addition, the out-of-band suppression levels at both ends of the passband are below 32 dB and 33 dB, respectively.

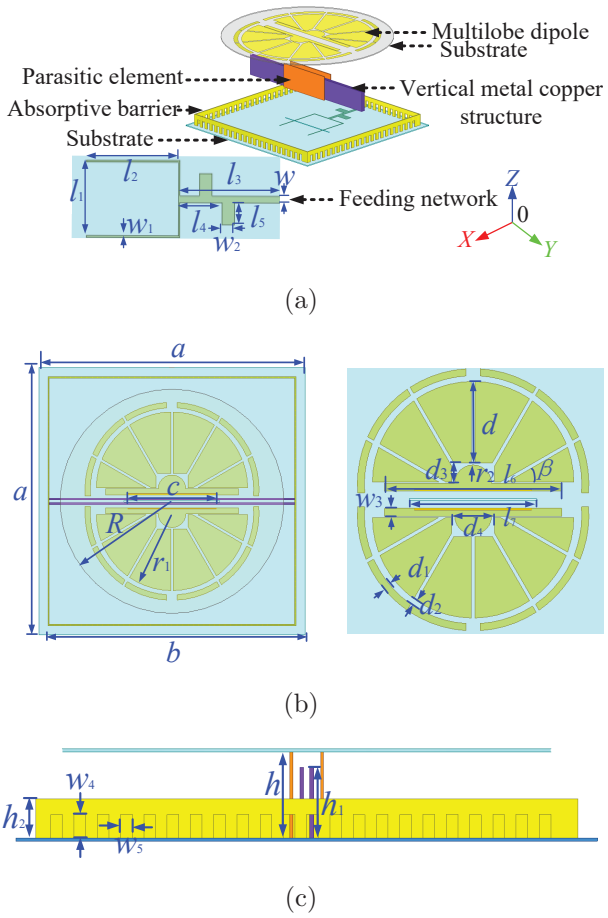

Fig. 1. The configuration of the proposed antenna. (a) 3D perspective, (b) Top view, (c) Side view.

Table 1: Dimensional parameters for the antenna (Unit: mm)

a	b	l_1	l_2	l_3	l_4	l_5
50	46.6	12	14.6	16	3	3.5
w	w_1	w_2	w_3	w_4	w_5	l_6
1	0.25	2	1.1	2.6	1	25
l_7	c	R	r_1	d	d_1	d_2
18	16.6	21	14.2	11.5	1	0.87
d_3	d_4	r_2	β	h	h_1	h_2
2.7	6	2.6	30	8.3	6	3.7

II. ANTENNA DESIGN AND OPTIMIZATION

A. Antenna configuration

As illustrated in Fig. 1, the antenna adopts Rogers 4035 with a thickness of 0.254 mm for both upper and lower substrates, vertical parasitic plates, and surrounding isolation walls, with two copper blocks of 0.34 mm thickness placed between the parasitic plates.

The antenna adopts a coupled feeding method, featuring a Y-shaped broadband feeding network on the substrate bottom plane with multi-branch configuration. The semicircular radiating dipoles on the upper substrate are split into several radiating lobes. Two semi-circular-rectangular dual-mode coupling structures are located between the two dipoles. The dimensional parameters of the antenna are summarized in Table 1.

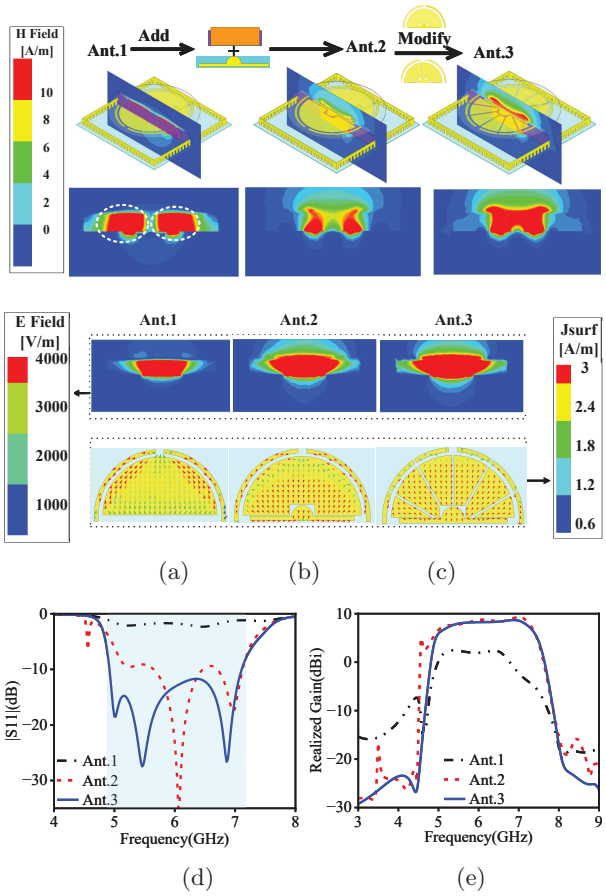

Fig. 2. (a) Magnetic Field, Electric Field and Current Field of Ant. 1, (b) Ant. 2, (c) Ant. 3 at 5.5Hz, (d) S11, (e) Realized gain.

B. Antenna design procedure

As can be seen from Fig. 2 (a), a classic three-layer configuration is adopted in Ant.1, composed of a substrate, patch, and supporting metal block. The current exhibits a multidirectional distribution. According to the Maxwell-Ampere law, when the current density J is spatially dispersed with inconsistent directions, it generates weak and scattered magnetic field H in specific areas. The reverse current causes the magnetic field components to cancel out, as shown in Ant.1 in Fig. 2. Ampere's circuital law indicates that curved current fields produce closed magnetic flux lines. The independence of current distribution reduces the effective value of loop integration, and the dispersed magnetic field prevents radiation energy from being concentrated. Combining the Poynting vector formula $S = \frac{1}{2}\mathrm{Re}[\tilde{E} \times \tilde{H}^*]$, $P_{\mathrm{rad}} = \int_S S \cdot dA$ and gain equation $G = 4\pi \frac{P_{\mathrm{rad}}}{P_{\mathrm{in}}}$, when the input power remains constant, the instability of the electric and magnetic fields reduces the Poynting vector, resulting in a decrease in bandwidth gain, which causes very low gain across the frequency band and the absence of distinct radiation nulls. To address the performance limitations of Ant.1 and mitigate the effects of closed magnetic flux lines, magnetic flux control technology is employed. Vertical parasitic plates are added to the metal block, and rectangular slots are etched into the upper semicircular radiating patch, thereby expanding the radiation coverage. Simultaneously, a dual-mode coupled impedance matching structure is introduced around the slots using reverse current guidance technology. At 5.5 GHz, the magnetic field of antenna shows a tendency to break the closed magnetic flux lines and converge towards the radiation center of antenna, significantly improving the coupling effect of the antenna. As evident from Fig. 2 (e), the gain passband improved by over 6 dBi compared to Ant.1.

In addition, by concentrating the current and coupling the magnetic field, the dipole is etched into six 30° lobes, and an electromagnetic shielding isolation wall is added, as shown in Fig. 2 (c), resulting in a bandwidth greater than 36%, a peak gain of 8.9 dBi, and out-of-band suppression levels exceeding 32 dBi and 33 dBi.

C. Analysis of dual-mode coupling

To optimize antenna coupling modes, this study leverages current vector distribution. As shown in Fig. 3 (a), the radiation patch of Ant A features a rectangular monopole shape, where the currents flow without concentration or directionality. This results in a dispersed current pattern that fails to effectively focus the radiation, leading to insufficient out-of-band suppression, as demonstrated in Fig. 3 (c). Ant B adopts a rectangular-rectangular monopole composite impedance matching coupling structure, the current on the coupling element shows obvious reverse concentration and dispersion trends, a stronger radiation direction is formed, where the main radiation wave of antenna is concentrated within a relatively narrow range, significantly enhancing out-of-band suppression. Ant C further implements semi-circular-rectangular dual-mode aggregated coupling, with strong current distributed around the coupling element. With concentrated flow paths, the strong current distribution is enhanced, leading to a further reduction in high-frequency out-of-band suppression.

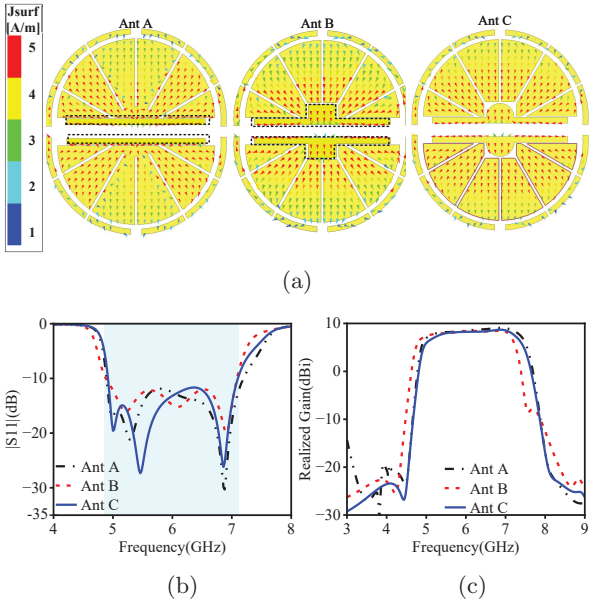

Fig. 3. (a) The effect of different coupling forms on the antenna current at 5.5 GHz, (b) S11, (c) Realized Gain.

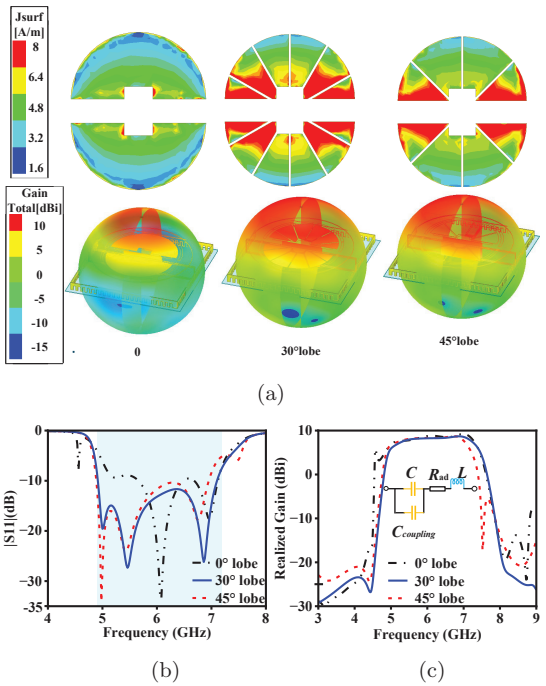

Fig. 4. (a) The effect of different angle lobe structures on antenna current distribution and 3D Gain Total at 5.5 GHz, (b) S11, (c) Realized Gain and equivalent circuit.

D. Transition from dipole to multi-lobe pattern

The study adopts a multi-lobe capacitive coupling strong current path topology reconstruction technology, which transforms irregular weak currents into regular and uniform strong current paths. As shown in Fig. 4 (a), when the semicircular radiation patch is without a slot, the antenna current is primarily concentrated around the edges of the dipole patch with weak intensity, resulting in radiation energy being dispersed. Thus, both the impedance bandwidth and out-of-band suppression are suboptimal. In the 45° lobe configuration, dipoles are mainly concentrated on the lobe radiating patch adjacent to the dual-mode coupling structure, the current gathers on these segments while enhancing the radiation intensity, leading to significant improvements in both impedance bandwidth and out-of-band suppression at low frequency. When the lobe angle is 30°, strong currents are primarily distributed on the first and second 30° lobe structures, which enhances the radiation effect in the main radiating region, impedance bandwidth is broadened and out-of-band suppression levels in the high-frequency range are improved. From the 3D gain patterns in Fig. 4 (a), compared to the 30° and 45° lobe configurations, when the lobe angle is 0°, the overall radiation performance of the antenna does not meet expectations, particularly in terms of the back lobe characteristics in the far-field radiation pattern, where significant deficiencies exist. In contrast, the 30° and 45° lobes demonstrate uniform radiation, with the 30° lobe configuration providing a wider and stronger radiation coverage area, as shown by the 3D gain in Fig. 4 (a).

In the antenna model, the insertion loss is equivalent to R_{ad}, the parasitic inductance of the intermediate layer is equivalent to L, the parallel capacitance between the radiating patch and the ground plane is equivalent to C, and the gap coupling capacitance between multi-lobe elements is equivalent to $C_{coupling}$, as illustrated in Fig. 4 (c). When the patch path is extended, the gap coupling equivalent capacitance increases. According to equation (1), since the high-frequency resonance frequencies exhibit strong fringe coupling effects, the increase in inductance leads to a decrease in the resonant frequency. In summary, by altering the distribution path of the current, the current concentration area is optimized. The dipoles of the antenna are divided into lobes, the radiation directionality and out-of-band suppression performance are optimized and the current distribution is optimized by controlling the lobe angle.

$$f = \frac{1}{2\pi\sqrt{L(C+C_{\text{coupling}})}}. \tag{1}$$

E. Generation of radiation nulls and analysis of isolation walls

To analyze the generation of radiation nulls and the role of the isolation walls of antenna, the current distribution vector diagrams at the null frequencies are shown in Fig. 5. From Fig. 5 (a), it can be observed that at frequencies of 4.3 GHz and 8.1 GHz, the dual-mode

coupling and the copper structure exhibit symmetrical and oppositely directed current distributions. The cancellation of the magnetic fields leads to radiation nulls on both sides of the passband. As illustrated in Fig. 5 (b), after the introduction of the isolation walls, the electromagnetic shielding effect significantly reduces the spread of electric fields and currents. The increased current density enhances polarization consistency, concentrates the radiation pattern, and cross-polarization levels are reduced, as demonstrated in Fig. 5 (c) and Fig. 5 (d). Therefore, the addition of isolation walls can suppress the diffusion of electric fields in ineffective directions, reducing radiation dispersion. This concentrates the electric field energy in specific regions, radiation directivity is improved and out-of-band suppression performance is enhanced.

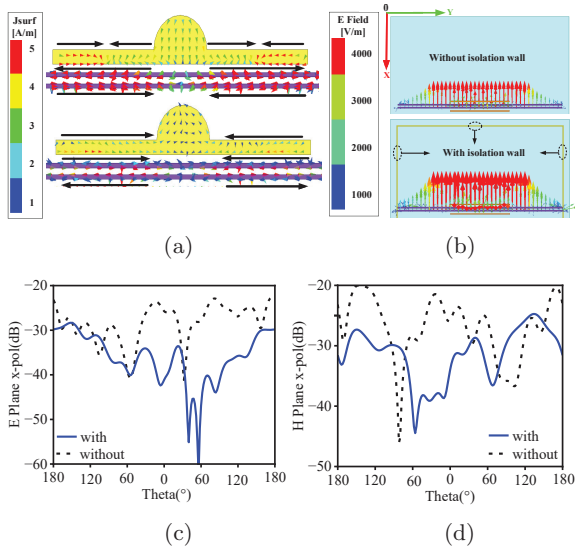

Fig. 5. (a) Current vector distribution of the dual-mode dipole and copper structures at frequencies of 4.3GHz and 8.1GHz, (b) The effect of with and without isolation wall on the electric field distribution at 5.5 GHz, (c)-(d) The effect of the isolation wall on the cross-polarization in both the E plane and H plane at 5.5 GHz.

III. PARAMETRIC ANALYSIS

In order to better assess the overall performance of the antenna, the parameters in Fig. 6 reveal the impact of key parameters on antenna performance. At low frequencies, the current flows along the expanded path of the main radiating structure. Increasing the radius of the coupling element extends the antenna's equivalent electrical length, which leads to a reduction in low-frequency resonance, while leaving high-frequency currents unaffected. The branch of the feeding network l_5 is only 3.5 mm, much smaller than the quarter wavelength at low-frequency resonance. Therefore, adjusting the

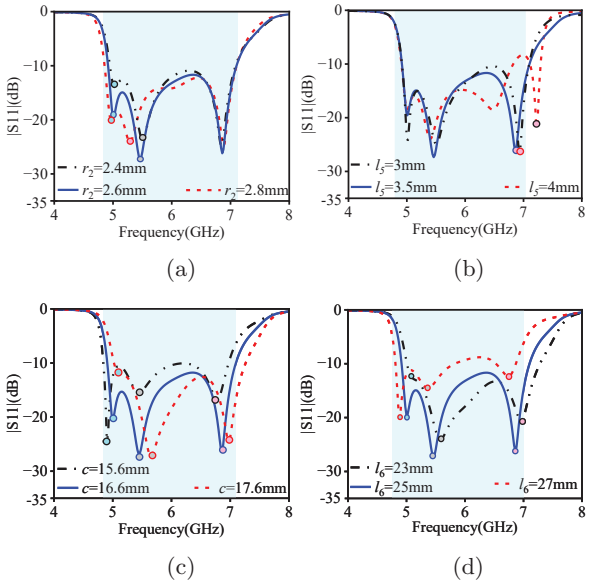

Fig. 6. The effect of different parameters on the left and right resonance frequencies: (a) r_1, (b) l_5, (c) c, (d) l_6.

branch length shifts the high-frequency resonance without affecting the low- and mid-frequency points.

When the length c of the parasitic element increases, all resonance points in the S-parameters shift toward higher frequencies. However, as c continues to increase, the resonance peak value first decreases and then increases, while minimum value of the high-frequency resonance first decreases, then returns to its original state. When increasing the rectangular element length l_6 in the dual-mode structure, all resonance points shift toward lower frequencies, with the low-frequency resonance point first decreasing and then increasing. In summary, the resonance frequency and impedance bandwidth of antenna can be effectively tuned by adjusting parameters r_2, l_5, c , and l_6. The optimal performance occurs when $r_2 = 2.4$ mm, $l_5 = 3$ mm, $c = 16.6$ mm, and $l_6 = 25$ mm and the impedance bandwidth of antenna reaches over 36%.

Since radiation nulls are a crucial feature of filtering antennas, this study conducts a comparative analysis of key parameters that influence radiation nulls, as shown in Fig. 7. The parasitic elements and radiating patches on the upper substrate are the primary radiating structures contributing to this effect. Therefore, changes in their shape, size, and layout play a dominant role in determining the position and number of radiation nulls. As shown in Figs. 7 (a–b), by adjusting the length of the parasitic elements, the petal angles of the multi-lobe dipole can be used to regulate the low-frequency and high-frequency radiation nulls, respectively. Furthermore, the radius of the semicircle on the upper patch and in the dual-shape coupler can be used to adjust

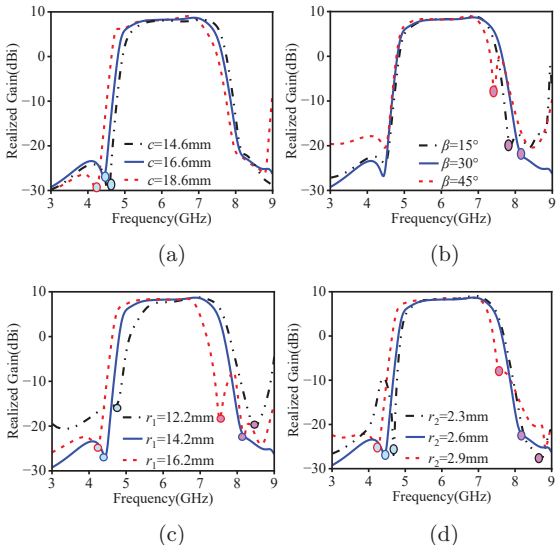

Fig. 7. The effect of different parameters on the radiation zero points: (a) c, (b) β, (c) r_1, (d) r_2.

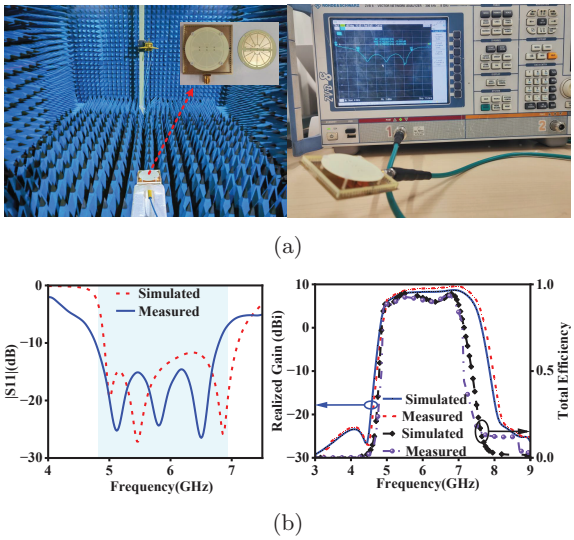

Fig. 8. (a) Testing environment of proposed antenna, (b) Comparison of simulated and measured results.

radiation nulls position on both sides of the passband. When increasing r_1 and r_2, combined with equation (1), the increased electrical length shifts both high- and low-frequency radiation nulls toward lower frequencies, as demonstrated in Figs. 7 (c–d). Therefore, by adjusting these parameters properly, the distribution of radiation nulls within the operating frequency band of antenna can be controlled effectively. This also further enhances the out-of-band suppression and radiation directionality, thereby improving the overall performance of the antenna.

IV. RESULTS AND DISCUSSION

To validate the feasibility of the experimental results, the antenna is fabricated and tested to validate its performance. The simulation and measurement results are shown in Fig. 8. The insertion loss remains stable within the 5–7 GHz operating frequency range. The measured gain peak reaches 9.5 dBi, with a deviation of less than 0.6 dBi from the simulation results, validating the accuracy of the model. The overall radiation efficiency is consistently maintained above 90%, with particularly high efficiency between 5–7 GHz. However, the processing tolerance of the dielectric substrate and manufacturing error in the coupling capacitance cause a slight shift in the resonant point. The impedance bandwidth is still consistent with the simulation. These results show the high degree of agreement between the measured and simulated data.

To better understand the distribution characteristics of the radiation and reception capability of antenna in electromagnetic waves, Fig. 9 presents the comparative radiation patterns in both the yoz-plane and xoy-plane,

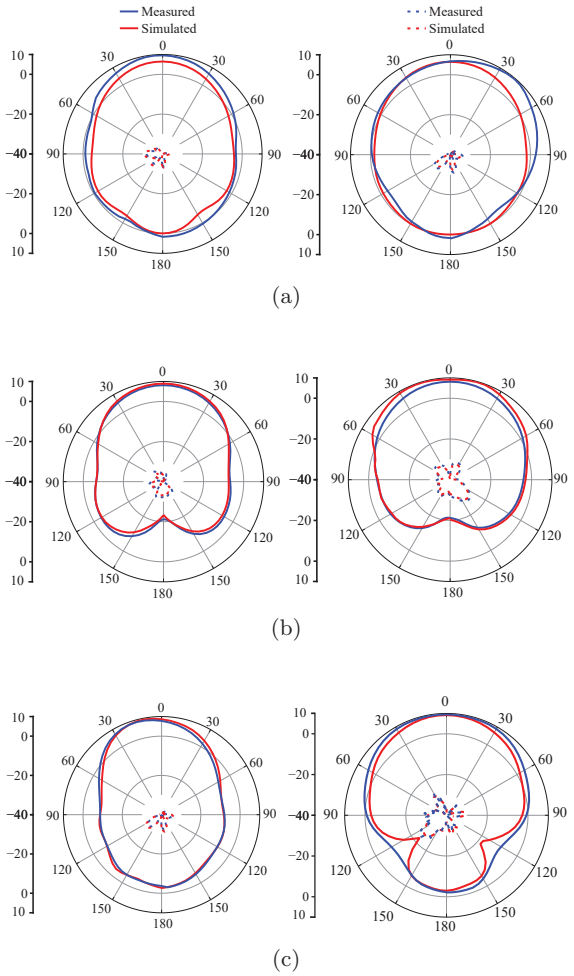

Fig. 9. Simulated and measured radiation patterns of the antenna at different frequencies: (a) at 5 GHz, (b) at 5.5 GHz, (c) at 6.9 GHz.

showing a strong agreement between the measured data and the simulated data in the same polarization direction. At 5 GHz and 5.5 GHz, the main polarization outperforms cross-polarization by 35 dB and 30 dB, respectively. The cross-polarization in the yoz-plane stays below −30 dB. At 6.9 GHz, the main and cross-polarization difference slightly decreases. The front-to-back ratio exceeds 13 dB at the high-frequency resonant point, showing stable and favorable radiation performance overall. At 5 GHz and 5.5 GHz, the main polarization outperforms cross-polarization by 35 dB and 30 dB, respectively. The cross-polarization in the yoz-plane stays below −30 dB. At 6.9 GHz, the main and cross-polarization difference slightly decreases. The front-to-back ratio exceeds 13 dB at the high-frequency resonant point, showing stable and favorable radiation performance overall.

Table 2 provides a detailed comparison of the performance of the proposed antenna with other antennas in similar frequency bands. The comparison data shows that the antenna designed in this study exhibits significant advantages in multiple key performance metrics.

In terms of operating bandwidth, the antenna demonstrates a impedance bandwidth from 4.92 GHz to 7.10 GHz. In comparison to all the references in Table 2, this antenna employs current-control technology and isolation wall electromagnetic shielding technology, resulting in higher out-of-band suppression and lower cross-polarization. In contrast to references [14, 15, 17], and [19], the proposed antenna demonstrates a more stable high gain.

Table 2: Comparison of the designed antenna with similar-band antennas from other literature

Ref.	Freq (GHz)	BW (%)	Gain (dBi)	OOBS (dB)	x-pol E/H (dBi)
[13]	2.29–2.69	16.10	9.60	>15 >17	−25/−20
[14]	1.11–1.39	22.40	4.50	>13 >12	−18/−19
[15]	9.80–10.20	4.00	8.50	>12 >13	−25/−25
[16]	3.19–3.85	18.80	9.50	>7 >9	−20/−18
[17]	4.45–5.52	21.50	4.80	>16 >19	−20/−16
[18]	3.28–3.79	14.40	11.14	>18 >18	−22/−21
[19]	8.50–10.00	16.20	8.50	>12 >19	−20/−20
[20]	4.28–5.34	22.04	10.40	>15 >16	−22/−20
This work	7.92–7.10	36.30	8.90	>32 >33	−30/−26

BW represents bandwidth, OOBS represents out-of-band suppression, x-pol represents cross-pol.

V. CONCLUSION

A double-layered filtering antenna based on a multi-lobe dipole structure is proposed in this study. A symmetrical upper-lower dielectric substrate configuration with integrated parasitic elements is featured in the antenna, combined with a distinctive semi-circular-rectangular composite impedance matching structure. The radiating dipole is decomposed into multiple monopoles through distributed current control technology. An electromagnetic shielding wall with etched rectangular apertures is incorporated, significantly improving the radiation performance of the antenna. The test results show that the antenna performs well in the 5.5 GHz frequency band, with an impedance bandwidth of 36%, a peak gain of 8.9 dBi, cross-polarization levels in the E-plane and H-plane below −30 dB and −26 dB, respectively, and an out-of-band suppression level greater than 32 dB.

ACKNOWLEDGMENT

This paper is supported by Yunnan Fundamental Research project [202401AT070351, 202401AT070376, 202301AV070003], Yunnan Key Laboratory of Computer Technologies Application Open Fund, the Natural Science Foundation of China [61971208], Yunnan Young Top Talents of Ten Thousands Plan [Shen Tao, Yunren Social Development No. 2018 73], College personnel training project [202101BE070001-008], and partially by the Major Science and Technology Projects in Yunnan Province under Grant [202302AG050009 and 202202AD080013].

REFERENCES

[1] S. Wang, F. Fan, R. Gomez-Garcia, L. Yang, Y. Li, and S.-W. Wong, "A planar absorptive-branch-loaded quasi-Yagi antenna with filtering capability, and flat gain," *IEEE Antennas Wireless Propag. Lett.*, vol. 20, no. 9, pp. 1626–1630, Sep. 2021.

[2] D. Li, C. Yang, L. Shi, Y. Liu, Q. Chen, and N. Shinohara, "A high-gain filtering quasi-yagi antenna based on compressed third-order mode dipole," *IEEE Antennas Wireless Propag. Lett.*, vol.23, no. 10, pp. 2860–2864, Oct. 2024.

[3] J. Deng, S. Hou, L. Zhao, and L. Guo, "A reconfigurable filtering antenna with integrated bandpass filters for UWB/WLAN applications," *IEEE Trans Antennas Propag.*, vol. 66, no. 1, pp. 401–404, Jan. 2018.

[4] O. A. Iupikov, J.-R. Perez-Cisneros, P. Meyer, D. Akesson, R. Maaskant, and K. Buisman, "A cavity-backed patch antenna with distributed multi-port feeding, enabling efficient integration with Doherty power amplifier and band-pass filter," *IEEE Trans Antennas Propag.*, vol. 69, no. 8, pp. 4412–4422, Aug. 2021.

[5] G. Cheng, J. Zhou, B. Huang, L. Yang, and Z. Huang, "Compact low-profile wideband filtering antenna without additional filtering structure," *IEEE Antennas Wireless Propag. Lett.*, vol. 22, no. 10, pp. 2477–2481, Oct. 2023.

[6] X. Liu, K. Ning, S. Xue, L. Ge, K. W. Leung, and J.-F. Mao, "Printed filtering dipole antenna with compact size and high selectivity," *IEEE Trans Antennas Propag.*, vol. 72, no. 3, pp. 2355–2367, March 2024.

[7] D. Zhao, F. Lin, H. Sun, and X. Y. Zhang, "A miniaturized dual-band SIW filtering antenna with improved out-of-band suppression," *IEEE Trans Antennas Propag.*, vol. 70, no. 1, pp. 126–134, Jan. 2022.

[8] G. Liu, P. F. Hu, G. D. Su, and Y. M. Pan, "Bandwidth and gain enhancement of a single-layer filtering patch antenna using reshaped TM mode," *IEEE Antennas Wireless Propag. Lett.*, vol. 23, no. 1, pp. 314–318, Jan. 2024.

[9] N. Yan, C. Wang, Y. Luo, and K. Ma, "A low-profile broadband filtering dielectric resonator antenna based on SISL with the improvement of suppression level," *IEEE Open J. Antennas Propag.*, vol. 5, no. 2, pp. 430–436, Apr. 2024.

[10] H. L. Yang, H. T. Liu, X. P. Li, Y. P. Li, S. Z. Wang, J. S. Zhang, C. H. Wang, and Y. Fang, "A wideband high front-to-back ratio directional filtering slot antenna and its application in MIMO terminals," *Applied Computational Electromagnetics Society (ACES) Journal*, vol. 39, no. 11, pp. 980–986, Nov. 2024.

[11] S. J. Yan, C. Q. Zhang, Q. Chen, and M. S. Tong, "A novel compact filtering antenna for 5.0-GHz WLAN communication system," *Applied Computational Electromagnetics Society (ACES) Journal*, vol. 37, no. 9, pp. 996–1004, Sep. 2022.

[12] R. Hou, J. Ren, Y.-T. Liu, Y.-M. Cai, J. Wang, and Y. Yin, "Broadband magnetoelectric dipole filtering antenna for 5G application," *IEEE Antennas Wireless Propag. Lett.*, vol. 22, no. 3, pp. 497–501, Mar. 2023.

[13] L. Li, H. D. Xiong, W. Y. Wu, A. B. Fu, and J. Y. Han, "A T-shaped strips loaded wideband filtering patch antenna with high selectivity," *IEEE Antennas Wireless Propag. Lett.*, vol. 23, no. 1, pp. 89–93, Jan. 2024.

[14] X. Chen, X. Fang, Z. Wu, and L. Zhu, "A pattern-reconfigurable, compact, wideband filtering directive dipole antenna enabled with mixed couplings," *IEEE Antennas Wireless Propag. Lett.*, vol. 24, no. 1, pp. 237–241, Jan. 2025.

[15] K.-R. Xiang, F.-C. Chen, and Q.-X. Chu, "High selectivity and high gain X-band waveguide filtering antenna based on triple-mode resonator," *IEEE Trans Antennas Propag.*, vol. 69, no. 10, pp. 6953–6938, Oct. 2021.

[16] H. Yuan, F.-C. Chen, and Q.-X. Chu, "A wideband and high gain dual-polarized filtering antenna based on multiple patches," *IEEE Trans Antennas Propag.*, vol. 70, no. 10, pp. 9843–9848, Oct. 2022.

[17] B.-J. Chen, X.-S. Yang, and B.-Z. Wang, "A compact high-selectivity wideband filtering antenna with multipath coupling structure," *IEEE Antennas Wireless Propag. Lett.*, vol. 21, no. 8, pp. 1654–1658, Aug. 2022.

[18] T. Wang, N. Yan, M. Tian, Y. Luo, and K. Ma, "A low-cost high-gain filtering patch antenna with enhanced frequency selectivity based on SISL for 5G application," *IEEE Antennas Wireless Propag. Lett.*, vol. 21, no. 9, pp. 1772–1776, Sep. 2022.

[19] Y.-H. Ke, L.-L. Yang, Y.-Y. Zhu, J. Wang, and J.-X. Chen, "Filtering quasi-Yagi strip-loaded DRR antenna with enhanced gain and selectivity by metamaterial," *IEEE Access*, vol. 9, pp. 31755–31761, 2021.

[20] M. Tian, N. Yan, Y. Luo, and K. Ma, "A low-cost high-gain filtering patch antenna using SISL technology for 5G application," *IEEE Antennas Wireless Propag. Lett.*, vol. 20, no. 12, pp. 2270–2274, Dec. 2021.

Jiangling Dou was born in 1985 in Jiangsu Province, China. She received her Ph.D. degree in Electromagnetic Fields and Microwave Technology from Southeast University in 2018. She is currently working at Kunming University of Science and Technology. Her research interests include electromagnetic field theory and applications.

Yinsu Yuan was born in 1997 in Qujing, Yunnan, China. She is currently pursuing a master's degree at Kunming University of Science and Technology, focusing on the design of miniaturized filtering antennas.

Tao Shen (Senior Member, IEEE) earned his Ph.D. from the Illinois Institute of Technology in Chicago, Illinois, USA, in 2013. Presently, he holds the position of President at Yunnan Vocational and Technical College of Mechanical and Electrical Engineering. Dr. Shen has contributed to over 20 publications in prestigious SCIE-indexed journals and leading

international conferences within his research domains. His areas of expertise include image processing, artificial intelligence, and the Internet of Energy.

Jian Song (Member, IEEE) obtained his Bachelor of Engineering degree in Electronics Information Engineering from Jiangxi University of Science and Technology in Ganzhou, China. He later earned his Ph.D. in Electromagnetic Fields and Microwave Technology from the University of Electronic Science and Technology of China in Chengdu in 2015. Between 2015 and 2019, he served as an Algorithm Engineer at Huawei Technology Co., Ltd. in Shenzhen, China.